



INVESTIGATION OF THERMAL MANAGEMENT AND METAMATERIALS

THESIS

Calvin T. Roman, Captain, USAF

AFIT/GE/ENG/10-26

**DEPARTMENT OF THE AIR FORCE
AIR UNIVERSITY**

AIR FORCE INSTITUTE OF TECHNOLOGY

Wright-Patterson Air Force Base, Ohio

APPROVED FOR PUBLIC RELEASE; DISTRIBUTION UNLIMITED

The views expressed in this thesis are those of the author and do not reflect the official policy or position of the United States Air Force, Department of Defense, or the U.S. Government.

AFIT/GE/ENG/10-26

INVESTIGATION OF THERMAL MANAGEMENT AND METAMATERIALS

THESIS

Presented to the Faculty

Department of Electrical and Computer Engineering

Graduate School of Engineering and Management

Air Force Institute of Technology

Air University

Air Education and Training Command

In Partial Fulfillment of the Requirements for the

Degree of Master of Science in Electrical Engineering

Calvin T. Roman, BSEE

Captain, USAF

March 2010

APPROVED FOR PUBLIC RELEASE; DISTRIBUTION UNLIMITED

AFIT/GE/ENG/10-26

INVESTIGATION OF THERMAL MANAGEMENT AND METAMATERIALS

Calvin T. Roman, BSEE

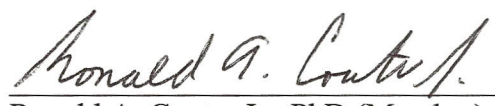
Captain, USAF

Approved:



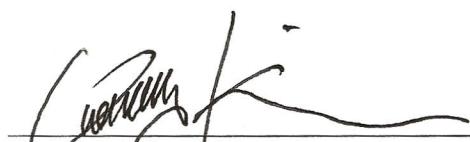
LaVern A. Starman, PhD, Major, USAF (Chairman)

15 Mar 10
Date



Ronald A. Couturier, Jr., PhD (Member)

11 May 10
Date



Yong C. Kim, PhD (Member)

11 MAR 10
Date

Abstract

Thermal metamaterials are materials composed of engineered, microscopic structures that exhibit unique thermal performance characteristics based primarily on their physical structures and patterning, rather than just their chemical composition or bulk material properties. The heat transfer performance attributes of a thermal metamaterial are such that similar performance cannot be obtained using conventional materials or compounds. Thermal metamaterials are an emerging technology, and are just now beginning to be acknowledged and developed by the microelectronics and material sciences community.

This thesis effort analyzed the current state of thermal metamaterial research, examined the physics and theory of heat transfer and electrical conductivity in thin film microelectronic designs, and then developed, modeled, fabricated, and characterized a series of ten proof-of-concept thermal metamaterial devices. Modeling and testing of these microelectromechanical systems (MEMS) based thermal metamaterial prototypes showed that the electrical and thermal conductivity of the material can be switched or tuned within a certain operational range, and that this switching is a function of actuation of the metamaterial's structural elements, not just its chemical composition.

In addition, this thesis presented the physics and fundamental principles of carbon nanotubes (CNTs). This background work supported later detailed description of a series of prototype CNT braided ropes. The diameter, electrical resistivity and conductivity, and heat transfer characteristics of these CNT braided rope prototypes was determined. These unique prototypes exhibited performance attributes that should prove useful to future thermal metamaterial designs.

Acknowledgments

I'd like to thank Major Starman, Dr. Coutu, and Dr. Kim for their expertise and advice regarding this research over the past year. Studying under such sharp and engaged leadership has been an honor and made the overall experience very rewarding. Thank you to my classmates: Mike, Rob, Brad, Nina, Derrick, Jonathan, and Richard. Having good friends made the tough times a wee bit more bearable. The best of luck to you all in your personal and professional endeavors. Thank you to the Lord God almighty, who has bestowed countless blessings upon myself, my family, and our great nation. Finally, I thank my wife, who lovingly and patiently has lived the life of an "AFIT widow" for the last 20 months! You may now return to your rightful seat at the center of my attention.

Calvin Roman

Table of Contents

	Page
<i>Abstract</i>	<i>vii</i>
<i>Acknowledgments</i>	<i>viii</i>
<i>Table of Contents</i>	<i>ix</i>
<i>Table of Figures</i>	<i>xii</i>
<i>List of Tables</i>	<i>xxiii</i>
<i>Acronym List</i>	<i>xxiv</i>
<i>Introduction</i>	<i>1</i>
1.1 Introduction to Metamaterials.....	2
1.2 Problem Background.....	4
1.3 Thesis Objective	5
1.4 Summary.....	6
<i>Background Theory</i>	<i>8</i>
2.1 Overview	8
2.2 PolyMUMPs™ Fabrication Process.....	8
2.3 Heat Transfer Theory Applied on a MEMS Scale.....	10
2.3.1 Overview	10
2.3.2 Thermal conduction	11
2.3.3 Thermal radiation.....	16
2.3.4 Thermal convection	24
2.3.5 Summary	26
2.4 Electrical Conductivity Applied on a MEMS Scale.....	27
2.5 MEMS Actuation Schemes.....	31
2.5.1 Overview	31
2.5.2 Bimorph cantilever beam actuators	31
2.5.3 Electrostatic Actuation.....	35
2.6 Introduction to Carbon Nanotubes	38
2.6.1 Overview.....	38
2.6.2 History of CNTs.....	38
2.6.3 Types of CNTs	39
2.6.4 Properties of CNTs	40
2.6.5 CNT physics overview.....	42

2.6.6	Techniques of fabricating CNTs	45
2.7	Summary.....	49
Methodology.....		50
3.1	Overview	50
3.2	Metamaterial Design Development and Layout.....	50
3.2.1	Design approach.....	50
3.2.2	Thermally-actuated bimorph cantilever beam array metamaterial	59
3.2.3	Electrostatic-actuated cantilever beam array metamaterial	63
3.3	Metamaterial Design Modeling	68
3.3.1	Overview	68
3.3.2	Thermally-actuated bimorph cantilever beam metamaterial modeling	69
3.3.3	Electrostatic-actuated cantilever beam array metamaterial modeling	73
3.4	Thermal Metamaterial Device Fabrication	78
3.4.1	Overview	78
3.4.2	Post-fabrication device processing	79
3.5	CNT-Based Braided Ropes	84
3.5.1	Introduction	84
3.5.2	CNT rope prototype description	85
3.6	Summary.....	88
Prototype Device Characterization and Results		89
4.1	Overview	89
4.2	Metamaterial Device Testing and Results	89
4.2.1	Overview	89
4.2.2	Test event #1: device optical inspection	90
4.2.3	Test event #2: interferometer-based beam displacement characterization	91
4.2.4	Test event #3: thermal imaging microscope device temperature mapping	101
4.2.5	Test event #4: metamaterial device electrical resistance characterization	118
4.3	CNT-Based Braided Rope Testing and Results	133
4.3.1	Overview	133
4.3.2	CNT rope test event #1: diameter measurement.....	133
4.3.3	CNT rope test event #2: electrical conductivity characterization	135
4.3.4	CNT rope test event #3: thermal imaging scope temperature mapping...	141
4.4	Summary.....	147
4.4.1	Thermal metamaterial device characterization summary	147
4.4.2	CNT braided rope device characterization summary.....	147
Conclusion and Recommendations.....		148
5.1	Conclusion	148
5.1.1	Thermal metamaterial design conclusion	148

5.1.2	CNT braided rope prototypes conclusion	148
5.2	Recommendations	149
5.2.1	Thermal metamaterial recommendations.....	149
5.2.2	CNT braided rope prototype recommendations.....	150
5.3	Contributions and Applications	150
<i>Appendix A.</i>	<i>Prototype Devices Detailed Images</i>	153
<i>References</i>		170
<i>Vita</i>		174

Table of Figures

Figure	Page
1.1: Permittivity verses permeability – a materials response to applied electromagnetic waves [2].....	3
Figure 1.2: Electrical verses thermal conductivity: a material's thermal properties.	5
2.1: Cross-sectional view of all seven layers of PolyMUMPs™ process [4].....	9
2.2: Heat transfer in PolyMUMPs™ – material and layer examples.	11
2.3: Thermal contact resistance – conduction between materials [13].	15
2.4: TIM filling in air gaps and roughness at contact interface.	16
2.5: Heat transfer by thermal radiation [15].....	17
2.6: Thermal radiation on the electromagnetic spectrum, adapted from [16].....	18
2.7: Graphical relationship between incident, reflected, absorbed, and transmitted radiation [15].....	21
2.8: Reflectivity verses applied wavelength for aluminum (Al), gold (Au), and silver (Ag); showing high reflectivity except at certain shorter wavelengths [17].....	23
2.9: Reflectivity verses wavelength and incident angle for PolyMUMPs™ gold layer (deposited on top of Poly2 layer) [18].	23
2.10: Reflectivity verses wavelength and incident angle for PolyMUMPs™ Poly2 layer [18].....	24
2.11: Convective heat transfer (top) compared to conduction (bottom) [15].	25
2.12: Summary of all three heat transfer methods at work in a typical MEMS structure.	27
2.13: Conductivity and resistivity values for various materials [21].	28
2.14: Doping concentration verses resistivity in semiconductor materials [21].	30
2.15: Joule heating causing thermal expansion in a MEMS beam [23].....	32
2.16: Example of a bimorph cantilever beam curling upward due to residual stress at room temperature, as modeled in CoventorWare 2008.	33

2.17: Example of cantilever beam curling due to residual stress [24].....	33
2.18: Force diagram for a parallel plate electrostatic actuation device [23].....	36
2.19: MWNT 3-D model showing tube within a tube detail [31].....	40
2.20: SWNTs of various electrical conductivity formed by “rolling” a sheet of graphene [31].....	42
2.21: Determining chirality of a CNT [34].....	43
2.22: Possible CNT structures based on chirality [34]	44
2.23: Basic arc discharge CNT fabrication setup [35].....	45
2.24: Laser ablation fabrication setup [35].....	47
2.25: Plasma enhanced CVD based CNT fabrication setup [35].....	49
3.1: Conceptual drawing of a thermally-actuated thermal metamaterial (a), and of an electrostatically-actuated thermal metamaterial (b).....	51
3.2: Conceptual drawing of thermal metamaterial in heat steering application. Heat generated by the “device” is conducted outward in the X-Y plane through an array of MEMS beams, and into a conductive thin film.	54
3.3: Bimorph cantilever beam array unit cell, cross-sectional view. Top (a) shows the unit cell when the “device” is off or in a low power state. Bottom (b) shows the unit cell when the “device” has generated sufficient heat to cause the bimorph beam to bend downwards, with heat conducting through the beam and into the conductive thin film. .	55
3.4: Electrostatic-actuated cantilever beam array metamaterial unit cell conceptual drawing, cross-sectional view. Top (a) shows the unit cell with the pull-in function not actuated. Bottom (b) shows the unit cell with beam pulled-in, and with heat conducting through the beam and into the conductive thin film.	58
3.5: Bimorph cantilever beam array metamaterial CAD layout. Bimorph cantilever beams curl upward and bend downward in response to ambient temperature and/or $I^2 \cdot R$ heating from resistive heating element, creating conductive paths through the system... .	61
3.6: Bimorph beam array metamaterial 3-D model (modeled in CoventorWare 2008). Heating element contact pads are not shown.....	63

3.7: Electrostatic-actuated cantilever beam array metamaterial CAD layout. Cantilever beams snap downwards (pull-in) in response to electrostatic attraction caused by a difference in potential between the polysilicon cantilever beams and the polysilicon electrodes attached to each electrostatic pull-in terminal. This actuation creates conductive paths through the system.	65
3.8: Electrostatic-actuated thermal metamaterial CAD layout showing variation of heater design. This variation added additional polysilicon connections between the polysilicon heater grid and the arrays of polysilicon beams to facilitate increased heat transfer between the heater and beam arrays.	67
3.9: Electrostatic-actuated cantilever beam array metamaterial, as modeled in CoventorWare 2008.	68
3.10: Bimorph cantilever beams curling upwards at room temperature (exaggerated 15X), as modeled in CoventorWare 2008. Bimorph beams curl upwards at low temperatures due to residual stress and the “as deposited” TCE of materials during the deposition process of fabrication.	70
3.11: Bimorph cantilever beams bending downward at elevated temperatures (130 °C), as modeled in CoventorWare 2008. Bimorph beams bend downwards at higher temperatures due to differences in the thermal coefficients of expansion between the polysilicon beam and the top gold layer.	70
3.12: Bimorph cantilever beam tip displacement versus applied voltage. Longer beams exhibit greater upward curl at low temperatures, and bend downward, making contact with the polysilicon heat sink layer below (represented by solid black line), at lower temperatures than their shorter counterparts.	71
3.13: Bimorph beam temperature versus applied voltage. Temperature is approximately a linear function of the voltage applied across the heater terminals.	72
3.14: Temperature of electrostatic cantilever beam versus applied voltage. Temperature is inversely related to sheet resistance of the heater material.	74
3.15: Electrostatic actuated cantilever beams torquing about their longitudinal axis at elevated temperatures (exaggerated 100X). Layout shown is version # 2 (Poly2 beams and Poly2 heater grid).	75
3.16: Simplified 3-D model developed for electrostatic pull-in analysis. Pull-in is due to electrostatic attraction between the polysilicon pull-in electrode and the polysilicon cantilever beam above it. It is caused by a difference in potential between these two structures. Note the Poly0 heat sink is not connected to the Poly0 pull-in electrode (5 μ m gap as shown in the upper insert).	76
3.17: CoventorWare MEMS modeling of electrostatic pull-in.	77

3.18: Electrostatic pull-in voltage verses temperature, as modeled in CoventorWare 2008.	78
3.19: PolyMUMPs™ fabricated devices as delivered in gelpack (a) and in hand to show scale (b).	79
3.20: Acid processing station in AFIT cleanroom (a). Protective oxide layers on PolyMUMPs™ samples are etched away using HF as shown in (b).	80
3.21: Tousimis autosamdri-815 series B supercritical point dryer.	81
3.22: Cleanroom dry box (a) and Anatech plasma cleaner (b).	82
3.23: Bimorph cantilever beam array based metamaterial before release. 250 μm beam length version shown, others similar. Bimorph beams are actuated by either increasing the system temperature, applying a voltage across the heater terminals, or a combination of both techniques.	83
3.24: Electrostatic actuated cantilever beam array based metamaterials before release. Version #3 shown (Poly1 and Poly2 stacked heater grid, Poly1 beams, heater style #1), others similar. Beam arrays are actuated by applying appropriate pull-in voltage between each pull-in terminal and the heater terminals.	83
3.25: CNT rope being spun from SWNT forest. Aligned SWNTs being pulled away from a silicon substrate are shown in (a). The drawing and spinning process is illustrated in (b), and (c) shows the resultant braided rope of SWNTs [37].	84
3.26: Uncoated SWNT braided rope under 50X optical zoom.	85
3.27: PVA coated SWNT braided rope under 50X optical zoom.	86
3.28: Four braided (1X4) PVA coated SWNT ropes under 50X optical zoom.	87
3.29: Four-ply CNT rope braiding process. A spool of PVA coated SWNT braided rope is shown in (a). The braided ropes from four spools are then braided together to form a four-ply rope (b). The finished product, a 1 X 4 braided rope, is shown in (c) [37].	88
4.1: Interferometer system, entire system (a) and close-up of stage (b).	91
4.2: Thermoelectric device calibration using bolometer.	92
4.3: Thermoelectric device calibration using bolometer (background temperature of 24.5 °C). Surface temperature is a non-linear function of voltage applied.	92
4.4: Logic flow and conditions for data collection.	93

4.5: Zygo interferometer software screenshot showing how Z-axis displacement data was measured on the bimorph cantilever beam based thermal metamaterial samples. Voltage was applied across the TED, uniformly heating the entire sample. At each temperature point, Z-axis beam displacement was measured for six beams, and then averaged and recorded as that samples average displacement.....	94
4.6: Zygo interferometer software screenshot showing how electrostatic pull-in data was measured on the electrostatic actuated cantilever beam based thermal metamaterial samples. Voltage was applied across the TED, uniformly heating the entire sample. At each temperature point, the voltage between the beam array and electrode was ramped up until pull-in occurred.....	95
4.7: Bimorph cantilever beam array based thermal metamaterial samples as imaged by Zygo interferometer software. In (a), an array of 150 μm beams is shown in its “curled-up” state at low temperature. In (b), an array of 250 μm beams at a test temperature of 100 $^{\circ}\text{C}$ is shown, illustrating how each beam individually recovers or snaps-back up when cooling down following closure. In (c), a close-up of one-half of one side of a beam array is shown, curled-up. In (d), 250 μm (top) and 300 μm (bottom) beam arrays are shown fully bent down or closed.	96
4.8: Bimorph cantilever beam tip position verses temperature. When the position equals zero, the beam tip has made contact with the heat sink layer beneath it. 150 μm beams make contact at 127 $^{\circ}\text{C}$, 200 μm beams make contact at 123 $^{\circ}\text{C}$, 250 μm beams make contact at 114 $^{\circ}\text{C}$, and 300 μm beams make contact at 110 $^{\circ}\text{C}$	97
4.9: Electrostatic actuated cantilever beam array thermal metamaterial samples as imaged by Zygo interferometer software. In (a), A 3-D image of layout version # 5 (versions detailed in Table 3.3) is shown without any pull-in voltage applied. Layout version # 3 is shown in (b) with 12 V of pull-in applied, the Poly1 beams are bent down slightly, and are on the verge of snapping-down due to electrostatic attractive forces. In (c), (d), and (e), layout version # 4 is shown with 6 V, 7 V, and 8 V applied, respectively. The beams bend downward slightly in (c) and (d), and snap-down completely in (e) once the required pull-in voltage is applied.	99
4.10: QFI thermal imaging microscope system: (a) is the test chamber, (b) shows a close-up of the stage, (c) is the operator’s station, and (d) shows the operator’s view during data collection.....	103

4.11: 250 μm bimorph beam array thermal metamaterial sample under 15X optical and 2X digital zoom with 24 VDC (300 mW) applied. The background temperature is 77 $^{\circ}\text{C}$, and the heater grid rises to 91-145 $^{\circ}\text{C}$ due to Joule heating. Thermal conduction into the beam arrays can be seen to the left and right center of the heater grid. The gold (top) layer of the bimorph beams is ≈ 10 $^{\circ}\text{C}$ hotter than the less conductive polysilicon layer below it. The beams curl downward making conductive contact with the heat sink layer below their tips. This results in heat from the heater grid conducting through the beams, through the thermal contact resistance where each tip meets the heat sink, and into the heat sinks..... 105

4.12: 300 μm bimorph beam array thermal metamaterial sample under 5X optical and 16X digital zoom with 20 VDC (215 mW) applied. The beam array is bent downward, making contact with the polysilicon heat sink layer. Due to the conduction occurring through the beams and into the heat sink, the heat sink's temperature is close to that of the polysilicon in the bimorph beams. This results in thermal energy originating from the heater grid being conducted into the heat sink sheets..... 106

4.13: Bimorph cantilever device operational sequence. In (a), at time T=0, the device and background is at 72 $^{\circ}\text{C}$, and 24 VDC is applied. In (b), at T=0.25 seconds, the polysilicon heater grid temperature has increased dramatically to ≈ 130 $^{\circ}\text{C}$. In (c), at T=0.5 seconds, initial thermal conduction into the beam array can be seen. In (d), at T=0.75 seconds, the outline of the gold layer can be clearly seen as heat is conducted away from the heater grid. In (e), conduction into the beam arrays continues, until in (f) where beam closure begins at T=1.25 seconds..... 108

4.14: Bimorph beam array heat transfer into the heat sink. The 250 μm sample is shown under a 15X optical and 4X digital zoom, with emphasis on the beam array and heat sink layers. In (a), the beam array and heat sink are shown $\frac{1}{2}$ second after voltage was applied across the heating element. The gold begins to heat, but the beams are still curled upwards with no thermal conduction into the heat sink. One second later in (b), the beams have all closed and conduction into the heat sink can now begin. At 2.5 seconds, a complete outline of the Poly0 heat sink layer can be seen, because it's temperature has been raised (heated) via conduction from the bimorph beams (c). Lastly, in (d), the system has reached steady state at 10 seconds. The outline of the gold layer in each beam is clearly seen, and is 15 $^{\circ}\text{C}$ hotter than the Poly2 structural layer of each beam. The heat sink's outline is clearly visible, and is nearly the same temperature as the Poly2 in the bimorph beams which are directly conducting heat into the sink..... 109

4.15: Bimorph beam metamaterial recovery sequence. The 300 um variant is shown under 15X optical and 2X digital zoom. In (a), power has just been removed from the heater grid. The top five beams are still bent down, while the bottom beam has already recovered (curled upwards). In both (b) and (c), individual beams recover and curl upwards. This recovery continues in (d) and (e) until in (f), where all beams have fully recovered. Note that when the beams are still bent down, the gold appears (under MWIR) over 15 °C hotter than the background, while the Poly2 in each beam appears 5 °C cooler than the background. Immediately upon snapping/curling upwards, the entire beam (gold and Poly2) appear approximately equal to the background temperature..... 111

4.16: Thermal conduction from heater grid into the bimorph beam array. Due to the thin silicon nitride layer beneath the heater grid providing only marginal thermal insulation, a substantial amount of the thermal energy input to the system is conducted into the substrate beneath the grid. This results in relatively poor conduction into the beam arrays, as shown on the upper right of the figure..... 113

4.17: Updated meshed 3-D model of thermal metamaterial device, as modeled in CoventorWare 2008. The 300 μm bimorph beam design is shown with the substrate included in the mesh. As postulated, the addition of the substrate's substantial thermal mass to the model resulted in a requirement for a greater amount of voltage applied across the heater terminal to actuate the beam arrays..... 114

4.18: Temperature mapping of the bimorph beam array thermal metamaterial. The 200 μm version is shown, others similar. Poly2 beam temperatures for each layout are listed in Table 4.3, and are 100 °C for the version shown here. For each version, the gold layer on the beams was 10-15 °C hotter than the Poly2. The Poly0 heat sink was approximately the same temperature as the Poly2 beams (within 1-2 °C). The substrate was 4-8 °C cooler than the heat sink..... 115

4.19: Comparison of heater grid layouts for the electrostatic actuated beam array based metamaterials. In (a), heater style #1 is shown, providing only one conductive path (circled) between the heater and the beam arrays. In (b), heater style #2 has multiple conductive paths (circled), providing for enhanced heat transfer between the heater and beam arrays. 118

4.20: In (a), the electrical resistance characterization measurement test points for the bimorph cantilever beam array based prototypes are shown. In (b), the test points for the electrostatic actuated cantilever beam array based prototypes are shown. 119

4.21: Thermal metamaterial electrical resistance characterization setup. In (a) the microscope probe workstation is shown. In (b), a close-up of the probe station stage is shown. In (c), electrostatic-actuated thermal metamaterial layout version # 2 is shown with test probes being placed into position. 120

4.22: Electrical resistance of bimorph cantilever beam array metamaterials, from test points B to C (heat sink to heat sink). All designs exhibited off scale high ($G\Omega$'s) resistance at temperatures less than approximately their closing temperature (from Table 4.1) minus 4 °C. As each design's closing temperature was approached, the resistance would drop from "overload" to approximately 100-150 k Ω . Increasing the temperature further resulted in the resistance decreasing to ≈ 7 -8 k Ω 121

4.23: Electrical resistance of bimorph cantilever beam array metamaterials, from test points A to B (heater terminal pad to heat sink). All designs exhibited off scale high ($G\Omega$'s) resistance at temperatures less than approximately their closing temperature (from Table 4.1) minus 4 °C. As each design's closing temperature was approached, the resistance would drop from "overload" to approximately 100-200 k Ω . Increasing the temperature further resulted in the resistance decreasing to ≈ 3 k Ω 122

4.24: Bimorph cantilever beam array electrical resistance analytical model. Test points B and C are considered the input and output terminals in this representation. Each of the 24 resistors shaded in blue represent the contact resistance at the beam tip to Poly0 heat sink interface. This contact resistance is variable, ranging from an "open circuit" when the bimorph beams are curling upwards to ≈ 36.6 k Ω when the beam arrays are closed. The 48 resistors shaded in red represent the 24 bimorph beams, where each beam has a gold layer and a polysilicon layer. Each of these two layers on each beam is represented by one resistor. The polysilicon resistive heating element is represented by a single resistor in the middle. Lastly, the resistance of each Poly0 heat sink is accounted for at the top and bottom of the figure. Resistance values for heat sink 1 and 2, polysilicon and gold layers of beam, and heater grid were known or measured, allowing an estimated solution for average beam tip contact resistance. 124

4.25: Bimorph cantilever beam array electrical resistance reduced analytical models. Each of the two rows of 12 beams shown in Figure 4.23 reduces to approximately 1/12 $R_{\text{contact resistance beam}}$ due to the low electrical resistance of the gold layer in each beam. $R_{\text{heat sink 1}}$, $R_{\text{heat sink 2}}$, and $R_{\text{heater grid}}$ are known values (measured), allowing for an approximation of $R_{\text{contact resistance beam}} \approx 36.6$ k Ω to be made. Test points B and C are considered the input and output terminals in this representation..... 125

4.26: Electrical resistance of electrostatic actuated cantilever beam array metamaterials, from test points A to B (heater terminal pad to heat sink), with beams pulled-in or closed. Variations in resistance between versions is due to sheet resistance differences in beam material (Poly1 or Poly2), heater grid material (Poly1, Poly2, or Poly1 & 2 stacked), and heater grid type. Versions were described in Table 3.3. Electrical resistance increased ≈ 2 -11% when heated from 25-135 °C. 127

4.27: Electrostatic actuated cantilever beam array electrical resistance analytical model. The I/O of the system (Poly0 heat sink sheets), is shown as test points B and C. The contact resistance at the beam tip to heat sink interface is variable, depending on whether the beams are open or pulled-in closed. It ranges from many $\text{G}\Omega$ (an open circuit) when open to $\approx 14\text{-}28 \text{ k}\Omega$ when closed (version dependent). The 24 polysilicon cantilever beams are represented by the 24 resistors shaded in red. The resistance of each beam is material dependent, $\approx 0.07 \text{ k}\Omega$ for Poly1 beams, and $\approx 0.13 \text{ k}\Omega$ for Poly2 beams. The polysilicon resistive heating element is represented by a single resistor in the middle, and is known to be $\approx 1.2 \text{ k}\Omega$ for layout version #1, $\approx 3.5 \text{ k}\Omega$ for version #2, $\approx 1.5 \text{ k}\Omega$ for versions #3 and #4, and $\approx 1.2 \text{ k}\Omega$ for versions #5 and #6. Lastly, the resistance of each Poly0 heat sink is accounted for by the resistor at the top and bottom of the figure. This resistor also accounts for the resistance occurring at the heat sink to I/O probe tip junction.	129
4.28: Electrostatic actuated cantilever beam array electrical resistance reduced analytical models. The two rows of 12 beams shown in Figure 4.26 each reduce to approximately $1/12 (R_{\text{contact resistance beam}} + R_{\text{beam}})$. $R_{\text{heat sink 1}}$, $R_{\text{heat sink 2}}$, R_{beam} , $R_{\text{heater grid}}$, and $R_{\text{B-C}}$ are known values (measured or estimated using Ω/\square techniques), allowing for an approximation of $R_{\text{contact resistance}} \approx 14\text{-}28 \text{ k}\Omega$ to be made. Test points B and C are considered the input and output terminals in this representation.	130
4.29: Comparison of bimorph cantilever beam tip to electrostatic actuated beam tip. The contact resistance of the electrostatic actuated beam tips was 23-62% lower than that of the bimorph beam tips. Test results suggest that, in this specific application, a tip design with less contact surface area and greater force per unit area provides increased conductivity when compared to a larger contact area with less force per unit area applied.	132
4.30: CNT rope diameter measurement using the Zygo interferometer (a), and a profilometer (b). In (a), the CNT rope is placed onto the bottom glass slide, then held straight and flat using the two top glass slides. In (b), the same three-slide setup is used, and is placed into the test chamber.	134
4.31: Electrical resistivity verses temperature test setup. During data collection the CNT rope sample and test leads were covered by a small cardboard box (not shown) to minimize thermal losses due to convection.	136
4.32: CNT rope resistance (Ω/cm) verses temperature. The resistance of each sample decreased approximately 3 % when heated from 22-110 $^{\circ}\text{C}$	138
4.33: CNT rope resistivity ($\Omega\text{-cm}$) verses temperature. The resistivity of each sample decreased approximately 3% when heated from 22-110 $^{\circ}\text{C}$. The resistivity of the CNT ropes is similar to that of a heavily doped semiconductor.	140

4.34: CNT rope electrical conductivity (S/cm) verses temperature. The conductivity increased approximately 3% when heated from 22-110 °C. The conductivity of the CNT ropes is similar to that of a heavily doped semiconductor.....	140
4.35: QFI thermal microscope system, CNT rope test setup: (a) test chamber, (b) close-up of test stage and unit under test, (c) thermoelectric device, and (d) operator view during data collection.....	142
4.36: CNT rope thermal imaging data collection examples. In (a), a CNT rope sample is shown coming off of the thermoelectric device. In (b) and (c), examples of the operators view during data collection are shown. In (d), the CNT rope's thermal signature when the thermoelectric is unpowered is shown. Note that when unpowered the sample is slightly cooler than the background stage temperature.....	144
4.37: CNT rope average temperature verses distance from TED. Within 10 mm from the edge of the TED all three samples were at or below the background temperature. The uncoated CNT rope exhibited the lowest heat retention, approaching the background temperature more rapidly than the PVA coated samples.....	146
A.1: 150 μ m version of bimorph cantilever beam based thermal metamaterial prototype after release.....	153
A.2: 200 μ m version of bimorph cantilever beam based thermal metamaterial prototype after release.....	154
A.3: SEM image of 200 μ m version of bimorph cantilever beam based thermal metamaterial prototype showing detail near the beam tip.....	155
A.4: 250 μ m version of bimorph cantilever beam based thermal metamaterial prototype after release. Beam tips appear out of focus due to their significant upward curl at room temperature.	156
A.5: 300 μ m version of bimorph cantilever beam based thermal metamaterial prototype after release. Beam tips appear out of focus due to their significant upward curl at room temperature.	157
A.6: SEM image of the 300 μ m version of bimorph cantilever beam based thermal metamaterial prototype after release.....	158
A.7: Version 1 of the electrostatic actuated cantilever beam based thermal metamaterial prototypes after release. This version features Poly1 beams and a Poly1 heater grid...	159
A.8: Version 2 of the electrostatic actuated cantilever beam based thermal metamaterial prototypes after release. This version features Poly2 beams and a Poly2 heater grid...	160

A.9: SEM image of version 2 of the electrostatic actuated cantilever beam based thermal metamaterial prototypes showing detail of the cantilever beams and electrodes.	161
A.10: Version 3 of the electrostatic actuated cantilever beam based thermal metamaterial prototypes after release. This version features Poly1 beams and a two-layer (Poly1/Poly2 stacked) heater.	162
A.11: SEM image of version 3 of the electrostatic actuated cantilever beam based thermal metamaterial prototypes showing detail of the cantilever beam tip.	163
A.12: Version 4 of the electrostatic actuated cantilever beam based thermal metamaterial prototypes after release. This version features Poly2 beams and a two-layer (Poly1/Poly2 stacked) heater.	164
A.13: Version 5 of the electrostatic actuated cantilever beam based thermal metamaterial prototypes after release. This version features Poly1 beams and a modified, two-layer heater grid (Poly1/Poly2 stacked).	165
A.14: Version 6 of the electrostatic actuated cantilever beam based thermal metamaterial prototypes after release. This version features Poly2 beams and a modified, two-layer heater grid (Poly1/Poly2 stacked).	166
A.15: Uncoated SWNT braided rope.	167
A.16: PVA coated SWNT braided rope.	168
A.17: Four braided (1X4) PVA coated SWNT ropes.	169

List of Tables

Table	Page
2.1: PolyMUMPs™ process layers [4].	10
2.2: Electrical conductivity of PolyMUMPs™ layers [7].....	30
3.1: L-Edit CAD layout layer coloring scheme.	62
3.2: 3-D layout layer coloring scheme.	63
3.3: Electrostatic-actuated metamaterial versions. Detailed images of each version fabricated are shown in Appendix A. For all versions, beam length and width are 200 μm and 30 μm , respectively. Beam thickness is 2.0 μm or 1.5 μm , for versions with Poly1 or Poly2 beams, respectively.....	67
3.4: Bimorph cantilever beam array metamaterial modeled contact temperature.	72
4.1: Bimorph cantilever beam array closing temperature: actual verses modeled. Actual closing temperatures recorded during testing were 8-11% higher than predicted by FEM. These results are compared to those obtained during thermal imaging testing later in Table 4.3.	98
4.2: Pull-in voltages for each of the six electrostatic actuated cantilever beam array metamaterials. All values are rounded to the nearest 0.5 V. Variants featuring Poly1 beams pulled-in at \approx 13 VDC, while versions with Poly2 beams pulled-in at \approx 8 VDC. Layout versions were detailed in Table 3.3.	100
4.3: Bimorph beam array closing temperatures, thermal imaging testing verses interferometer based testing and modeling.	116
4.4: CNT rope average diameter and calculated cross-sectional area.	135
4.5: Electrical resistance of CNT ropes verses temperature.	137
4.6: Electrical resistivity and conductivity of CNT ropes verses temperature.	139
4.7: CNT rope thermal imaging temperature mapping.....	145

Acronym List

AFIT	Air Force Institute of Technology
AFRL	Air Force Research Laboratory
BNC	Bayonet Neill-Concelman
BW	Backward-Wave
CAD	Computer-Aided Drawing
CCA	Circuit Card Assembly
CNT	Carbon Nanotube
CSA	Cross-sectional Area
CVD	Chemical Vapor Deposition
DARPA	Defense Advanced Research Projects Agency
DC	Direct Current
DoD	Department of Defense
DNG	Double Negative
FEM	Finite Element Modeling
HF	Hydrofluoric Acid
I/O	Input/Output
IR	Infrared
LHM	Left-Handed Media
LPCVD	Low-Pressure Chemical Vapor Deposition
MEMS	Micro-Electro-Mechanical Systems
MUMPs®	Multi-User MEMS Process
MWIR	Medium-Wavelength Infrared
PVA	PolyVinyl Alcohol
PolyMUMPs™	Polysilicon Multi-User MEMS Process
QFI	Quantum Focus Instruments
RIE	Reactive Ion Etch
RMS	Root Mean Square
RF	Radio Frequency
SEM	Scanning Electron Microscope
SiN	Silicon Nitride
SWaP	Size, Weight, and Power
SWNT	Single-Walled Nanotube
TCE	Thermal Coefficients of Expansion
TED	Thermoelectric Device
TIM	Thermal Interface Material
TM	Trademark
UV	Ultraviolet

INVESTIGATION OF THERMAL MANAGEMENT AND METAMATERIALS

Introduction

Throughout mankind's history, people have strived to create and construct things that are not available in their natural surroundings. This first occurred by exploiting natural materials, and later by developing complex chemical compounds. By the 20th century, manipulation at the molecular and even atomic level was occurring. Today, scientists and engineers have a plethora of materials, both natural and synthetic, encompassing a wide spectrum of physical properties at their disposal. Metamaterials, which are fabricated structures with response functions that do not occur in natural materials or chemical compounds, are a next step in the ongoing quest for new and novel material properties [1].

The vast majority of metamaterial-related research conducted to date has focused on engineering the manner in which a material responds to an applied electromagnetic field or optical wave. Commonly researched metamaterial properties include negative dielectric permittivity ($-\epsilon$) and negative magnetic permeability ($-\mu$). Materials with these properties are also commonly referred to as double-negative (DNG) materials, left-handed media (LHM), or backward-wave media (BW media), and can have a negative index of refraction when evaluating their response to RF energy of a certain wavelength [1]. In general, metamaterials with DNG properties consist of very-small, periodic structures fabricated onto a substrate using a microelectronics fabrication or patterning process. These structural elements are engineered such that the material responds to a

specific wavelength or band of RF energy in a manner that is not possible ($-\varepsilon$ and $-\mu$) using natural materials or chemical compounds [1].

While the electromagnetic and optical responses of metamaterials is a well-researched area, few have considered thermal metamaterials – which are materials composed of engineered, microscopic structures that exhibit thermal performance characteristics based primarily on their physical structures and patterning rather than their chemical composition or bulk material properties. This thesis effort examined thermal metamaterials analytically, characterized several carbon nanotube (CNT) based braided rope structures with potential metamaterial applications, and presented a series of microelectromechanical systems (MEMS) based metamaterial designs that exhibit these unique thermal material properties.

1.1 Introduction to Metamaterials

“Meta” is Greek for “after”, “beyond”, or “post” [2]. Metamaterials can be considered the next step in obtaining theoretically possible, but presently unavailable, material properties as the limits of natural and chemically-synthesized materials are approached. Existing substances exhibit only a subset of the material properties that are hypothetically available. Metamaterials increase the available range of material properties through the use of engineered, microscopic patterning or structures which, when viewed macroscopically, respond to an external stimulus in a manner not normally possible [2].

There has been significant interest in metamaterials over the last decade primarily because of their potential to realize electromagnetic properties not previously available. The term “metamaterials” was coined in 2001, and was defined by Valerie Browning and

Stu Wolf of the Defense Advanced Research Projects Agency (DARPA) as part of the ongoing DARPA Metamaterials program that had kicked-off in 2001 [2]. Their definition:

“Metamaterials are a new class of ordered composites that exhibit exceptional properties not readily observed in nature. These properties arise from qualitatively new response functions that are: (1) not observed in the constituent materials and (2) result from the inclusion of artificially fabricated, extrinsic, low dimensional inhomogeneities.” [2]

While this general definition encompasses all material properties, most of the subsequent research has focused on the electromagnetic properties of metamaterials [2].

When discussing the electromagnetic or optical properties of metamaterials, the material properties of interest are generally dielectric permittivity and magnetic permeability. Figure 1.1 shows the four possible quadrants of a material’s response to an applied electromagnetic wave. The upper right quadrant, where ϵ and μ are both positive, most materials

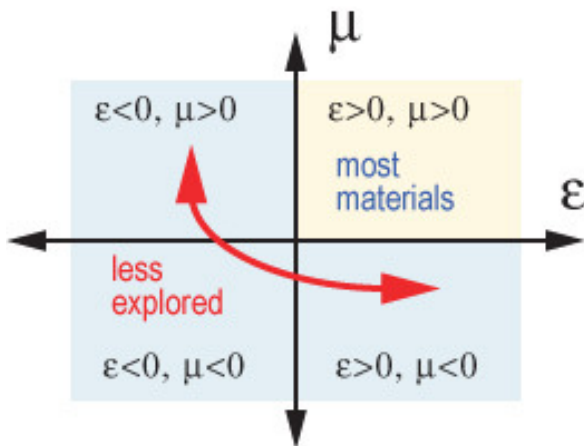


Figure 1.1: Permittivity verses permeability – a materials response to applied electromagnetic waves [2].

encompasses the electromagnetic response of most known materials, and is by far the most explored. The other three quadrants are much less explored – as natural materials or chemical compounds rarely respond to electromagnetic waves with $-\epsilon$ or $-\mu$ [2]. In fact, materials with responses in the third quadrant, where the permittivity and permeability are both negative, do not appear in nature at all [2]. This quadrant ($-\epsilon$ and $-\mu$) is exclusively within the realm of artificially structured metamaterials [2].

While the bulk of metamaterial research performed since 2001 has involved engineering and tuning a material’s ϵ and μ response – the broad definition of metamaterials does not limit them to only unusual electromagnetic properties. The remainder of this document is focused on exploring the thermal properties of metamaterials.

1.2 Problem Background

DARPA’s original metamaterials definition encompassed far more than the electromagnetic and optical responses that have been, nearly exclusively, the focus of research performed to date. Several organizations have investigated the thermal characteristics of RF-tuned metamaterials, however there does not appear to be a documented effort of defining and developing purely thermal metamaterials.

Metamaterials engineered for their electromagnetic properties focus on dielectric permittivity and magnetic permeability as the primary material properties of interest. Metamaterials engineered for their thermal properties focus on different material properties, including, but not limited to, thermal conductivity and electrical conductivity (κ and σ) [3]. Figure 1.2 shows a few example materials covering a wide range of κ and σ

characteristics. Note that κ and σ are not zero or negative in any quadrant, as was the case with ε and μ in Figure 1.1. Existing chemical compounds and natural materials provide for many combinations of κ and σ , as illustrated in Figure 1.2. However, the allure of a thermally-tuned metamaterial is not only that the designer can independently select the value of κ and σ needed for the material application, it is that the material's κ and σ may be actively controlled within a certain range via an actuation scheme.

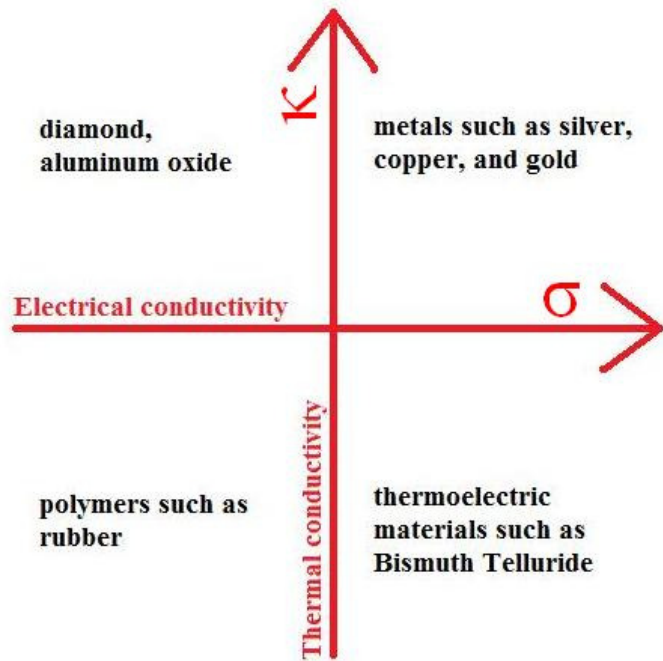


Figure 1.2: Electrical verses thermal conductivity: a material's thermal properties.

1.3 Thesis Objective

This is the first thermal metamaterials research effort performed by the Air Force Institute of Technology (AFIT). Fundamentally, the idea of a thermally-tuned metamaterial has not been previously well defined. The first objective of this effort was to explore heat transfer theory and determine what role the various mechanisms (thermal conductivity, thermal contact resistance, radiative transfer, ect) play in dictating the

performance of a MEMS-based thermal metamaterial. This included examining how the various methods of heat transfer apply to structures on a MEMS-scale. Building upon this background work, the second objective was to design, model, fabricate, and test a series of MEMS-based thermal metamaterial designs. Modeling and testing of these prototype designs showed that materials composed of nano or microscopic structures can realize tuned thermal performance characteristics based primarily on actuation of their physical structures rather than just their chemical composition. Lastly, the third objective was to test and characterize a set of prototype CNT-based braided ropes. Exploitation of this applied nanotechnology has potential applications as structural elements of future thermal metamaterial designs.

1.4 Summary

This effort begins in Chapter 2 (Background Theory) by exploring the various mechanisms of heat transfer theory as they apply to thin film processes. Electrical conductivity on a MEMS scale, as well as mechanical actuation techniques to be used are covered. Lastly, carbon nanotube theory, properties, physics, and fabrication are presented. Chapter 3 (Methodology) deals with the entire process of creating a series of thermal metamaterial prototypes. This includes designing, layout, computer modeling, and fabrication of ten proof-of-concept devices. Additionally, Chapter 3 details the CNT braided rope prototypes. In Chapter 4 (Prototype Device Characterization and Results), an extensive series of tests is conducted to characterize the performance and capabilities of the 10 MEMS-based thermal metamaterial devices and the three CNT braided rope prototypes. Test results and analysis are presented and discussed. Finally, Chapter 5

(Conclusions and Recommendations) summarizes the accomplishments of this thesis and details a path forward.

Metamaterials engineered exclusively for tailored or tuned heat transfer properties are an unexplored topic. This thesis effort expands academia's understanding of what constitutes a thermal metamaterial. The prototype designs presented, discussed, and tested in this thesis are just a few examples of the countless material possibilities that can be realized by exploiting thermal metamaterials.

Background Theory

2.1 Overview

There has been little previous research activity in the area of metamaterials engineered specifically for their thermal response. However, the heat transfer properties of thin film materials and MEMS, the essential building blocks of a thermally-tuned metamaterial, are fairly well documented subjects. To design an effective thermal metamaterial, the engineer must first have a solid understanding of the manner in which the materials of interest transfer heat energy.

This chapter first introduces the fabrication process used to create the prototype thermal metamaterial devices. Second, it examines the basics of heat transfer, including the conductive, radiative, and convective properties of the materials available in the PolyMUMPs™ process. Third, electrical conductivity is examined, with an emphasis on conductivity in semiconductors such as polysilicon, the primary structural material in PolyMUMPs™. Fourth, methods of actuating or switching MEMS structures are described, including bimorph beam bending and electrostatic pull-in effects. Lastly, an introduction to CNTs is presented. Together these topics form the theoretical foundation on which this thesis is built.

2.2 PolyMUMPs™ Fabrication Process

The polysilicon deposition multi-user MEMS process, or PolyMUMPs™, was selected as the fabrication process for this research effort. This fabrication process was chosen due to its appropriate feature size and material capabilities, quick and reliable turnaround, and relatively low cost. This section introduces the PolyMUMPs™ process.

PolyMUMPs™ is a three-layer polysilicon surface micromachining process that utilizes two sacrificial layers of silicon dioxide to provide separation between three mechanical layers of polysilicon [4]. Eight mask levels result in seven material layers [4]. The minimum feature size is 2 μm . Figure 2.1 shows a cross-section of the PolyMUMPs™ process layers.

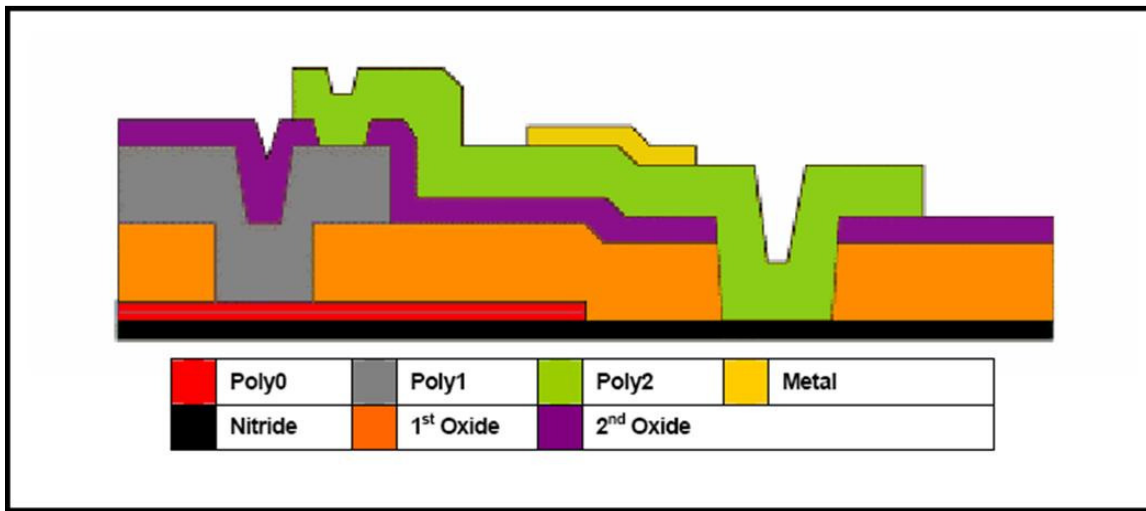


Figure 2.1: Cross-sectional view of all seven layers of PolyMUMPs™ process [4].

Table 2.1 summarizes each of the PolyMUMPs™ process layers. The PolyMUMPs™ process builds upon a 150 mm diameter n-type (100) doped silicon wafer of 1-2 $\Omega\text{-cm}$ resistivity. For detailed information on the PolyMUMPs™ process, please refer to the PolyMUMPs™ Design Handbook [4].

Table 2.1: PolyMUMPs™ process layers [4].

Material Layer	Layer Thickness	Layer Description
Nitride	0.6 μm	Provide electrical isolation from wafer
Poly0	0.5 μm	Electrical layer for ground plane/electrode formation.
1st Oxide	2.0 μm	First sacrificial layer providing gap between Poly0 and Poly1 layers.
Poly1	2.0 μm	First mechanical layer
2nd Oxide	0.75 μm	Second sacrificial layer providing gap between Poly1 and Poly2.
Poly2	1.5 μm	Second mechanical layer
Metal	0.5 μm	Electrical contact layer or optically reflective surface

2.3 Heat Transfer Theory Applied on a MEMS Scale

2.3.1 Overview

Like many other bulk material properties, classical heat transfer theory becomes decreasingly valid as the size and scale of the material being examined shrinks down to the sub-micron level. In the fabrication process used for this effort, the material thicknesses range from 500 – 2000 nm. Figure 2.2 depicts a cross-sectional example of the layers and materials present in the process – all of which interact with each other via conduction, radiation, and convection. This section examines these heat transfer relationships.

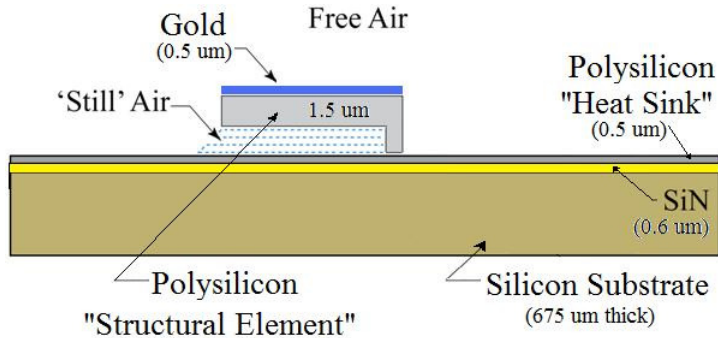


Figure 2.2: Heat transfer in PolyMUMPs™ – material and layer examples.

2.3.2 Thermal conduction

Most people learn about conduction at an early age when they grab the metal handle of a hot pan off of a stovetop burner. Although the handle was not directly heated – it is connected to a material that was heated, and the heat conducted through the material and into the handle. Conduction is the transfer of thermal energy that occurs when adjacent molecules vibrate against one another, or as free electrons move between neighboring molecules [5]. This transfer occurs at the molecular level via diffusion of free electrons and/or phonon vibrations due to a temperature gradient [5]. These two effects are additive, such that the total thermal conductivity of a material is the sum of the conductivity due to electron diffusion (electrical component) and phonon vibration (lattice vibration component) [5]. The type of material dictates which method (electron diffusion or phonon vibration) is most prevalent [5]. In most metals, such as the gold shown in Figure 2.2, freely-moving electrons are responsible for the bulk of thermal and electrical conduction [5]. Most non-metals rely primarily on phonon vibrations to conduct heat energy through a substance [5].

Conduction occurs most easily within solid materials, or between solids in direct contact. In crystalline materials, the regularity of the lattice arrangement generally results in higher thermal conductivities than amorphous materials such as glass [5]. In all cases the thermal energy transfer occurs from a point of a higher temperature (higher thermal energy) to a point at a lower temperature (thermal gradient). Conduction can and does occur in gases such as the “still air” shown in Figure 2.2, however the molecules of a gas are much farther apart – greatly reducing the opportunity to collide and transfer thermal energy [5].

The primary parameter of interest when examining conduction of thermal energy within a material is thermal conductivity or κ . Thermal conductivity is a material property indicative of a substance’s ability to conduct heat [6]. It is defined mathematically by:

$$\kappa = \frac{\Delta Q}{\Delta t} \cdot \frac{d}{\Delta T} \cdot A^{-1} \quad (2.1)$$

where ΔQ is a quantity of heat, Δt is an amount of time, d is the thickness of the material, such as the length of a conductive beam, ΔT is the temperature difference between the hot and cold ends or sides of the material, and A is the cross-sectional area [6]. The standard unit of thermal conductivity is $\text{W}/(\text{m}\cdot\text{K})$ [6]. The components of thermal conductivity due to electron diffusion and phonon lattice vibration are κ_e and κ_l , respectively, where $\kappa = \kappa_e + \kappa_l$ [6].

Thermal conductivity is a function of the material temperature in most cases. In metals and highly doped semiconductors, electron diffusion is inhibited by excessive lattice vibrations that occur at elevated temperatures [7]. This results in a decreased κ_e component, and an accordingly lower κ , at higher temperatures. Most non-metals do not

have large numbers of free electrons, and thereby phonon or lattice vibrations are the dominant method by which thermal conduction occurs in these materials [7]. As temperature rises, an increase in the scattering of phonon vibrations causes a reduction in the κ_l term, and a correspondingly lower thermal conductivity for the material.

The materials available in the PolyMUMPs™ process cover a wide range of thermal conductivities. The most conductive material is gold, which like most other metals, has excellent thermal and electrical conductivity. The thermal conductivity of the gold layer used in this process is $\approx 297 \text{ W}/(\text{m}\cdot\text{K})$, which is about 7% lower than that of bulk gold [8]. The thermal conductivity of this 0.5 μm layer of gold is less, due to the prominence of electron surface scattering in thin films, as the surface area of a thin film is a significant part of its total volume [9]. In gold, thermal conduction is over 99% due to electron diffusion, with phonon vibration contributing the remainder [10]. This dominance of κ_e in the κ of the material is the reason that gold is also an excellent electrical conductor, as discussed in Section 2.4.

Polysilicon, which is the primary structural component in the PolyMUMPs™ process, has a $\kappa \approx 32 \text{ W}/(\text{m}\cdot\text{K})$ [8]. The bulk of this thermal conduction ($\approx 97\%$) occurs due to phonon vibration/interaction (κ_l effects) [10]. While these phonon vibration effects are responsible for polysilicon's fairly good thermal conductivity, the lack of a significant κ_e component in the κ of the material results in a mediocre electrical conductivity (discussed in Section 2.4). The polysilicon used in this process is heavily doped with phosphorus resulting in a strong n-type material (doped $\approx 10^{19}$ donors/cm) [11]. The doping concentration and grain size vary significantly when comparing polysilicon fabricated in different processes. Therefore, one must insure the material properties being used are

specific to and correct for the targeted process. Polysilicon exhibits decreasing thermal conductivity at elevated temperatures (above ≈ 500 K), which must be accounted for in high temperature applications [10].

Silicon nitride (SiN) is used in the PolyMUMPsTM process to provide electrical isolation between the polysilicon structures and the n-type silicon wafer. As SiN is a poor electrical conductor, nearly all of its thermal conduction is due to κ_l phonon vibration effects [12]. The SiN layer in this process is relatively thin at 0.6 μm , and has a measured $\kappa \approx 2.5 \text{ W}/(\text{m}\cdot\text{K})$ [12]. SiN's thermal conductivity is especially sensitive to thin film effects - with bulk silicon nitride having a thermal conductivity approximately 12 times greater ($\approx 30 \text{ W}/(\text{m}\cdot\text{K})$) than the thin film [12].

Air, like most gasses, is an exceptionally poor thermal conductor, having a $\kappa \approx 0.025 \text{ W}/(\text{m}\cdot\text{K})$ at sea level and room temperature [13]. Its thermal conductivity is heavily influenced by atmospheric pressure, temperature, and gas content (i.e. water as a function of humidity). In the PolyMUMPsTM process, air gaps between polysilicon and underlying polysilicon or nitride layers are on the order of 0.75 – 2.75 μm , small enough that conduction through the air gap should be accounted for. The “still air” shown in Figure 2.2 is an example of a situation in which there would be conduction through an air gap.

While thermal conductivity is a measure of how well heat conducts through a single material, thermal contact conductance (h_c) is a measure of how well heat conducts between two materials in contact [14]. In any MEMS design, there are numerous junctions where dissimilar materials contact each other. When there is a temperature difference between materials in contact, a temperature drop is observed at the junction

due to thermal contact resistance (h_c^{-1}) [14]. Thermal contact resistance is the ratio between this temperature drop and the average heat flow across the junction [14]. Figure 2.3 illustrates the air gaps and contact discontinuities due to roughness and imperfections in mating surfaces that account for the majority of thermal contact resistance. It is typical for thermal contact resistance to be a dominant factor in retarding heat transfer when considering a contact junction between two excellent conductors, such as copper or silver [14].

A variety of factors influence thermal contact resistance; including contact pressure, thermal interface materials, and surface roughness. Increasing the contact pressure (pushing the two materials together more forcefully) can substantially increase thermal contact conductance and thereby decrease thermal contact resistance [14]. This is due to an increase in the actual contact area as the materials are pressed together and their

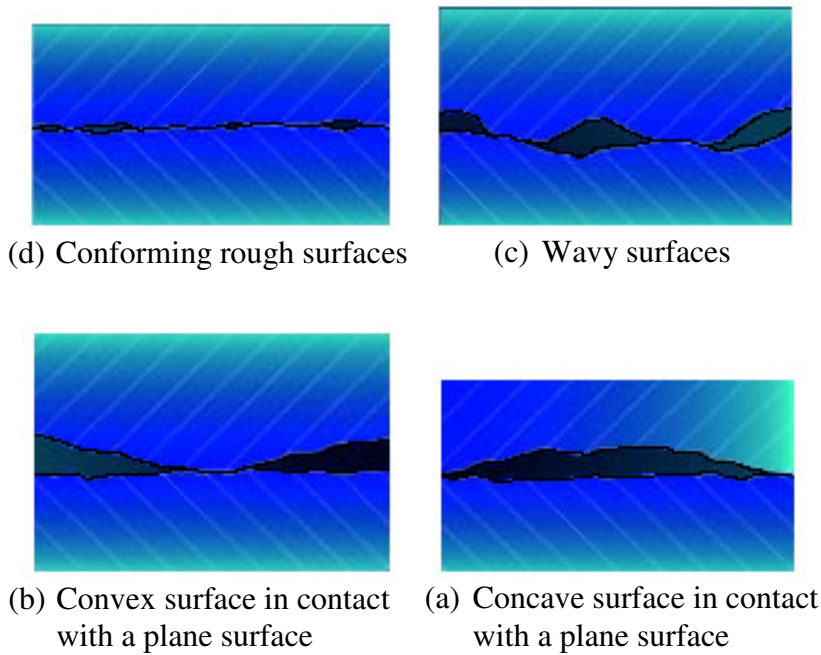


Figure 2.3: Thermal contact resistance – conduction between materials [14].

surfaces conform slightly to each other [14]. The second factor is the interstitial material or thermal interface material (TIM). This is the microscopic filler material trapped in the nooks and crannies formed when the two materials contact each other as illustrated in Figure 2.3 (b). In most cases this interface material would simply be trapped air pockets, however it could be a specifically selected TIM such as a conductive particle laden thermal paste. Engineered TIMs fill-in the microscopic gaps in the mating surface between the two materials in contact (see Figure 2.4), providing a decreased thermal contact resistance and enhanced overall thermal conductivity. The third factor influencing thermal contact resistance is surface roughness. As was illustrated in Figure 2.3 (a), the rougher the mating surfaces of the two materials, the less direct contact will be made, leading to higher thermal contact resistance [14].

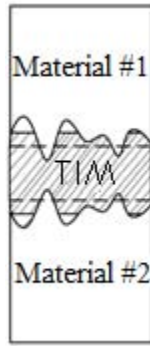


Figure 2.4: TIM filling in air gaps and roughness at contact interface.

2.3.3 Thermal radiation

Heat transfer via radiation is something that everyone has seen and felt, yet few really understand. Every day people experience the radiative heat of the sun, white light and heat emitted by an energized light bulb filament, and the familiar red glow and heat of a hot electric stovetop element. Thermal radiation is the emission of electromagnetic

waves from an objects surface because of the objects temperature [15]. The electrons, atoms, and molecules of all substances above absolute zero are constantly in motion, emitting thermal radiation on a continuous basis [16]. Radiation is a significantly different mechanism than conduction and convection in that it does not require a material medium to travel through. For example, in Figure 2.5 a person standing several feet away from a small fire is exposed to thermal radiation emitted by the fire without heating the air in between them. With other heat transfer methods – the transfer occurs only from an area of higher temperature into an area of lower temperature. Radiative heat transfer can occur between two objects separated by air or some other medium that is colder than

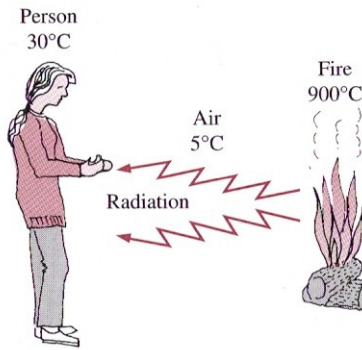


Figure 2.5: Heat transfer by thermal radiation [16].

either object. Radiation occurs in a vacuum with no medium, not even air, to transfer heat energy through.

Thermal radiation encompasses part of the electromagnetic spectrum including all visible light, infrared, and some ultraviolet wavelengths [16]. Figure 2.6 illustrates thermal radiation as it relates to the overall electromagnetic spectrum. Note that all visible light falls within the band of thermal radiation, meaning that if a person can see something – it is emitting some thermal radiation. Also, ultraviolet (UV) wavelengths

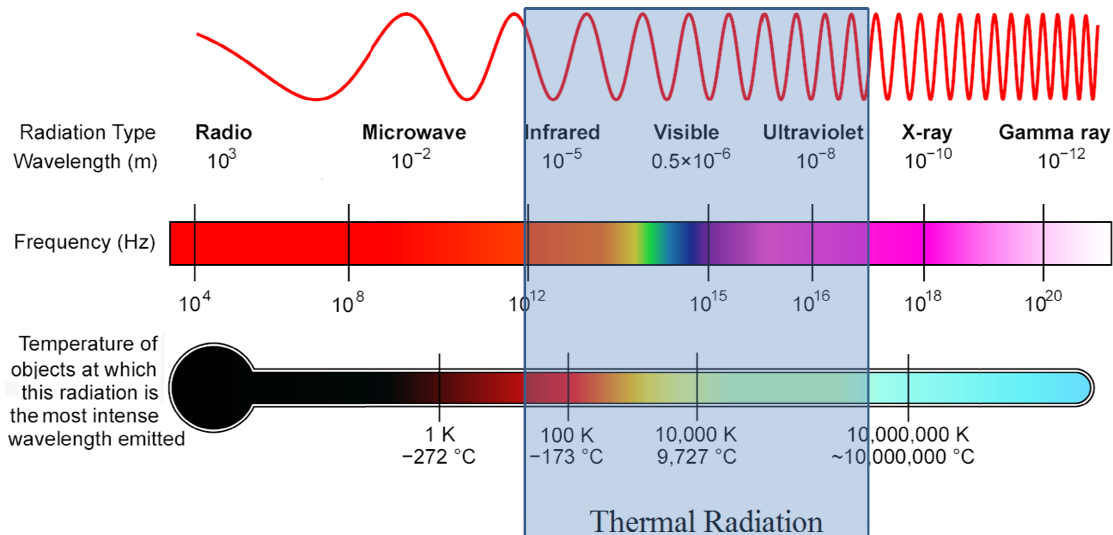


Figure 2.6: Thermal radiation on the electromagnetic spectrum, adapted from [17].

cannot be seen, but are within the band of thermal radiation. It is common for people to become “sun-burned” when their bodies absorb UV thermal radiation emitted by the sun. Like all other electromagnetic waves, thermal radiation transports energy.

Thermal radiation is characterized by the same parameters as other electromagnetic waves. The wavelength (λ) of the radiation emitted is related to the frequency (ν) of the wave by:

$$\lambda = \frac{c}{\nu} \quad (2.2)$$

where C is the speed of propagation of a wave in a particular medium (such as air) [16]. C is also related to the speed of light in a vacuum ($C_o \approx 3 \cdot 10^8$ m/s) by:

$$C = \frac{C_o}{n} \quad (2.3)$$

where n is the index of refraction of a medium [16]. In air at sea level, $n \approx 1.0003$ [16].

As mentioned in the introduction, metamaterials are often tuned to respond with a negative index of refraction ($n < 0$). This property results from how n is defined:

$$n = \sqrt{\epsilon \cdot \mu} \quad (2.4)$$

where recall ϵ is the dielectric permittivity and μ is the magnetic permeability [16].

In addition to the wave-like qualities of emitted thermal radiation, there are also particle-like qualities. These particles are discrete packets of energy referred to as photons, and are part of the basis of quantum physics [16]. These emitted photons have an energy (E) governed by:

$$E = h \cdot v = \frac{h \cdot c}{\lambda} \quad (2.5)$$

where h is Planck's constant $6.626 \cdot 10^{-34}$ J·s and the other variables are as previously defined [16]. Emitted photons with a shorter wavelength deliver a greater amount of energy. This greater energy per photon is why electromagnetic radiation of shorter wavelengths, such as UV and X-rays, causes more damage to objects such as people and electronic components.

The amount of radiation energy per unit surface area an object emits is described by the Stefan-Boltzmann Law:

$$J^* = \epsilon \cdot \sigma \cdot T_s^4 \quad (2.6)$$

where J^* is energy emitted per unit surface area (W/m^2), ϵ is the emissivity of the surface (to be described shortly), σ is Stephan-Boltzmann constant $5.67 \cdot 10^{-8} \text{ W/m}^2 \cdot \text{K}^{-4}$, and T_s is the surface temperature in Kelvin [16]. Also, the total energy lost by an object due to thermal radiative emissions can be described by:

$$Q_{radiation} = A \cdot \varepsilon \cdot \sigma \cdot (T_s^4 - T_{surroundings}^4) \quad (2.7)$$

where $Q_{radiation}$ is the total emitted energy, A is the surface area of the radiating object, $T_{surroundings}$ is the ambient temperature of the surroundings in Kelvin, and the other parameters are as previously defined [16]. Defining emissivity requires first understanding the definition of a blackbody. A blackbody is a perfect emitter and absorber of radiation. At any given temperature, no object can emit more radiation than a blackbody. Emissivity (ε) is the ratio of the radiation emitted by an object at a certain temperature to the radiation emitted by a blackbody at the same temperature [16]. For a blackbody, $\varepsilon = 1$ [16]. Highly reflective materials, such as silver, have very low emissivity (close to 0) [16]. Emissivity is also impacted by temperature, wavelength of the energy applied to the object, and the angle at which the emission is being considered [16].

Unlike conduction and convection, radiation is a strong function of an objects absolute temperature. The total amount of radiation emitted by a material increases by T_s^4 , where again T_s is the temperature of the material in Kelvin [15]. An object at room temperature (300 K) would only emit 1/16 the total radiation energy as the same object at 600 K. It is for this reason that thermal radiation is often considered insignificant in many MEMS applications – but can become significant in those that operate in a medium to high temperature range.

In addition to the thermal radiation that an object emits due to its absolute temperature, every object is exposed to the radiative emissions of other structures around it. Objects are constantly bombarded by radiation coming from all directions over a wide range of wavelengths [16]. When this electromagnetic energy contacts the object being

examined, it can be absorbed, reflected, and/or transmitted [16]. Figure 2.7 illustrates these phenomena. Incident radiation (G), also known as irradiation, is the total radiation

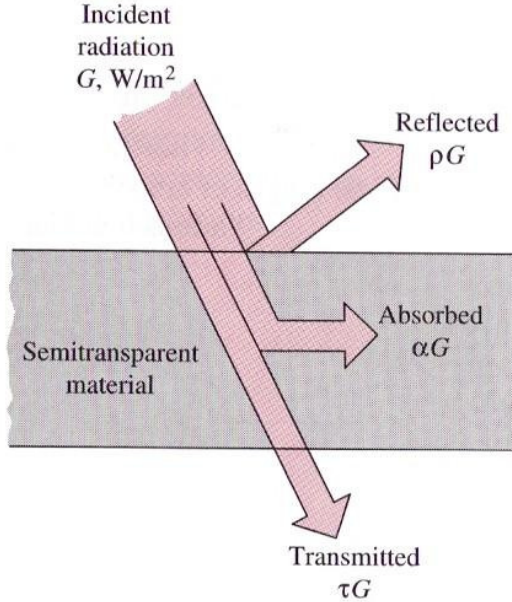


Figure 2.7: Graphical relationship between incident, reflected, absorbed, and transmitted radiation [16].

of all wavelengths impacting a surface [16]. When irradiation strikes a material, part of it is reflected ($\rho \cdot G$), part of it is absorbed by the material ($\alpha \cdot G$), and the remainder (if any) is transmitted through the material ($\tau \cdot G$) [16]. Reflectivity, absorptivity, and transmissivity each have a value between 0 and 1, and the three parameters sum to 1, where the incident radiation (G) equals 1 [16].

$$\rho + \alpha + \tau = G = 1 \quad (2.8)$$

$$\rho = \frac{\text{reflected radiation}}{\text{incident radiation}} , 0 \leq \rho \leq 1 \quad (2.9)$$

$$\alpha = \frac{\text{absorbed radiation}}{\text{incident radiation}} , 0 \leq \alpha \leq 1 \quad (2.10)$$

$$\tau = \frac{\text{transmitted radiation}}{\text{incident radiation}} , 0 \leq \tau \leq 1 \quad (2.11)$$

It is important to note, especially when considering metamaterials, that reflectivity, absorptivity, and transmissivity are average properties of a material for all directions and all wavelengths [16]. As was the case with emissivity, each of these properties can be defined for a specific wavelength and impact angle of the incident electromagnetic energy. When discussing metamaterials tuned for their electromagnetic response, the designer will specify the band of wavelengths and range of impact angles for which the material performs as a metamaterial (i.e. has a $-\epsilon$ and/or $-\mu$ response to incident radiation) as most metamaterials will only perform as such under a relatively narrow range of conditions.

The materials available in the PolyMUMPsTM process possess a wide range of emissivity, reflectivity, absorptivity, and transmissivity characteristics. Gold, like most other metals, has low emissivity (around 0.3) - meaning that it emits a relatively low amount of thermal radiation [18]. Also, the emissivity of gold and other metals is a strong function of the surface condition (i.e. polishing, roughness, and any oxidation) [18]. Metals with a smoothly polished surface have far lower emissivity than rough, unpolished surfaces [18]. Additionally, the emissivity of gold and other metals increases with temperature [18].

Gold, again like most metals, reflects most of the electromagnetic energy that is applied to it. The reflectivity is a strong function of the gold's surface roughness (which is ≈ 7 nm RMS for PolyMUMPsTM) and also of the wavelength of the radiation [19]. Figure 2.8 is an example of how the reflectivity of a gold film varies as a function of wavelength. Figure 2.9 illustrates how dramatically the reflectivity of gold varies as a

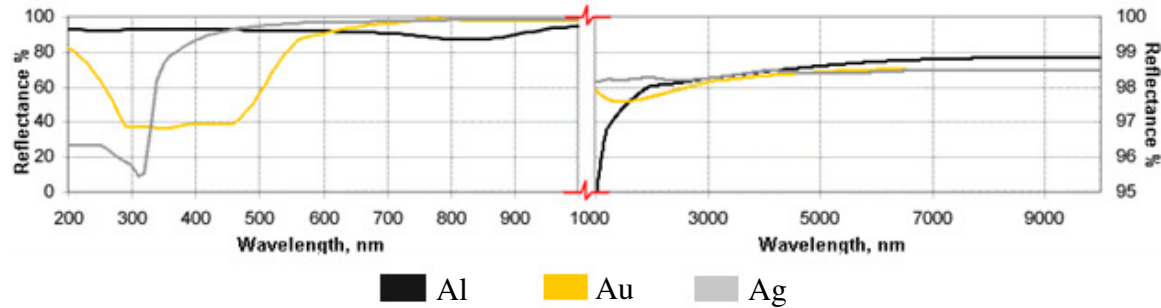


Figure 2.8: Reflectivity versus applied wavelength for aluminum (Al), gold (Au), and silver (Ag); showing high reflectivity except at certain shorter wavelengths [18].

function of the wavelength of the applied radiative energy and also the incident angle at which it impacts the sample. Note this data is specifically for the PolyMUMPs™ process. As transmissivity and absorptivity are directly related to reflectivity by Equation 2.8, they too vary as a strong function of the wavelength of the applied radiation and surface roughness.

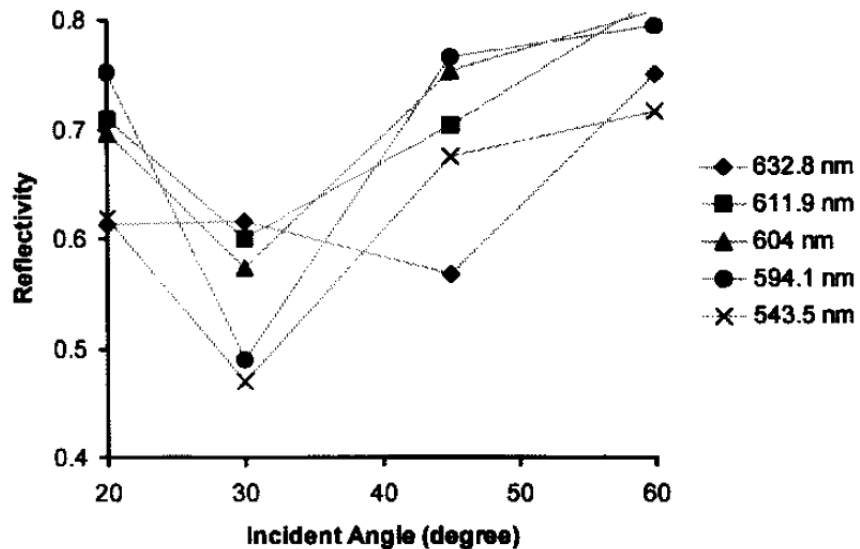


Figure 2.9: Reflectivity versus wavelength and incident angle for PolyMUMPs™ gold layer (deposited on top of Poly2 layer) [19].

Polysilicon, which is a strong n-type semiconductor in this process, has an emissivity of ≈ 0.5 at room temperature, meaning that it emits about $\frac{1}{2}$ the radiative energy that a perfect blackbody would under similar conditions [20]. As with many other materials, this value is a strong function of temperature and surface roughness. Polysilicon as deposited in the PolyMUMPsTM process has an RMS roughness of 7.1 nm [19]. Figure 2.10 shows how the reflectivity of polysilicon, specifically Poly2 from the PolyMUMPsTM process, varies as a function of the wavelength of applied radiative energy and the angle at which it impacts the surface of the polysilicon.

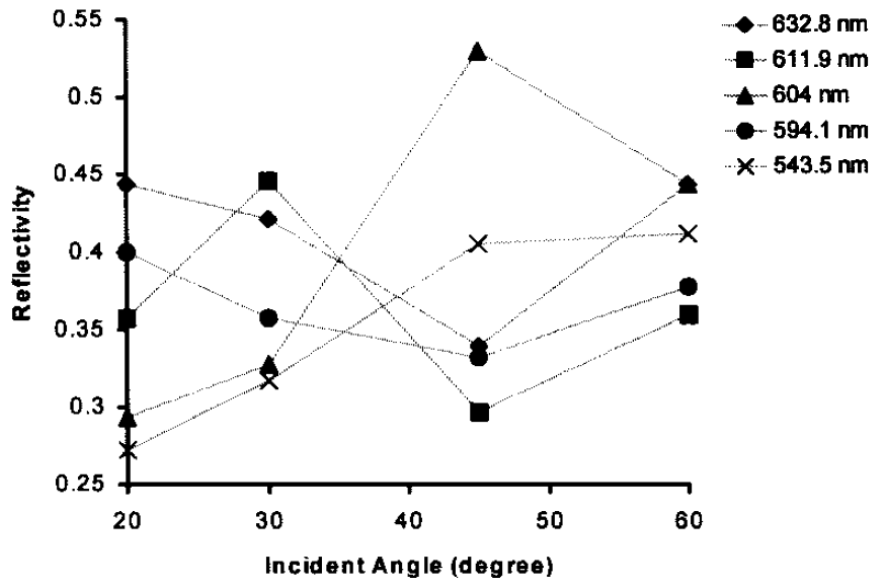


Figure 2.10: Reflectivity versus wavelength and incident angle for PolyMUMPs™ Poly2 layer [19].

2.3.4 Thermal convection

Convection is the transfer of heat energy between a material's surface and the surrounding flowing air [16]. Convection is similar to conduction in that it requires a material medium – but different in that convection requires motion or movement of the

air [16]. Heat transfer through a solid substance is always by conduction, while heat transfer between a solid substance and air can be by conduction or convection – the differentiating factor being whether or not the air is in motion [16]. Conduction into air, or from air into a substance, can be treated like convection as the air motion approaches zero [16]. Figure 2.11 illustrates this difference between convection and conduction.

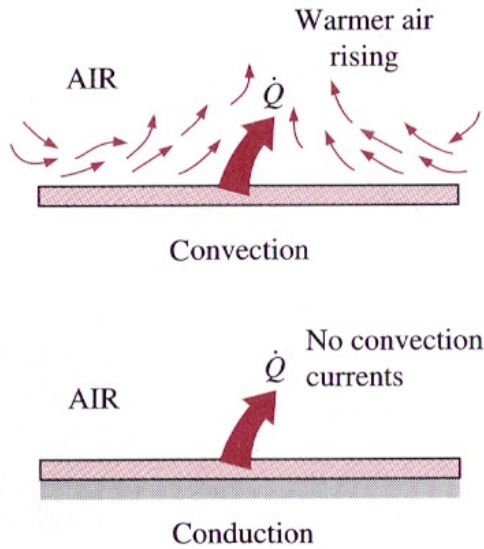


Figure 2.11: Convective heat transfer (top) compared to conduction (bottom) [16].

Convection is generally considered to be the most complex mechanism of heat transfer [16]. It is a strong function of dynamic viscosity, thermal conductivity, density, specific heat, fluid velocity, and the geometry and roughness of the surface [16]. In Newton's law of cooling, all of these variables influence the convective heat transfer coefficient, h [16]. This coefficient can be defined as the “rate of heat transfer between a solid surface and a fluid per unit surface area per unit temperature difference” [16]. The convective heat transfer coefficient is difficult to determine analytically and in most cases

is experimentally estimated for a specific structure/application [16]. Heat transfer by convection is governed by:

$$Q_{convection} = h \cdot A_s \cdot (T_s - T_{surroundings}) \quad (2.12)$$

where $Q_{convection}$ is the total energy transfer due to convection in Watts, A_s is the heat transfer surface area in m^2 , T_s is the surface temperature in Kelvin, and $T_{surroundings}$ is the ambient temperature of the surroundings in Kelvin [16]. Several sources (including Dechev) state that h for ambient air at standard temperature and pressure near typical PolyMUMPs™ cantilever beam structures is $\approx 1400 \text{ W}/(m^2 \cdot K)$ [16].

Heat transfer by convection is oftentimes ignored by MEMS device designers, largely due to the fact that MEMS devices are quite often hermetically sealed during the packaging process. This is primarily done to maintain a pristine operating environment for the MEMS device, as they are particularly sensitive to humidity, oxidation, and particle contamination. However, a side effect of this hermetic packaging is that there is approximately zero airflow around the MEMS device, resulting in heat transfer from the device into the still air via conduction, not convection. In an application where the MEMS device is not hermetically sealed, and especially in any application where there is forced air cooling or some fluid motion, convection can become a significant if not a dominant part of the heat transfer problem.

2.3.5 Summary

The conductive, radiative, and convective properties of a material or structure each play varying roles in the overall heat transfer process. Figure 2.12 summarizes the various heat transfer mechanisms as they occur in a simple MEMS beam example. Some

heat energy in the gold layer conducts throughout the gold, and through the thermal contact resistance of the gold/polysilicon junction into the polysilicon layer beneath it. Other heat energy in the gold is emitted in the form of thermal radiation to the surrounding environment. Additional heat energy is given off by convection as small amounts of air flows near and above the gold layer. Furthermore, the gold is exposed to incident radiation from its surroundings, some of which is reflected, some absorbed, and some transmitted through the layer and into the polysilicon. This scenario occurs for each of the materials, structures, and layers in the process. Heat transfer is a dynamic, multifaceted discipline with implications in nearly all engineering undertakings. It is for this reason that the ability to engineer and control these mechanisms using thermally-tuned metamaterials is so lucrative, and is the focus of this thesis effort.

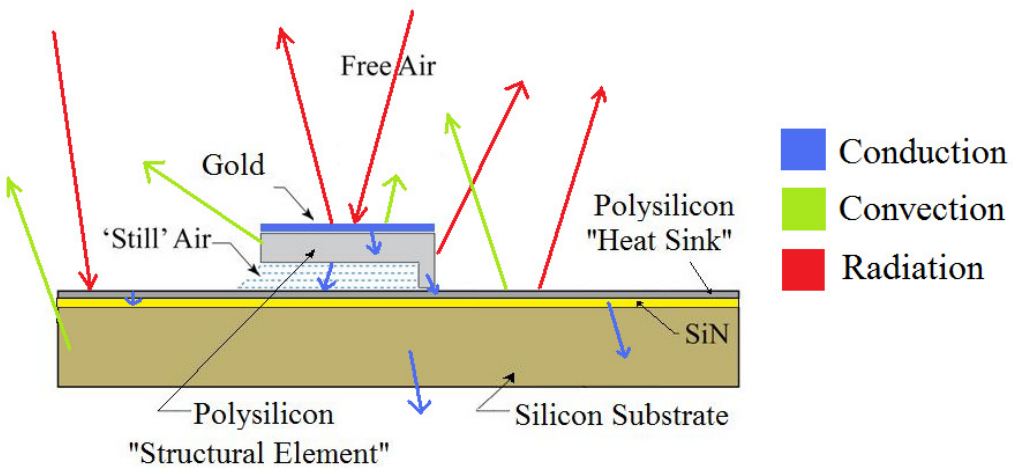


Figure 2.12: Summary of all three heat transfer methods at work in a typical MEMS structure.

2.4 Electrical Conductivity Applied on a MEMS Scale

While not explicitly part of the heat transfer process, electrical conductivity is intimately related to thermal conductivity in many materials. Electrical conductivity is a

measure of how well a material conducts an electric current. As mentioned in the introduction, its symbol is σ and it is defined by:

$$J = \sigma \cdot E \quad (2.13)$$

where J is the current density in A/m^2 , σ is the electrical conductivity in S/m , and E is the electric field strength in V/m [21]. Conductivity is directly related to resistivity by:

$$\sigma = \frac{1}{\rho} \quad (2.14)$$

where ρ is the resistivity in $\Omega \cdot \text{m}$ [21]. Figure 2.13 shows resistivity and conductivity values for materials common in microelectronics fabrication.

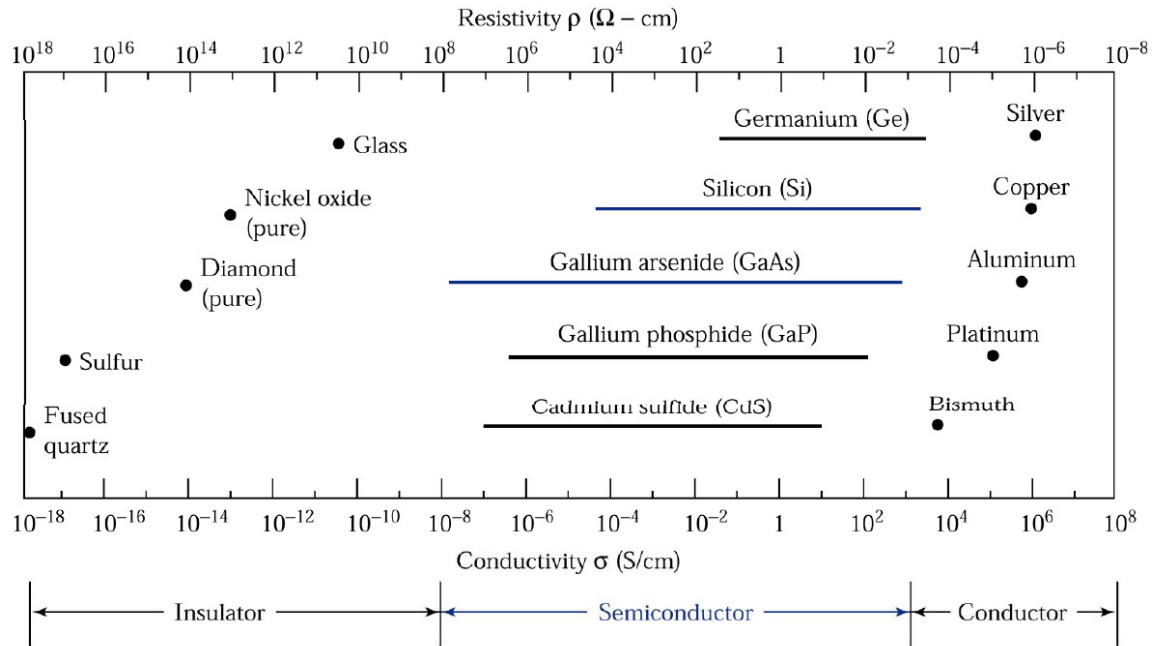


Figure 2.13: Conductivity and resistivity values for various materials [22].

Electrical conductivity is a strong function of temperature in most materials. In metals such as gold, the electrical conductivity decreases as the material temperature increases [16]. In heavily doped semiconductors such as the polysilicon used in PolyMUMPSTM, the electrical conductivity also decreases as temperature increases. This decrease in

electrical conductivity is due to an increase in lattice vibrations in the material at elevated temperatures [7]. In a high lattice vibration environment, electron movement or diffusion, the main ingredient in electrical conduction, is inhibited [7]. This is also why metals, which rely on electron diffusion to facilitate thermal conduction (have a dominant κ_e term), exhibit decreased thermal conductivity as temperature increases. This relationship between electrical conductivity/resistivity and temperature for the polysilicon in PolyMUMPS is described by Equation 2.15:

$$\rho = 3.2 \cdot 10^{-18} \cdot T^{\frac{2}{3}} \cdot e^{(0.6 \text{ eV}/kT)} \quad (2.15)$$

where ρ is the resistivity in $\Omega \cdot \text{m}$, T is the temperature in Kelvin, eV is an electron-volt ($1.6 \cdot 10^{-19} \text{ J}$), and k is the Boltzmann constant [21]. Also in semiconductors, the doping concentration is a major factor dictating the material's conductivity. Figure 2.14 illustrates how resistivity decreases (and thereby conductivity increases) as a function of increasing doping concentration.

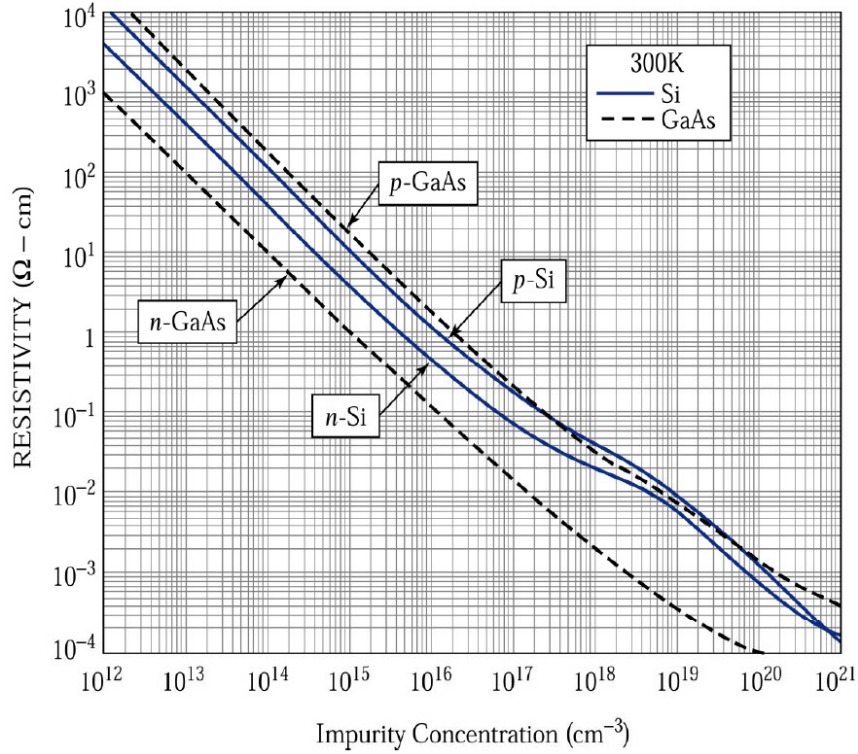


Figure 2.14: Doping concentration verses resistivity in semiconductor materials [22].

Of importance to this research, MEMSCAP, who performs the PolyMUMPs™ process, measures and publishes electrical conductivity values for each layer for every fabrication run. A review of their data shows that even in a routine, repeatable process, electrical conductivity can vary by nearly 20% from run to run [11]. The data from fabrication run # 87, which was used for this research effort, is shown in Table 2.2.

Table 2.2: Electrical conductivity of PolyMUMPs™ layers [8].

Layer	Electrical Conductivity (S/m)
Poly0	64520
Poly1	46300
Poly2	31150
Gold	33670000

2.5 MEMS Actuation Schemes

2.5.1 Overview

The advantage of using MEMS to implement a thermally-tuned metamaterial is the ease and availability of reliable actuation techniques. The purpose of an actuation technique is to convert an input signal of some sort into a mechanical movement of a structure. Incorporating actuation and thereby moving structures into a thermal metamaterial design allows for dynamic tuning far beyond what is possible with fixed structures and patterning. This section covers thermally actuated and electrostatically actuated approaches – both of which are implemented later in this research effort.

2.5.2 Bimorph cantilever beam actuators

Bimorph thermal actuators operate due to residual stress and a difference in the thermal expansion coefficients between two materials. The term bimorph refers to a structure with two layers, normally consisting of dissimilar materials. When current passes through a material, such as a polysilicon beam, it heats up due to $I^2 \cdot R$ losses, which is also known as resistive or Joule heating [23]. This heating causes the beam to expand in length due to thermal expansion. Alternatively, as seen later in this research, the beam can be heated via conduction from a heat source. The increase in beam length can be exploited to create physical displacements in MEMS devices. Figure 2.15 illustrates this phenomenon, where L_o is the initial beam length, L_{new} is the final length of the beam after thermal expansion, A is the cross-sectional area of the beam, and ΔL is the change in beam length [24]. Applying these parameters, the thermal elongation of a

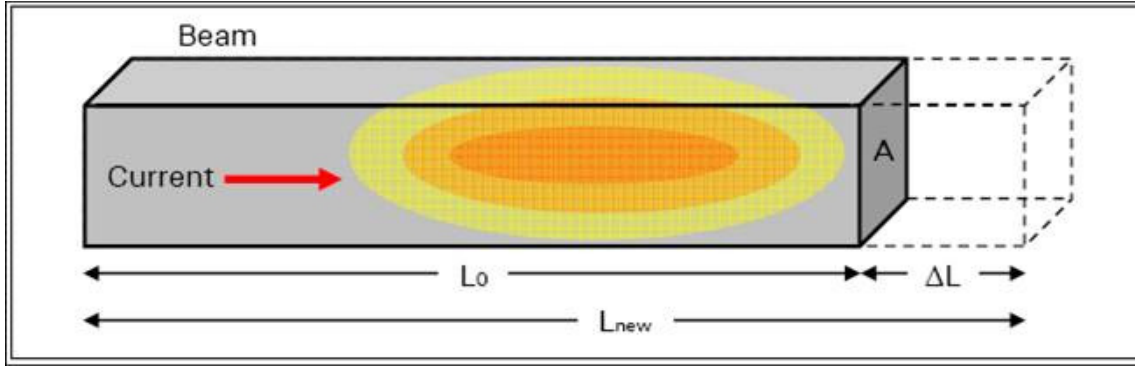


Figure 2.15: Joule heating causing thermal expansion in a MEMS beam [24].

MEMS beam can be described by Equation 2.16 [24].

$$L_{new} = L_0 + \alpha_L \left[L_0 (T_{avg} - T_0) \right] \quad (2.16)$$

The PolyMUMPs™ process accommodates depositing a layer of gold directly onto a layer of polysilicon. These two materials have notably different thermal coefficients of expansion (TCE), $2.8 \cdot 10^{-6} \text{ K}^{-1}$ for polysilicon and $14 \cdot 10^{-6} \text{ K}^{-1}$ for gold [8]. Therefore, during material temperature changes, gold expands and contracts much more dramatically than polysilicon. When these layers are both present in a structure such as a bimorph beam, the difference in expansion rates causes the bimorph beam to curl upwards slightly at lower temperatures, and bend downwards slightly at elevated temperatures. The longer the bimorph beam – the more curling up and bending down will occur. Figure 2.16 is a model (performed in CoventorWare 2008) of a typical bimorph cantilever beam where a layer of gold is deposited on top of a layer of polysilicon.

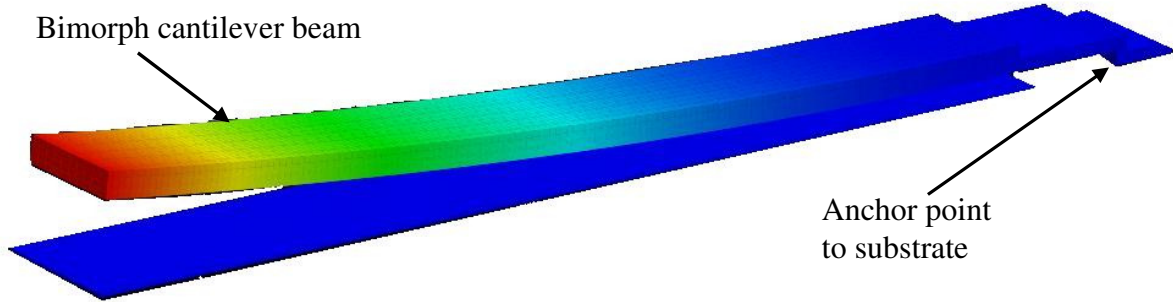


Figure 2.16: Example of a bimorph cantilever beam curling upward due to residual stress at room temperature, as modeled in CoventorWare 2008.

Curling of a bimorph cantilever beam due to residual stress is illustrated in Figure 2.17. Prior to release (described in Section 3.4.3), the cantilever beam is level due to the oxide layers preventing movement. After release, the residual stresses in the gold (tensile stress) and Poly2 (compressive stress) layers cause the free end of the bimorph cantilever to curl upward [23]. These stresses are primarily due to the gold having been deposited at an elevated temperature, whereas the release takes place at room temperature. After release, the gold layer contracts much more than the polysilicon, resulting in an upward curl of the bimorph beam. The amount of curl or deflection is a

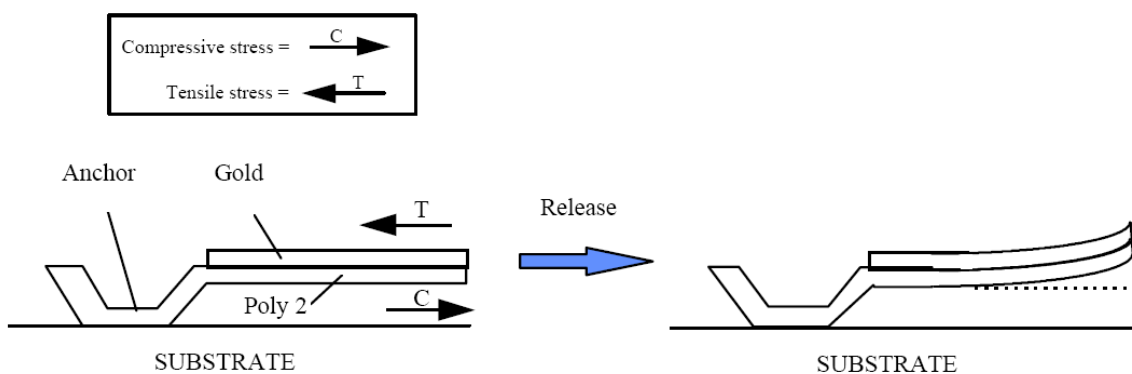


Figure 2.17: Example of cantilever beam curling due to residual stress [26].

function of the materials present, layer thicknesses, length of the bimorph beam, and temperature. By using controlled $I^2 \cdot R$ heating or heating the bimorph beam via conduction – the designer can effectively dictate the beams curl. This allows the beam to be used as a switch, or even as part of a MEMS-scale mechanical self-assembly system.

There are several advantages and disadvantages to using a bimorph cantilever beam as a MEMS actuator. The first advantage is that the movement of the implemented cantilever (curling up and bending down) is only a function of the beams temperature, and requires no active control inputs or logic. During the design phase, the engineer selects the materials, thicknesses, and beam lengths, which together with beam temperature dictate the bending position of the beam. The second advantage is that the actuation of the beams (if not heated using $I^2 \cdot R$ heating) requires no power, as it draws no current. The movement is strictly due to thermal expansion and contraction. The third advantage, which is a side effect of the first, is that the beams can be very densely packed in with other beams or structures without having to account for place and routing of control wiring traces and logic, which can take up valuable area on a small MEMS device.

The first disadvantage to using bimorph cantilever beams as actuators is that the movement cannot be actively controlled unless control logic is connected to the gold layer to facilitate $I^2 \cdot R$ heating, which would nullify the first and third advantages. A second disadvantage is that this actuation scheme is only appropriate for situations where there is a certain margin for position errors in the amount of curl or bending at a given temperature. This is because variations and inconsistencies in the fabrication process result in slightly different layer thicknesses and thereby slightly different amounts of curl

or bending at a specific temperature. Applications that require a precise position at an exact temperature would be better served by an actively controlled actuation scheme. The third disadvantage is that the response time of the actuation event is slow when compared to other actuation methods, including electrostatic actuation. This is due to the actuation being caused primarily by conductive heating throughout a beam structure, which is orders of magnitude slower than the switching of electrical potential used in other actuation methods.

2.5.3 Electrostatic Actuation

Electrostatic actuation is a common actuation approach used with MEMS structures. It is similar in theory to an electrical relay, where a small low-power control signal is responsible for switching on/off a higher power circuit. The difference being with the MEMS device, the high power side is actually a moving mechanical structure. The principle of operation is a difference in potential applied to parallel plates generates Coulomb attractive forces, which can become strong enough to overcome the mechanical restoring forces of the structure to which the potential is being applied [24]. Figure 2.18 illustrates these forces at work. The restoring force (F_r), is a function of the axial spring constant (k_z) which in turn is a function of the layout and material layer properties of the device [24]. Electrostatic force (F_e) is a function of the applied potential (V) the surface area of the plate (A), the permittivity (ϵ_0) of the air between the plates, and the gap in between the plates (z_0) [24]. The difference in potential causes electrons (negative charge carriers) and holes (positive charge carriers) to collect on the bottom and top plate,

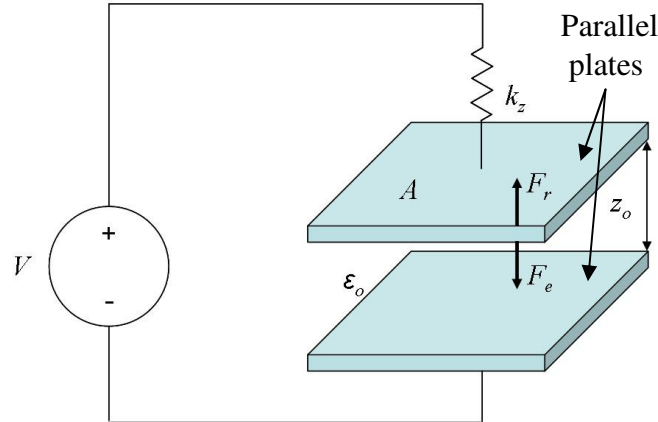


Figure 2.18: Force diagram for a parallel plate electrostatic actuation device [24].

respectively [24]. This potential difference creates an electrostatic force. If this electrostatic force is strong enough to overcome the mechanical restoring force of the structure, the top plate will move downward, closing the gap [24].

The amount of force generated by this phenomenon is calculated by applying Coulomb's Law to Figure 2.18, resulting in:

$$F_e = k_e \frac{\epsilon_0^2 A^2 V^2}{d^4} \quad (2.17)$$

where F_e is electrostatic force, k_e is Coulomb's constant, ϵ_0 is the permittivity of free space, A is the surface area of the electrode plate, V is the potential difference between the two plates, and d is the distance between the plates [24]. Note that the d^4 term in the denominator of Equation 2.17 means the electrostatic pull-in force will drop off rapidly as the gap (d) gets larger.

The non-linear electrostatic force (F_e) works against the linear mechanical restoring force (F_r) to pull the top plate downward toward the bottom plate or electrode. For a parallel plate arrangement, such as the one shown in Figure 2.18, an event known as

“pull-in” occurs once the top plate has been pulled downwards by F_e a distance $\approx 1/3$ the total gap between the plates (z_0) [25]. This position of the top plate (pulled downwards $z_0/3$) represents its maximum static stable displacement from its initial position [25]. Any further increase in F_e due to an increase in voltage V results in pull-in, where the top plate snaps downward the remaining $2 \cdot z_0/3$ making physical contact with the electrode or bottom plate [25]. The voltage V that corresponds to this maximum stable displacement of the top plate at $z_0/3$ is known as the pull-in voltage [25]. Pull-in voltage calculations for the designs presented in this effort are discussed in Section 3.2.3 and Equation 3.1.

As was with bimorph thermal actuators, there are several advantages and disadvantages to using an electrostatic actuator. The first and most obvious advantage is that the pull in event is actively controlled via an appropriately applied potential. This allows the designer to provision for very accurate timing and control of the actuation. The second and less obvious advantage is that once the potential that caused pull in to occur is removed, the structure will quickly snap back to its nominal position due to the mechanical restoring force. This “switching off” is significantly faster than what can be accomplished using the bimorph beams, due to the bimorph designs need to dissipate heat away from its structure in order to curl upwards or switch off. This switching speed makes an electrostatically actuated setup a much better choice for any application using MEMS switches for low speed logic.

The primary disadvantage to an electrostatic actuation scheme is that even in a MEMS process where the gap between electrodes is only 0.75-2.0 μm , the voltage required to pull in a beam is quite often higher than what is normally available in a microelectronics circuit (commonly 1.3 – 5.0 VDC). This can be a size, weight, and power (SWaP)

burden on the overall design as another voltage regulator may be required just to supply the electrostatically-actuated MEMS features. A second disadvantage which is directly related to the first is that the amount of pull in force generated is very small despite requiring relatively high voltages. This limits the application of this type of actuation scheme to mechanical structures with a fairly small restoring force to overcome. Lastly, as previously mentioned, electrostatic actuation requires routing control logic traces and electrode pads – consuming valuable real estate on a wafer.

2.6 Introduction to Carbon Nanotubes

2.6.1 Overview

CNTs are one of the more popular types of nanotechnology. They form as a cylindrical nanostructure composed of the element carbon. There has been a great deal of interest in them due to their high tensile strength, outstanding thermal conductivity, good electrical conductivity, and relatively high current carrying ability. Continuous CNTs can be formed with incredibly high length to width ratio's of several million to one, which is much greater than any other known material [27]. The objective of this section is to give the reader a basic understanding of CNTs. It begins by introducing the technology, its history, variants, and basic properties. Next, the physics behind CNTs is explained. Lastly, CNT fabrication techniques are examined.

2.6.2 History of CNTs

Most sources identify Sumio Iijima of the NEC Corporation as the first to discover CNTs. This 1991 discovery was accidental and occurred during his research of graphite electrodes used as part of an electric arc discharge [28]. The CNTs were found to be

formed in the soot of the electric arc discharge [29]. However, several other sources point to a journal paper published in 1952 by two Soviet scientists (L. Radushkevich and V. Lukyanovich) in which they obtained clear images of 50 nm (diameter) carbon tubes [29]. Due to the Cold War, this occurred largely if not entirely unknown to scientists outside of Warsaw Pact nations [29]. Theoretical experimentation and discussion of extremely thin carbon filaments dates back to the late 1800's when much research was being conducted to find optimal incandescent bulb filaments [29]. Microscope resolution and technology are likely the primary reason that many sources credit Sumio Iijima with the discovery as the earlier researchers lacked sufficient magnification to accurately identify the structural layout of the CNTs.

Since the early 1990's, CNT research has been extensive. The first experimental devices made using CNTs were CNT-based field effect transistors (FETs) made in 1998 at IBM [30]. By 2003, NEC had developed a fabrication process to produce CNT-based transistors [31]. In the 6 years since, CNTs research has taken many directions, including light-bulb filaments, ideal diodes, television pixels, and as a strengthener in high-end bicycle frames [32].

2.6.3 Types of CNTs

CNTs can be grouped into two categories – single-walled nanotubes (SWNTs) and multi-walled nanotubes (MWNTs). As the names imply, the SWNTs are composed of a single layer/sheet of graphene “rolled up” to form a tube, and the MWNTs are multiple layers/sheets rolled up, like tubes within a tube [33]. SWNTs as small as 0.4 nm in diameter are possible and have been fabricated, whereas about 1.2 nm is a more typical

diameter [33]. SWNTs are much more flexible than the MWNTs and can be bent and twisted significantly without discontinuities or breaking [33].

MWNTs are usually 100-200 times longer than wide and have diameters around 10 nm [33]. The distance between each “tube within a tube” is normally 3.4 Å or 0.34 nm [33]. In general, they are easier to produce in large quantities – but are subject to a higher defect rate than SWNTs [33]. Figure 2.19 shows a computer model of the MWNT structure. This more complicated structure leads to unusual and unexpected shapes as the length of each “tube” is independent of the total length, causing bending and other defects [33].

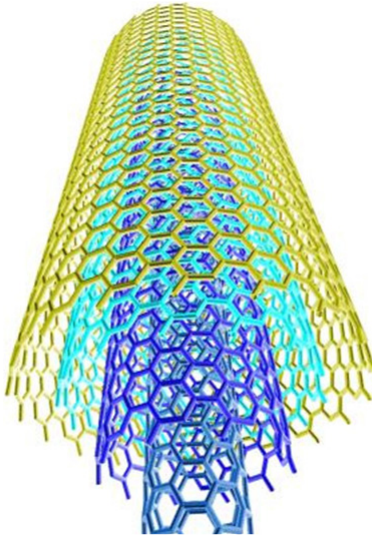


Figure 2.19: MWNT 3-D model showing tube within a tube detail [33].

2.6.4 Properties of CNTs

One of the main reasons there has been so much research focus on CNTs is the remarkable properties they possess. Some of the most important ones, strength, thermal conductivity, and electrical conductivity, are discussed below.

2.6.4.1 Strength of CNTs

CNTs “are the strongest and stiffest materials yet discovered on Earth, in terms of tensile strength and elastic modulus” [34]. The actual value of tensile strength varies based on type - values between 13-120 GPa have been reported for SWNTs, and around 150 GPa for MWNTs [34]. To put that in perspective – it is about 3X stronger than Kevlar and about 50X stronger than stainless steel. CNTs have a Young’s modulus of around 1 TPa – which is approximately 6X greater than Kevlar and 5X greater than stainless steel [34]. It is important to note that they are very weak under compression (opposite of tension) and tend to buckle [34].

2.6.4.2 Thermal conductivity of CNTs

CNTs are outstanding thermal conductors. They are ballistic conductors – meaning they are highly conductive along the tube, while being a good insulator to the sides of the tube [34]. SWNTs have shown thermal conductivity as high as 6000 W/(m·K) (about 15X better than copper) [34]. Very importantly – CNTs have not yet provided this high level of performance in bulk, only in very small quantities and single tubes [34].

2.6.4.3 Electrical conductivity of CNTs

The specific structure of a CNT dictates its electrical conductivity performance. CNTs can behave electrically either like metals, or like semiconductors. Metal-like configurations possess outstanding current carrying ability, on the order of $4 \cdot 10^9$ A/cm [34]. This configuration-dependent performance is discussed more in Section 2.6.5.

2.6.5 CNT physics overview

A SWNT can be simply described as a sheet of graphene (which is a form of carbon) rolled up to create a cylindrical surface [35]. This is illustrated in Figure 2.20. The manner in which the sheet is “rolled” (known as its “chirality”) dictates whether it will be highly electrically conductive (as in the left-most CNT in Figure 2.20) or if it will behave more like a semi-conductor (as in the two CNTs on the right of Figure 2.20) [33]. The CNT on the left of the figure is a type referred to as an “armchair” (behaves like a metal), while the one on the right is considered a “zigzag” (behaves like a much more electrically insulating semi-conductor) [33]. The one in the middle is referred to as “chiral”, and the degree to which it electrically conducts is dictated by its chirality, which can vary between that of the armchair and zigzag [33].

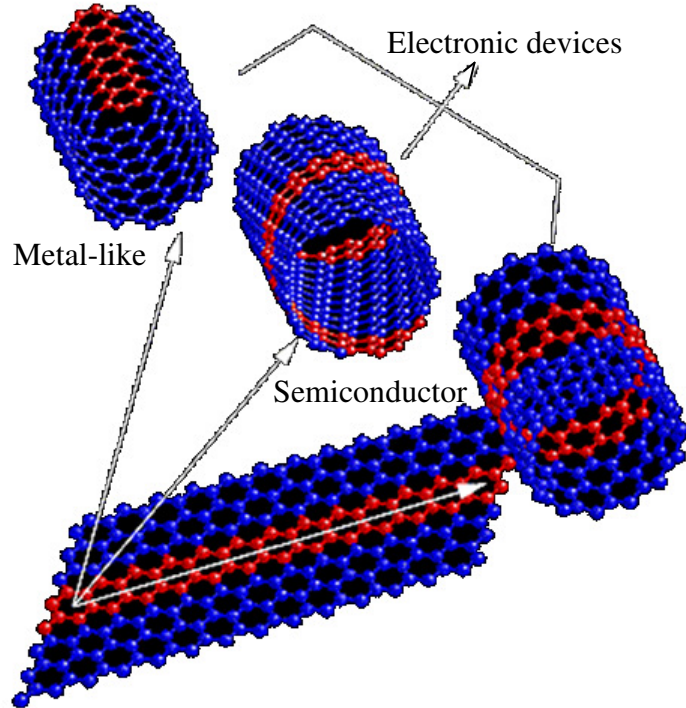


Figure 2.20: SWNTs of various electrical conductivity formed by “rolling” a sheet of graphene [33].

To determine the chirality of a SWNT, first two atoms in the graphene sheet are selected as the origins, shown as O and B in Figure 2.21 [36]. Second, the desired SWNT circumference is selected, and is annotated as vector OA and as vector BB' in Figure 2.21 [36]. Now the length of vector OA (which is equal to the length of vector BB') represents the circumference of the rolled sheet (SWNT) [36]. The tube is rolled such that O touches A , and B touches B' [36]. As shown in Figure 2.21 by the nearly vertical dashed parallel lines, the tube's axis is perpendicular to the vectors OA and BB' [36]. The “chiral vector” of the nanotube, which is vector OA or vector BB' , is defined as:

$$OA = BB' = n \cdot \hat{a}_1 + m \cdot \hat{a}_2 \quad (2.18)$$

where \hat{a}_1 and \hat{a}_2 are “unit vectors in the two-dimensional hexagonal lattice, and n and m are integers” [36].

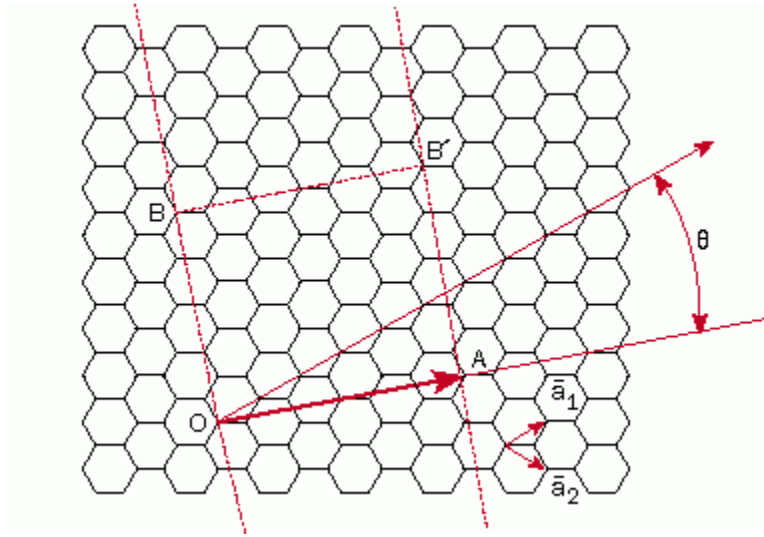


Figure 2.21: Determining chirality of a CNT [36].

In addition to the chiral vector OA (or BB'), the other key parameter used in describing SWNTs is the chiral angle (shown as θ in Figure 2.21) [36]. The chiral angle is the angle between vector OA and vector \hat{a}_1 , and must be between 0° and 30° [36]. As

seen in Figure 2.22, when this chiral angle is 0° , the SWNT is of the zigzag variety, and when $\theta = 30^\circ$, the SWNT is an armchair type [36]. Between 0° and 30° , it is chiral. As θ increases, the electrical conductivity increases [36].

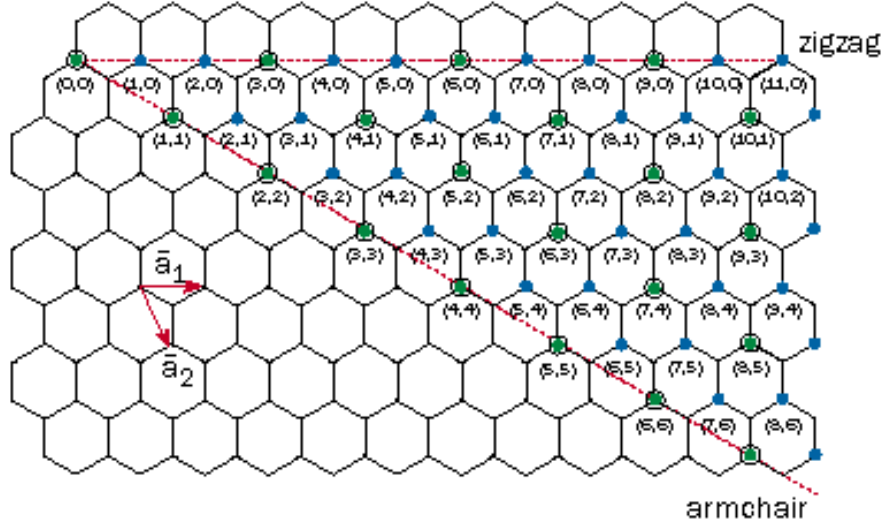


Figure 2.22: Possible CNT structures based on chirality [36].

Until recently, all available methods of producing CNTs would produce a mix of CNTs of varying chirality (i.e. there was a random combination of zigzag, armchair, and chiral types) [33]. This made it difficult to fabricate electronic devices as the electrical conductivity of the tube is a critical parameter. Recent research suggests that reliable means of producing quantities of CNTs in only the zigzag (semiconducting) form are in work [33]. One current approach to obtaining only semiconducting (zigzag) SWNTs begins with producing a random mix of SWNTs of varying chirality [33]. Then, an appropriate potential is applied in order to vaporize the armchair SWNTs (they blow like a fuse from too much current), leaving just the zigzag SWNTs intact [33]. This is a crucial hurdle to jump in order for CNTs to find a place in mainstream electronic devices.

2.6.6 Techniques of fabricating CNTs

There are three mainstream techniques for growing CNT's: arc discharge, laser ablation, and chemical vapor deposition. Each of these is presented in this section.

2.6.6.1 Arc discharge method

The arc discharge method is the most common and simple technique to fabricate CNTs [37]. It produces a complex mixture of components, and requires purification techniques to isolate the CNTs “from the soot and the residual catalytic metals present in the crude product” [38]. A simple arc discharge CNT fabrication setup is shown in Figure 2.23. This method creates CNTs “through arc-vaporization of two carbon rods

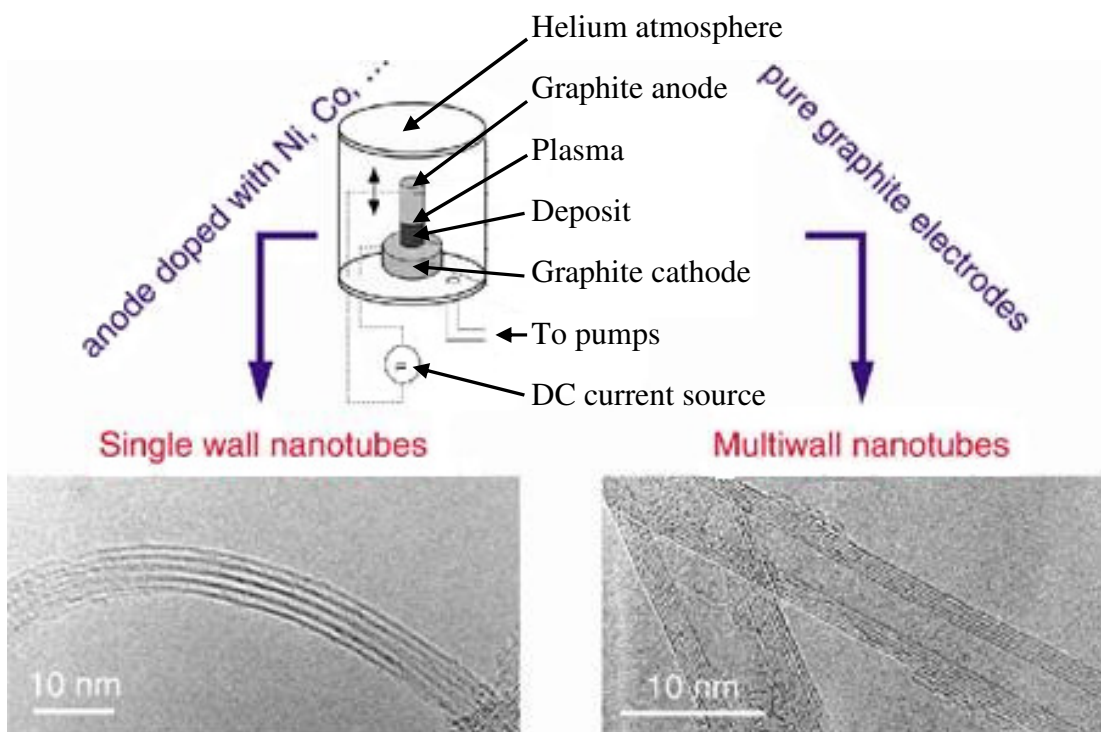


Figure 2.23: Basic arc discharge CNT fabrication setup [37].

placed end to end, separated by approximately 1 mm, in an enclosure that is usually filled with inert gas (helium, argon) at low pressure (between 50 and 700 mbar)” [37]. Next, “a

direct current of 50 to 100A, driven by a potential difference of approximately 20 V, creates a high temperature discharge between the two electrodes” [38]. Then, this discharge “vaporizes one of the carbon rods and forms a small rod shaped deposit on the other rod” [37].

Factors impacting the yield of CNTs produced include the “uniformity of the plasma arc” and the “temperature of the deposit formed on the carbon electrodes” [37]. This technique allows the manufacturer to selectively grow either SWNTs or MWNTs [37].

2.6.6.2 Laser ablation method

Laser ablation (also referred to as laser vaporization) is the most common way of producing relatively small quantities of very high quality CNTs [38]. In use since 1995, this method results in both a higher yield of CNTs and produces CNTs with more consistent properties than those produced by arc discharge [37]. CNTs produced by laser ablation are significantly more pure ($\approx 90\%$ purity) than those produced in the arc discharge process ($\approx 60\%$ purity) [37]. The fabrication setup is illustrated in Figure 2.24.

The fabrication (or synthesis) process begins with a laser vaporizing a graphite rod with a catalyst mixture of cobalt and nickel in a 1200 °C oven [37]. This sealed oven is filled with helium or argon at a constant pressure of ≈ 500 Torr [37]. Next, a superheated vapor plume forms – and then expands and cools rapidly [37]. As this vapor cools, small carbon molecules and atoms condense to form large clusters [37]. The catalysts also begin to condense, and attach to the carbon clusters, preventing them from “closing into cage structures” [37]. Starting from these clusters, tubular molecules grow into SWNTs until the catalyst particles become too large, or until the heated vapor has cooled to the

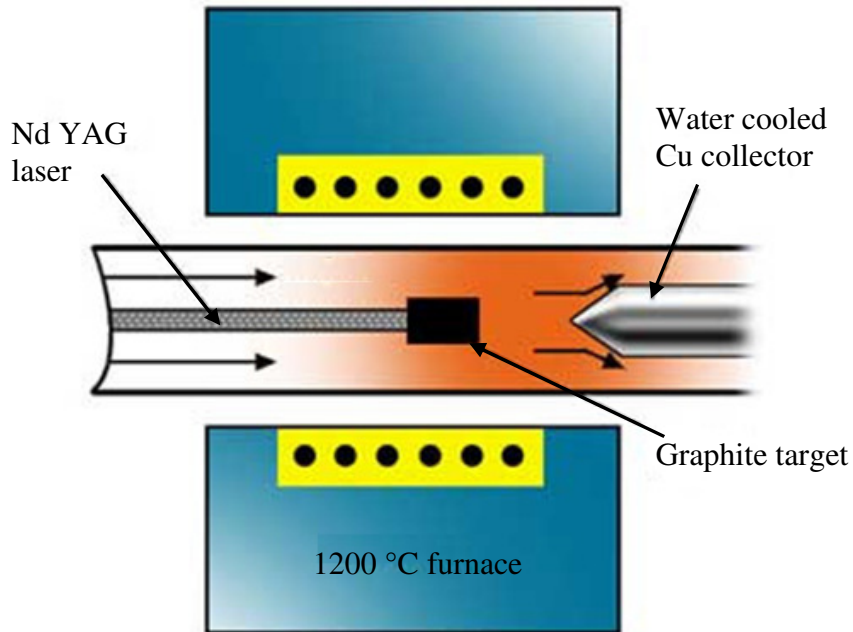


Figure 2.24: Laser ablation fabrication setup [37].

point where carbon can no longer diffuse through the surface of the catalyst particles [37]. It is also possible that the particles become completely coated with a layer of carbon and cannot absorb any more, in which case the SWNT stops growing [37]. The SWNTs formed in this case tend to bundle tightly together due to the van der Waals forces [37].

The CNTs produced by laser ablation appear as a flat group of bundles of SWNTs, each around 10-20 nm in diameter and about 100 μm in length [38]. The average SWNT diameter and length can be controlled by varying the growth temperature and catalyst ratio (cobalt to nickel ratio) [38]. Drawbacks to this fabrication method include it does not scale up well (only works well when small amounts are synthesized) and the resulting SWNTs are bundled and tangled – making them difficult to align or process for many scientific applications [38].

2.6.6.3 Chemical vapor deposition method

Chemical vapor deposition (CVD) based CNT fabrication involves putting a carbon source in the gas phase and using an energy source, such as plasma, to transfer energy to a gaseous carbon molecule [37]. Frequently used “gaseous carbon sources include methane, carbon monoxide and acetylene” [37]. The plasma “cracks” the molecule into reactive atomic carbon [37]. Next, the carbon diffuses towards the substrate, which is heated and coated with a catalyst (usually Ni, Fe or Co) where it binds [37]. This process results in consistent (diameter), well aligned CNTs [37].

Figure 2.25 shows a basic plasma enhanced CVD (PECVD) setup. This process begins by placing a substrate on the grounded (bottom) electrode [37]. Next, a reaction gas is supplied from the opposite side (top) plate [37]. Then, a catalytic metal, such as nickel, is deposited onto the substrate [37]. CNTs will grow on the catalyst (nickel) via “glow discharge generated from high frequency power” [37]. The catalyst used determines the resulting CNTs diameter, growth rate, and wall thickness [37]. When nickel is used, yields of nearly 50% are possible and at fairly low temperatures (around 330 °C) [37].

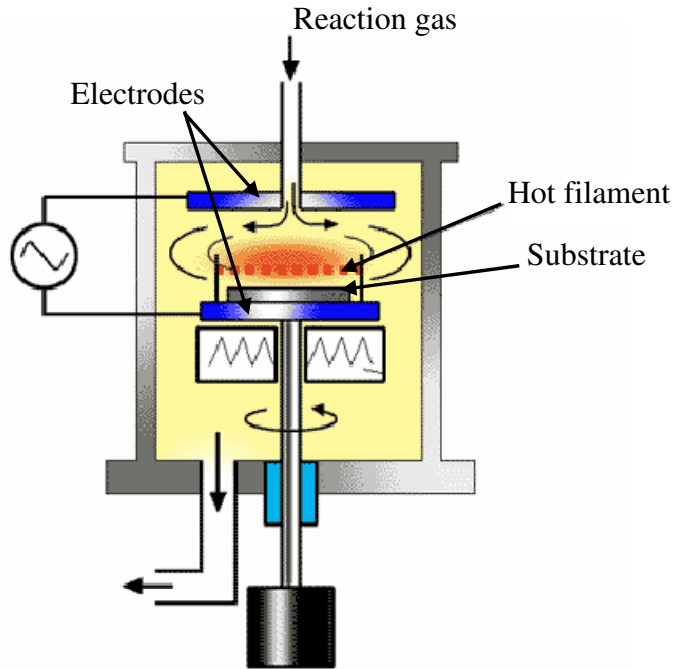


Figure 2.25: Plasma enhanced CVD based CNT fabrication setup [37].

2.7 Summary

This chapter examined the basics of heat transfer applied to small structures and thin layers found in the PolyMUMPs™ process. Electrical conductivity, and its relationship to thermal conductivity in many materials, was explored. Actuation and switching methods that are used later in this research effort were described. Lastly, an introduction to CNTs, essential to understanding the test and characterization tasks to be performed later, was presented. Understanding these principles is prerequisite to appreciating the performance of a MEMS based thermal metamaterial.

Methodology

3.1 Overview

Building upon the background research performed earlier, this chapter details the process of designing, modeling, and fabricating a series of proof-of-concept thermal metamaterials. The thermal metamaterial design development steps, from high-level idea to computer-aided design (CAD) layout, are covered. Finite element computer modeling (FEM) of the metamaterial designs is executed to fine tune each design's performance parameters. The fabrication process of transforming a CAD layout into a prototype device is detailed. Lastly, a series of prototype CNT-based braided ropes are introduced.

3.2 Metamaterial Design Development and Layout

3.2.1 Design approach

The design process began by brainstorming on which thermal-related material properties would be most appropriate for this thermal metamaterial design effort. Many ideas were considered, the first being a metamaterial where the wavelength of emitted thermal radiation was actively controlled within a certain range. A second idea considered a metamaterial which, through actuation of structural components, could switch between being opaque and transparent to a certain wavelength of thermal radiation. Either of these could be employed as part of a thermal radiative obfuscation scheme. A third idea involved designing a metamaterial in which the thermal and electrical conductivities can be decoupled, or tuned independently of one another, within a certain range. This could be accomplished via a switching network comprised of microscopic MEMS structures which, through mechanical switching, select various

conductive paths of various thin film materials to deliver the user-desired electrical and thermal conductivity properties. The fourth idea was to design a metamaterial composed of dense arrays of MEMS cantilever beams. These beams, which could be actuated thermally or electrostatically, create a metasurface (a 2-D metamaterial). This metasurface could have variable electrical and thermal conductivity via switching (opening/closing) of the arrays of cantilever beams. Although all four ideas are potentially fruitful research areas within thermal metamaterials, the fourth idea was selected for AFIT's first thermal metamaterial design.

The first potential application of this metasurface includes use as a thin film (less than $5\text{ }\mu\text{m}$ thick) which exhibits a somewhat tunable (not independently tunable) σ and κ when considered from an input side to an output side. Figure 3.1 (a) and (b) illustrate a conceptual drawing of this idea, in thermally-actuated and electrostatic-actuated versions, respectively.

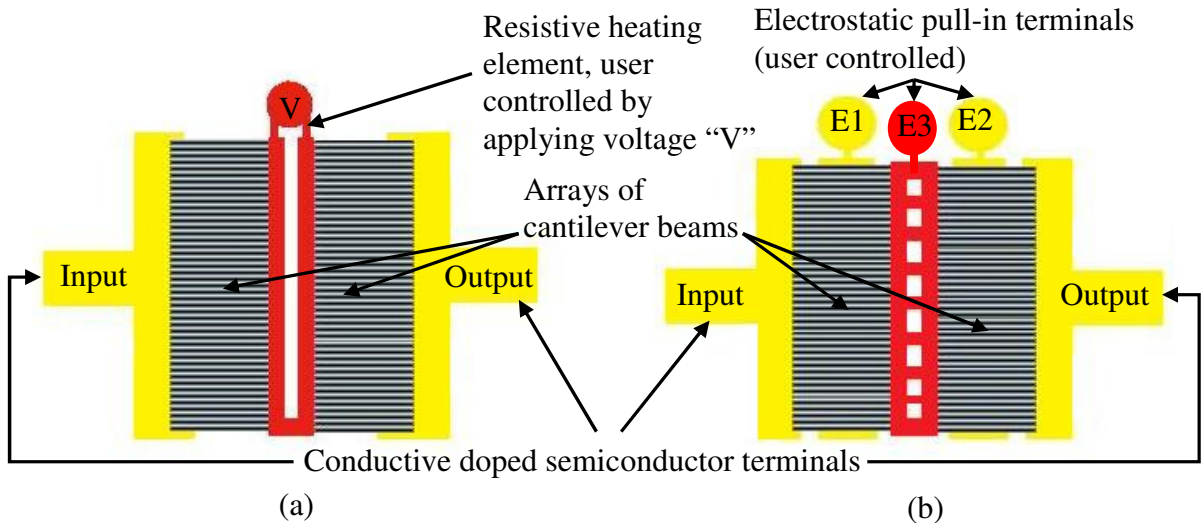


Figure 3.1: Conceptual drawing of a thermally-actuated thermal metamaterial (a), and of an electrostatically-actuated thermal metamaterial (b).

In Figure 3.1 (a), a thin film of MEMS structures facilitating a user and/or temperature controlled σ and κ is shown. This concept can operate in two ways. The first is when the user or application manages the control voltage “ V ”. This control signal generates resistive $I^2 \cdot R$ heating in the heating element shown in red. This heating causes the bimorph cantilever beams to close and make contact with the I/O terminals shown in yellow. As the beams begin to close, the σ and κ of the system, when considered from the I/O, will begin to dramatically increase as more conductive “paths” through the system appear. Therefore, the user, through manipulation of the control signal “ V ”, can vary or tune σ and κ within a certain range with respect to the system’s I/O.

The second way to operate this concept is simply through system temperature dependence. In this scenario, the bimorph cantilever beams close and make contact with the I/O terminals as a function of temperature only, with no user input to control “ V ”. The result is a thin film which, when evaluated from the I/O terminals, passively switches from a low/poor σ and κ at lower system temperatures to a higher σ and κ at a selected higher temperature.

Another spin on this same idea involved actuating the arrays of beams via electrostatic pull in instead of through heating of a bimorph device, as shown in Figure 3.1 (b). This is advantageous as it draws less power than resistive heating, has a reduced IR signature, and allows for faster, more active switching control of the beam arrays. In Figure 3.1 (b), the user or application manages the electrostatic pull in control voltages “ $E1$ ”, “ $E2$ ”, and “ $E3$ ”. These control signals cause the beam arrays to snap down and complete a conductive path between each I/O terminal and the middle structural element shown in red. “ $E1$ ” controls all of the beams to the left of center, “ $E2$ ” all those on the right, and

“E3” holds all beams at a common potential to facilitate pull-in. As the beams snap down, the σ and κ of the system, when considered from the I/O, will dramatically increase. Therefore, the user, through manipulation of the control signals, can vary or tune κ and σ within a certain range with respect to the system’s I/O.

In addition to the tuned κ and σ thin film application just presented, this same concept has a potential application as a “heat steering” device. In this application, the metamaterial could provide tailored, highly localized thermal management to a microelectronic device. More specifically, as part of a small space vehicle’s thermal management system, in which this metamaterial could be used to “steer heat” in the X-Y plane via variable conductivity. This could allow heat to be retained by the microelectronic device being managed during periods of extreme cold, and conducted away to the space vehicles radiative heat exchanger system during periods of elevated operating temperatures when the space vehicle must rid itself of excess thermal energy.

A conceptual drawing of this application is shown in Figure 3.2. A microelectronic device under metamaterial-based thermal management is surrounded by a dense array of MEMS cantilever beams. The MEMS beams are anchored to the substrate as one element of the substrate’s surface. When actuated, the arrays of cantilever beams make conductive contact with a heat sink material layer, effectively steering some of the microelectronic devices thermal energy via conduction. From the device’s perspective, the metamaterial surrounding it in its X-Y plane has variable thermal and electrical conductivity. This is because, for this structural arrangement, κ and σ properties are a function of which and how many cantilever beams are open or closed.

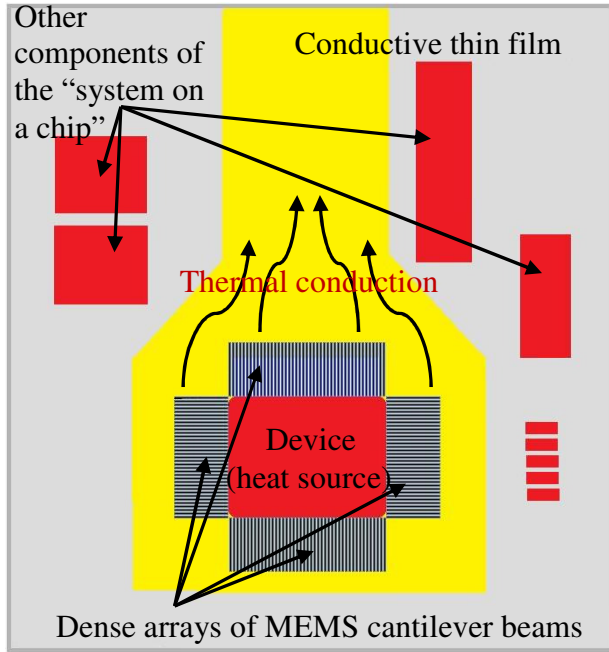


Figure 3.2: Conceptual drawing of thermal metamaterial in heat steering application. Heat generated by the “device” is conducted outward in the X-Y plane through an array of MEMS beams, and into a conductive thin film.

As with the tuned κ and σ thin film application, this “heat steering” application could be implemented in either a bimorph actuated or electrostatic actuated version. A conceptual drawing of a single unit cell of the bimorph cantilever beam array version is shown in Figure 3.3. Figure 3.3 (a) shows the orientation of the structural cantilever beams when the microelectronic device is off or in a low power state, where the temperature of the beam is close to ambient temperature. In this state, from the device’s perspective, the material surrounding the device in its X-Y plane has very poor thermal and electrical conductivity. This is of course due to the device’s perimeter being surrounded by a temperature actuated switching structure.

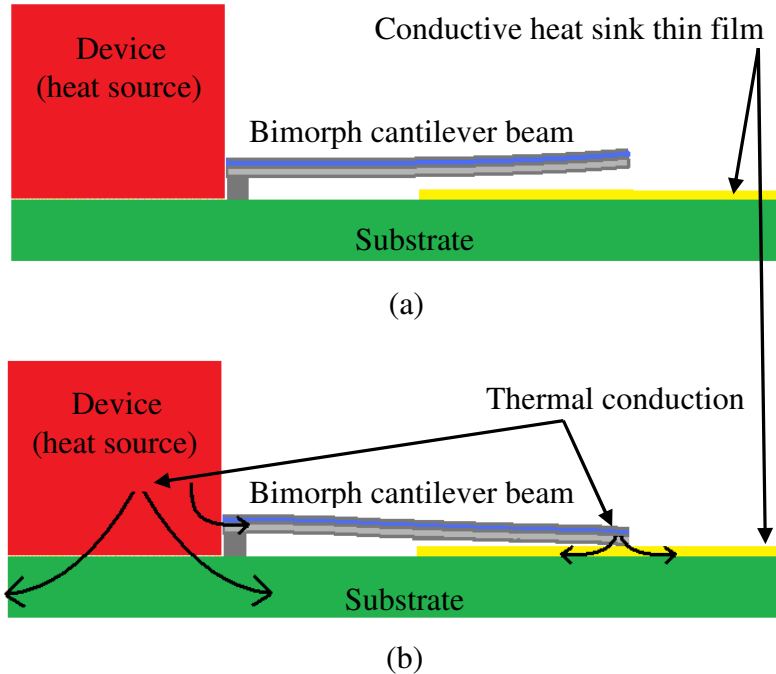


Figure 3.3: Bimorph cantilever beam array unit cell, cross-sectional view. Top (a) shows the unit cell when the “device” is off or in a low power state. Bottom (b) shows the unit cell when the “device” has generated sufficient heat to cause the bimorph beam to bend downwards, with heat conducting through the beam and into the conductive thin film.

As the microelectronic device is powered on and heat is generated as a byproduct of the device’s power consumption, several things start to happen. First, certain spots within the device become hot relative to the device’s average temperature. The temperature difference between these hot spots and the cooler surrounding device structure causes thermal conduction to occur within the device. As this conduction continues throughout the device, the device surfaces will begin to heat. This surface heating is not uniform, some surface locations will be hotter, sometimes much hotter, than the devices average temperature. Bimorph cantilever beams near the hottest surface locations will warm due to thermal conduction. These conductively-heated beams begin

to bend downward and make mechanical contact with a conductive thin film layer which functions as a heat sink. Once each individual beam makes contact with the heat sink, heat begins to conduct on a path from the hot microelectronic device, through the individual bimorph beam, and into the heat sink layer. This path is shown in Figure 3.3 (b). Thermal conduction occurs throughout the heat sink layer such that the heat energy can be steered to some extent by the layout/routing of the heat sink.

Bimorph cantilever beams near cooler surfaces of the device will also begin to heat due to thermal conduction, but at a slower rate and attain a lower temperature than those near the hotter spots. Beams near these cooler areas may not reach a temperature high enough to cause sufficient beam bending to close the conductive path from the device to the heat sink. As the device surface temperatures continue changing due to varying device power consumption and other factors, each beam will continue to individually bend down slightly or curl up slightly in response. The net result is the hotter surfaces will “see” a low resistance conductive path, while the cooler surfaces will “see” a high resistance, less conductive path. The hotter areas will conduct away some heat, and the cooler areas will be more insulated, conducting away much less energy. Steady state, the result is the temperatures at the device’s hot spots and cool spots will both be closer to the average device temperature than without the surrounding metamaterial structure.

The bimorph beam array structural arrangement results in a material which, from the device’s perspective, has an electrical and thermal conductivity that is both highly localized (varies by moving just 10’s of micrometers), and varies as a strong function of temperature. This metamaterial has localized poor thermal and electrical conductivity at lower temperatures, but has localized good thermal and electrical conductivity at elevated

temperatures. Additionally, the material switches between these characteristics at a designer dictated temperature, as the switching temperature is a function of beam length and material. Lastly, because this mechanical switching is due to thermal expansion and not an electrical input signal, the metamaterials functionality is completely autonomous and consumes no electrical power.

A conceptual drawing of a single unit cell of the electrostatic-actuated cantilever beam array version is shown in Figure 3.4. Figure 3.4 (a) shows the orientation of the structural cantilever beams in their default, non-actuated state. In this state, from the device's perspective, the material surrounding the device in its X-Y plane has very poor thermal and electrical conductivity. The position of the cantilever beams is almost completely unaffected by temperature changes in the microelectronic device. Beam position can only be altered by actively applying an appropriate control signal to the electrostatic pull-in electrode beneath each cantilever beam.

Once the appropriate control signal is applied to the electrostatic pull-in electrode, the cantilever beams snap downward and make mechanical contact with a conductive thin film layer which functions as a heat sink. Once each beam makes contact with the heat sink, heat begins to conduct on a path from the hot microelectronic device, through the individual cantilever beam, and into the heat sink layer. This path is shown in Figure 3.4 (b). Thermal conduction occurs throughout the heat sink layer such that the heat energy can be steered to some extent by the layout/routing of the heat sink.

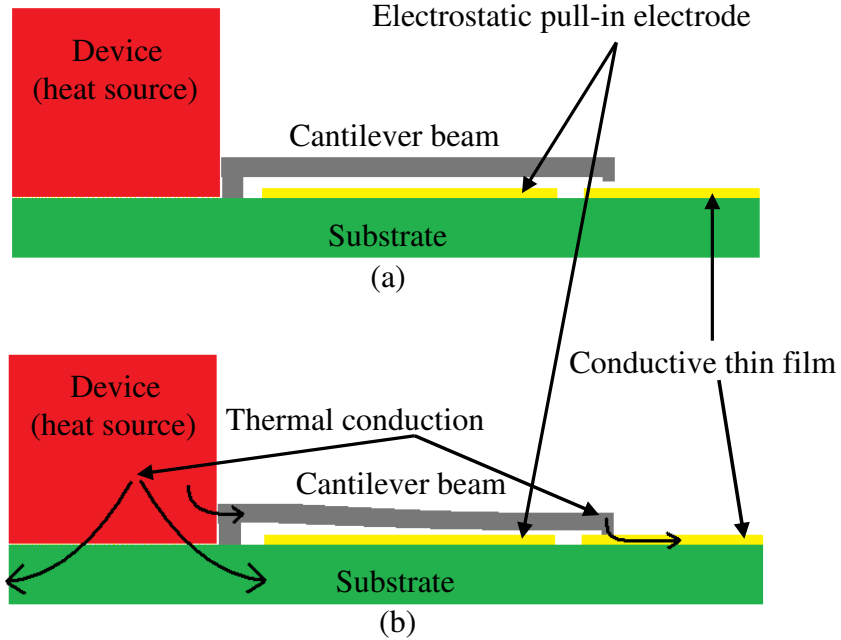


Figure 3.4: Electrostatic-actuated cantilever beam array metamaterial unit cell conceptual drawing, cross-sectional view. Top (a) shows the unit cell with the pull-in function not actuated. Bottom (b) shows the unit cell with beam pulled-in, and with heat conducting through the beam and into the conductive thin film.

The electrostatic-actuated cantilever beam array structural arrangement results in a material which, from the device's perspective, has variable electrical and thermal conductivity. These parameters are dictated by application of the electrostatic pull-in control signal. This metamaterial has localized poor thermal and electrical conductivity when not actuated, and has localized good thermal and electrical conductivity when actuated. Additionally, the control logic can be designed such that, again from the device's perspective, there can be several intermediate values of σ and κ . This can be accomplished by opening/closing certain combinations of the beams. Unlike the bimorph actuated version of this concept, these electrostatic-actuated metamaterials do consume a small amount of electrical power in operation. This is primarily due to $I^2 \cdot R$ losses in the

transmission/routing of the electrostatic pull-in control signals to the electrodes through the resistive polysilicon (Poly0) layer.

Both versions of the “heat steering” conceptual drawing addressed thermal management in the X-Y plane of the device. However, device cooling is a three-dimensional discipline. This metamaterial-based thermal management concept would be used in conjunction with, not as a complete replacement of, a traditional thermal management/heat sink setup. That said, given the MEMS scale of these cantilever beam arrays, and the fact that the beams can be designed to actuate either individually or in small groups, they could be used to help manage hot spots on a microelectronic device. A dense array of hundreds of beams anchored near a hot spot could effectively increase the surface area of the spot, allowing the primary heat sink system to more uniformly transfer heat away from the device. The goal of a heat sink system is to keep the hottest spot of the device below a certain threshold temperature. The addition of these MEMS beam arrays near hot spots could reduce sizing requirements on the overall heat sink system by keeping hot spot temperatures closer to the devices average temperature. The scale of these beams allows for highly localized management of the devices temperature, and effectively spreads out the power density of the hot spots.

3.2.2 Thermally-actuated bimorph cantilever beam array metamaterial

Building upon the tuned κ and σ thin film and “heat steering” conceptual drawings, the next step was to translate the concepts into functional design layouts that could be modeled and fabricated. As is often done in MEMS prototyping efforts, several variants of the conceptual design were prototyped. This included versions featuring passively

actuated, bimorph cantilever beam arrays as the main structural feature of the metamaterial. These versions are presented first.

The conceptual designs of the bimorph cantilever beam array based metamaterial were translated into a CAD program to facilitate modeling and prototyping. The CAD program used was MEMSCAP Tanner EDA's L-Edit. The software was selected due to its availability on AFIT's MEMS laboratory computers, and is commonly used by MEMS design engineers. There were several significant compromises, changes, and alterations made during the transition from conceptual drawing to CAD design. First, a modified version of the resistive heating element from the tunable thin film concept was chosen over the microelectronic device from the "heat steering" concept. This was done primarily because of size constraints, as each MEMS researcher was only allotted a 3 mm X 3 mm die site - onto which all versions of the design must fit together. Additionally, utilizing a resistive heating element allowed for more accurate and repeatable control over the amount of electrical power input to the system. Secondly, the cantilever beam arrays were only placed on two sides of the resistive heating element. This was also done as a space saving compromise.

The L-Edit layout for the bimorph cantilever beam array metamaterial is shown in Figure 3.5. The layout features a dense array of thermally-actuated bimorph cantilever beams anchored near and attached to a polysilicon resistive heating element. These bimorph beams bend downward when heated due to the differences in thermal coefficients of expansion between the top layer of gold and the underlying structural layer of polysilicon. When thermally actuated, the cantilever beams make contact with a large polysilicon sheet which acts either as an I/O terminal or a heat sink, depending on

the application being considered. The layer coloring scheme for the L-Edit CAD layouts is summarized in Table 3.1.

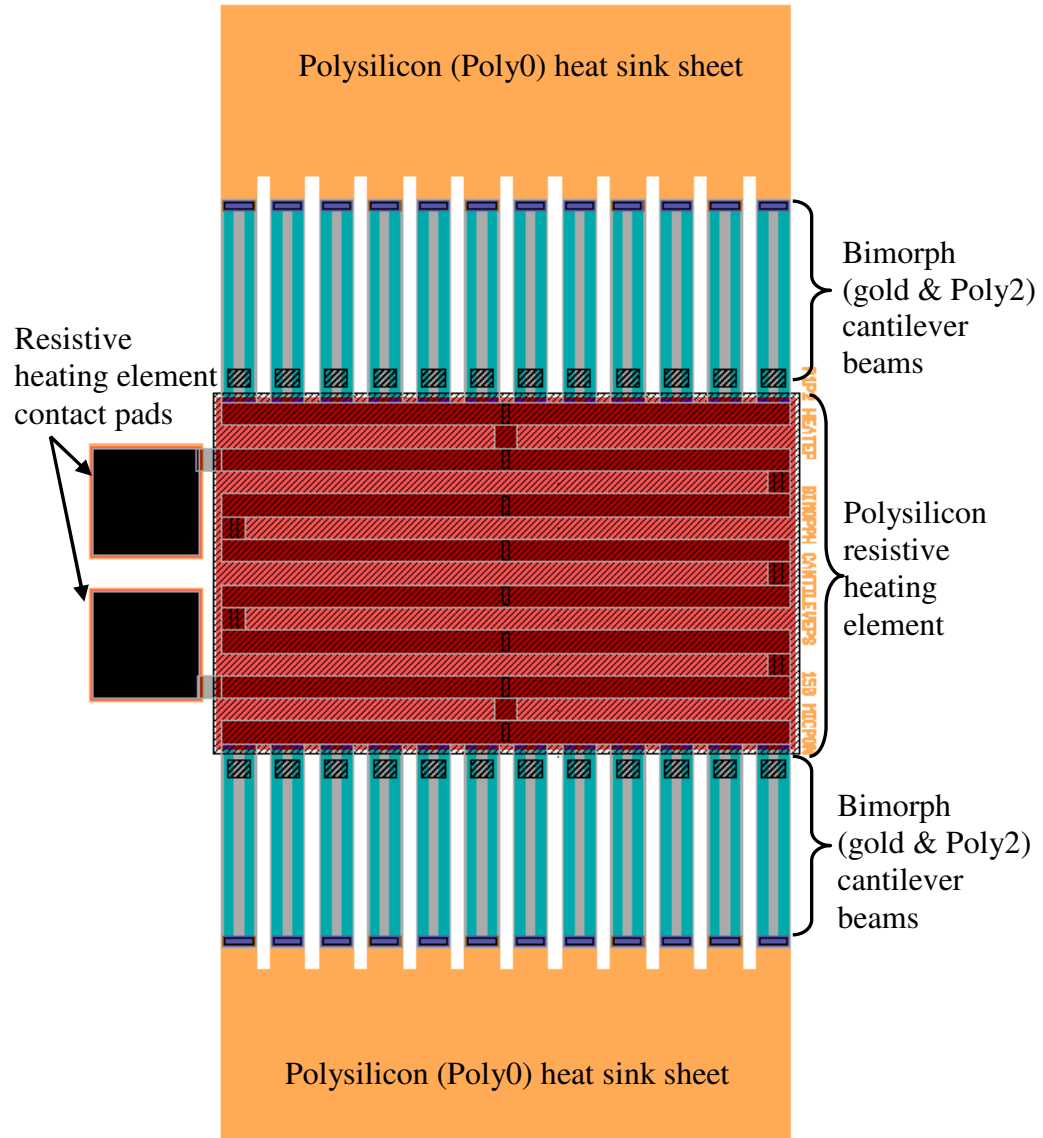


Figure 3.5: Bimorph cantilever beam array metamaterial CAD layout. Bimorph cantilever beams curl upward and bend downward in response to ambient temperature and/or $I^2 \cdot R$ heating from resistive heating element, creating conductive paths through the system.

Table 3.1: L-Edit CAD layout layer coloring scheme.

Material Layer	Color
Polysilicon 0 (Poly0)	Orange
Polysilicon 1 (Poly1)	Red
Polysilicon 2 (Poly2)	Grey
Gold (Metal)	Light Blue
Poly1 & Poly2 Stacked	Dark Red with Checkering

As was discussed with the “heat steering” conceptual drawing, each cantilever beam responds independently to the heat source, such that the beams connected to higher temperature parts of the heater will “close” or make contact sooner. This has the effect of drawing heat away from the hottest spots first – effectively managing the temperature of the heat source on a very localized level.

Four variations of this design were developed, with cantilever beam length being the only variable. The temperature at which the bimorph beams bend down and make conductive contact with the Poly0 layer below is a function of beam length. Lengths of 150, 200, 250, and 300 μm were made. Beam width is 30 μm in all cases. Bimorph beam thickness, which was dictated by the fabrication process, is 2 μm (1.5 μm of polysilicon and 0.5 μm of gold). The resistive heating element, effectively a 2 $\text{k}\Omega$ polysilicon resistor, is controlled by applying a potential across the two terminals. Figure 3.6 is a 3-D model (CoventorWare 2008) representation of the CAD layout shown in Figure 3.5. In the figure, green is an n-type substrate, light blue is an insulative silicon nitride layer, yellow is the first layer of polysilicon (Poly0), red is the second layer of polysilicon (Poly1), peach is the third polysilicon layer (Poly2), and blue is a gold layer.

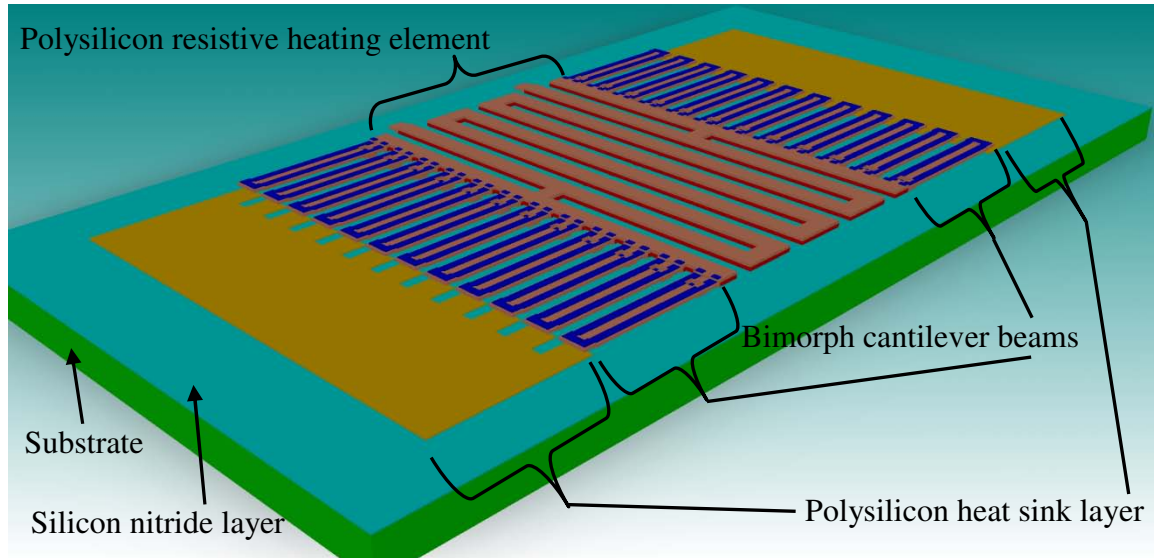


Figure 3.6: Bimorph beam array metamaterial 3-D model (modeled in CoventorWare 2008). Heating element contact pads are not shown.

This coloring scheme, along with the thickness of each layer, is summarized in Table 3.2.

Note that in this 3-D model the resistive heating element contact pads are not shown.

Table 3.2: 3-D layout layer coloring scheme.

Material Layer	Color	Thickness
n-type Substrate	Green	675 μm
Silicon Nitride	Light Blue	0.6 μm
Polysilicon 0 (Poly0)	Dark Yellow	0.5 μm
Polysilicon 1 (Poly1)	Red	2.0 μm
Polysilicon 2 (Poly2)	Peach	1.5 μm
Gold (Metal)	Blue	0.5 μm

3.2.3 Electrostatic-actuated cantilever beam array metamaterial

In addition to the bimorph cantilever beam array based metamaterial layouts just discussed, six versions featuring electrostatic-actuated cantilever beam arrays as the main structural feature of the metamaterial were designed. These versions spotlight a

significantly different beam actuation technique, which provides somewhat different overall capabilities.

The conceptual designs for the electrostatic-actuated cantilever beam array based metamaterial were translated into the L-Edit program to facilitate modeling and prototyping. Like with the bimorph beam based designs, there were several significant changes made during the transition from conceptual drawing to CAD design. The resistive heating element from the tunable thin film concept was again chosen over the microelectronic device from the “heat steering” concept. Also, the cantilever beam arrays were again only placed on two sides of the “device” (resistive heating element).

The L-Edit layout for the electrostatic-actuated cantilever beam array metamaterial is shown in Figure 3.7 (see Table 3.1 for layer coloring scheme). The layout features a dense array of electrostatic-actuated cantilever beams anchored near a polysilicon resistive heating element.

There are several significant differences between this design and the bimorph beam based design. Here, since the opening/closing of the cantilever beam contacts is actively controlled via electrostatic pull-in, two additional contact pads are added (pull-in terminal #1 and #2 in Figure 3.7). Each pad is connected to polysilicon sheets (Poly0) which run along the length of each cantilever beam, 2 μm beneath them. A sufficient potential difference between the bottom sheet of polysilicon and the cantilever beam above will cause the beam to pull-in and make contact with the polysilicon (Poly0) heat sink. Note that this design uses cantilever beams consisting of only a single polysilicon layer (no metal layer on top).

Unlike the previous design in which each beam actuated individually, these cantilever beams make contact in sets of 12 when the appropriate voltage is applied to the pull-in

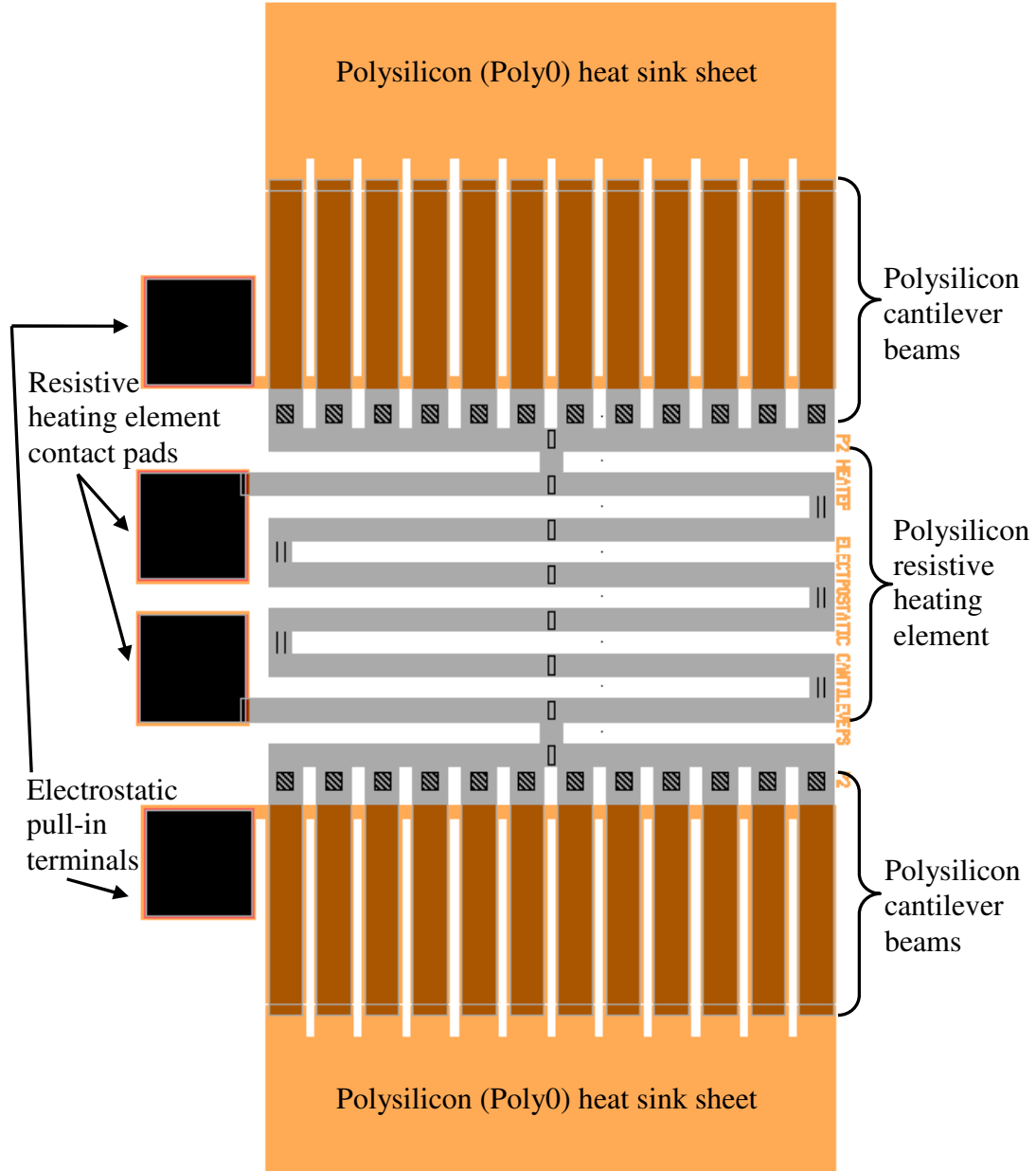


Figure 3.7: Electrostatic-actuated cantilever beam array metamaterial CAD layout. Cantilever beams snap downwards (pull-in) in response to electrostatic attraction caused by a difference in potential between the polysilicon cantilever beams and the polysilicon electrodes attached to each electrostatic pull-in terminal. This actuation creates conductive paths through the system.

terminals. This results in trading highly localized passive thermal management for more active control. The equation used to determine structure sizing for pull-in voltage was:

$$V_p = \sqrt{\frac{8 \cdot k \cdot g^3}{27 \cdot \epsilon_0 \cdot W \cdot W_e}} \quad (3.1)$$

where V_p is the pull-in voltage (V), k is a spring force constant (N/m) and is a function of the beam material and dimensions, g is the air gap between the Poly0 electrode and cantilever beam (μm), ϵ_0 is the permittivity of free space (F/m), W is the cantilever beam width (μm), and W_e is the width of the electrode (μm). The electrode was sized to accommodate a pull-in voltage of approximately 8 V and 12 V, for the designs with Poly2 beams and Poly1 beams, respectively.

Six variations of this design were developed, with cantilever beam material (Poly1 versus Poly2) and resistive heater grid layout/material being the variables. The first variation featured a Poly1 resistive heater element and Poly1 cantilever beams. Second, a design using Poly2 for both the heater element and cantilever beams was drawn. The third design had a heater element consisting of Poly1 and Poly2 stacked with Poly1 cantilever beams. The fourth version also had a heater element consisting of Poly1 and Poly2 stacked, but with Poly2 cantilever beams. The fifth and sixth variants featured a somewhat different heater arrangement (shown in Figure 3.8), with Poly1 (fifth version) and Poly2 (sixth version) cantilever beams. All six variants had 200 μm long, and 30 μm wide beams. Beam thickness, which was dictated by the fabrication process, is 2 μm for versions with Poly1 beams, and 1.5 μm for those with Poly2 beams. Distinguishing characteristics of these six versions are summarized in Table 3.3.

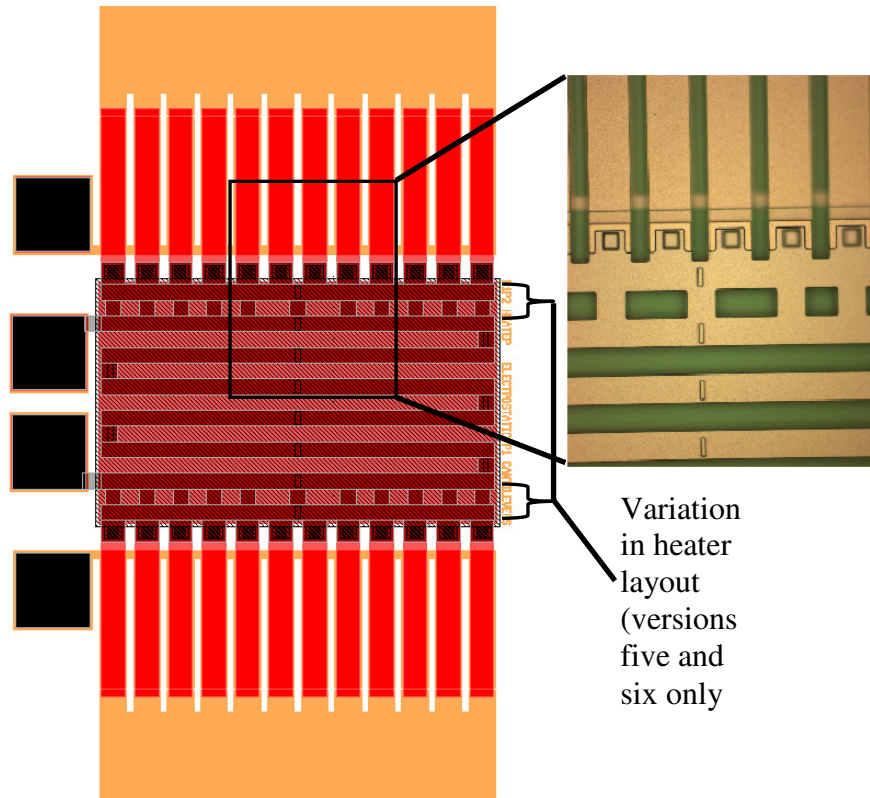


Figure 3.8: Electrostatic-actuated thermal metamaterial CAD layout showing variation of heater design. This variation added additional polysilicon connections between the polysilicon heater grid and the arrays of polysilicon beams to facilitate increased heat transfer between the heater and beam arrays.

Table 3.3: Electrostatic-actuated metamaterial versions. Detailed images of each version fabricated are shown in Appendix A. For all versions, beam length and width are 200 μm and 30 μm , respectively. Beam thickness is 2.0 μm or 1.5 μm , for versions with Poly1 or Poly2 beams, respectively.

Layout Version	Beam Material	Heater Style 1 = Figure 3.7 2 = Figure 3.8	Heater Material
1	Poly1	1	Poly1
2	Poly2	1	Poly2
3	Poly1	1	Poly1/Poly2 stack
4	Poly2	1	Poly1/Poly2 stack
5	Poly1	2	Poly1/Poly2 stack
6	Poly2	2	Poly1/Poly2 stack

Figure 3.9 is a 3-D model (using CoventorWare 2008) of the CAD layout shown in Figure 3.7 (layout version #2 shown, others similar). The coloring scheme is as defined in Table 3.2. Note that in this 3-D model the resistive heating element contact pads and the pull-in terminals are not shown.

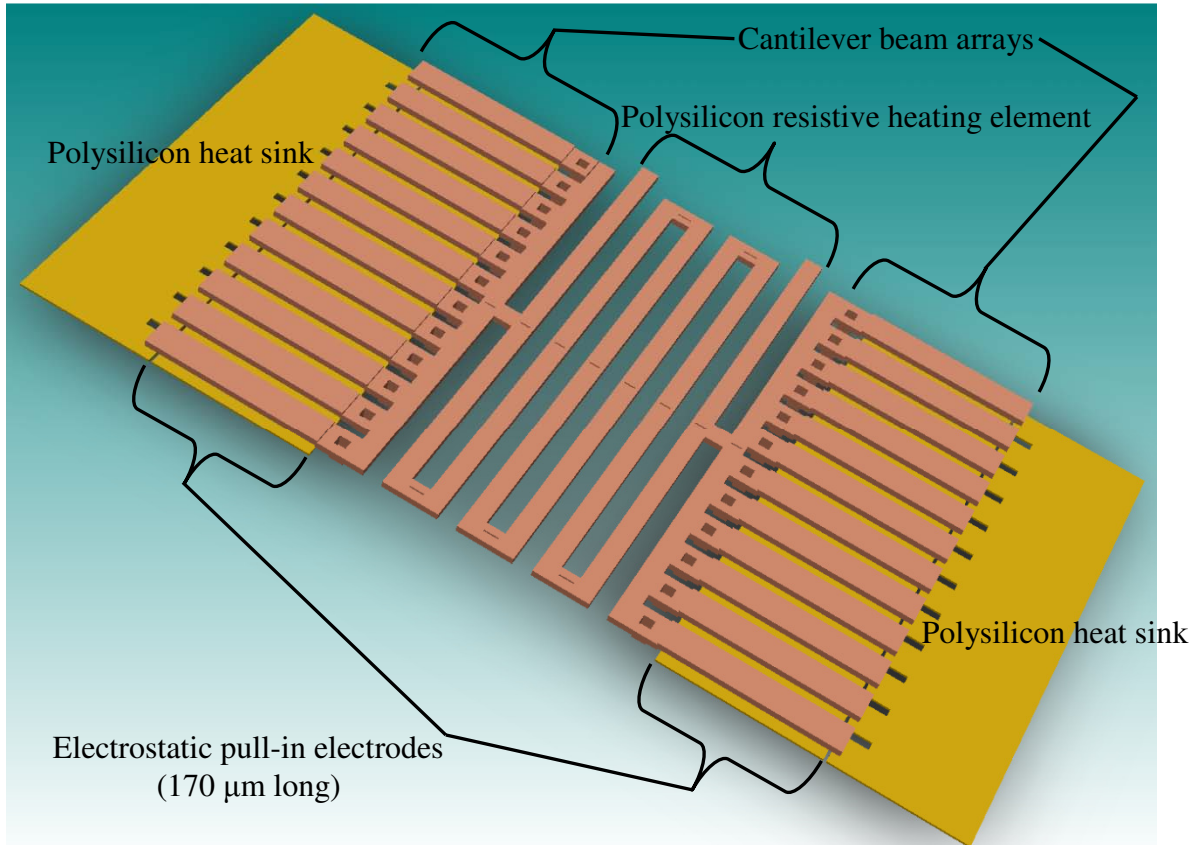


Figure 3.9: Electrostatic-actuated cantilever beam array metamaterial, as modeled in CoventorWare 2008.

3.3 Metamaterial Design Modeling

3.3.1 Overview

Each of the ten thermal metamaterial design variants presented in Section 3.2 were analyzed using finite element modeling (FEM). FEM was an important part of the overall design process as it allowed verification of the major metamaterial design

functions prior to beginning the costly fabrication process. The metamaterial layouts were modeled using the CoventorWare MEMS 2008 software package. CoventorWare MEMS is a popular FEM tool within the MEMS product development, manufacturing, and academic community.

3.3.2 Thermally-actuated bimorph cantilever beam metamaterial modeling

Each of the four bimorph cantilever beam array based metamaterial layouts (150, 200, 250, and 300 μm length bimorph beams) were exported from L-Edit to CoventorWare MEMS for FEM. Using CoventorWare, the 3-D model shown in Figure 3.6 was generated. Each of the four layouts was subjected to a series of parametric modeling simulations which examined beam displacement and temperature versus applied voltage. As expected, the arrays of bimorph beams curl slightly upwards at lower temperatures, and bend downward, making conductive contact with the polysilicon layer below, when heated. Figure 3.10 and Figure 3.11 illustrate how the bimorph beams curl upwards at low temperatures due to residual stress and the “as deposited” TCE of materials during the deposition process during time of fabrication, and bend downwards at higher temperatures due to differences in the thermal coefficients of expansion between the polysilicon beam and the top gold layer.

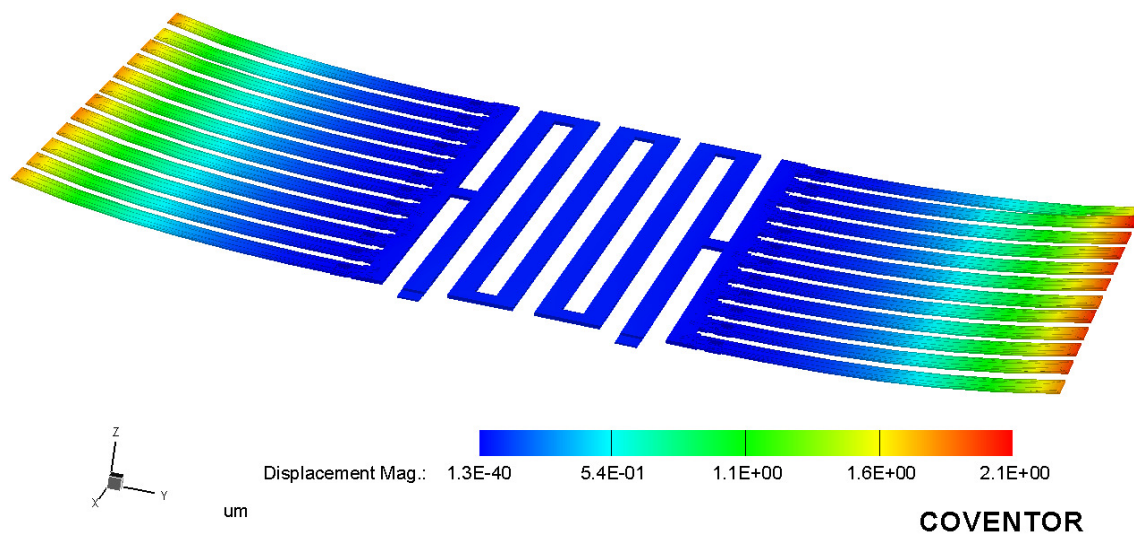


Figure 3.10: Bimorph cantilever beams curling upwards at room temperature (exaggerated 15X), as modeled in CoventorWare 2008. Bimorph beams curl upwards at low temperatures due to residual stress and the “as deposited” TCE of materials during the deposition process during time of fabrication.

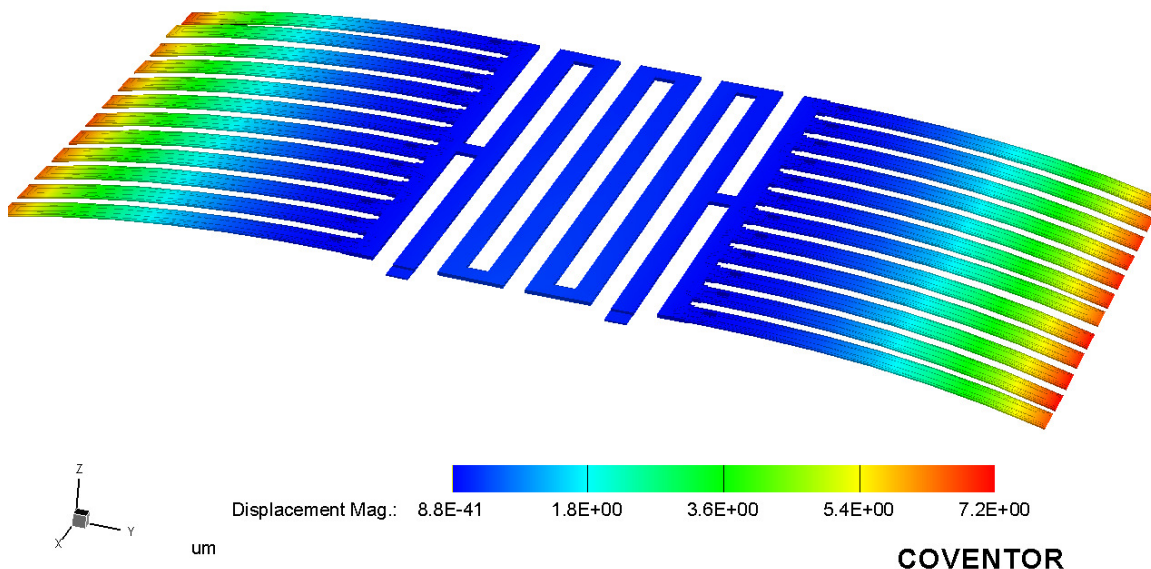


Figure 3.11: Bimorph cantilever beams bending downward at elevated temperatures (130 °C), as modeled in CoventorWare 2008. Bimorph beams bend downwards at higher temperatures due to differences in the thermal coefficients of expansion between the polysilicon beam and the top gold layer.

Figure 3.12 shows how the bimorph cantilever beams react to voltage applied across the heater terminals. The bimorph beams curl upwards at room temp with no voltage applied due to residual stress. Once sufficient voltage has been applied to heat the beams to approximately 50-60 °C, they appear to be nearly straight or horizontal. Continued heating via increased applied voltage eventually results in mechanical contact being made between the beam tip and the polysilicon sheet beneath it, closing the contact, and conducting heat and electricity from the heater grid into the polysilicon layer below.

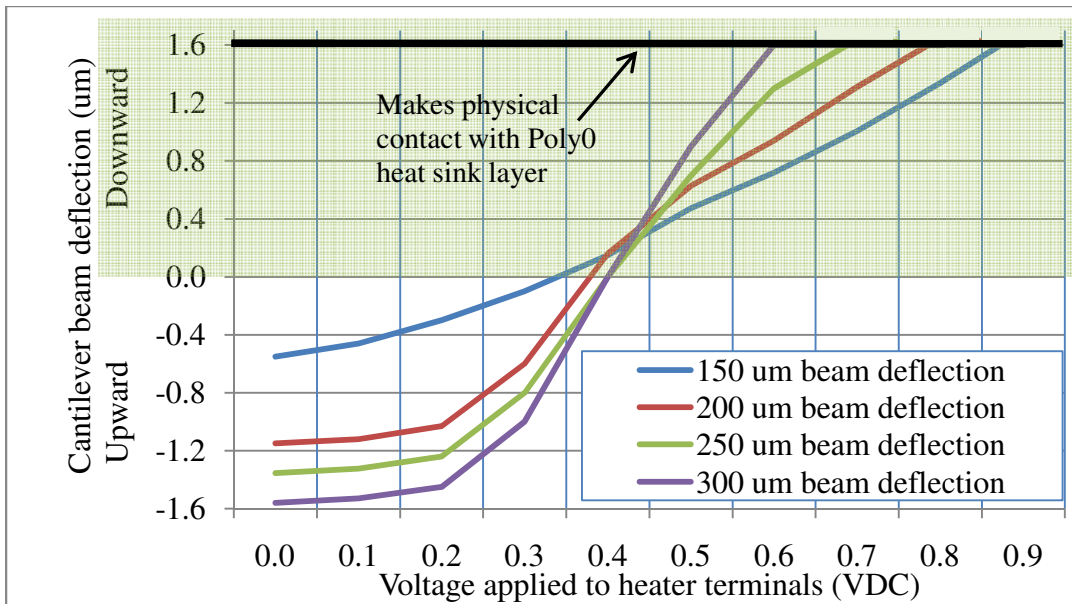


Figure 3.12: Bimorph cantilever beam tip displacement verses applied voltage. Longer beams exhibit greater upward curl at low temperatures, and bend downward, making contact with the polysilicon heat sink layer below (represented by solid black line), at lower temperatures than their shorter counterparts.

Figure 3.13 shows the correlation between applied voltage and steady state beam temperature (average temperature when voltage has been applied for a long time).

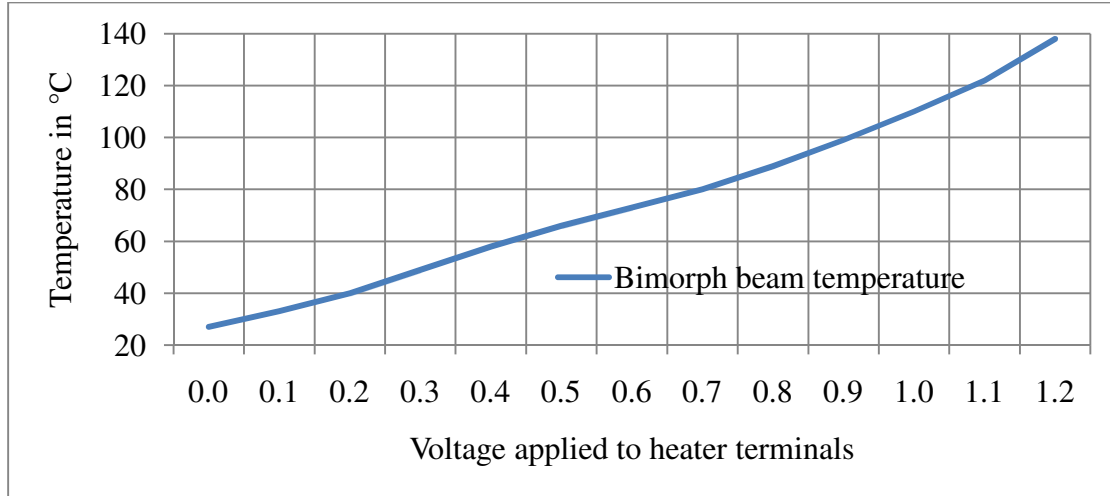


Figure 3.13: Bimorph beam temperature verses applied voltage. Temperature is approximately a linear function of the voltage applied across the heater terminals.

Examining Figure 3.12 reveals the shorter-length beams exhibit less initial upward curl, and take a greater applied voltage and thereby a higher beam temperature to make contact. Table 3.4 shows this relationship between bimorph cantilever beam length and the temperature at which the beam contacts the heat sink. Varying the length of the bimorph beam effectively allows the designer to tune the metamaterials σ and κ properties.

Table 3.4: Bimorph cantilever beam array metamaterial modeled contact temperature.

Beam length (μm)	Beam temperature at which contact is made (bend down)	Voltage applied to heater (VDC)
150	99 °C	0.9
200	89 °C	0.8
250	80 °C	0.7
300	73 °C	0.6

The bimorph cantilever beam array based metamaterial generally performed as expected in the FEM tool. However, there was a significant limitation to the FEM conducted. CoventorWare MEMS is unable to model heat transfer between two initially

unconnected objects that move into contact during the simulation, such as the bimorph beam tips contacting the polysilicon heat sink sheet. This results in the model being unable to quantify the conductive heat transfer that occurs from the polysilicon resistive heating element, through the bimorph beams, and into the Poly0 heat sink.

3.3.3 Electrostatic-actuated cantilever beam array metamaterial modeling

Each of the six electrostatic actuated cantilever beam array based metamaterial layouts (listed in Table 3.3) were exported from L-Edit to CoventorWare MEMS for FEM. Using CoventorWare, 3-D models (as shown in Figure 3.9) were generated. Each of the six layouts were meshed and subjected to a series of parametric modeling tests which examined beam displacement and electrostatic pull-in voltage verses temperature.

Before electrostatic pull-in was considered, a series of parametric studies were conducted to examine structural movement due to thermal effects only. This situation occurs when a voltage is applied across the heater terminals, and the electrostatic pull-in terminals are not connected. Figure 3.14 shows how steady-state cantilever beam temperature varied as a function of applied voltage and heater material. As expected, the thicker heater elements (Poly1 and Poly2 stacked) had a lower electrical resistance and attained a higher temperature for a given input voltage when compared to the thinner heater elements. Also, the all Poly2 design ran the coolest due to Poly2 having a greater sheet resistance (ohms/square) than the Poly1 design or the stacked grid designs. When heated, the cantilever beam arrays bend and torque slightly about their length, but do not

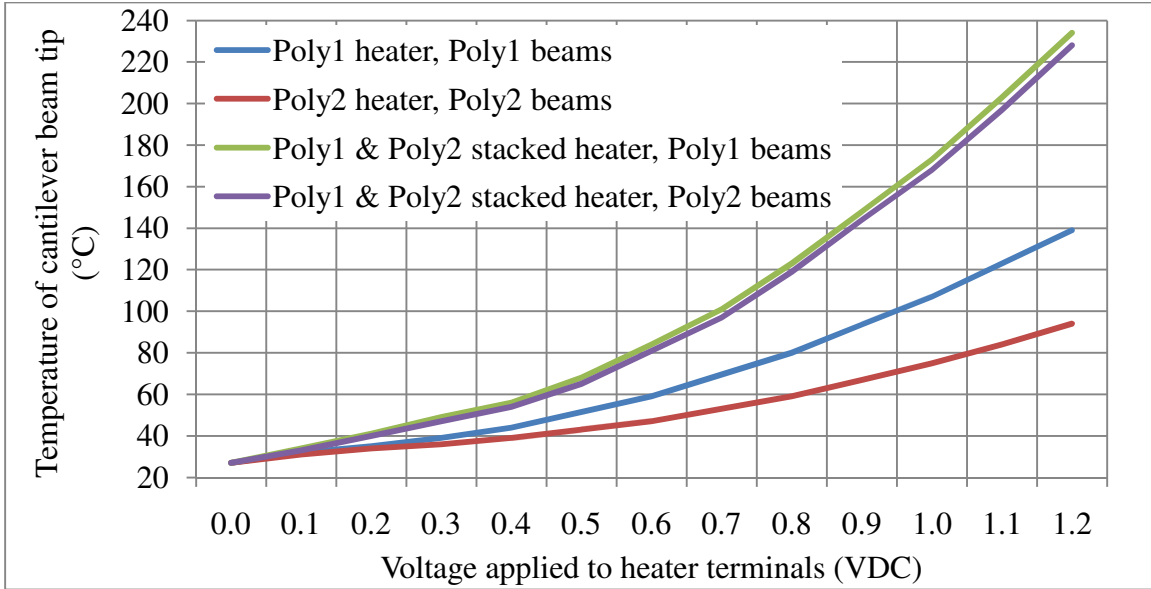


Figure 3.14: Temperature of electrostatic cantilever beam verses applied voltage. Temperature is inversely related to sheet resistance of the heater material.

curl up or bend down appreciably. The maximum movement from horizontal was only $0.3 \mu\text{m}$ – in a twisting manner. This small amount of deformation is likely due to the polysilicon structural layer softening due to significantly elevated temperatures. Figure 3.15 illustrates this twisting displacement due solely to thermal effects.

A possible side-effect of this torquing is an increase in the thermal contact resistance at the beam tip to polysilicon heat sink junction. This is due to a slight reduction in the actual contact area between the beam tip and the polysilicon layer/heat sink, which reduces the overall heat transfer and conductivity performance.

Unlike the bimorph cantilever beam based metamaterial modeled earlier, these single material (polysilicon) beams do not curl up at room temperature, nor do they bend down at elevated temperatures. Their displacement is almost entirely due to electrostatic pull-in effects only.

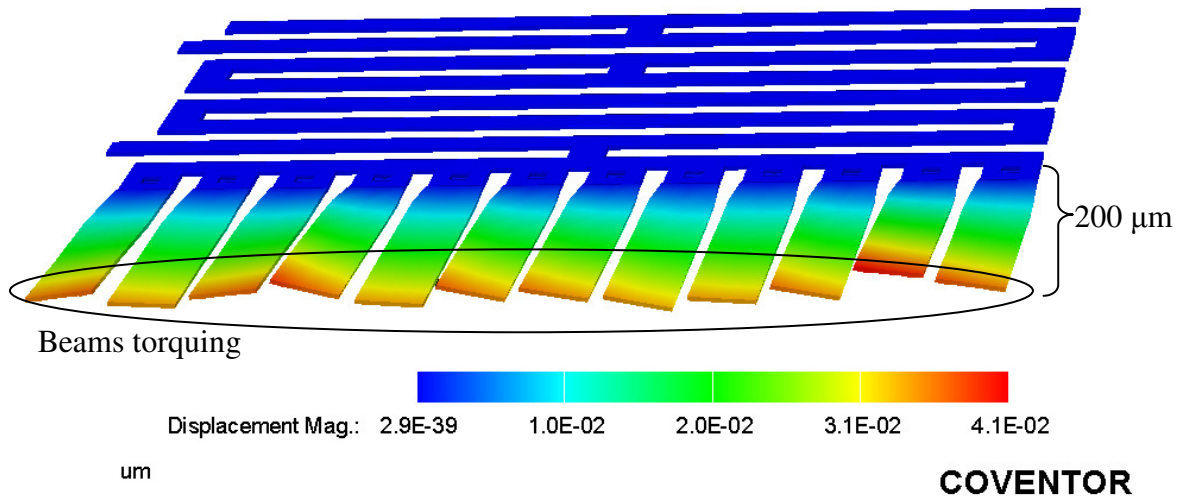


Figure 3.15: Electrostatic actuated cantilever beams torquing about their longitudinal axis at elevated temperatures (exaggerated 100X). Layout shown is version # 2 (Poly2 beams and Poly2 heater grid).

Following the thermal effects modeling, an exhaustive series of parametric FEM studies were conducted to examine electrostatic pull-in verses temperature for each of the six designs. Since parametric pull-in modeling is exceptionally computer resource intensive, a simplified 3-D model, shown in Figure 3.16, was developed for this analysis. Modeling pull-in effects on a single beam and electrode accurately represents pull-in effects of the entire array of beams, since each beam and electrode pair is an independent structure that does not interact with any neighboring beams.

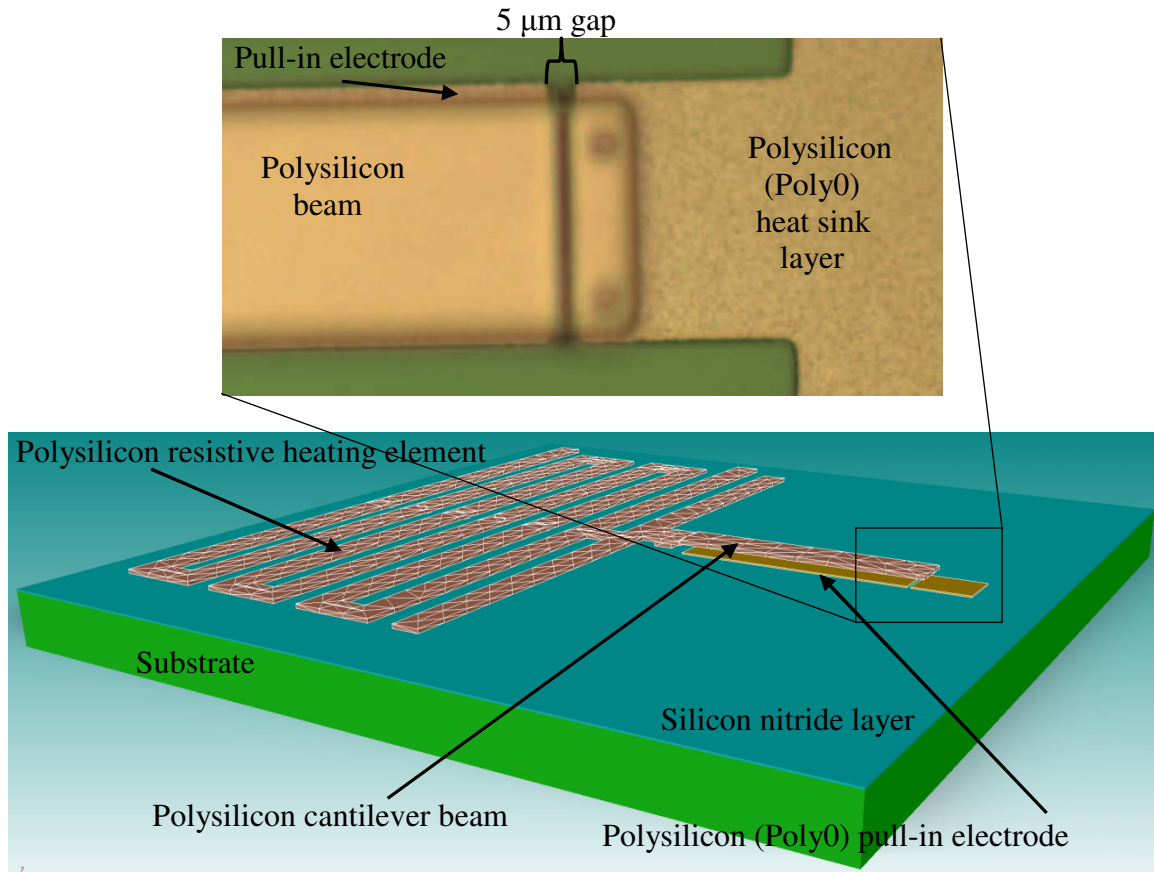


Figure 3.16: Simplified 3-D model developed for electrostatic pull-in analysis. Pull-in is due to electrostatic attraction between the polysilicon pull-in electrode and the polysilicon cantilever beam above it. It is caused by a difference in potential between these two structures. Note the Poly0 heat sink is not connected to the Poly0 pull-in electrode (5 μm gap as shown in the upper insert).

Figure 3.17 illustrates the simplified 3-D model under a pull-in condition, where the cantilever beam has snapped down and made physical contact with the Poly0 heat sink layer beneath its tip. Notice the Poly0 pull-in electrode is not connected to the Poly0 heat sink (5 μm gap between providing electrical and thermal isolation).

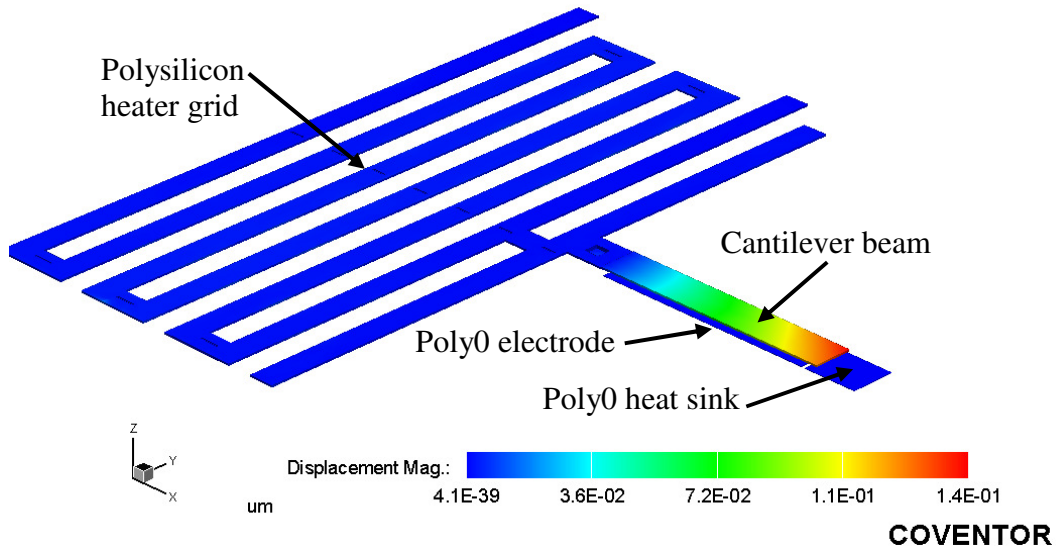


Figure 3.17: CoventorWare MEMS modeling of electrostatic pull-in.

Figure 3.18 illustrates how electrostatic pull-in of cantilever beams is a function of system temperature, as modeled in CoventorWare 2008. The polysilicon cantilevers “soften” slightly as their temperature is increased – resulting in reduced restoring force and a lower pull-in voltage. The main reason for the difference between the Poly1 and Poly2 pull in voltages is the Poly2 beams are 25% thinner than the Poly1 beams, which reduces pull-in voltage. In general, the modeling indicated that the pull in voltage required to make the cantilever beam snap downward towards the electrode is inversely proportional to beam temperature. Therefore, an important electrostatic pull-in control logic design consideration is that pull-in voltage is a function of device/beam temperature.

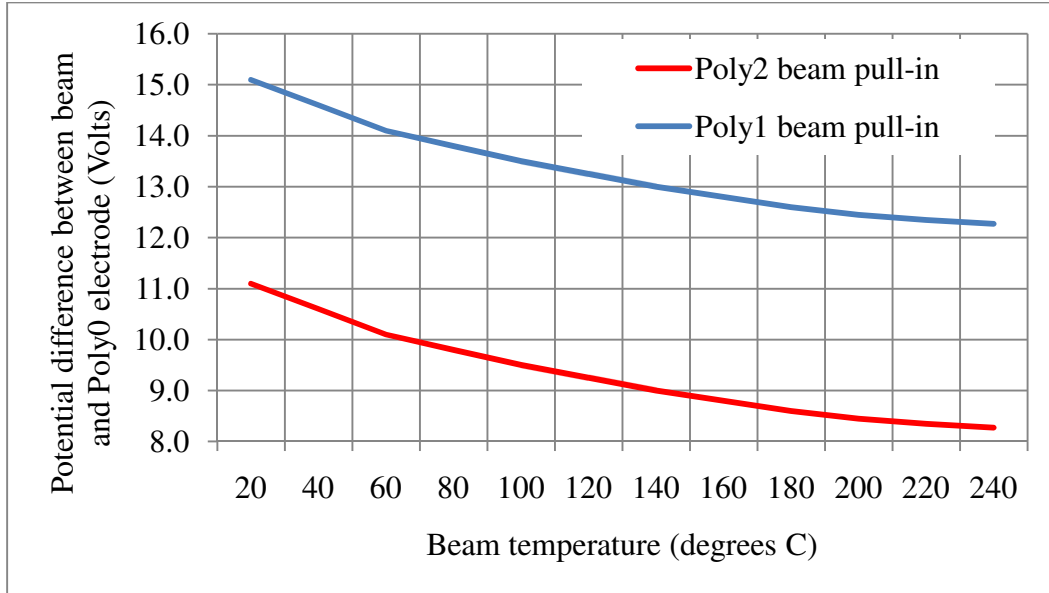


Figure 3.18: Electrostatic pull-in voltage verses temperature, as modeled in CoventorWare 2008.

The electrostatic cantilever beam array based metamaterial performed as expected in the FEM tool, with the exception of the beam torquing that occurred at elevated temperatures. As was the case with the bimorph cantilever beam based metamaterial, FEM of these designs was limited in that CoventorWare was unable to model heat transfer between two initially unconnected objects. However, the FEM was still valuable in that the design functionality was validated prior to investing in the fabrication of these prototype metamaterial devices.

3.4 Thermal Metamaterial Device Fabrication

3.4.1 Overview

Following successful FEM of the ten proof-of-concept thermal metamaterial designs, the next step in the design process was fabrication of prototype devices. Given the scope

and time constraints of this thesis (one engineer working for approximately five months), the MEMSCAP PolyMUMPs™ process was selected for fabrication of all prototype devices. As was discussed in Section 2.2, PolyMUMPs™ was chosen due to its appropriate feature size and material capabilities, quick and reliable turnaround, and relatively low cost. This section presents the fabricated devices, and the post processing activities that were accomplished in the AFIT cleanroom facility in order to prepare the fabricated devices for testing.

3.4.2 Post-fabrication device processing

Upon completion of the PolyMUMPs™ process, the prototype devices were delivered to AFIT as shown in Figure 3.19. Each 3 X 3 mm sample contained all ten proof-of-concept metamaterial devices. PolyMUMPs™ produced 15 copies of these samples.

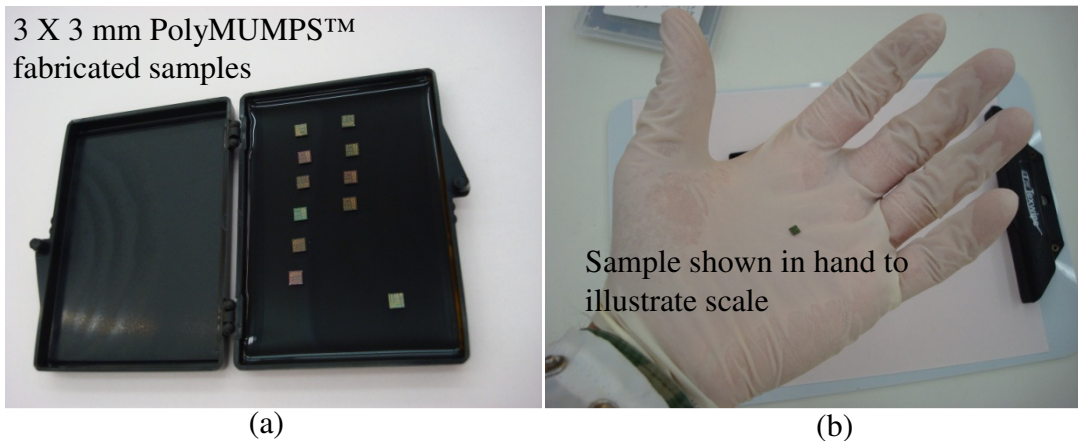


Figure 3.19: PolyMUMPs™ fabricated devices as delivered in gelpack (a) and in hand to show scale (b).

When delivered, the samples are “unreleased”, meaning that they still contain two layers of sacrificial oxide, as well as a thick coating of photoresist. The purpose of these layers is to protect the fragile MEMS structures during shipping and wafer dicing. In

order to prepare the samples for testing, a “release” process was conducted. First, the samples were submerged into acetone for 25 minutes to remove the layer of photoresist. Next, the samples were placed in a solution of 49% hydrofluoric acid (HF) for 2.5 minutes. The HF etches the sacrificial oxide layers, “releasing” the MEMS structures. The acid hood under which this etching is conducted is shown in Figure 3.20 (a). The

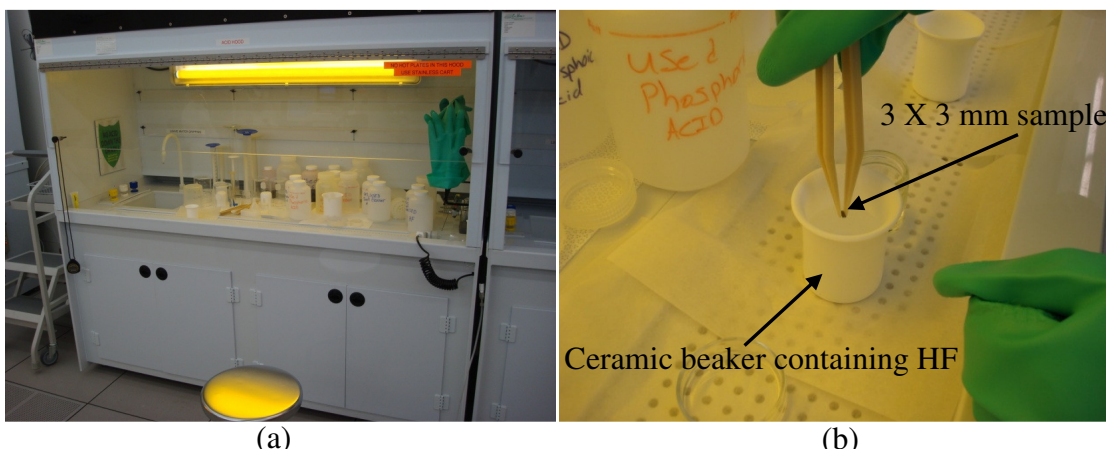


Figure 3.20: Acid processing station in AFIT cleanroom (a). Protective oxide layers on PolyMUMPs™ samples are etched away using HF as shown in (b).

samples were then placed into a container of methanol and moved to the Tousimis Autosamdry 815 Series B supercritical point dryer (Figure 3.21). Drying the samples is a sensitive process due to a phenomenon known as stiction. Stiction is when a MEMS structure (such as a cantilever beam) unintentionally sticks to another layer or the substrate. One way in which this is caused is by surface tension of the liquid between the MEMS structure and layer during the drying process that follows wet etching. Using a supercritical point dryer reduces the chance of this initial stiction event and results in a higher yield of functional devices.

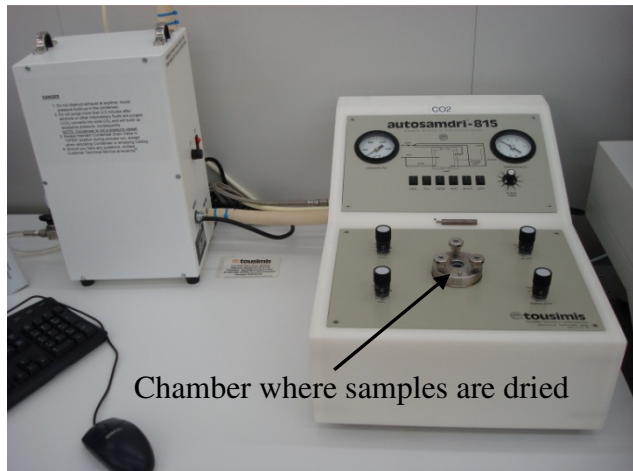


Figure 3.21: Tousimis autosamdry-815 series B supercritical point dryer.

Following the drying process, the samples were stored in a “dry box”. This term refers to containers which are kept above atmospheric pressure by a steady supply of nitrogen. The nitrogen overpressure serves to keep the samples dry in a low-humidity environment. It also prevents the formation of native oxides on silicon wafers and structures, which can form quickly in an oxygen rich environment. One of the dry boxes used to store these devices is shown in Figure 3.22 (a).

Even when stored in a dry box within a cleanroom environment, if the samples have been stored for several days it is beneficial to clean them prior to testing. This task was accomplished using the Anatech SP-100 plasma cleaner (Figure 3.22 (b)). The plasma cleaner removed small deposits of photoresist and any debris that was present on the metamaterial devices, and was used whenever testing was conducted on samples that had

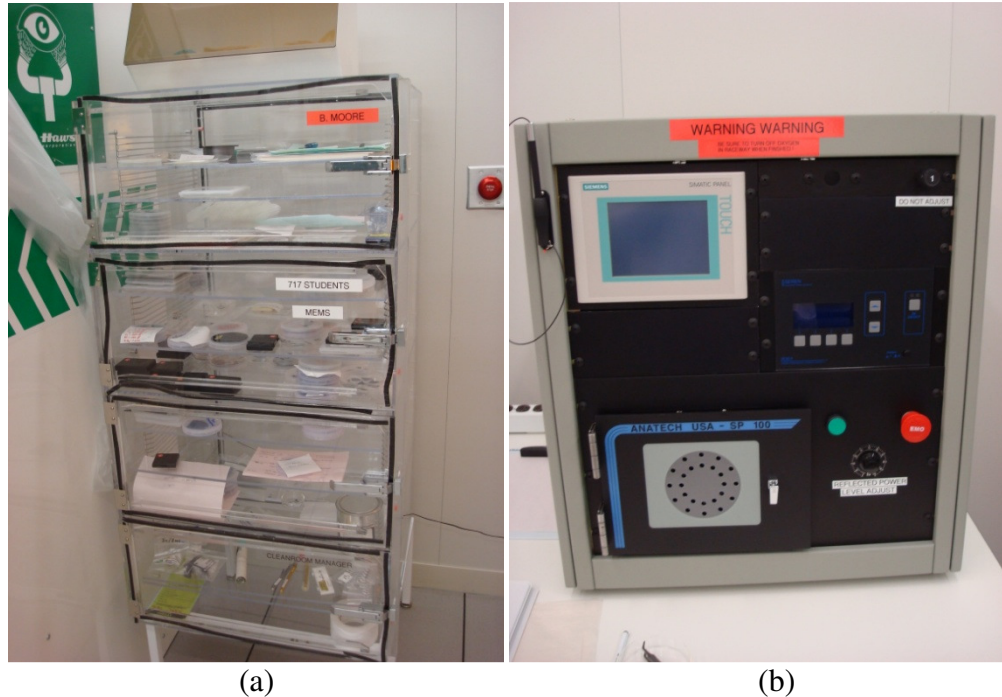


Figure 3.22: Cleanroom dry box (a) and Anatech plasma cleaner (b).

been stored for several days. Figure 3.23 and Figure 3.24 illustrates how each of the two design types (bimorph beams and electrostatic actuated beams) appeared under an optical microscope after fabrication but prior to the release process. Appendix A details each of the ten designs as they appeared following the release process, under both optical and scanning electron microscopes.

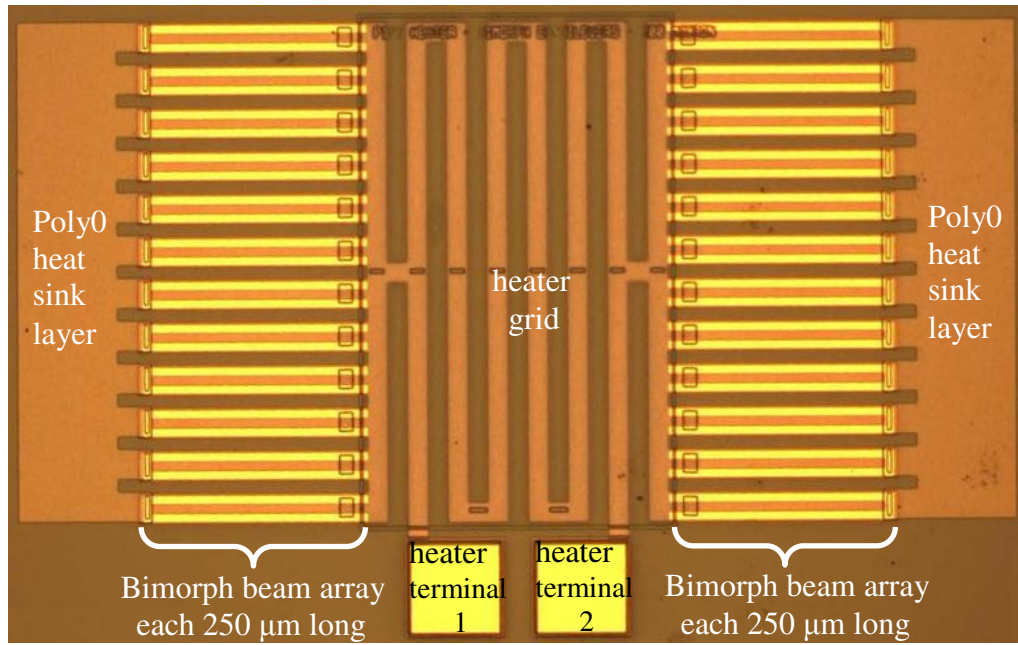


Figure 3.23: Bimorph cantilever beam array based metamaterial before release. 250 μm beam length version shown, others similar. Bimorph beams are actuated by either increasing the system temperature, applying a voltage across the heater terminals, or a combination of both techniques.

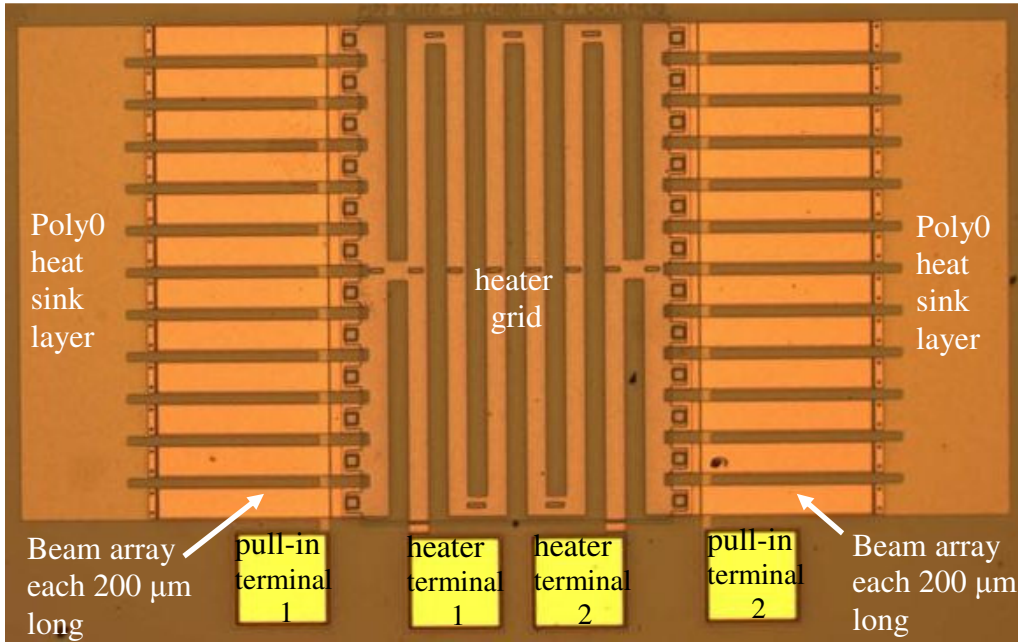


Figure 3.24: Electrostatic actuated cantilever beam array based metamaterials before release. Version #3 shown (Poly1 and Poly2 stacked heater grid, Poly1 beams, heater style #1), others similar. Beam arrays are actuated by applying appropriate pull-in voltage between each pull-in terminal and the heater terminals.

3.5 CNT-Based Braided Ropes

3.5.1 Introduction

In addition to the prototype thermal metamaterial designs, this research effort evaluated a series of SWNT-based braided ropes. These braided ropes were provided for evaluation by Dr. Young Hee Lee of the Center for Nanotubes and Nanostructured Composites at Sungkyunkwan Advanced Institute of Nanotechnology, Sungkyunkwan University. The ropes are spun directly from an aligned SWNT “forest” as shown in Figure 3.25 [39]. In the figure, “A” shows the aligned SWNTs being pulled away from a silicon substrate. “B” shows detail of the drawing and spinning process, while “C” shows the resulting braided rope of SWNTs, which is similar to the first test variant described in Section 3.5.2 [39].

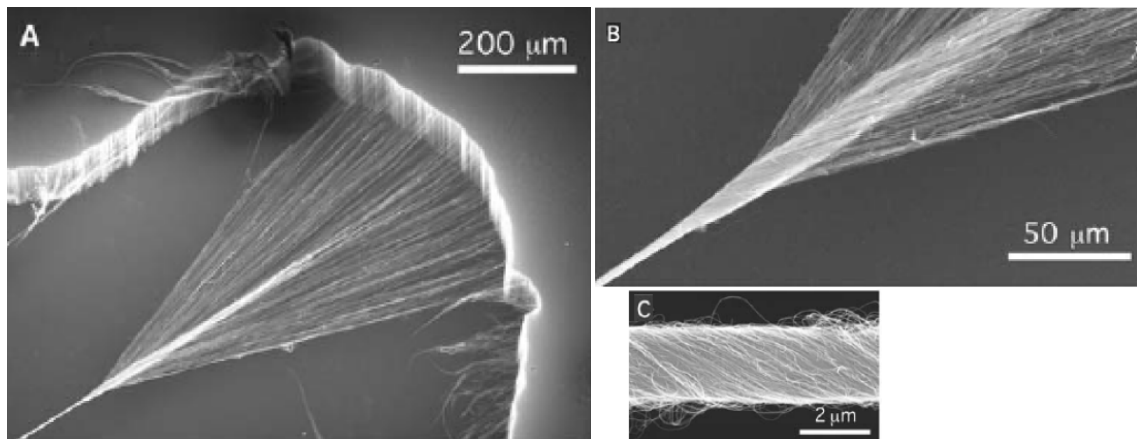


Figure 3.25: CNT rope being spun from SWNT forest. Aligned SWNTs being pulled away from a silicon substrate are shown in (a). The drawing and spinning process is illustrated in (b), and (c) shows the resultant braided rope of SWNTs [39].

While likely designed primarily for their exceptional tensile strength, these ropes may have applications in thermal metamaterials, since SWNTs have outstanding thermal

conductivity and variable electrical conductivity as discussed in Section 2.5.4. This section describes these test articles, and details the plan for characterizing their thermal and electrical performance.

3.5.2 CNT rope prototype description

Three variants of the SWNT-based braided rope were supplied to AFIT/ENG for characterization. The first is a dense braid of SWNTs with no coating applied over the braided rope. Figure 3.26 shows this variant under a 50X optical zoom. As seen in the figure, without any coating, there are bundles of SWNTs protruding from the main braid of the rope. The length of the rope featured dozens of irregularities and seemed

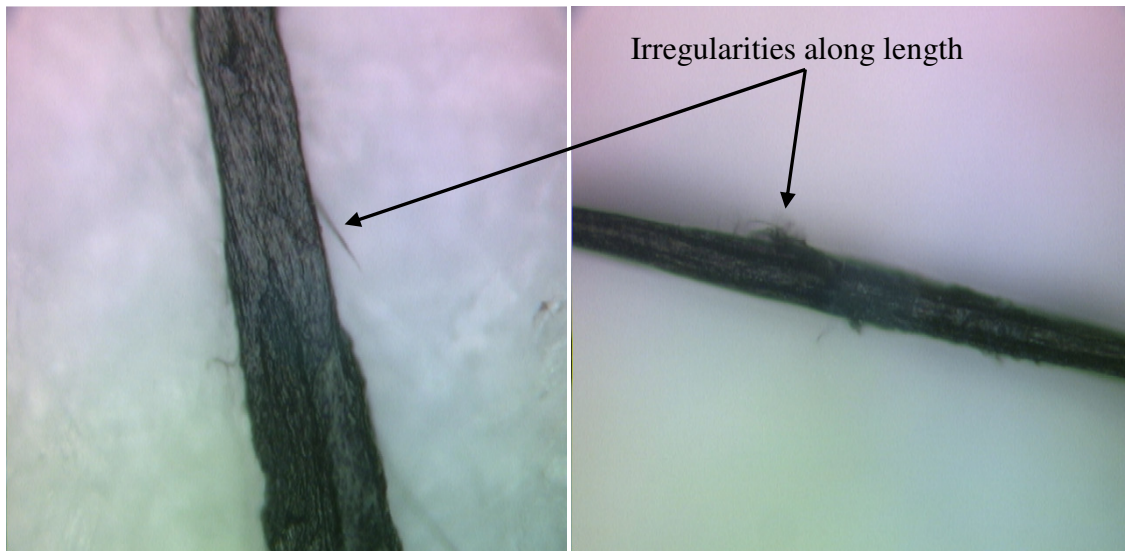


Figure 3.26: Uncoated SWNT braided rope under 50X optical zoom.

considerably stronger (tensile strength) than would be expected from a rope of such small diameter.

The second variant, shown in Figure 3.27, is the same as the first except that a thin coating of polyvinyl alcohol (PVA), a water-soluble synthetic polymer, has been applied.

Figure 3.27 shows this variant under a 50X optical zoom. As seen in the figure, the PVA coating gives the rope a smoother, more uniform appearance. The coating did not seem to decrease the flexibility of the rope in informal handling. Upon examination, the PVA coating appeared to be rather uniformly applied along the length of the sample.

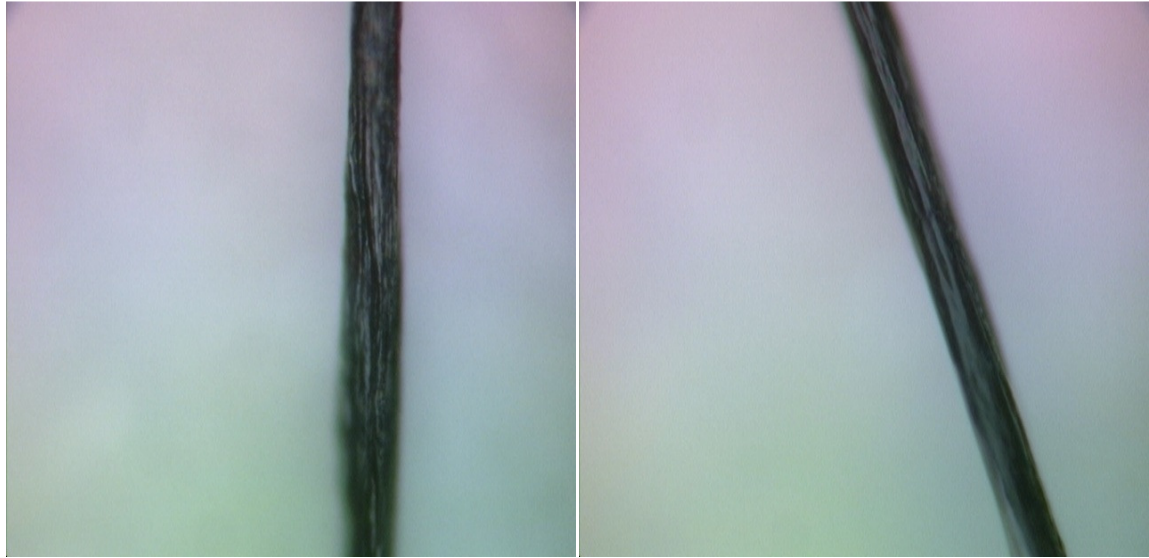


Figure 3.27: PVA coated SWNT braided rope under 50X optical zoom.

The third and final variant is four strands of the second variant braided together. The four individual ropes can be seen under a 50X optical zoom in Figure 3.28. As would be expected, this sample seemed much more durable in informal handling. As with the previous variant, this 1X4 sample had a black plastic appearance. Additional detailed pictures of each of the three samples can be seen in Appendix A.

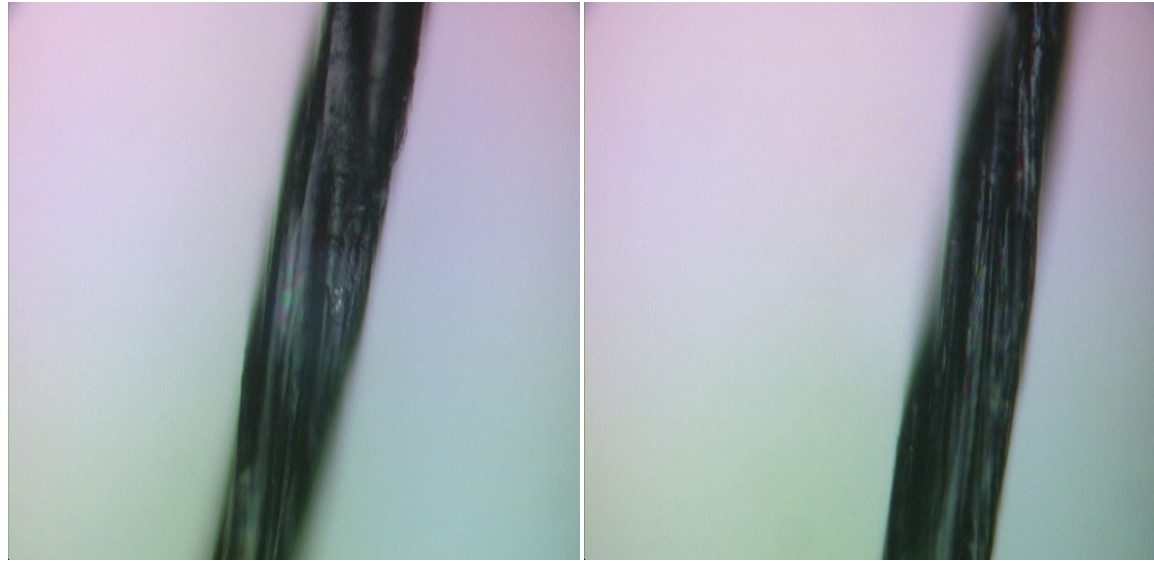


Figure 3.28: Four braided (1X4) PVA coated SWNT ropes under 50X optical zoom.

The technique used to braid four strands of the second variant into this third variant is shown in Figure 3.29. During the braiding process, the strands are rotated at between 100-300 rpm while being drawn from the spindle (top left of figure) at 100 rpm [39]. Again, as one would expect, this version was slightly less flexible than the previous two. This variant was approximately 6.5" long.

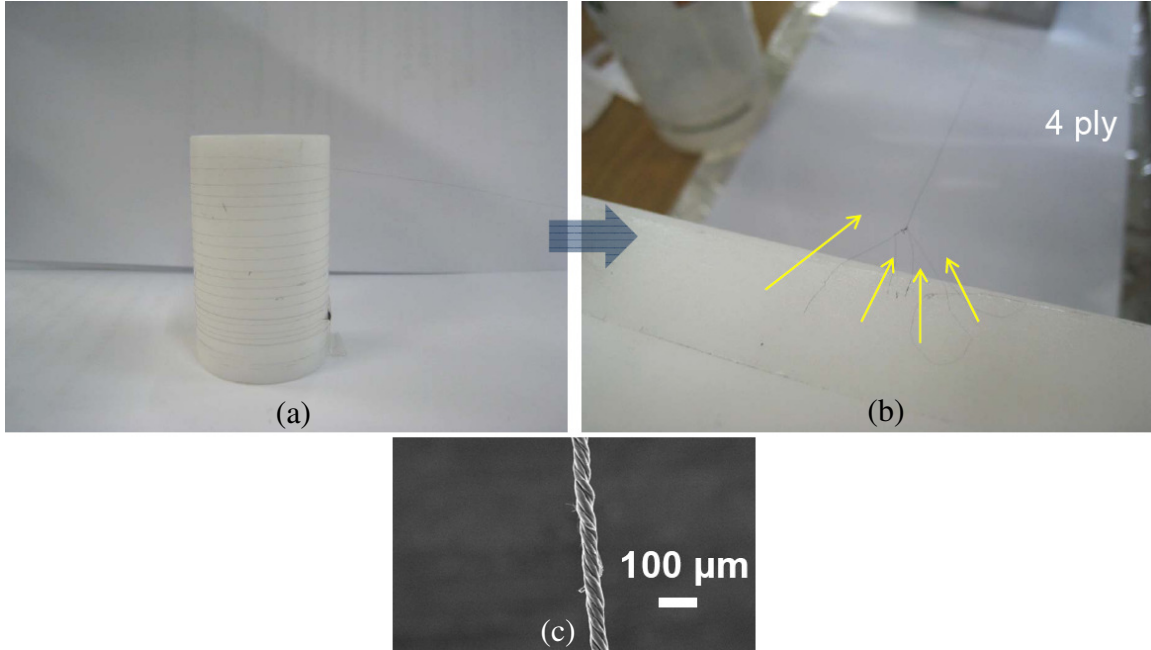


Figure 3.29: Four-ply CNT rope braiding process. A spool of PVA coated SWNT braided rope is shown in (a). The braided ropes from four spools are then braided together to form a four-ply rope (b). The finished product, a 1 X 4 braided rope, is shown in (c) [39].

3.6 Summary

This chapter followed the thermal metamaterial design process from a CAD drawing, into FEM, and through the fabrication process. Additionally, the SWNT-based braided ropes were introduced. Modeling of these prototype designs showed that materials composed of nano or microscopic structures can realize tuned electrical conductivity and thermal performance characteristics based primarily on their physical structures rather than just their chemical composition. Testing planned and conducted in the following chapter quantified the performance of these proof-of-concept devices.

Prototype Device Characterization and Results

4.1 Overview

While FEM provided some insight to the operation of the ten thermal metamaterial prototypes, conducting device characterization and testing on fabricated devices can reveal operational issues that were not considered during modeling. Heat transfer within a system is a complex, multifaceted problem, and modeling it is only as good as the assumptions input to the model. This section begins by detailing the characterization conducted to evaluate the performance of the ten prototype metamaterial devices. Then, testing of the CNT braided rope prototypes is conducted, presented, and discussed. These test events and the resultant data quantify the effectiveness of these proof-of-concept designs.

4.2 Metamaterial Device Testing and Results

4.2.1 Overview

Each of the ten proof-of-concept thermal metamaterial devices was characterized by executing a series of test events. First, each design was optically inspected to insure the design was correctly fabricated and was not physically damaged. Next, device structural performance was evaluated using an interferometer system. Then, the designs were operated under a thermal imaging microscope system to quantify their heat transfer capabilities. Lastly, the electrical resistivity of each device was evaluated under a variety of conditions. The data collected during these test events is presented and discussed.

4.2.2 Test event #1: device optical inspection

4.2.2.1 Device optical inspection test description

Upon completion of fabrication and release activities, each prototype device was inspected under a 50X optical microscope. This inspection included examining the samples for any signs of physical damage due to fabrication misalignments, errors, particulate damage, incomplete release, or stiction. The device was unpowered during this inspection, which was conducted at standard temperature and pressure in an ambient lab environment. Any suspicious looking devices were rejected and not used for subsequent tests. Note that since all ten devices were present on each of the 15 wafer samples, this test event was conducted on each wafer sample that was used for testing.

4.2.2.2 Device optical inspection test results

A total of eleven die samples, each one containing all ten prototype thermal metamaterials, were released for use in device characterization. Each of the eleven were inspected immediately following release, and again prior to being used for a test. With one exception, the releases were completely successful with all ten devices being stiction and largely contaminant free. The one exception was heavily contaminated with particulate damage resulting from operating in the C0₂ dryer.

Although the devices were fully serviceable immediately following release, several of the samples experienced stiction and/or physical damage after several days of use. Additionally, several of the samples exhibited increased contact resistance at the beam tip to Poly0 sheet interfaces. This was the result of mild oxidation from the samples being exposed to humid environments during several of the test activities. This damage was not visible under magnification, and was discovered as increased electrical resistance

and/or decreased heat transfer. To mitigate the risk of this mild oxidation skewing test results, freshly released samples were used for testing to the maximum degree possible.

4.2.3 Test event #2: interferometer-based beam displacement characterization

4.2.3.1 Interferometer-based beam displacement test description

The mechanical motion of the prototype metamaterial devices is nearly entirely in the Z-axis. The most accurate tool for measuring vertical displacement in MEMS structures is the interferometer (shown in Figure 4.1). For each of the four bimorph cantilever

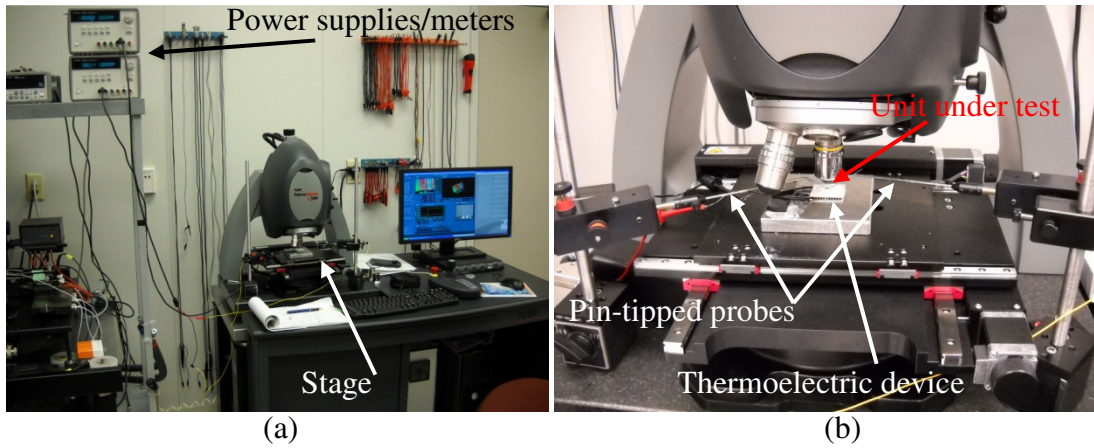


Figure 4.1: Interferometer system, entire system (a) and close-up of stage (b).

beam array based prototypes, beam displacement versus system temperature was measured. For each of the six electrostatic-actuated cantilever beam array based prototypes, beam pull-in voltage versus system temperature was recorded. System temperature was swept using a small thermoelectric heating/cooling device. Prior to testing, the thermoelectric device (TED) was calibrated using a bolometer as shown in Figure 4.2. The results of this calibration are shown in Figure 4.3.

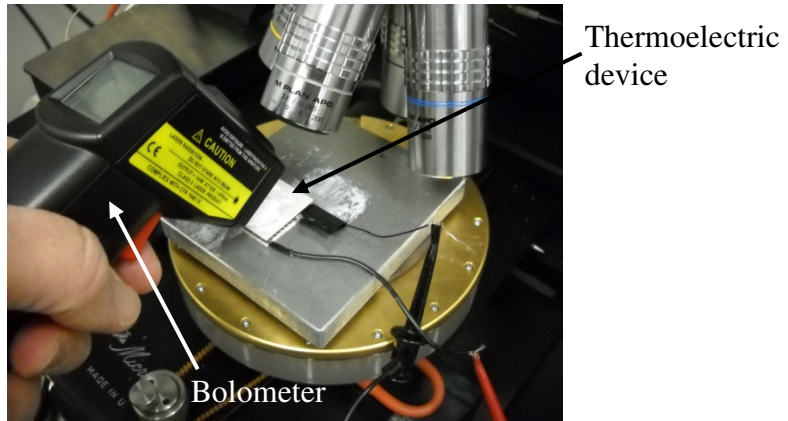


Figure 4.2: Thermoelectric device calibration using bolometer.

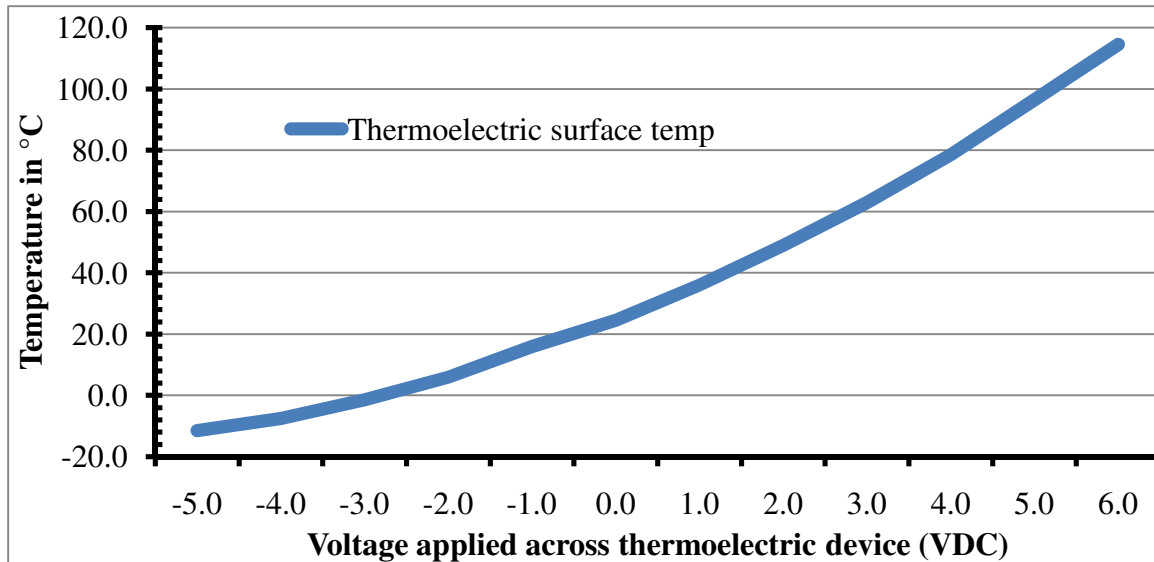


Figure 4.3: Thermoelectric device calibration using bolometer (background temperature of 24.5 °C). Surface temperature is a non-linear function of voltage applied.

All measurements were conducted on two copies of each of the ten prototypes. In any case where the data from the two copies varied by greater than 10%, data was collected on a third copy. In this situation, if data from any two of the three prototypes agreed within 10%, data from the third prototype was rejected. Figure 4.4 illustrates this logic

flow, which was used to reduce the likelihood of invalid data points being included in the test results.

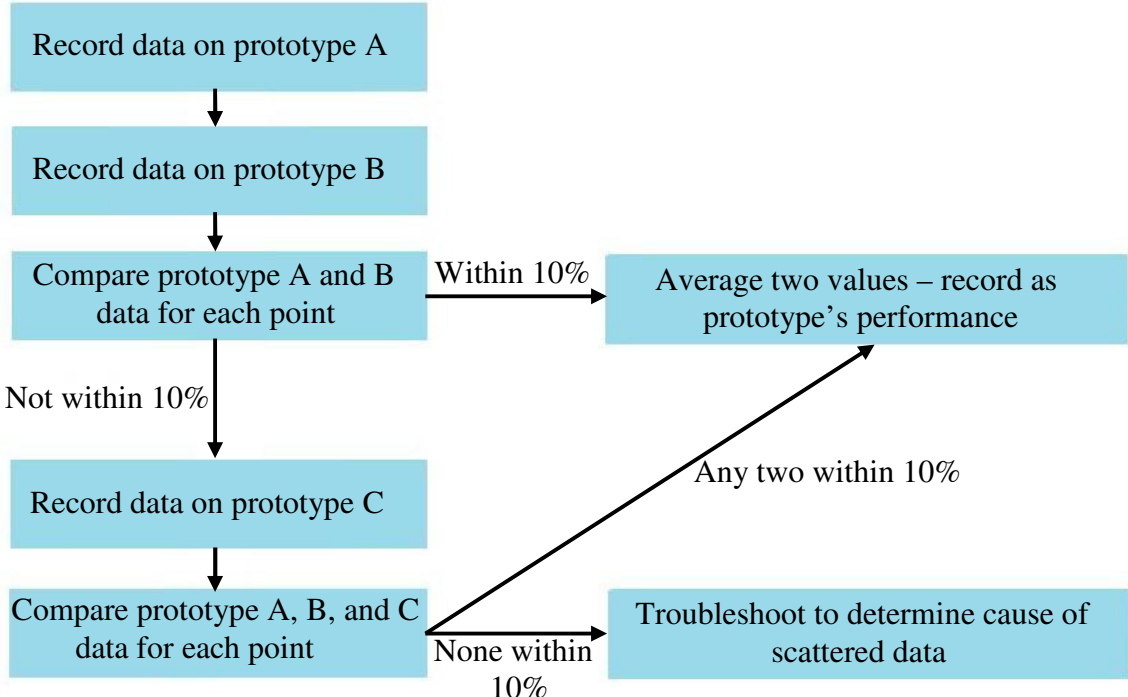


Figure 4.4: Logic flow and conditions for data collection.

Figure 4.5 illustrates how Z-axis displacement data was measured on the bimorph cantilever beam based thermal metamaterial samples. Using the calibrated thermoelectric device, the sample was uniformly heated or cooled to the temperature required for each test point. At each temperature point, Z-axis beam displacement was measured for six beams, and then averaged and recorded as that samples average displacement IAW the logic flow presented in Figure 4.4.

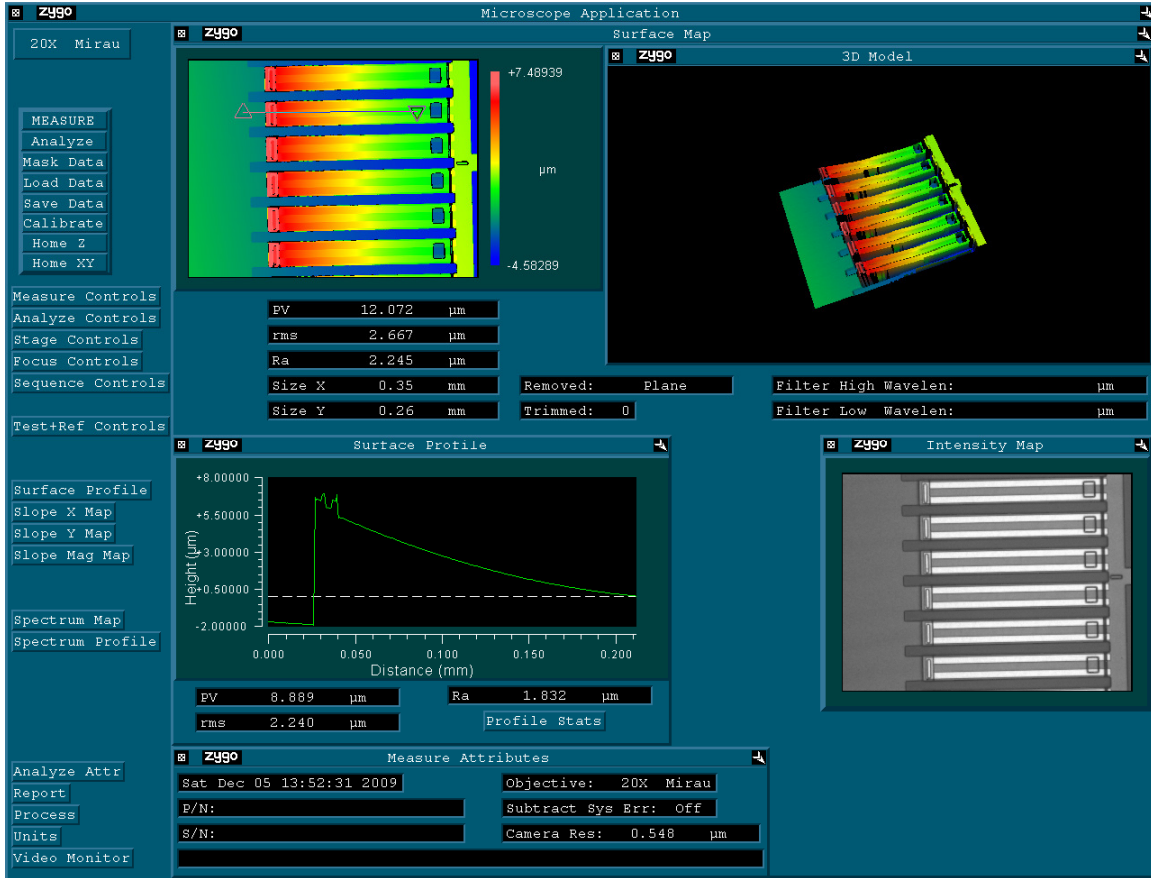


Figure 4.5: Zygo interferometer software screenshot showing how Z-axis displacement data was measured on the bimorph cantilever beam based thermal metamaterial samples. Voltage was applied across the TED, uniformly heating the entire sample. At each temperature point, Z-axis beam displacement was measured for six beams, and then averaged and recorded as that samples average displacement.

Figure 4.6 illustrates how pull-in data was measured on the electrostatic actuated cantilever beam array metamaterial samples. Using the calibrated thermoelectric device, the sample was held at the temperature required for each test point. At each temperature point, the voltage between the beam array and electrode was ramped up slowly (0.1 V per second) until pull-in occurred. Pull-in voltage was averaged and recorded IAW the logic flow presented in Figure 4.4.

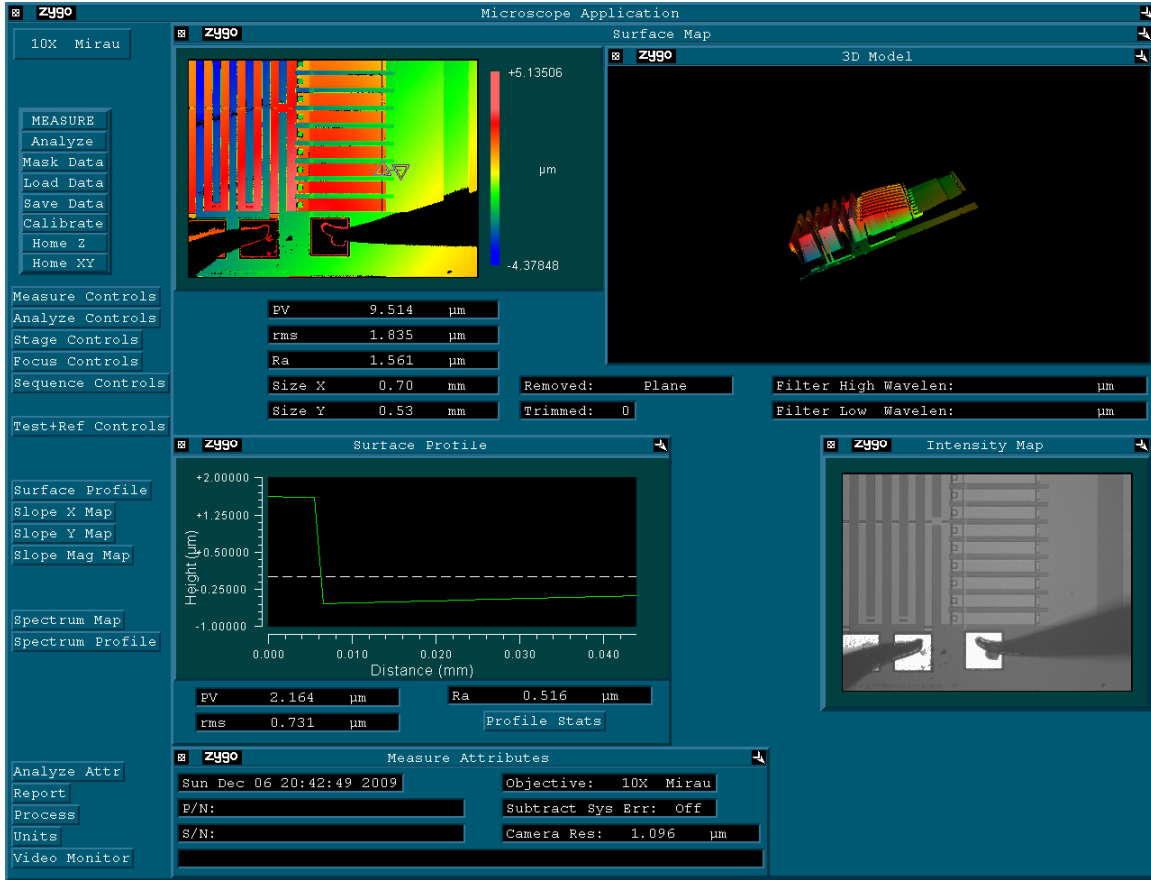


Figure 4.6: Zygo interferometer software screenshot showing how electrostatic pull-in data was measured on the electrostatic actuated cantilever beam based thermal metamaterial samples. Voltage was applied across the TED, uniformly heating the entire sample. At each temperature point, the voltage between the beam array and electrode was ramped up until pull-in occurred.

4.2.3.2 Interferometer-based beam displacement test results

As detailed in Section 4.2.3.1, the thermal metamaterial prototype's beam displacements and pull-in voltages were characterized. First, beam displacement versus system temperature was measured for each of the four bimorph cantilever beam array based prototypes. Figure 4.7 illustrates how the bimorph cantilever beam array based thermal metamaterial samples were imaged by the Zygo interferometer software. In (a), an array of 150 μm beams at room temperature curling upwards is shown. Figure 4.7 (b)

shows an array of 250 μm long beams that is cooling off following a test at 115 $^{\circ}\text{C}$. As the arrays cool, the beams tendency to curl upwards overcomes the stiction forces, and each beam individually recovers or snaps-back up. In (c), a 3-D close-up image of six beams in a beam array is shown. The test temperature is 50 $^{\circ}\text{C}$, and the beams are curled-up or open accordingly. Lastly, (d) illustrates how the beam arrays appear when fully bent down or closed due to elevated test temperatures.

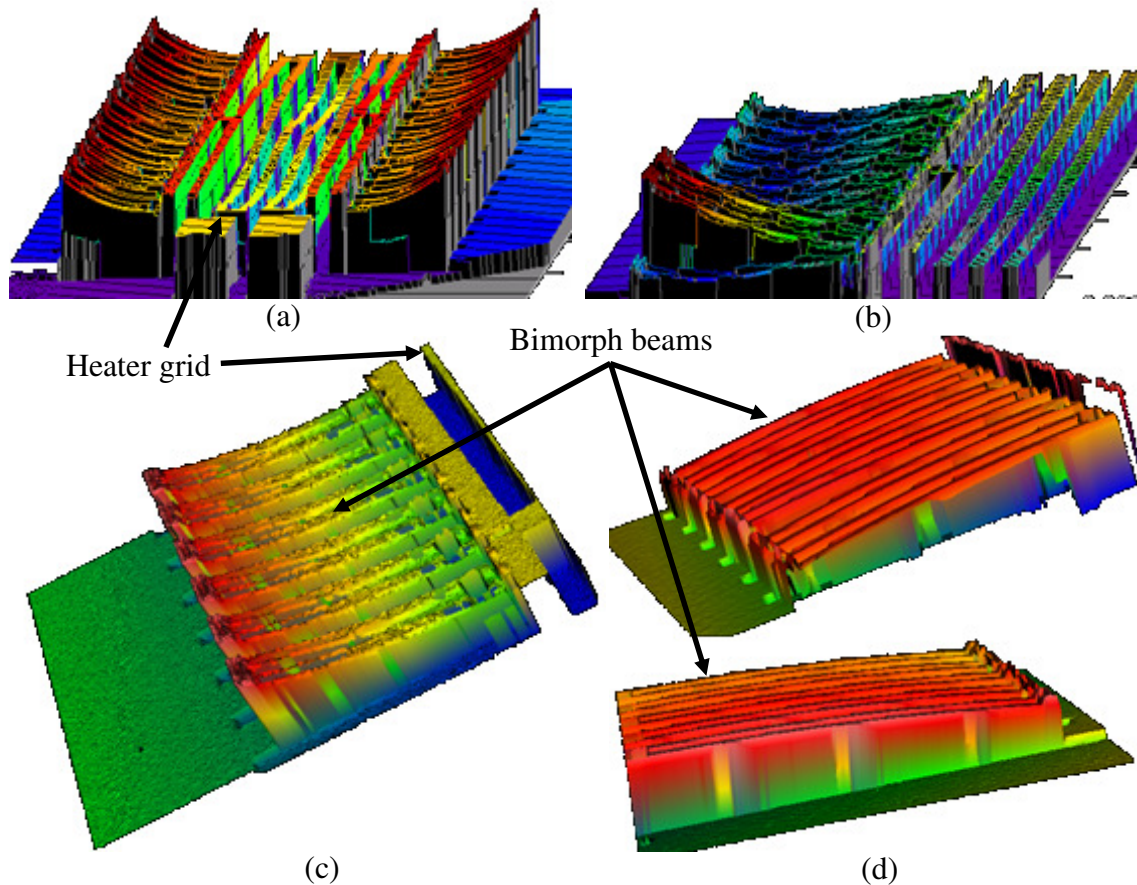


Figure 4.7: Bimorph cantilever beam array based thermal metamaterial samples as imaged by Zygometer software. In (a), an array of 150 μm beams is shown in its “curled-up” state at low temperature. In (b), an array of 250 μm beams at a test temperature of 100 $^{\circ}\text{C}$ is shown, illustrating how each beam individually recovers or snaps-back up when cooling down following closure. In (c), a close-up of one-half of one side of a beam array is shown, curled-up. In (d), 250 μm (top) and 300 μm (bottom) beam arrays are shown fully bent down or closed.

Test results for the bimorph cantilever beam array based metamaterials are plotted in Figure 4.8. As seen in the figure, the beams curled upwards much more than the FEM predicted. Modeling results showed an upward curl of 0.6, 1.2, 1.4, and 1.6 μm for the 150, 200, 250, and 300 μm length beam arrays, respectively (shown in Figure 3.12). The actual curl upwards was approximately 4, 8, 14, and 21 μm for the 150, 200, 250, and 300 μm length beams, respectively. Depending on variant, the actual curl was 7-13X greater than what was predicted by the model. More importantly, the temperature at which the array of cantilever beams “closed” or made conductive contact with the Poly0

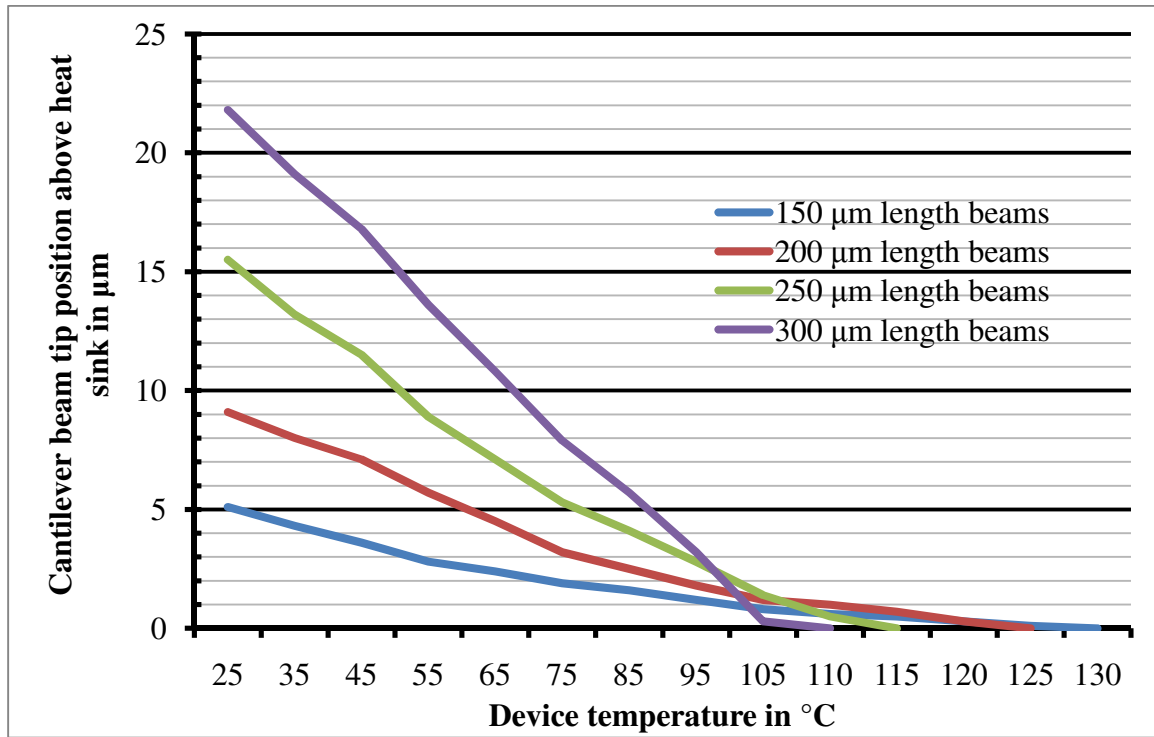


Figure 4.8: Bimorph cantilever beam tip position verses temperature. When the position equals zero, the beam tip has made contact with the heat sink layer beneath it. 150 μm beams make contact at 127 $^{\circ}\text{C}$, 200 μm beams make contact at 123 $^{\circ}\text{C}$, 250 μm beams make contact at 114 $^{\circ}\text{C}$, and 300 μm beams make contact at 110 $^{\circ}\text{C}$.

heat sink layer was significantly higher than predicted by FEM. This is due to the heating in FEM having been accomplished through use of the resistive heating element, whereas here the entire wafer sample is being uniformly heated. When heated via conduction from the heater grid, the gold layer becomes significantly hotter than the polysilicon – resulting in a lower closing temperature than when uniformly heating the device. Table 4.1 compares the interferometer-gathered test results to those obtained through FEM. Actual beam array closing temperatures were 28-37 °C higher than predicted. This significant temperature difference highlights the importance of verifying

Table 4.1: Bimorph cantilever beam array closing temperature: actual verses modeled. Actual closing temperatures recorded during testing were 8-11% higher than predicted by FEM. These results are compared to those obtained during thermal imaging testing later in Table 4.3.

Beam length	<u>Actual:</u> temperature at which contact is made	<u>Modeled:</u> temperature at which contact is made	Absolute difference
150 μm	127 °C	99 °C	7.5%
200 μm	123 °C	89 °C	9.4%
250 μm	114 °C	80 °C	9.6%
300 μm	110 °C	73 °C	10.7%

design performance through testing and characterization. Each of the four bimorph cantilever beam array designs performed repeatably and reliably – but with much more initial upward curl and requiring a higher temperature to close than what was anticipated.

Following completion of the bimorph cantilever beam array based prototypes characterization, each of the six electrostatic actuated cantilever beam array based prototypes were evaluated. Electrostatic pull-in voltage verses system temperature was measured for each of these six thermal metamaterial prototypes. Figure 4.9 illustrates how the electrostatic actuated cantilever beam array based thermal metamaterial samples were imaged by the Zygo interferometer software. In (a), A 3-D image of layout version

5 (versions detailed in Table 3.3) is shown with no voltage applied across the pull-in terminals. The beams are parallel to the Poly0 layer below them (no Z-axis component). In (b), layout version # 3 is shown with 12 V applied across the pull-in terminals, the Poly1 beams are bent down slightly, and are on the verge of snapping-down due to electrostatic attractive forces. Figure 4.9 (c), (d), and (e), show layout version # 4 with 6 V, 7 V, and 8 V applied across the pull-in terminals, respectively. The beams bend downward slightly in (c), bend down a bit more in (d), and snap-down completely in (e), once the required pull-in voltage of 8 V is applied.

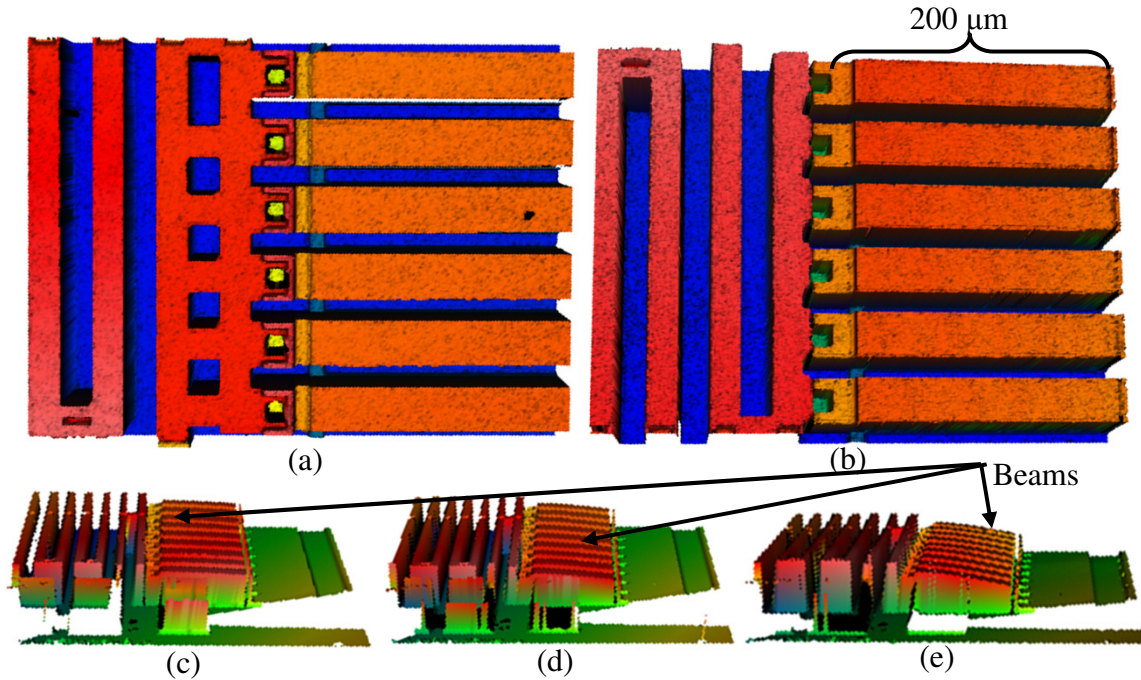


Figure 4.9: Electrostatic actuated cantilever beam array thermal metamaterial samples as imaged by Zygo interferometer software. In (a), A 3-D image of layout version # 5 (versions detailed in Table 3.3) is shown without any pull-in voltage applied. Layout version # 3 is shown in (b) with 12 V of pull-in applied, the Poly1 beams are bent down slightly, and are on the verge of snapping-down due to electrostatic attractive forces. In (c), (d), and (e), layout version # 4 is shown with 6 V, 7 V, and 8 V applied, respectively. The beams bend downward slightly in (c) and (d), and snap-down completely in (e) once the required pull-in voltage is applied.

Test results for the electrostatic actuated cantilever beam array based metamaterials are listed in Table 4.2. As seen in the table, measured pull-in voltage for each electrostatic actuated thermal metamaterial variant very closely correlated with the

Table 4.2: Pull-in voltages for each of the six electrostatic actuated cantilever beam array metamaterials. All values are rounded to the nearest 0.5 V. Variants featuring Poly1 beams pulled-in at \approx 13 VDC, while versions with Poly2 beams pulled-in at \approx 8 VDC. Layout versions were detailed in Table 3.3.

Layout version	Measured pull-in voltage (VDC)	Measured recovery voltage (VDC) ¹	FEM predicted pull-in voltage (VDC) ²	Calculated pull-in voltage (VDC) ³
1	13.0	12.0	13.5-15.0	12.0
2	8.0	6.5	9.5-11.0	8.0
3	13.0	11.5	13.5-15.0	12.0
4	8.0	6.5	9.5-11.0	8.0
5	12.5	11.5	13.5-15.0	12.0
6	8.0	6.5	9.5-11.0	8.0

¹ “Recovery voltage” is the point at which the beam structure is restored to its nominal position during a slow voltage ramp downward following the pull-in event. The restoring force overcomes both stiction and pull-in forces at this voltage point.

² “FEM predicted” pull-in voltage was presented in Figure 3.18 and was a function of temperature. The actual and calculated pull-in values were not temperature dependent.

³ “Calculated” pull-in voltage was determined using Equation 3.1 and was discussed in Section 3.2.3.

mathematically calculated (using Equation 3.1) pull-in voltages. For the versions featuring Poly1 beam arrays (versions 1, 3, and 5), the calculated pull-in was within 8% of the average measured pull-in. For the Poly2 beam variants (versions 2, 4, and 6), the calculated and measured values were within 3% in all cases. When rounded to the nearest 0.5 V, the calculated values for Poly2 beams matched the measured voltages.

Unlike in the FEM presented in Figure 3.18, pull-in voltage was not impacted by system temperature over the range tested (24-115 °C). Modeling had predicted that pull-in would decrease from 15-13.5 V and 11-9.5 V for the Poly1 and Poly2 beams, respectively, when evaluated over a 25-115 °C range. None of the samples evaluated

(three copies of six designs, or 18 total test articles) exhibited any temperature dependency in their pull-in performance. The cause of this discrepancy in the modeling is not known, but possibly involves the manner in which the samples were heated for this test event (uniform heating using the TED verses resistive heating element used in FEM) and/or issues with the CoventorWare 2008 polysilicon material properties database relating to temperature coefficients for certain material properties.

Upon completion of each pull-in test event, the applied voltage was slowly ramped down in order to measure the point at which the beam would overcome stiction and pull-in forces and “snap-up”. As shown in Table 4.2, this occurred at $\approx 8\%$ less than pull-in voltage (12 V verses 13 V) for the versions with Poly1 beam arrays. Poly2 variants “snapped-back” at a voltage $\approx 18\%$ less than what was required for pull-in (6.5 V verses 8 V). This “snap-back” or “recovery” voltage is an important consideration when designing electrostatic actuation control logic, as there may be situations in which it is advantageous to have the beam arrays “snap-back”, but still have some potential applied across the beams and electrodes.

4.2.4 Test event #3: thermal imaging microscope device temperature mapping

4.2.4.1 Thermal imaging microscope device temperature mapping description

In a metamaterial engineered to provide a unique or tailored thermal response, the most important test of all is characterization of heat transfer throughout the device. The most accurate way to measure heat transfer on a MEMS-scale device is by using a thermal imaging microscope (Figure 4.10). Each of the four bimorph cantilever beam array based prototypes were temperature mapped over the course of an operational

sequence. This sequence began with each device at a uniform temperature (no power applied to the heater grid). Then, at time $T=0$ seconds, 24 VDC was applied across the polysilicon resistive heating element. Over the next several seconds, the device would heat up, causing the bimorph beam arrays to bend downwards and close. At approximately $T=10$ seconds, the device had reached a steady state thermal condition. The potential was then removed from the heater grid – causing the device to rapidly cool and the bimorph beams to curl upwards. Once all 24 of the bimorph beams had recovered to their open position, the operational sequence was complete.

For each of the six electrostatic-actuated cantilever beam array based prototypes, the test sequence again began with each device at a uniform temperature (no power applied to the heater grid). At time $T=0$ seconds, 24 VDC was applied across the polysilicon resistive heating element. Over the next several seconds, the device would heat up, causing significant thermal conduction into the 24 electrostatic actuated polysilicon beams. At approximately $T=10$ seconds, the device had reached a steady state temperature. An appropriate pull-in potential was then applied to the electrostatic pull-in electrodes. This caused the beam arrays to immediately snap downwards, making conductive contact with the Poly0 heat sink layer below their tips. Once the device had once again reached a steady state temperature, the potential was removed from the pull-in electrodes – causing the beam arrays to snap back to the open position. Lastly, the potential was then removed from the heater grid – causing the device to rapidly cool back down to its starting temperature. This completed the operational sequence.

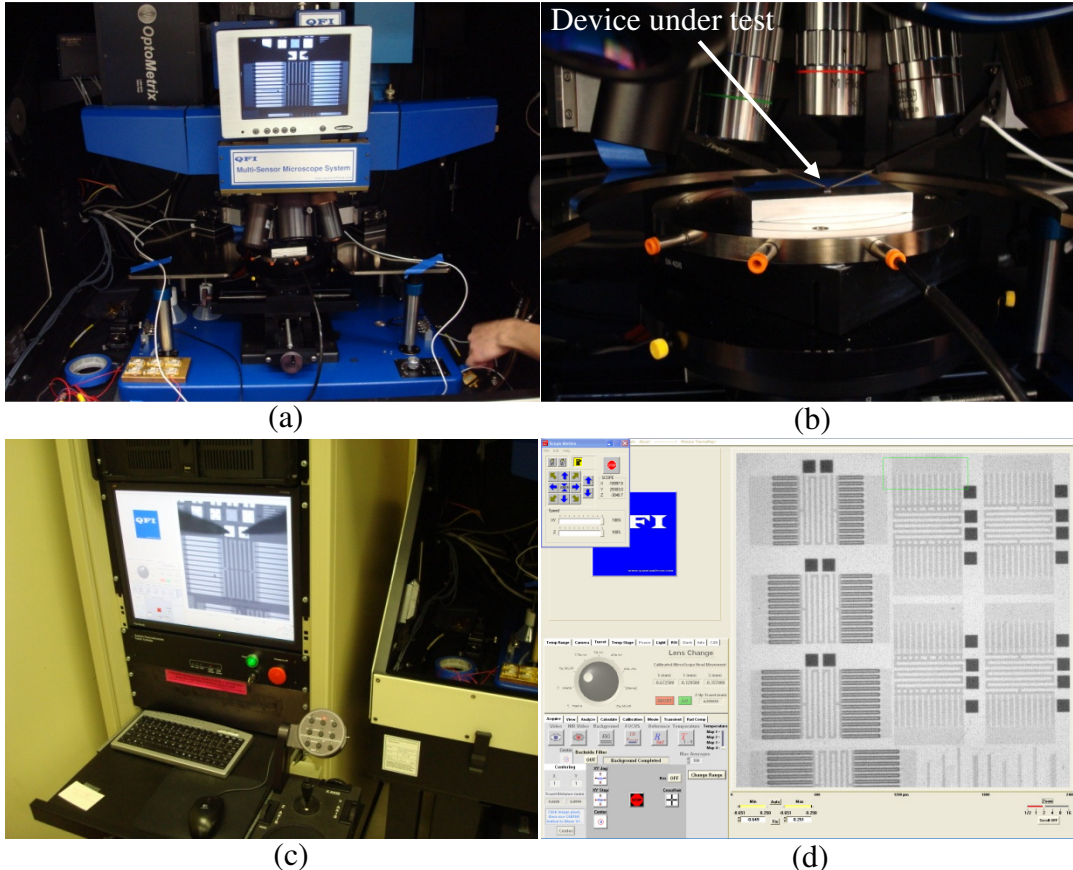


Figure 4.10: QFI thermal imaging microscope system: (a) is the test chamber, (b) shows a close-up of the stage, (c) is the operator's station, and (d) shows the operator's view during data collection.

As with the other test events, all measurements were conducted on two copies of each of the ten prototypes, with data averaged and recorded IAW the logic flow detailed in Figure 4.4. This data quantified the effect of the metamaterial structural elements on the system's overall thermal conductivity and heat transfer capabilities, demonstrating how κ can be controlled within a certain range by actuation of the metamaterial structural components.

4.2.4.2 Bimorph beam array based device temperature mapping results

Each of the ten proof-of-concept thermal metamaterial devices was characterized using the thermal imaging microscope system as described in Section 4.2.4.1. First, the four bimorph cantilever beam array based devices were tested.

As an introduction to the bimorph beam thermal mapping results, Figure 4.11 shows how the samples appeared when powered during testing. In the figure, the 250 μm beam device is shown under a 15X optical magnification, plus a 2X digital zoom. The device is on a temperature controlled stage, which is held at 77.0 ± 0.25 $^{\circ}\text{C}$. A potential of 24 VDC is applied across the sample's heater terminals, resulting in $I^2 \cdot R$ heating occurring throughout the heater grid. The application of this potential across the polysilicon structure causes ($P = V^2 / R$) approximately 300 mW of power consumption by the design. The heater grid's temperature rises to between 91-145 $^{\circ}\text{C}$, as shown in Figure 4.11.

Thermal conduction due to phonon vibration and interaction occurs between the polysilicon heater grid and the polysilicon beam arrays as the material seeks thermal equilibrium. Once the conducted heat energy reaches the cantilever beam anchor area, it encounters the much more thermally conductive gold layer atop the polysilicon beams. The heat easily conducts along the gold layer, resulting in the gold's temperature being 10-15 $^{\circ}\text{C}$ higher than that of the less conductive polysilicon beam beneath it. The hotter gold layer outline on each beam can be clearly seen in Figure 4.11 and Figure 4.12.

A consequence of the gold attaining a higher temperature than the polysilicon beneath it is that the beams bend down at a lower temperature than what was presented in the “actual” results column of Table 4.1. This is because that test event heated the entire

structure uniformly, such that the polysilicon and the gold were at the same temperature. The thermal imaging testing shows that, in normal operation, the gold is notably hotter than the polysilicon. This results in a closing temperature close to what was predicted during FEM, and was shown in the “modeled” column of Table 4.1. These results are

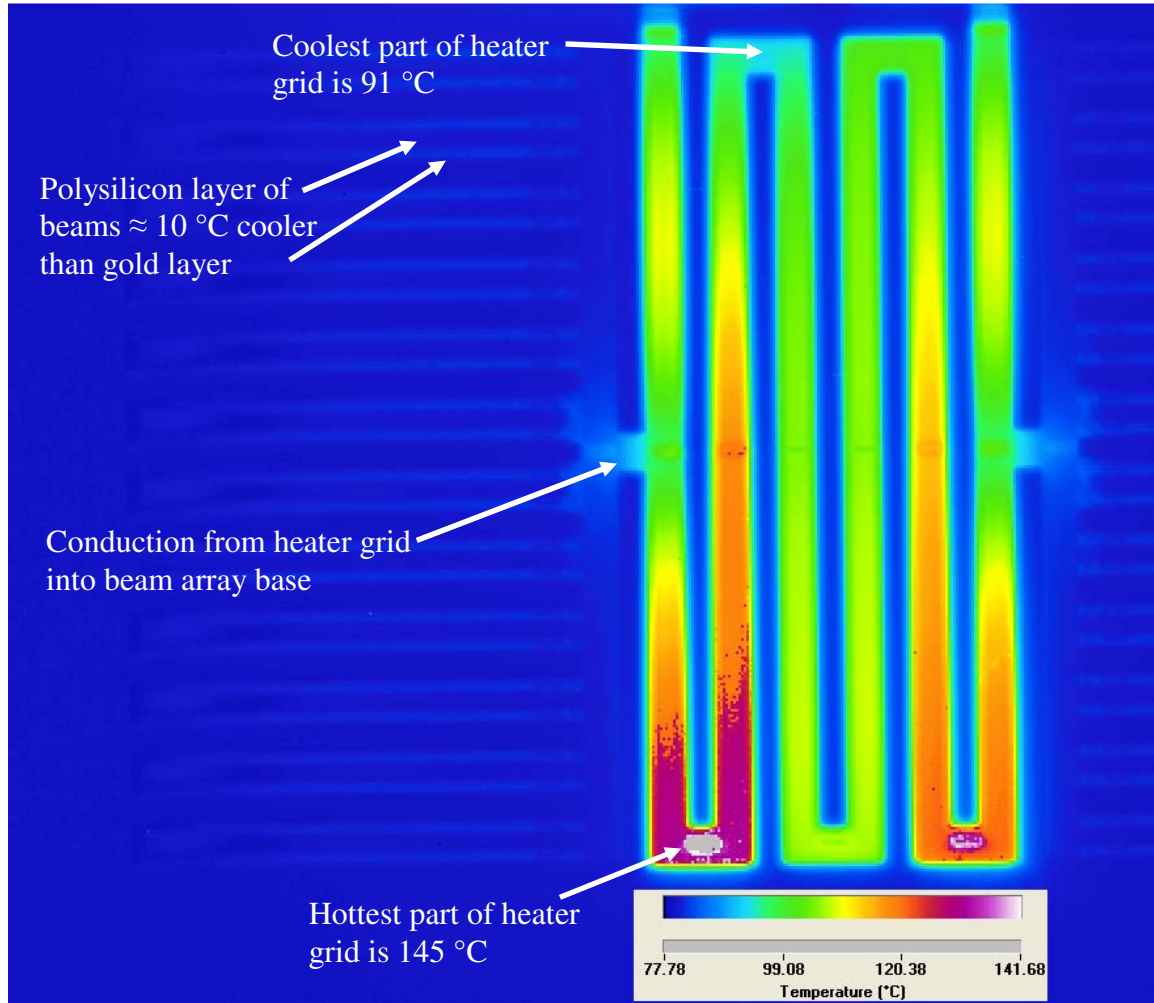


Figure 4.11: 250 μm bimorph beam array thermal metamaterial sample under 15X optical and 2X digital zoom with 24 VDC (300 mW) applied. The background temperature is 77 °C, and the heater grid rises to 91-145 °C due to Joule heating. Thermal conduction into the beam arrays can be seen to the left and right center of the heater grid. The gold (top) layer of the bimorph beams is ≈ 10 °C hotter than the less conductive polysilicon layer below it. The beams curl downward making conductive contact with the heat sink layer below their tips. This results in heat from the heater grid conducting through the beams, through the thermal contact resistance where each tip meets the heat sink, and into the heat sinks.

detailed later in this section in Table 4.3.

As each beam bends down in response to the difference in TCE between the polysilicon and gold, it contacts the polysilicon heat sink layer beneath its tip. At this physical junction between the bimorph beam tip and the Poly0 heat sink, a thermal contact resistance is present. As was discussed in Section 2.3.2, this contact resistance impedes the transfer of thermal energy between the two structures, resulting in a

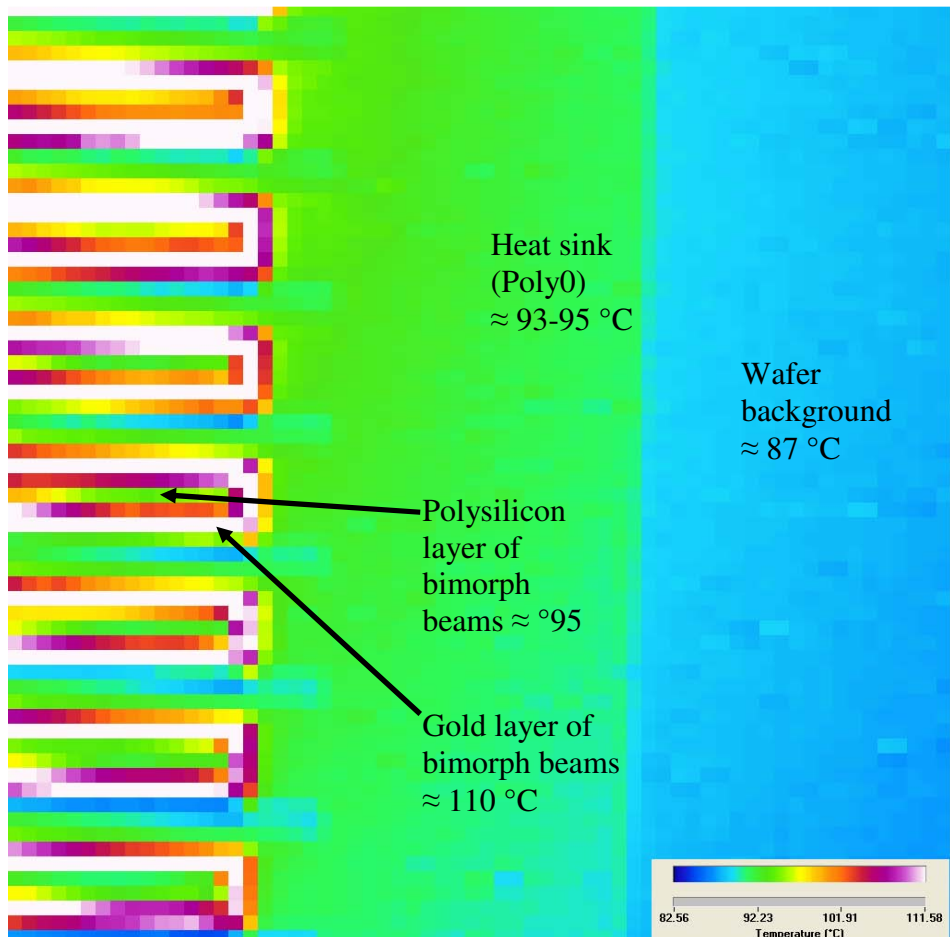


Figure 4.12: 300 μm bimorph beam array thermal metamaterial sample under 5X optical and 16X digital zoom with 20 VDC (215 mW) applied. The beam array is bent downward, making contact with the polysilicon heat sink layer. Due to the conduction occurring through the beams and into the heat sink, the heat sink's temperature is close to that of the polysilicon in the bimorph beams. This results in thermal energy originating from the heater grid being conducted into the heat sink sheets.

temperature gradient at the junction. Figure 4.12 shows the beam array bent downward or closed – conducting heat energy into the heat sink sheet or layer. This steady stream of heat conducted into the heat sink keeps it elevated 6-8 °C hotter than the background wafer. The heat in the heat sink is ultimately transferred into the surrounding environment through a combination of conduction into the wafer substrate, convection into the moving air above it, and thermal radiation outward from its surface.

The operational sequence of the bimorph cantilever beam array thermal metamaterial is shown graphically in Figure 4.13. In the figure, (a) shows the entire device unpowered at a background temperature of 72 °C. Figure 4.13 (b) through (e) shows the device rapidly heating, with conduction into the beam arrays occurring. Finally, in (f), 1.25 seconds after power was applied, the beams begin to fully close – completing a conductive path from the heater grid, through the bimorph beams, and into the heat sink.

This sequence illustrates one notable limitation of using bimorph beams as an actuation technique. When bimorph beams are heated solely via thermal conduction, they react much slower than when actuated by applying a potential across the gold layer of the beam (a common bimorph MEMS actuation method). Relying on conduction from an adjacent structure alone results in a relatively slow (1+ second) beam actuation. Additionally, the beams do not immediately snap back up or curl upward as soon as heat is removed. Residual heat and stiction forces result in the beam arrays often taking several seconds to fully recover to their up or off position (discussed later in Figure 4.15). While this slow response is acceptable for many thermal management applications, it is sub-optimal for thermal metamaterial applications where a switched or tunable electrical conductivity is desired.

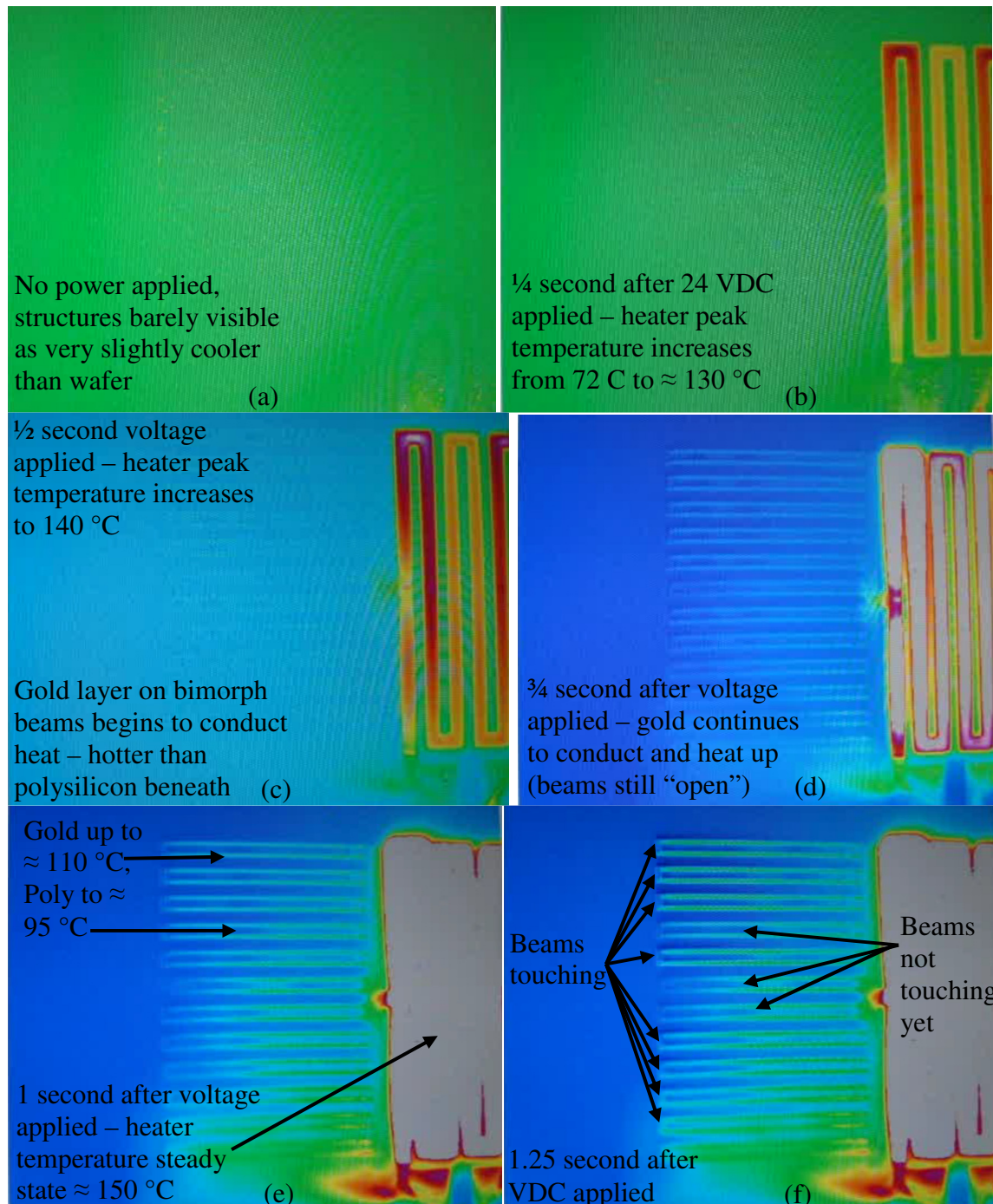


Figure 4.13: Bimorph cantilever device operational sequence. In (a), at time $T=0$, the device and background is at 72 °C, and 24 VDC is applied. In (b), at $T=0.25$ seconds, the polysilicon heater grid temperature has increased dramatically to ≈ 130 °C. In (c), at $T=0.5$ seconds, initial thermal conduction into the beam array can be seen. In (d), at $T=0.75$ seconds, the outline of the gold layer can be clearly seen as heat is conducted away from the heater grid. In (e), conduction into the beam arrays continues, until in (f) where beam closure begins at $T=1.25$ seconds.

Figure 4.14 illustrates thermal characterization of the bimorph beam array thermal metamaterial from initial power application through steady state operation, with particular emphasis placed on thermal conduction from the bimorph beams into the heat sink. At time $T=0$, a 24 VDC potential is applied across the heater grid. Figure 4.14

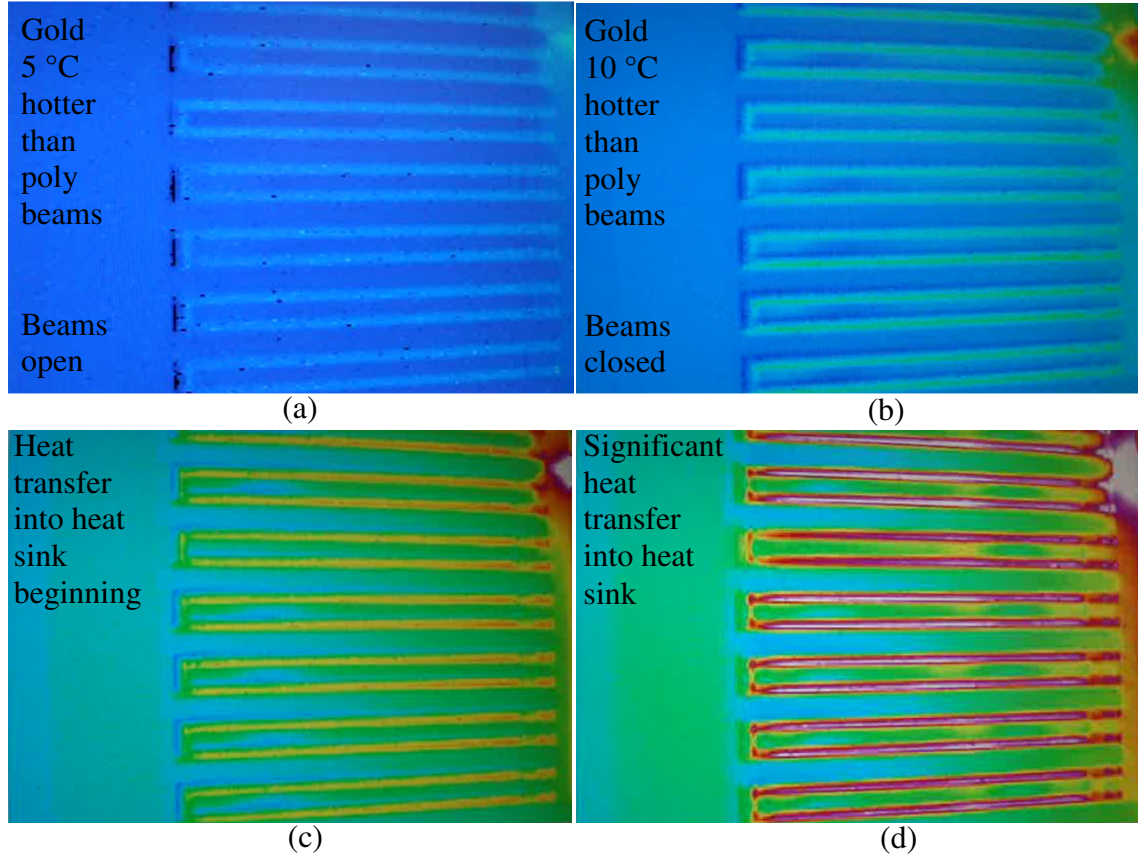


Figure 4.14: Bimorph beam array heat transfer into the heat sink. The $250 \mu\text{m}$ sample is shown under a 15X optical and 4X digital zoom, with emphasis on the beam array and heat sink layers. In (a), the beam array and heat sink are shown $\frac{1}{2}$ second after voltage was applied across the heating element. The gold begins to heat, but the beams are still curled upwards with no thermal conduction into the heat sink. One second later in (b), the beams have all closed and conduction into the heat sink can now begin. At 2.5 seconds, a complete outline of the Poly0 heat sink layer can be seen, because it's temperature has been raised (heated) via conduction from the bimorph beams (c). Lastly, in (d), the system has reached steady state at 10 seconds. The outline of the gold layer in each beam is clearly seen, and is 15°C hotter than the Poly2 structural layer of each beam. The heat sink's outline is clearly visible, and is nearly the same temperature as the Poly2 in the bimorph beams which are directly conducting heat into the sink.

shows how the device structures heat and move in response to this Joule heating, which is occurring off the right side of the figure. The device reaches its thermal steady state at $\approx T=10$ seconds. At steady state, thermal conduction from the heater grid, through the 12 bent down bimorph beams, and into the heat sink layer heats the sink to ≈ 10 °C hotter than the background wafer.

The thermal characterization presented thus far has addressed the device performance from power up through reaching a steady state temperature. The post-powered operation of the bimorph beam array thermal metamaterials reveals several characteristics not seen in FEM. Figure 4.15 illustrates a time lapse sequence of the device's performance after voltage is removed from the heater grid. As mentioned earlier in this section, the bimorph beams do not react very quickly to the application or the removal of potential across the heater grid. This slow reaction time is exaggerated in situations where the device temperature is below, but close to, the rated switching temperature of the beam array. In Figure 4.15, the bimorph beams are shown individually recovering, curling upwards one at a time over a few seconds.

While the bimorph beams take longer to recover than expected, the most unexpected result of this test event is how the recovering beams appear under the medium wavelength infrared (MWIR) microscope. As seen in Figure 4.15, upon removal of the voltage across the heater grid, the entire structure very quickly (less than $\frac{1}{4}$ second) cools to approximately the background temperature. The notable exception to this is the bimorph beams that are still stuck down. These beams, which in theory are also approximately at the background temperature, appear under MWIR to be ≈ 15 °C hotter than the background and other parts of the design's structure. Additionally, the Poly2

structure beneath the gold layer appears to be 5 °C cooler than the background and surrounding structure. As soon as each of these bimorph beams snaps or curls upwards, it immediately appears under MWIR to be uniformly at the background temperature.

It is not known why both layers of the bent down bimorph beams appear this way under MWIR. Clearly both the anchor end and the heat sink end are at approximately the

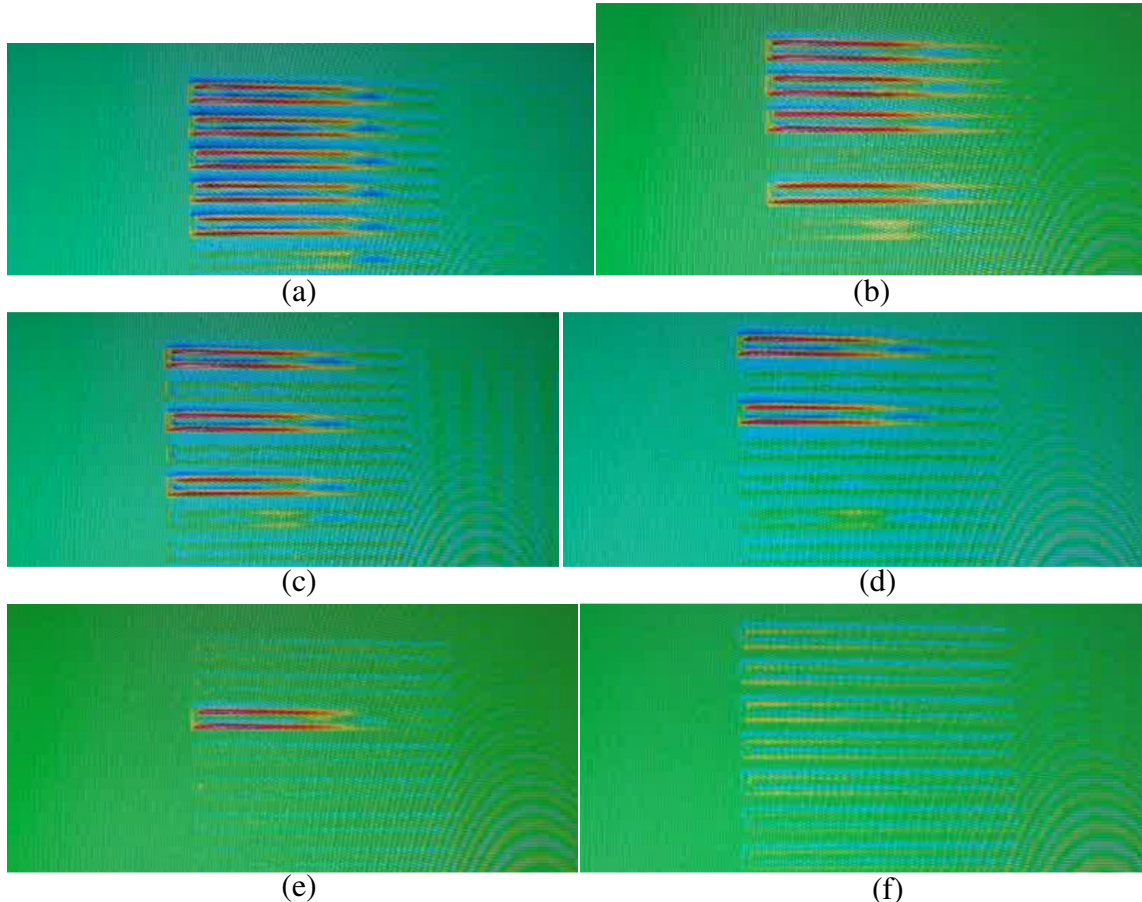


Figure 4.15: Bimorph beam metamaterial recovery sequence. The 300 μm variant is shown under 15X optical and 2X digital zoom. In (a), power has just been removed from the heater grid. The top five beams are still bent down, while the bottom beam has already recovered (curled upwards). In both (b) and (c), individual beams recover and curl upwards. This recovery continues in (d) and (e) until in (f), where all beams have fully recovered. Note that when the beams are still bent down, the gold appears (under MWIR) over 15 °C hotter than the background, while the Poly2 in each beam appears 5 °C cooler than the background. Immediately upon snapping/curling upwards, the entire beam (gold and Poly2) appear approximately equal to the background temperature.

stage background temperature. Therefore, no conduction is occurring from either the heat sink or from the heater grid into the bimorph beams. The beams are not retaining heat for more than a few tenths of a second, so the apparent elevated gold temperature is not due to heat “trapped” in the beam. Unfortunately, because the MWIR thermal imaging microscope is a low-density, high demand system, there was not sufficient test time allotted to further explore this recovering bimorph beam imaging issue. However, the initial results presented here suggest that there may be some potential applications in thermal obfuscation. This is because the bimorph beam arrays of the thermal metamaterial design can appear under MWIR to be both hotter (gold layer) and cooler (Poly 2 beams) than they actually are.

In addition to the bent down bimorph beam temperature issue just discussed, another unexpected result was the amount of power required to heat the polysilicon heater grid, and thereby the entire device. As presented earlier in Figure 3.12 and Figure 3.13, FEM predicted the device operation would require 0.5-0.6 mW. This modeling prediction was well over two orders of magnitude less than the actual power required. Even with the devices at an elevated stage temperature of 70-80 °C, it still required \approx 300 mW to fully actuate the bimorph beam arrays.

The reason for this power consumption discrepancy between the FEM and actual results is that FEM was executed with the substrate or wafer excluded from the system model. When FEM was conducted in the pre-fabrication stage, it was thought that the silicon nitride layer, which provides electrical isolation between the polysilicon structures and the wafer below, would also provide sufficient thermal isolation between these layers. This was thought to be a reasonable assumption, as polysilicon is \approx 12.8 times

more thermally conductive than silicon nitride in the PolyMUMPsTM process, as was presented in Section 2.3.2. However, in this process, the SiN layer is very thin (0.6 μm), and this testing suggests that a more thermally insulative layer is necessary to optimize performance. Figure 4.16 illustrates this issue. In the figure, the heater grid, at the point where it attaches to the beam array, is at 102 °C. Although it is directly connected to the polysilicon beam array just 20 μm away, it loses over 10 °C conducting over that short distance. This is because of what is not seen, which is a substantial amount of thermal conduction straight down from the heater into the substrate. This was not seen in the FEM due to the substrate being excluded from the model. Therefore, in FEM, the thermal conduction only occurred in the X-Y plane, with no losses in the Z axis as was seen in this testing. This illustrates the importance of including the substrate in any FEM in which heat transfer throughout the device is an important operational consideration.

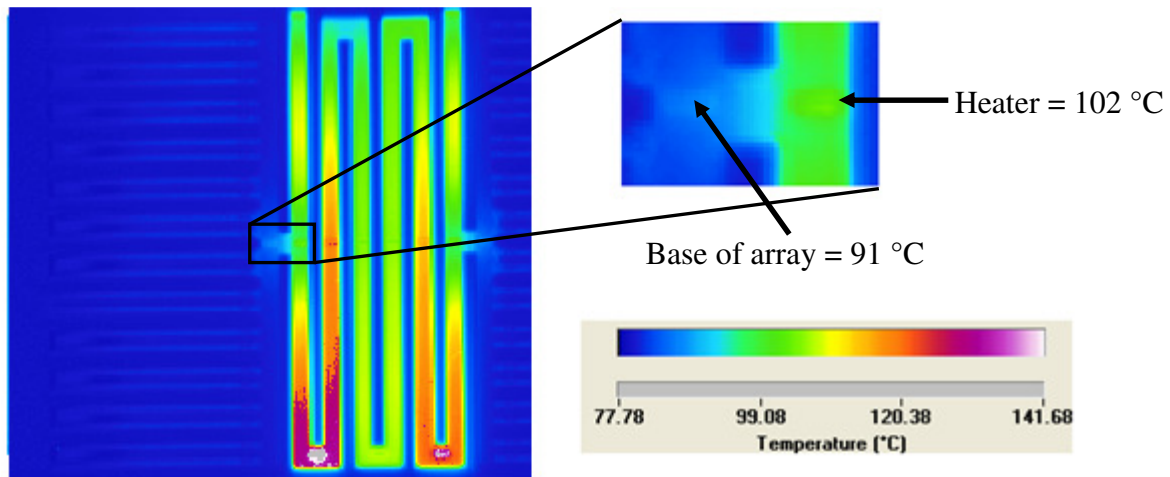


Figure 4.16: Thermal conduction from heater grid into the bimorph beam array. Due to the thin silicon nitride layer beneath the heater grid providing only marginal thermal insulation, a substantial amount of the thermal energy input to the system is conducted into the substrate beneath the grid. This results in relatively poor conduction into the beam arrays, as shown on the upper right of the figure.

Upon discovery of this discrepancy, FEM for these devices was partially reaccomplished to quantify the impact of including the substrate in the model. An example of the revised meshed model is shown in Figure 4.17. Execution of transient analysis on the model shown in Figure 4.17 showed that \approx 300-700 mW of power is required to fully actuate the beam arrays. This number varies based primarily on the ambient starting temperature used in the model. For example, performing FEM with a starting temperature of 23 °C requires \approx 700 mW (\approx 36 VDC applied) to be consumed by the resistive heating element in order to actuate the beam arrays in a timely manner. As expected, starting at a higher system temperature requires less applied voltage and power consumption to actuate the design features. This closely correlated with the results presented earlier in this section.

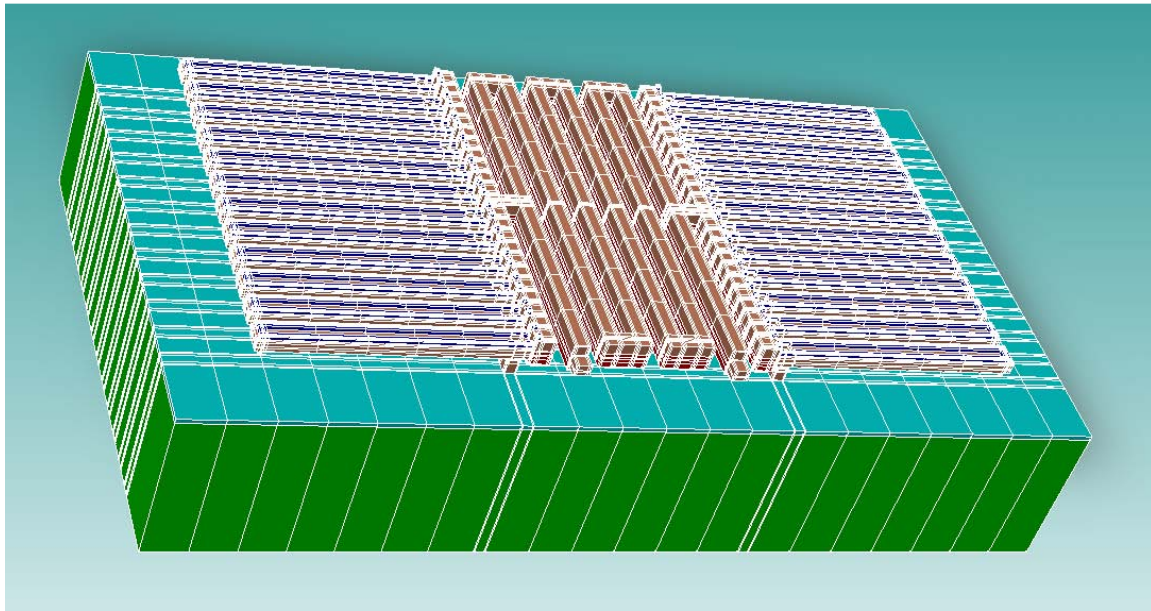


Figure 4.17: Updated meshed 3-D model of thermal metamaterial device, as modeled in CoventorWare 2008. The 300 μ m bimorph beam design is shown with the substrate included in the mesh. As postulated, the addition of the substrate's substantial thermal mass to the model resulted in a requirement for a greater amount of voltage applied across the heater terminal to actuate the beam arrays.

All four versions of the bimorph cantilever beam array metamaterial performed similarly in this test event. Gold temperatures, peak heater temperatures, polysilicon beam temperatures, and heat sink temperatures were within 2-3% in all cases. In fact, there was no more variation between versions than there was between different copies of the same version. This temperature mapping is shown graphically in Figure 4.18. The

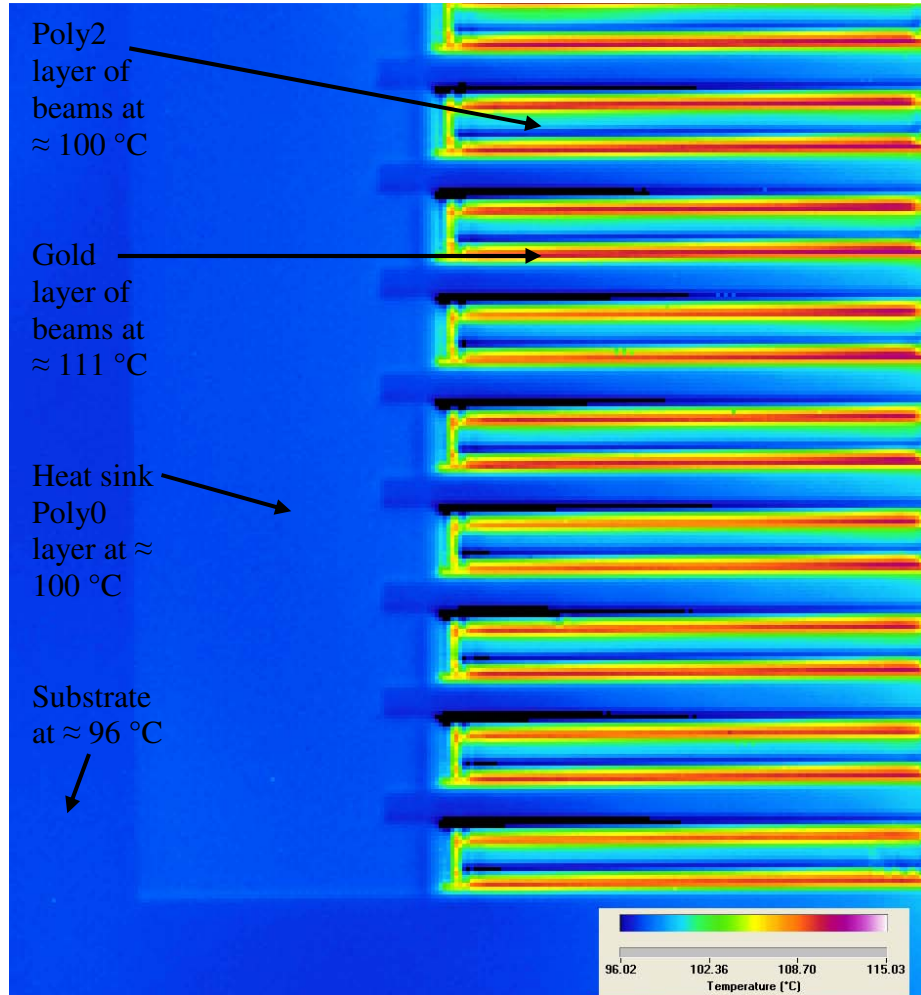


Figure 4.18: Temperature mapping of the bimorph beam array thermal metamaterial. The 200 μm version is shown, others similar. Poly2 beam temperatures for each layout are listed in Table 4.3, and are 100 °C for the version shown here. For each version, the gold layer on the beams was 10-15 °C hotter than the Poly2. The Poly0 heat sink was approximately the same temperature as the Poly2 beams (within 1-2 °C). The substrate was 4-8 °C cooler than the heat sink.

one important exception to the versions similarity is beam closing temperature. Bimorph beam closing temperatures were within 2% of the values predicted during FEM, and are summarized in Table 4.3. As mentioned earlier, the values recorded in this test were

Table 4.3: Bimorph beam array closing temperatures, thermal imaging testing versus interferometer based testing and modeling.

Beam length	MWIR testing: beam temperature at which contact is made (°C) ¹	Interferometer testing: beam temperature at which contact is made (°C) ²	FEM: beam temperature at which contact is made (°C) ¹
150 μm	107	127	99
200 μm	100	123	89
250 μm	87	114	80
300 μm	79	110	73

¹ Temperature of the Poly2 layer of the beam – gold temperature is $\approx 10\text{--}15$ °C hotter

² Temperature of the entire sample was uniform for this test event

significantly lower than those seen during the interferometer based bimorph beam array testing, first summarized in Table 4.1 and reiterated here. This is again due to that earlier test being conducted on a uniformly heated device, in which the polysilicon and gold layers of the beams were at the same temperature. In the thermal imaging testing conducted here, the devices were heated using a combination of overall device heating (heated stage) and localized heating via each devices resistive heating element. In this case, the more conductive gold became hotter than the less conductive polysilicon, resulting in the beam bending down at a significantly cooler temperature. These performance differences illustrate that the designs σ and κ switching characteristics are not only temperature dependent, but also depend on how that temperature is attained.

4.2.4.3 Electrostatic beam array based device temperature mapping results

Following the completion of testing the four bimorph beam based variants, it was planned to characterize each of the six electrostatic-actuated cantilever beam array based

prototypes as detailed in Section 4.2.4.1. However, due to extended downtime of the QFI thermal imaging microscope system (down for unscheduled maintenance for approximately three months), this test point has not yet been conducted. In the event that characterization of the electrostatic actuated devices is accomplished at a later date, it will be published as an appendix to this document.

Based upon the results of the bimorph beam array based prototype testing presented in Section 4.2.4.2, some assumptions can be made about the electrostatic actuated thermal metamaterial's heat transfer performance. In the bimorph beam based devices, thermal conduction along the gold layer dominated heat transfer in the device's X-Y plane. Because the six electrostatic beam based prototypes feature an all polysilicon construction, it is likely that their ability to conduct heat from the resistive heating element outward into the heat sink sheet is relatively poor in comparison. This should be most apparent in layout versions 1-4, which have the same heater arrangement as the bimorph beam based designs (heater style #1). The thermal conductivity of each all-polysilicon beam is significantly lower than that of the gold/polysilicon combination of the bimorph beam.

Based on their physical layout, versions 5 and 6 should facilitate an enhanced κ when compared to the other electrostatic actuated versions. This is due to the additional conductive paths between the heater grid and electrostatic beam arrays. Figure 4.19 illustrates the differences between the layouts, showing why versions 5 and 6 provide decreased thermal resistance and provide for an increase in the devices κ .

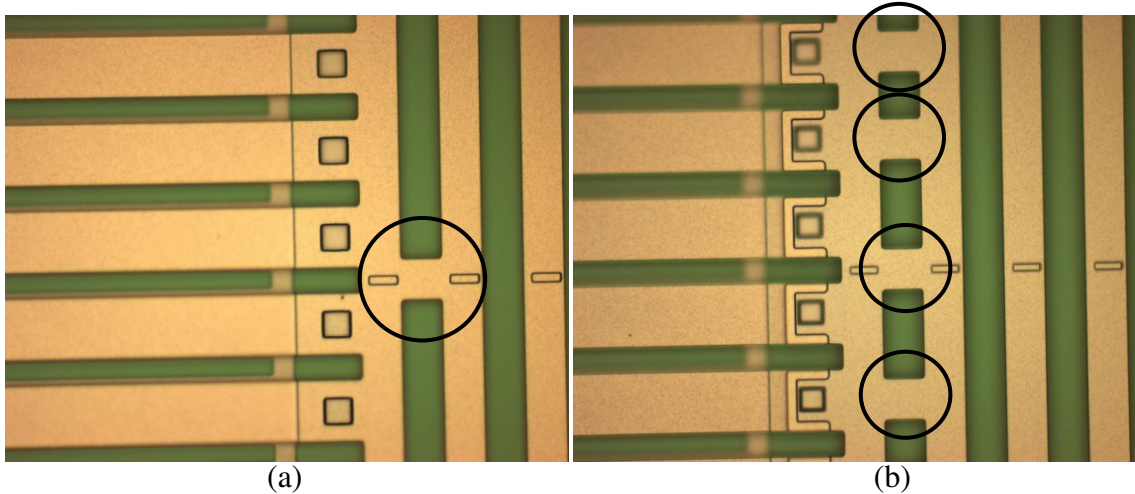


Figure 4.19: Comparison of heater grid layouts for the electrostatic actuated beam array based metamaterials. In (a), heater style #1 (versions 1-4) is shown, providing only one conductive path (circled) between the heater and the beam arrays. In (b), heater style #2 (versions 5 & 6) has multiple conductive paths (circled), providing for enhanced heat transfer between the heater and beam arrays.

4.2.5 Test event #4: metamaterial device electrical resistance characterization

4.2.5.1 Device electrical resistance test description

The ability to provide “tunable” electrical conductivity is fundamental to the functionality of the thermal metamaterial prototypes. For each of the four bimorph cantilever beam array based prototypes, electrical resistance from both the heater terminal to heat sink, and from the heat sink to heat sink, was measured. Resistance from the heater terminal to heat sink was measured from “A” to “B” as shown in Figure 4.20 (a), and heat sink to heat sink was from “B” to “C”. Measurements were conducted at 10 °C intervals for device temperatures of 25 °C to 135 °C. The resultant data product was electrical resistance verses device temperature.

For each of the six electrostatic actuated cantilever beam array based prototypes, resistance from the heater terminal to heat sink was measured from “A” to “B” as shown in Figure 4.20 (b). Measurements were again conducted at 10 °C intervals for device

temperatures of 25 °C to 135 °C. For each test point, a measurement was made with the beams “open” and also with them “pulled-in”. Direct heat sink to heat sink measurements were not possible on the six electrostatic actuated devices. This was due to the requirement for the beams arrays/heater grid to be held at a certain potential to facilitate pull-in, which prevented proper ohmmeter operation when considering the heat sink areas as the I/O. The resultant data product was electrical resistance verses device temperature verses beam array position.

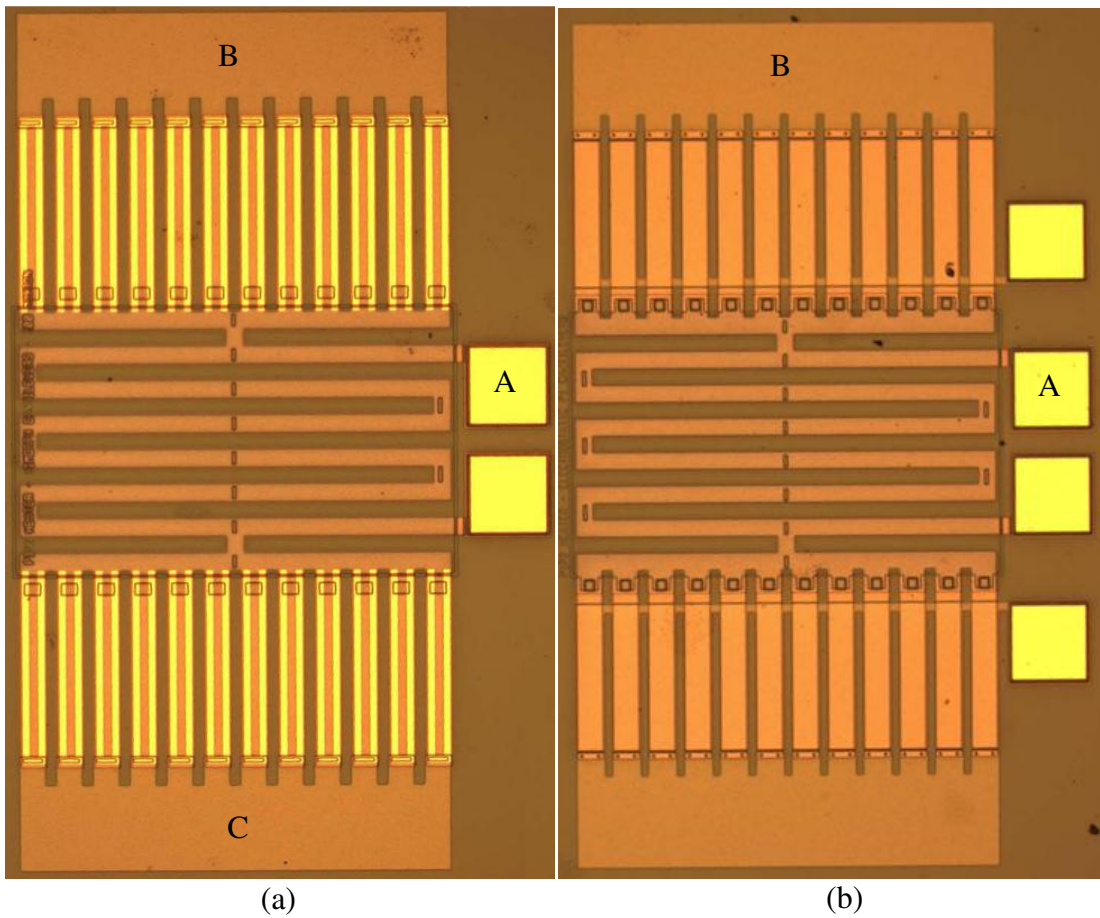


Figure 4.20: In (a), the electrical resistance characterization measurement test points for the bimorph cantilever beam array based prototypes are shown. In (b), the test points for the electrostatic actuated cantilever beam array based prototypes are shown.

All test points were conducted IAW the test logic flow detailed in Figure 4.4. The test setup is shown in Figure 4.21, and consisted of the unit under test (UUT) placed atop a thermoelectric device. The thermoelectric device was placed onto a probe station stage with magnified optics to facilitate test probe connection and manipulation. DC power supplies were used to control the thermoelectric device (as shown in Figure 4.21 (a)) and also to control pull-in on the electrostatic actuated designs. An Agilent digital multimeter was connected to the probes and used to record the resistance for each test point.

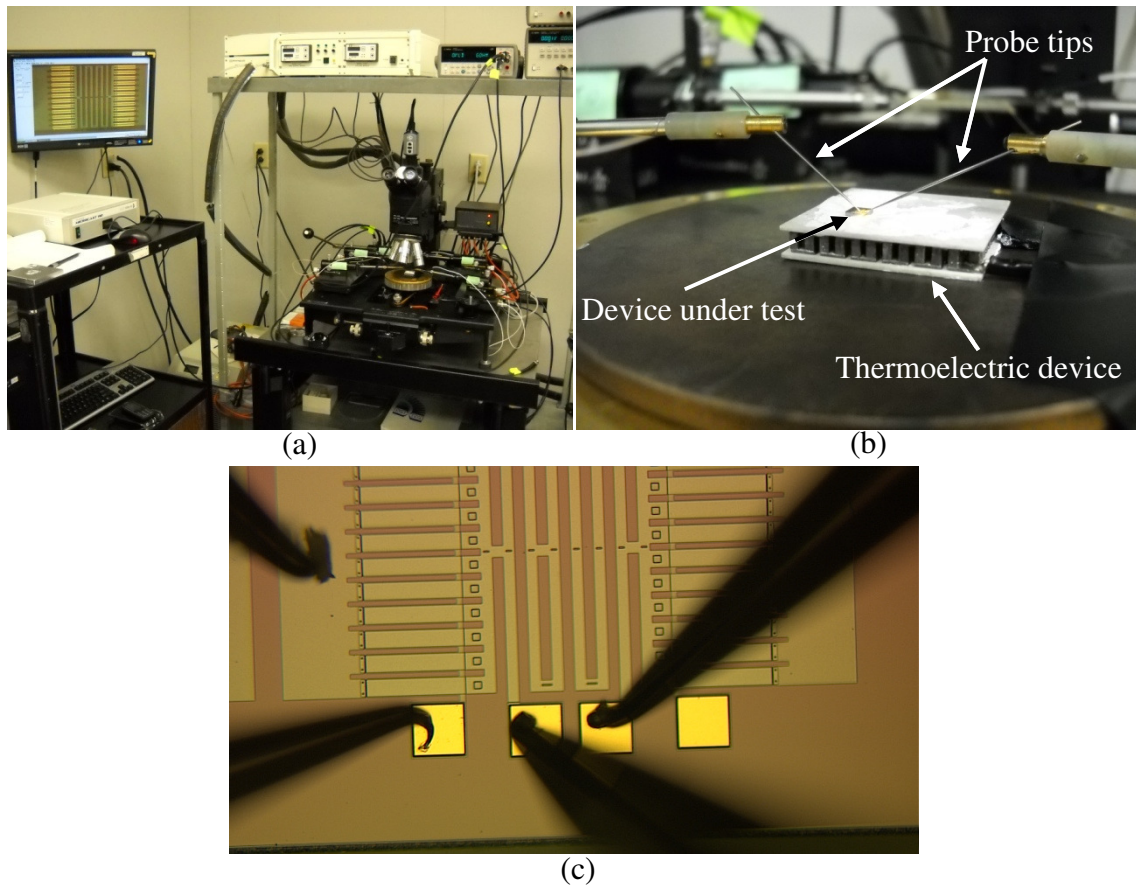


Figure 4.21: Thermal metamaterial electrical resistance characterization setup. In (a) the microscope probe workstation is shown. In (b), a close-up of the probe station stage is shown. In (c), electrostatic-actuated thermal metamaterial layout version # 2 is shown with test probes being placed into position.

4.2.5.2 Device electrical resistance test results

As detailed in Section 4.2.5.1, the thermal metamaterial prototype's electrical resistance was characterized. First, each of the four bimorph cantilever beam array based prototypes electrical resistance was determined, and is presented in Figure 4.22 and Figure 4.23.

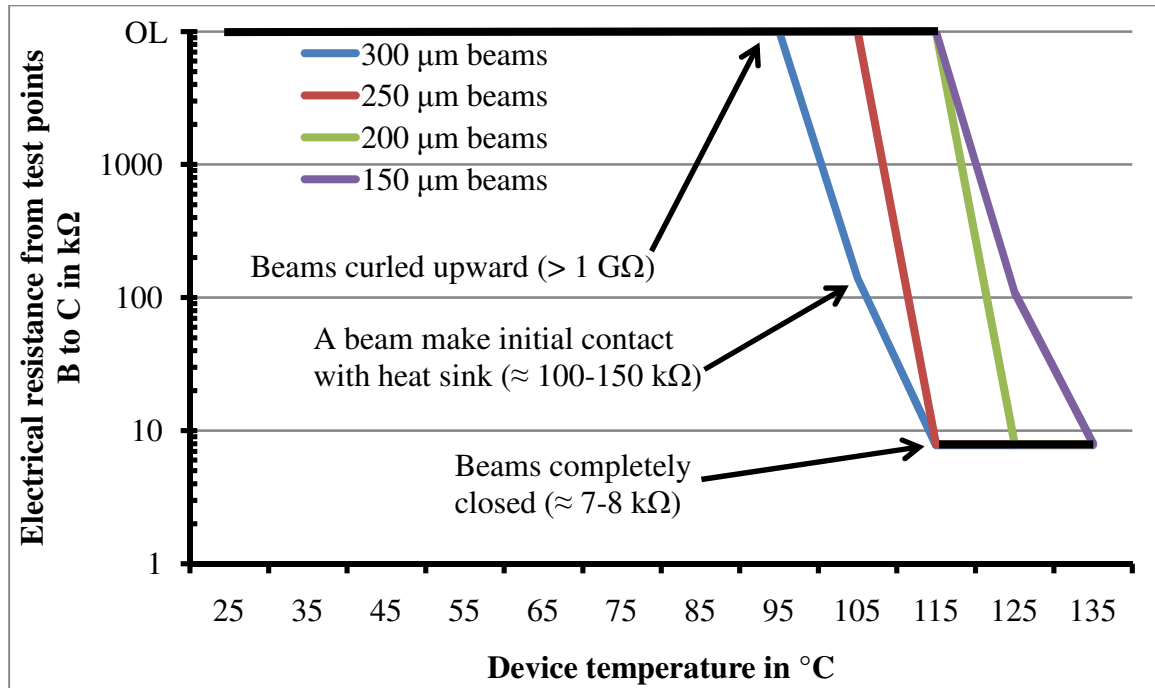


Figure 4.22: Electrical resistance of bimorph cantilever beam array metamaterials, from test points B to C (heat sink to heat sink). All designs exhibited off scale high ($\text{G}\Omega$'s) resistance at temperatures less than approximately their closing temperature (from Table 4.1) minus $4\text{ }^{\circ}\text{C}$. As each design's closing temperature was approached, the resistance would drop from “overload” to approximately $100\text{--}150\text{ k}\Omega$. Increasing the temperature further resulted in the resistance decreasing to $\approx 7\text{--}8\text{ k}\Omega$.

In Figure 4.22, the electrical resistance, measured from one heat sink to the other heat sink, of each bimorph cantilever beam array design is plotted. Each of the four designs performed similarly, with “off scale high” ($> 1\text{ G}\Omega$) resistance at temperatures less than their beam closing temperature (from Table 4.1) minus $\approx 4\text{ }^{\circ}\text{C}$. This high resistance is

due to a several micron “open circuit” at each of the 24 beam tip to heat sink interfaces. As the temperature was increased to within ≈ 4 °C of the beam array closing temperature, some of the beams began to make conductive contact with the heat sink below. At this point, the resistance dropped from “off scale high” to between 100-150 k Ω . Further increasing the system temperature resulted in complete beam array closure, with the resistance reaching a minimum value of ≈ 7 -8 k Ω .

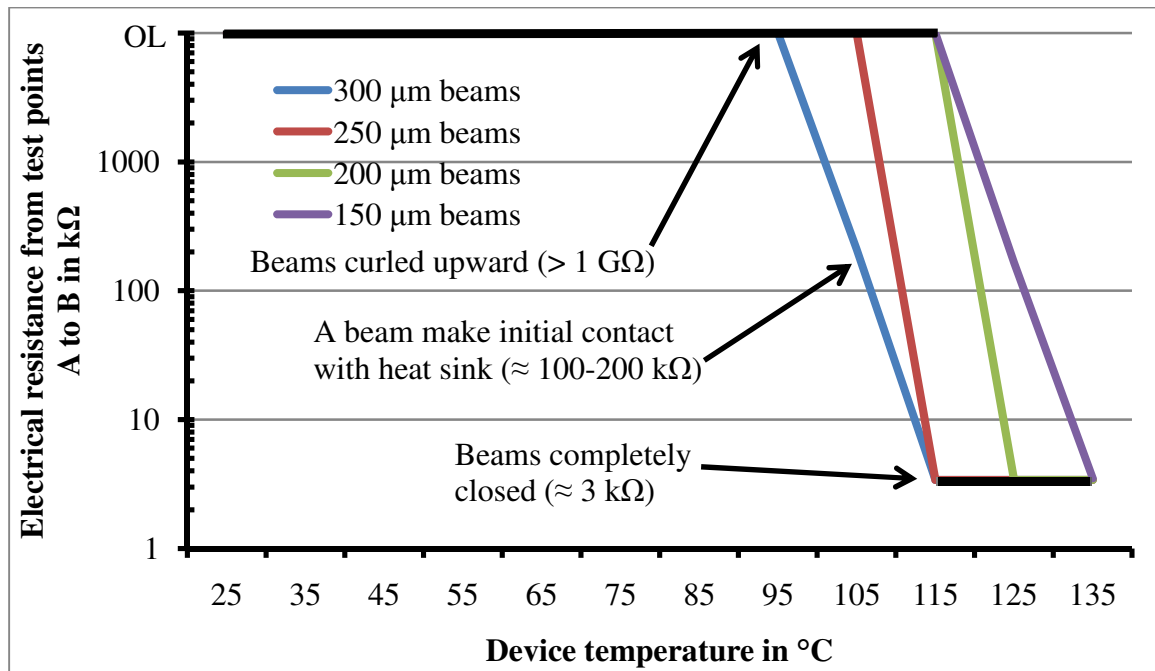


Figure 4.23: Electrical resistance of bimorph cantilever beam array metamaterials, from test points A to B (heater terminal pad to heat sink). All designs exhibited off scale high (G Ω 's) resistance at temperatures less than approximately their closing temperature (from Table 4.1) minus 4 °C. As each design's closing temperature was approached, the resistance would drop from “overload” to approximately 100-200 k Ω . Increasing the temperature further resulted in the resistance decreasing to ≈ 3 k Ω .

In Figure 4.23, the electrical resistance, measured from a heater terminal pad to a heat sink, of each bimorph cantilever beam array design is shown. The overall performance

was very similar to that seen in the previous heat sink to heat sink resistance testing. Each of the four designs exhibited “off scale high” ($> 1 \text{ G}\Omega$) resistance at temperatures less than their beam closing temperature (from Table 4.1) minus $\approx 3\text{-}4 \text{ }^\circ\text{C}$. This high resistance is again due to a several micron “open circuit” at each of the 12 beam tip to heat sink interfaces. As the temperature was increased further, the beam array closed, resulting in the resistance reaching a minimum value of $\approx 3 \text{ k}\Omega$.

Using the device resistance data presented in Figure 4.22 and Figure 4.23, an analytical resistive model of the bimorph cantilever beam array metamaterial was produced. This was accomplished to facilitate estimation of each major structural components contribution to the systems electrical resistance. The analytical model is shown in Figure 4.24. In the figure, the I/O of the system (Poly0 heat sink sheets), is shown as test points B and C. The contact resistance at the beam tip to heat sink interface is variable depending on the position of each beam, and can range from many $\text{G}\Omega$ (an open circuit) when curled upwards to an average of $\approx 36.6 \text{ k}\Omega$ when closed. This contact resistance is represented by each of the 24 resistors shaded in blue. Each of the 24 bimorph beams has a polysilicon layer and a gold layer, which are effectively two different resistors in parallel when considered from the I/O’s perspective. The 24 bimorph beams are represented by the 48 resistors shaded in red in Figure 4.24. Each beam is represented by two resistors, one for each of its two layers. The polysilicon resistive heating element is represented by a single resistor in the middle, and is known to be $\approx 1.6 \text{ k}\Omega$. Lastly, the resistance of each Poly0 heat sink is accounted for by the resistor at the top and bottom of the figure. This resistor also accounts for the resistance

occurring at the heat sink to I/O probe tip junction. Each of these two resistances has a measured value of $\approx 0.1 \text{ k}\Omega$.

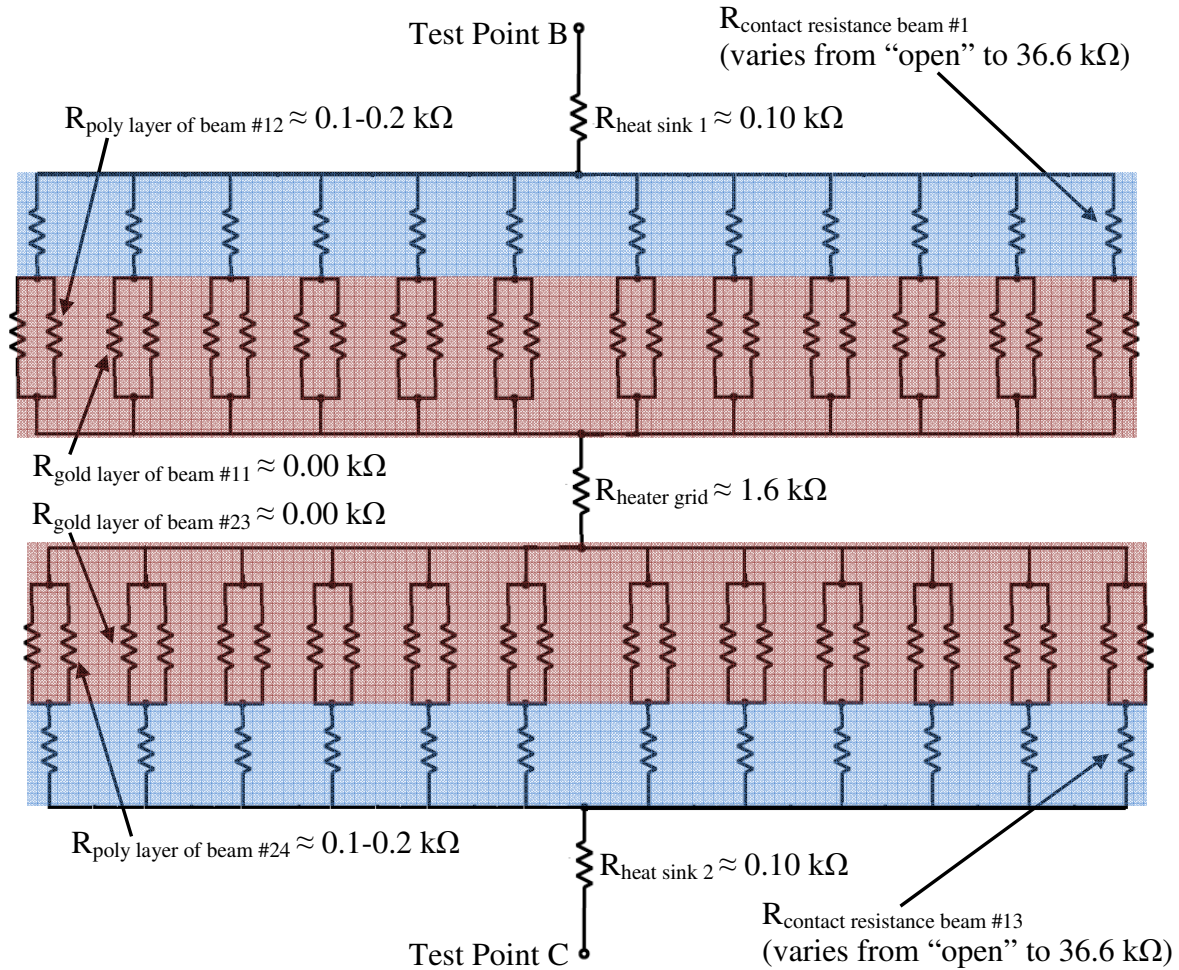


Figure 4.24: Bimorph cantilever beam array electrical resistance analytical model. Test points B and C are considered the input and output terminals in this representation. Each of the 24 resistors shaded in blue represent the contact resistance at the beam tip to Poly0 heat sink interface. This contact resistance is variable, ranging from an “open circuit” when the bimorph beams are curling upwards to $\approx 36.6 \text{ k}\Omega$ when the beam arrays are closed. The 48 resistors shaded in red represent the 24 bimorph beams, where each beam has a gold layer and a polysilicon layer. Each of these two layers on each beam is represented by one resistor. The polysilicon resistive heating element is represented by a single resistor in the middle. Lastly, the resistance of each Poly0 heat sink is accounted for at the top and bottom of the figure. Resistance values for heat sink 1 and 2, polysilicon and gold layers of beam, and heater grid were known or measured, allowing an estimated solution for average beam tip contact resistance.

Figure 4.25 illustrates how Figure 4.24 was reduced in order to solve for and estimate “ $R_{\text{contact resistance beam}}$ ” for each of the 24 beams. The “ $R_{\text{poly layer of beam}}$ ” and “ $R_{\text{gold layer of beam}}$ ” resistors in parallel reduce to approximately 0 k Ω due to gold’s low sheet resistance. The 12 “ $R_{\text{contact resistance beam}}$ ” in parallel on each side reduced to “ $\frac{1}{12} R_{\text{contact resistance beam}}$ ”, which reduced the whole system to five resistances in series, as shown in Figure 4.25. Three of these five were known or measured, with the other two being unknown but approximately equal, allowing an estimated solution for “ $R_{\text{contact resistance beam}}$ ” of 36.6 k Ω .

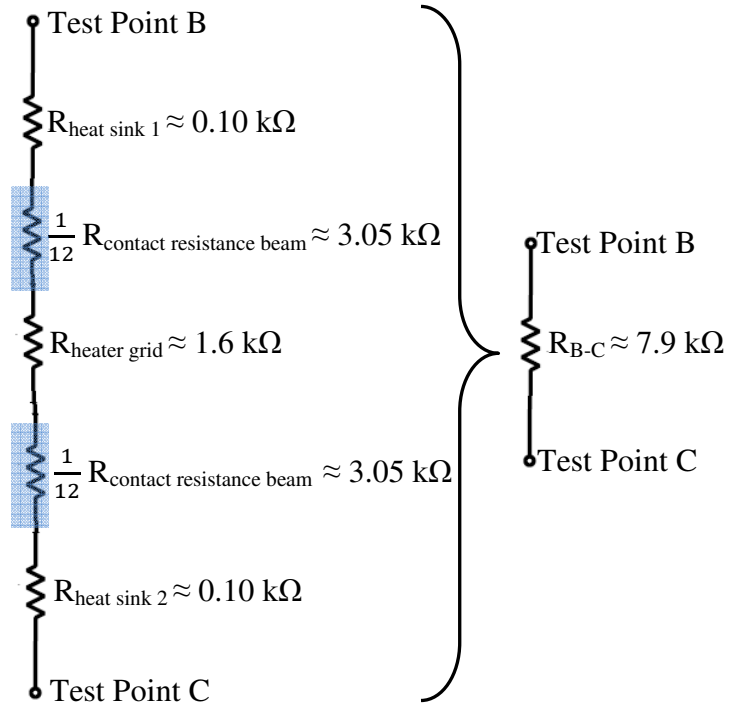


Figure 4.25: Bimorph cantilever beam array electrical resistance reduced analytical models. Each of the two rows of 12 beams shown in Figure 4.24 reduces to approximately $\frac{1}{12} R_{\text{contact resistance beam}}$ due to the low electrical resistance of the gold layer in each beam. $R_{\text{heat sink } 1}$, $R_{\text{heat sink } 2}$, and $R_{\text{heater grid}}$ are known values (measured), allowing for an approximation of $R_{\text{contact resistance beam}} \approx 36.6 \text{ k}\Omega$ to be made. Test points B and C are considered the input and output terminals in this representation.

This test event quantified the temperature dependent electrical resistance of these four bimorph cantilever beam array based thermal metamaterials. The resistance of the bimorph beam arrays is effectively a thermostat type “on/off switch”, where “off” is $> 1 \text{ G}\Omega$ and on is $3 \text{ k}\Omega$ or $7 \text{ k}\Omega$, depending on which terminals the I/O is using. The contact resistances present at each of the 24 beam tip to Poly0 sheet interfaces was the dominant factor in the systems overall resistance. This data showed that the σ of the bimorph beam based metamaterial can be tuned based on motion of its structural features, not simply its material composition. Additionally, if potentiometer-type performance is desired, arrays of beams of varying lengths could be employed. In this configuration, each beam would close at a varying temperature based on its length, instead of all closing at the same time as presented here. This would allow the metamaterial to provide for a wide range of temperature-selected resistances.

Following completion of the bimorph cantilever beam based design electrical resistance characterization, each of the six electrostatic actuated cantilever beam array based design’s electrical resistance was measured, and is presented in Figure 4.26.

In Figure 4.26, the electrical resistance of each electrostatic actuated cantilever beam array design is plotted. All six designs exhibited “off scale high” ($> 1 \text{ G}\Omega$) resistance when their arrays of beams were in the open position (not pulled-in). This high resistance is due to an approximately $1 \mu\text{m}$ “open circuit” at each of the beam tip to heat sink interfaces. As seen in Figure 4.26, the resistance across each design increased $\approx 2\text{-}11\%$ when heated from $25\text{-}135 \text{ }^\circ\text{C}$. This increase is expected as polysilicon’s resistivity increases approximately 24% when heated from $25\text{-}135 \text{ }^\circ\text{C}$, as determined using

Equation 2.15. The reason that the resistance of each sample increased only 2-11% over the same range is that the dominant factor in the samples resistance is the contact

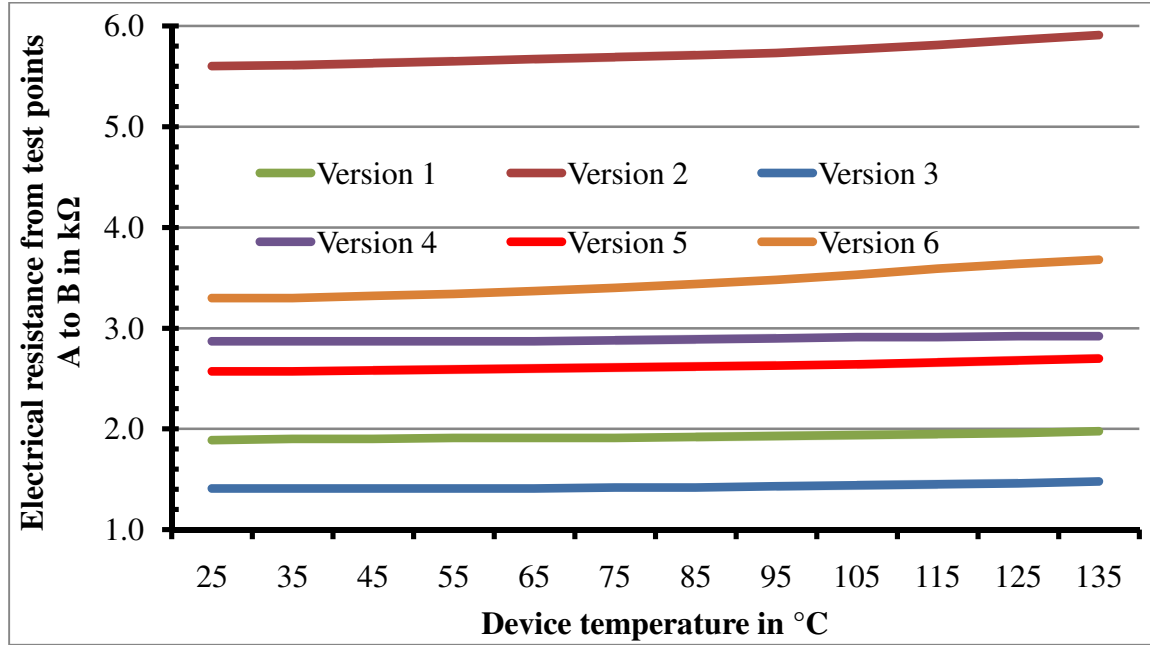


Figure 4.26: Electrical resistance of electrostatic actuated cantilever beam array metamaterials, from test points A to B (heater terminal pad to heat sink), with beams pulled-in or closed. Variations in resistance between versions is due to sheet resistance differences in beam material (Poly1 or Poly2), heater grid material (Poly1, Poly2, or Poly1 & 2 stacked), and heater grid type. Versions were described in Table 3.3. Electrical resistance increased \approx 2-11% when heated from 25-135 °C.

resistance at each of the 24 beam tips, not the polysilicon structural resistance. As expected, versions constructed of materials with greater sheet resistance generally exhibited higher resistance.

As was done with the bimorph beam based devices, the electrostatic actuated device resistance data was used to develop an analytical resistive model of the prototypes. This was accomplished to facilitate estimation of each major structural components contribution to the systems electrical resistance. The analytical model is shown in Figure 4.27. In the figure, the I/O of the system (Poly0 heat sink sheets), is shown as test

points B and C. The contact resistance at the beam tip to heat sink interface is variable, depending on whether the beams are open or pulled-in. It ranges from many $\text{G}\Omega$ (an open circuit) when open, to $\approx 14\text{-}28 \text{ k}\Omega$ when closed. Each beam's contact resistance is represented by the 24 resistors shaded in blue. Each of the 24 polysilicon cantilever beams is represented by the 24 resistors shaded in red in Figure 4.27. The resistance of each beam is dependent on the material used, and is $\approx 0.07 \text{ k}\Omega$ for Poly1 beams, and $\approx 0.13 \text{ k}\Omega$ for Poly2 beams. The polysilicon resistive heating element is represented by a single resistor in the middle, and is known to be $\approx 1.2 \text{ k}\Omega$ for layout version #1, $\approx 3.5 \text{ k}\Omega$ for version #2, $\approx 1.5 \text{ k}\Omega$ for versions #3 and #4, and $\approx 1.2 \text{ k}\Omega$ for versions #5 and #6. Lastly, the resistance of each Poly0 heat sink is accounted for by the resistor at the top and bottom of the figure. This resistor also accounts for the resistance occurring at the heat sink to I/O probe tip junction. Each of these two resistances has a measured value of $\approx 0.1 \text{ k}\Omega$.

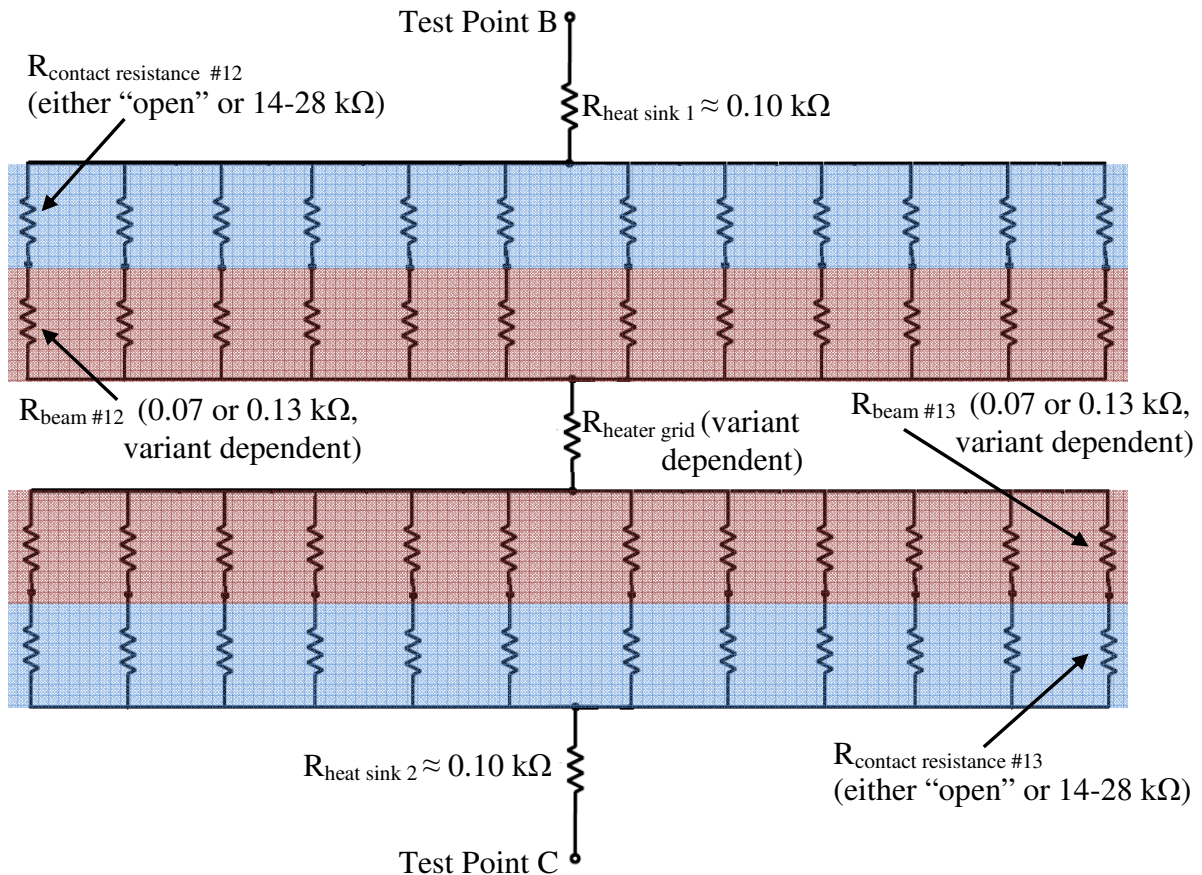


Figure 4.27: Electrostatic actuated cantilever beam array electrical resistance analytical model. The I/O of the system (Poly0 heat sink sheets), is shown as test points B and C. The contact resistance at the beam tip to heat sink interface is variable, depending on whether the beams are open or pulled-in closed. It ranges from many $\text{G}\Omega$ (an open circuit) when open to $\approx 14-28 \text{ k}\Omega$ when closed (version dependent). The 24 polysilicon cantilever beams are represented by the 24 resistors shaded in red. The resistance of each beam is material dependent, $\approx 0.07 \text{ k}\Omega$ for Poly1 beams, and $\approx 0.13 \text{ k}\Omega$ for Poly2 beams. The polysilicon resistive heating element is represented by a single resistor in the middle, and is known to be $\approx 1.2 \text{ k}\Omega$ for layout version #1, $\approx 3.5 \text{ k}\Omega$ for version #2, $\approx 1.5 \text{ k}\Omega$ for versions #3 and #4, and $\approx 1.2 \text{ k}\Omega$ for versions #5 and #6. Lastly, the resistance of each Poly0 heat sink is accounted for by the resistor at the top and bottom of the figure. This resistor also accounts for the resistance occurring at the heat sink to I/O probe tip junction.

Figure 4.28 illustrates how Figure 4.27 was reduced in order to solve for and estimate “ $R_{\text{contact resistance}}$ ” for each of the 24 beams. The two rows of 12 beams shown in

Figure 4.27 each reduce to approximately $\frac{1}{12} (R_{\text{contact resistance beam}} + R_{\text{beam}})$, which reduced the whole system to five resistances in series, as shown in Figure 4.28. Since $R_{\text{heat sink } 1}$, $R_{\text{heat sink } 2}$, R_{beam} , $R_{\text{heater grid}}$, and R_{B-C} are known values (measured or estimated using Ω/\square techniques), an approximation of $R_{\text{contact resistance}} \approx 13.9-28.1 \text{ k}\Omega$ was able to be made (variant dependent). The resistance for these six electrostatic actuated designs was very non-repeatable, with back to back measurements on the same device varying up to 40%. This large deviation is due to the inconsistent nature of contact resistance between the moving polysilicon beam tips and the Poly0 heat sink sheet. This contact resistance is

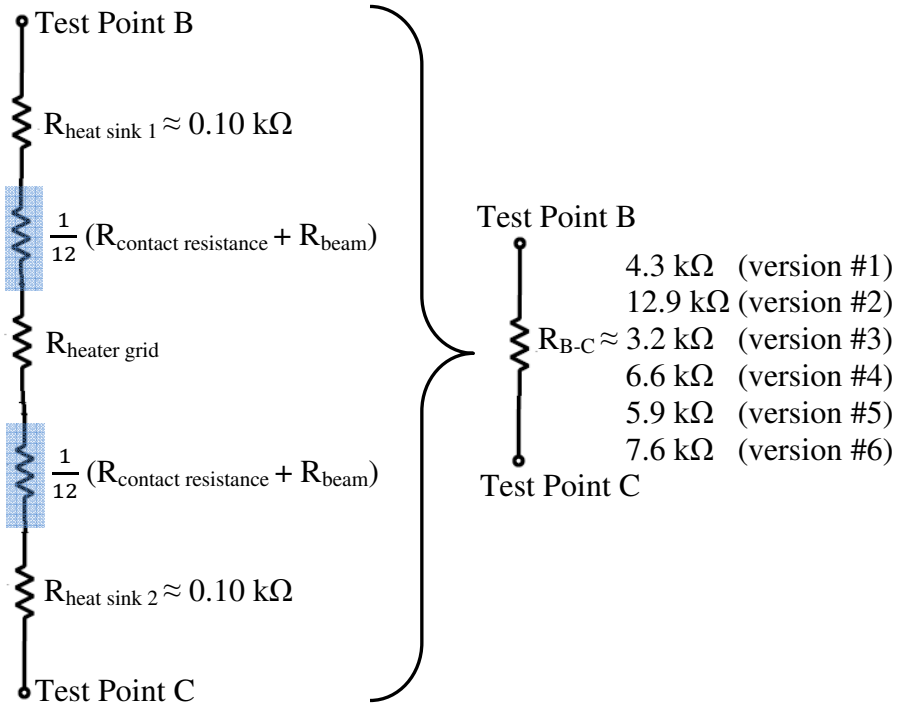


Figure 4.28: Electrostatic actuated cantilever beam array electrical resistance reduced analytical models. The two rows of 12 beams shown in Figure 4.27 each reduce to approximately $\frac{1}{12} (R_{\text{contact resistance beam}} + R_{\text{beam}})$. $R_{\text{heat sink } 1}$, $R_{\text{heat sink } 2}$, R_{beam} , $R_{\text{heater grid}}$, and R_{B-C} are known values (measured or estimated using Ω/\square techniques), allowing for an approximation of $R_{\text{contact resistance}} \approx 14-28 \text{ k}\Omega$ to be made. Test points B and C are considered the input and output terminals in this representation.

likely influenced by mild photoresist contamination and the growth of native oxides on the polysilicon tips and heat sink. During extended device operation the contact resistance should reach a more repeatable, steady state value. All resistances presented are averages of three measurements, and represent room temperature values.

This test event quantified the pull-in and temperature dependent electrical resistance of these six electrostatic actuated cantilever beam array based thermal metamaterials. The resistance of the electrostatic actuated beam arrays is effectively an “on/off switch”, where “off” is $> 1 \text{ G}\Omega$ and on is between $3\text{-}13 \text{ k}\Omega$, depending on which materials were used in the design.

The beam tip layout chosen for the electrostatic actuated versions provided a lower contact resistance than that of the bimorph beam versions. The bimorph beams had an average beam tip contact resistance of $36.6 \text{ k}\Omega$. This is 1.3-2.6 times greater than the electrostatic actuated versions average beam tip contact resistance of $13.9\text{-}28.1 \text{ k}\Omega$. Ultimately, this lower contact resistance allowed the six electrostatic actuated versions to provide a reduced resistance when considered from heat sink to heat sink. The beam tip layouts for the four bimorph cantilever beam designs and for the six electrostatic actuated designs are compared in Figure 4.29. The test results presented here suggest that, in this application, a tip design with less contact surface area and greater force per unit area provides increased electrical conductivity when compared to a larger contact area with less force per unit area applied. These results apply only to this specific contact orientation and application, as in general a larger contact area provides a lower contact resistance.

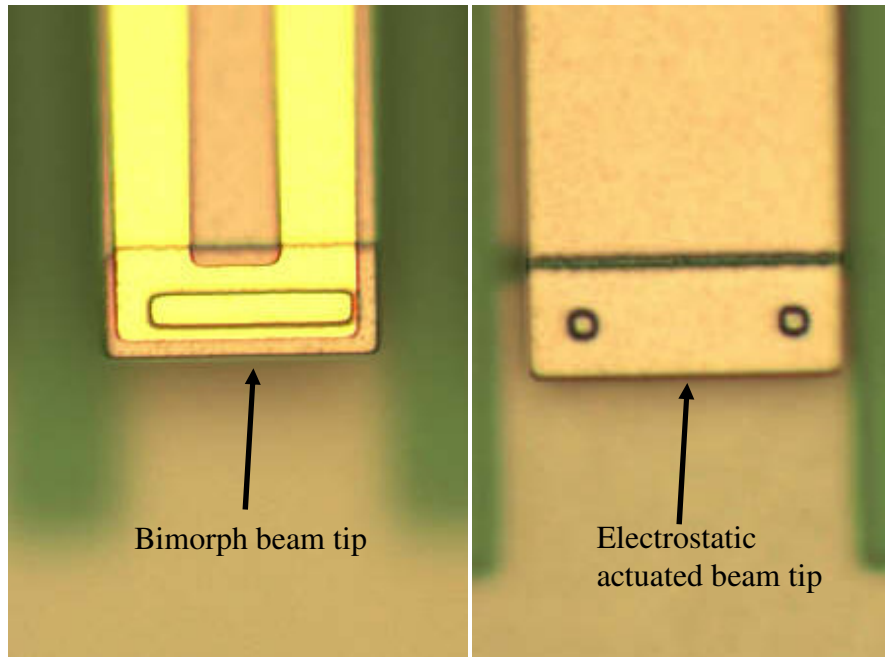


Figure 4.29: Comparison of bimorph cantilever beam tip to electrostatic actuated beam tip. The contact resistance of the electrostatic actuated beam tips was 23-62% lower than that of the bimorph beam tips. Test results suggest that, in this specific application, a tip design with less contact surface area and greater force per unit area provides increased conductivity when compared to a larger contact area with less force per unit area applied.

This data and analysis showed that the electrical resistivity and conductivity of the electrostatic actuated beam based metamaterial can be switched based on actuation of its structural features, not simply its material composition. As was discussed with the bimorph beam based designs, if potentiometer-type performance is desired, the electrostatic pull-in electrodes of each beam could be designed to be individually actuated instead of actuating in groups of 12. In this configuration, each beam would close independently as commanded by control logic, instead of all closing at the same time as presented here. This would allow the metamaterial to provide for a wide range of selected resistances.

4.3 CNT-Based Braided Rope Testing and Results

4.3.1 Overview

The objective of this evaluation was to characterize the electrical conductivity and heat transfer properties of each CNT rope variant. To accomplish this objective, a series of test events were conducted. First, the diameter of each variant was accurately measured to support calculations of resistivity and conductivity. Next, the electrical resistance versus temperature of each variant was measured, also to support resistivity and conductivity calculations. Lastly, the heat transfer characteristics of each variant were determined using a thermal imaging microscope system and temperature mapping. Characterization of these electrical and thermal properties is a prerequisite for CNT rope's potential use as a structural element within a future thermal metamaterial design.

4.3.2 CNT rope test event #1: diameter measurement

4.3.2.1 Diameter measurement test description

The physical diameter of each sample was measured to support later calculations which required an accurate cross-sectional area (CSA). This was performed by two methods, first using an interferometer, and secondly with a profilometer. Figure 4.30 (a) shows a close-up view of the Zygo interferometer stage during data collection. As shown in the figure, each CNT rope sample was placed on top of a glass slide, and then pulled tightly between two additional glass slides in order to keep the CNT rope flat and straight. Five measurements were taken at various points along each rope. These were then averaged and recorded as the sample's average diameter.

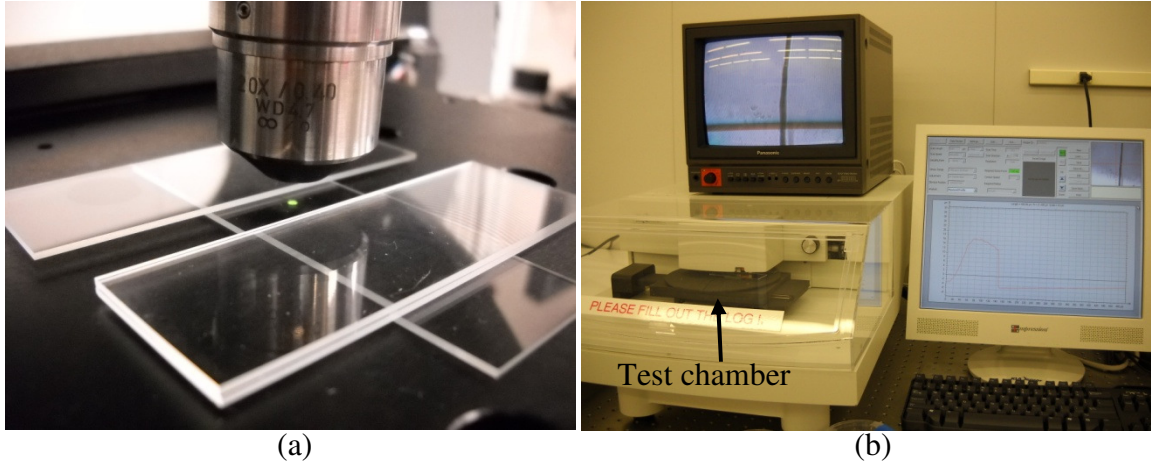


Figure 4.30: CNT rope diameter measurement using the Zygo interferometer (a), and a profilometer (b). In (a), the CNT rope is placed onto the bottom glass slide, then held straight and flat using the two top glass slides. In (b), the same three-slide setup is used, and is placed into the test chamber.

Figure 4.30 (b) shows the profilometer system during data collection. As was done with the interferometer, each CNT rope sample was placed on top of a glass slide, and then pulled tightly between two additional glass slides. Five measurements were taken at various points along each rope. These were then averaged and recorded as the sample's average diameter.

4.3.2.2 Diameter measurement results

As detailed in Section 4.3.2.1, the objective of this evaluation was to accurately measure the physical diameter of the samples in support of cross-sectional area calculations. While it was planned to be executed by two methods (interferometer and profilometer), the data taken using the interferometer was of such exceptionally poor quality and non-repeatability that it was rejected. The profilometer data had a much smaller standard deviation and was very repeatable.

Results obtained using the profilometer system are summarized in Table 4.4. The diameters listed are averages of five measurements. Note the 1X4 PVA coated sample

diameter was not measured because it is a braid of four PVA coated strands and thereby has an irregular, non-circular cross-section. Its CSA is simply estimated as four times that of the single PVA coated strand.

Table 4.4: CNT rope average diameter and calculated cross-sectional area.

Sample	Average diameter (μm)	Cross-sectional area (μm^2)
1 strand uncoated	24.6	475
1 strand PVA coated	20.9	343
1X4 strands PVA coated	-	1372*

* Cross-sectional area for the “1X4 strands PVA coated” sample was not measured, but calculated as four times that of the “1 strand PVA coated” sample. As discussed in Section 4.3.3.2, the actual value of the “1X4 strands PVA coated” sample is likely closer to four times that of the “1 strand uncoated” sample, or $1900 \mu\text{m}^2$.

The diameter of the PVA coated strand was, counter-intuitively, over 15% less than that of the uncoated strand. During previous optical inspection it was noted that the coated strand appeared thinner – this data quantified that observation. Possible reasons for this include the CNTs within the strand may bond more closely together (more densely packed) as a consequence of the PVA-coating process. This could be the case if the PVA-coating is applied at an elevated temperature and then contacts inward laterally at cooler temperatures. Also, this diameter delta could be within the normal variation of the rope braiding/fabrication process. As only one copy of each variant was provided for this characterization, no statistically relevant explanation for this diameter variation can be determined from this data set.

4.3.3 CNT rope test event #2: electrical conductivity characterization

4.3.3.1 Electrical conductivity characterization test description

Upon completion of the diameter measurements; the electrical resistance of each variant was measured, as shown in Figure 4.31. The temperature of the sample was

ramped (using a DataPlate digital hot plate) from 22-110 °C over a 25 minute period, with resistance of the variant recorded every 4 °C. The sample length between the meter leads was accurately measured, using glass slides and a ruler, to facilitate a data product of resistance in Ω/cm verses sample temperature. Then, the relationship:

$$\rho = R \cdot \frac{A}{l} \quad (4.1)$$

where ρ is resistivity in $\Omega\text{-cm}$, R is resistance in Ω , A is cross-sectional area in cm^2 , and l is sample length in cm, was used to determine resistivity and its inverse, conductivity, verses temperature. The resistance of the test equipment leads of 0.15 Ω was subtracted from all recorded measurements.

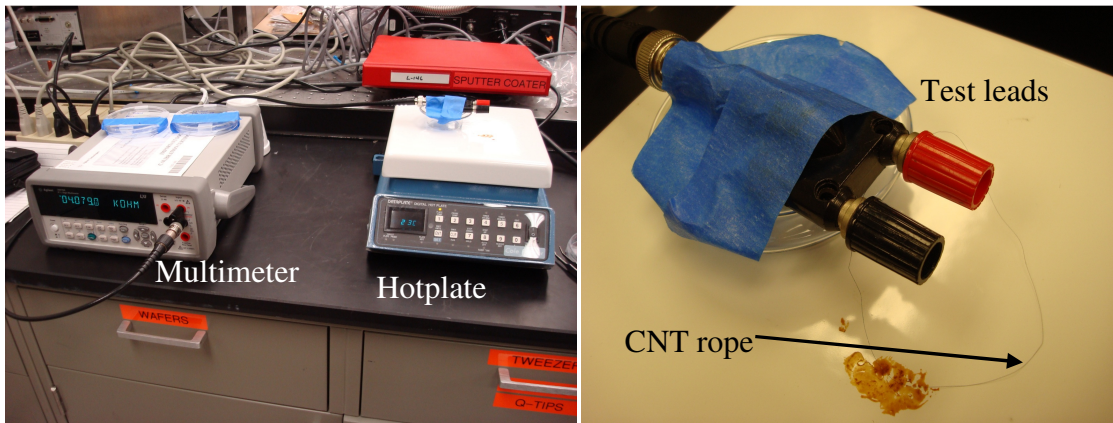


Figure 4.31: Electrical resistivity verses temperature test setup. During data collection the CNT rope sample and test leads were covered by a small cardboard box (not shown) to minimize thermal losses due to convection.

4.3.3.2 Electrical conductivity characterization test results

As detailed in Section 4.3.3.1, the objective of this evaluation was to characterize the electrical conductivity of the samples. First, the electrical resistance of each sample verses temperature was measured, and is shown in Table 4.5. For accurate Ω/cm

calculations, the sample lengths were measured to be 5.4 cm, 5.1 cm, and 11.1 cm for the single uncoated strand, PVA-coated single strand, and 1X4 PVA-coated rope, respectively.

Table 4.5: Electrical resistance of CNT ropes verses temperature.

TEMP (°C)	1 Strand Uncoated		1 Strand PVA Coated		1X4 Strands PVA Coated	
	Resistance (kΩ)	Ω/cm	Resistance (kΩ)	Ω/cm	Resistance (kΩ)	Ω/cm
22	5.47	1013.0	4.82	945.1	3.32	299.1
26	5.46	1011.1	4.82	945.1	3.32	299.1
30	5.46	1011.1	4.82	945.1	3.31	298.2
34	5.46	1011.1	4.81	943.1	3.31	298.2
38	5.45	1009.3	4.81	943.1	3.30	297.3
42	5.45	1009.3	4.80	941.2	3.30	297.3
46	5.44	1007.4	4.80	941.2	3.30	297.3
50	5.44	1007.4	4.79	939.2	3.29	296.4
54	5.43	1005.6	4.78	937.3	3.29	296.4
58	5.42	1003.7	4.78	937.3	3.28	295.5
62	5.42	1003.7	4.77	935.3	3.28	295.5
66	5.41	1001.9	4.76	933.3	3.27	294.6
70	5.40	1000.0	4.75	931.4	3.27	294.6
74	5.40	1000.0	4.74	929.4	3.26	293.7
78	5.39	998.1	4.73	927.5	3.26	293.7
82	5.38	996.3	4.73	927.5	3.25	292.8
86	5.38	996.3	4.72	925.5	3.24	291.9
90	5.37	994.4	4.71	923.5	3.24	291.9
94	5.36	992.6	4.71	923.5	3.23	291.0
98	5.35	990.7	4.70	921.6	3.22	290.1
102	5.34	988.9	4.70	921.6	3.22	290.1
106	5.33	987.0	4.69	919.6	3.21	289.2
110	5.32	985.2	4.68	917.6	3.20	288.3

Figure 4.32 is a plot of each samples resistance in Ω/cm verses temperature. As expected, the sample with the greatest CSA presented the least resistance to current flow. The resistance of the PVA coated four-strand braided SWNT rope was consistently less

than 1/3 that of the other two samples. The resistance of the single-strand variants was very similar, with the PVA coated sample having a resistance about 6% less than the uncoated sample. A possible explanation for this is the PVA coating reduces the amount of fraying, which was prominent on the uncoated sample (as was shown in Figure 3.26), resulting in slightly better conductivity.

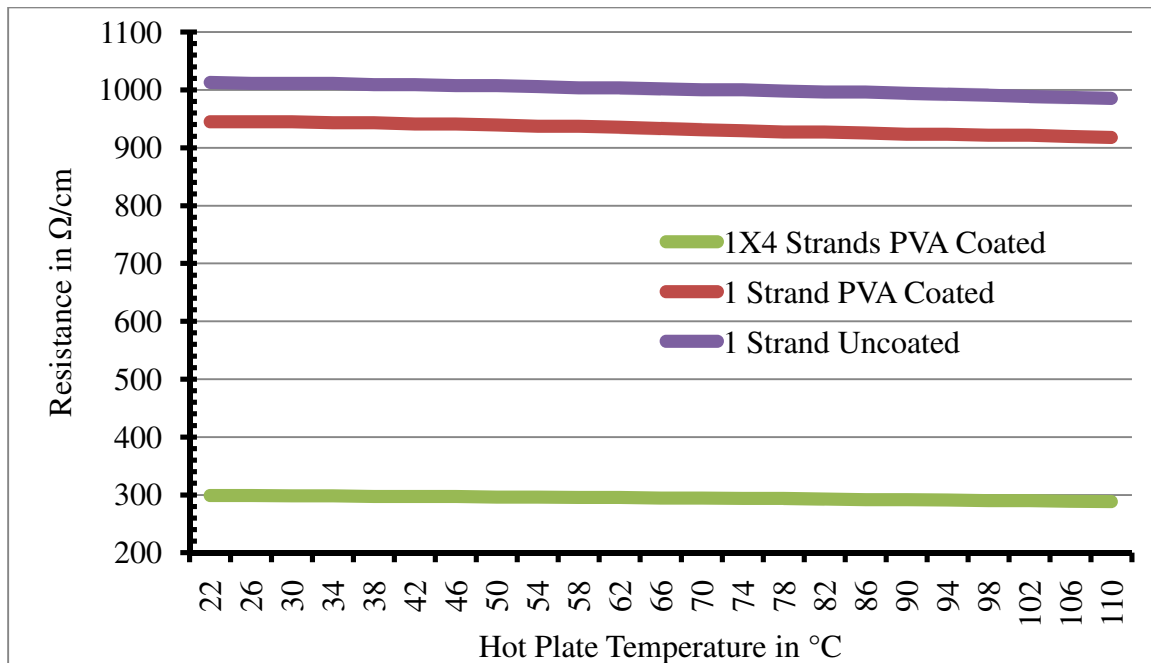


Figure 4.32: CNT rope resistance (Ω/cm) verses temperature. The resistance of each sample decreased approximately 3 % when heated from 22-110 $^{\circ}\text{C}$.

Using the cross-sectional area and Ω/cm data presented in Table 4.4 and Table 4.5, resistivity (ρ) and its inverse, conductivity (σ) verses temperature were calculated for each sample using Equation 4.1. Table 4.6 lists each variants ρ and σ verses temperature. The resistivity and conductivity values for the CNT ropes are similar to those of a heavily doped semiconductor material. Resistivity and conductivity verses temperature is plotted in Figure 4.33 and Figure 4.34, respectively.

Table 4.6: Electrical resistivity and conductivity of CNT ropes verses temperature.

TEMP (°C)	1 Strand Uncoated		1 Strand PVA Coated		1X4 Strands PVA Coated	
	Resistivity (Ω-cm)	Conductivity (S/cm)	Resistivity (Ω-cm)	Conductivity (S/cm)	Resistivity (Ω-cm)	Conductivity (S/cm)
22	0.0048116	207.83	0.0032417	308.48	0.0041036	243.69
26	0.0048028	208.21	0.0032417	308.48	0.0041036	243.69
30	0.0048028	208.21	0.0032417	308.48	0.0040913	244.42
34	0.0048028	208.21	0.0032350	309.12	0.0040913	244.42
38	0.0047940	208.59	0.0032350	309.12	0.0040789	245.16
42	0.0047940	208.59	0.0032282	309.77	0.0040789	245.16
46	0.0047852	208.98	0.0032282	309.77	0.0040789	245.16
50	0.0047852	208.98	0.0032215	310.41	0.0040666	245.91
54	0.0047764	209.36	0.0032148	311.06	0.0040666	245.91
58	0.0047676	209.75	0.0032148	311.06	0.0040542	246.66
62	0.0047676	209.75	0.0032081	311.71	0.0040542	246.66
66	0.0047588	210.14	0.0032013	312.37	0.0040418	247.41
70	0.0047500	210.53	0.0031946	313.03	0.0040418	247.41
74	0.0047500	210.53	0.0031879	313.69	0.0040295	248.17
78	0.0047412	210.92	0.0031812	314.35	0.0040295	248.17
82	0.0047324	211.31	0.0031812	314.35	0.0040171	248.93
86	0.0047324	211.31	0.0031744	315.02	0.0040048	249.70
90	0.0047236	211.70	0.0031677	315.69	0.0040048	249.70
94	0.0047148	212.10	0.0031677	315.69	0.0039924	250.48
98	0.0047060	212.49	0.0031610	316.36	0.0039800	251.25
102	0.0046972	212.89	0.0031610	316.36	0.0039800	251.25
106	0.0046884	213.29	0.0031543	317.03	0.0039677	252.04
110	0.0046796	213.69	0.0031475	317.71	0.0039553	252.82

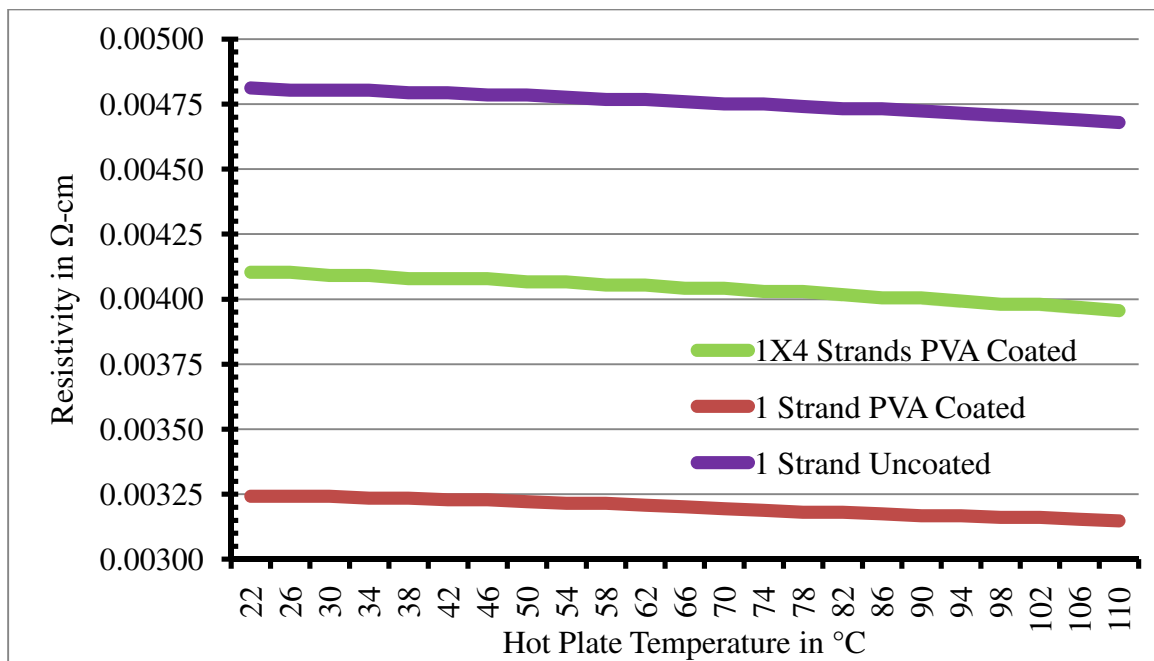


Figure 4.33: CNT rope resistivity ($\Omega\text{-cm}$) verses temperature. The resistivity of each sample decreased approximately 3% when heated from 22-110 $^{\circ}\text{C}$. The resistivity of the CNT ropes is similar to that of a heavily doped semiconductor.

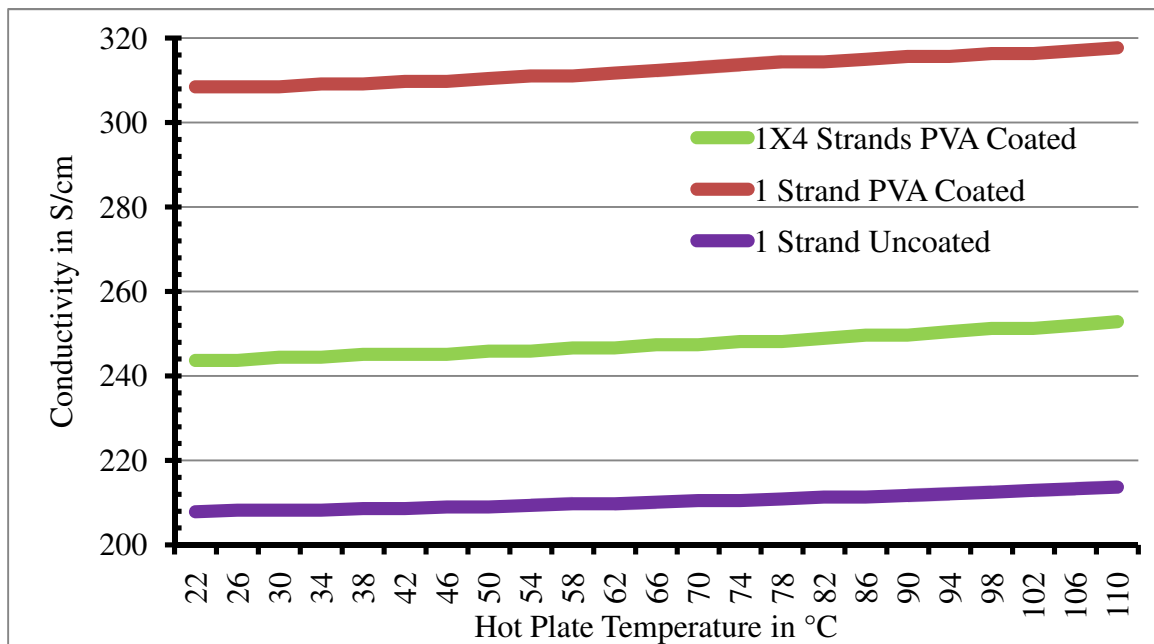


Figure 4.34: CNT rope electrical conductivity (S/cm) verses temperature. The conductivity increased approximately 3% when heated from 22-110 $^{\circ}\text{C}$. The conductivity of the CNT ropes is similar to that of a heavily doped semiconductor.

In theory, the resistivity and conductivity of the “1 strand PVA coated” and “1X4 strands PVA coated” variants should be approximately equal. This testing showed the single strand of PVA coated rope has 27% greater conductivity (and likewise 27% lower resistivity) than its four strands braided counterpart. The most likely reason for this performance discrepancy is that the diameter of each of the four PVA coated strands in the braided rope is greater than the diameter of the single PVA coated strand. This would result in the 1X4 braided sample having a higher total CSA, and thereby a greater ρ and a lower σ . Further supporting this explanation is that the single PVA coated strand sample had a smaller diameter and CSA than the uncoated strand, as was presented in Table 4.4. In fact, the CSA of the single PVA coated sample was, nearly exactly, 27% less than that of the uncoated sample. Therefore, it is likely that the diameter, and thereby the CSA, of the single PVA coated sample is less than that of each of the four PVA coated strands in the 1X4 braided rope. The diameter and CSA of each of these four PVA coated strands in the braided rope is most likely very close to that of the single uncoated strand. This apparent inconsistency in sample-to-sample CNT rope diameter illustrates the importance of measuring the diameter in any application that requires a specific ρ and σ .

4.3.4 CNT rope test event #3: thermal imaging scope temperature mapping

4.3.4.1 Thermal imaging microscope temperature mapping test description

Following the electrical conductivity testing, characterization of heat transfer throughout the samples was conducted. The QFI thermal imaging microscope system, used to perform testing on the thermal metamaterial prototypes, was again used to perform this characterization. The test setup is shown in Figure 4.35.

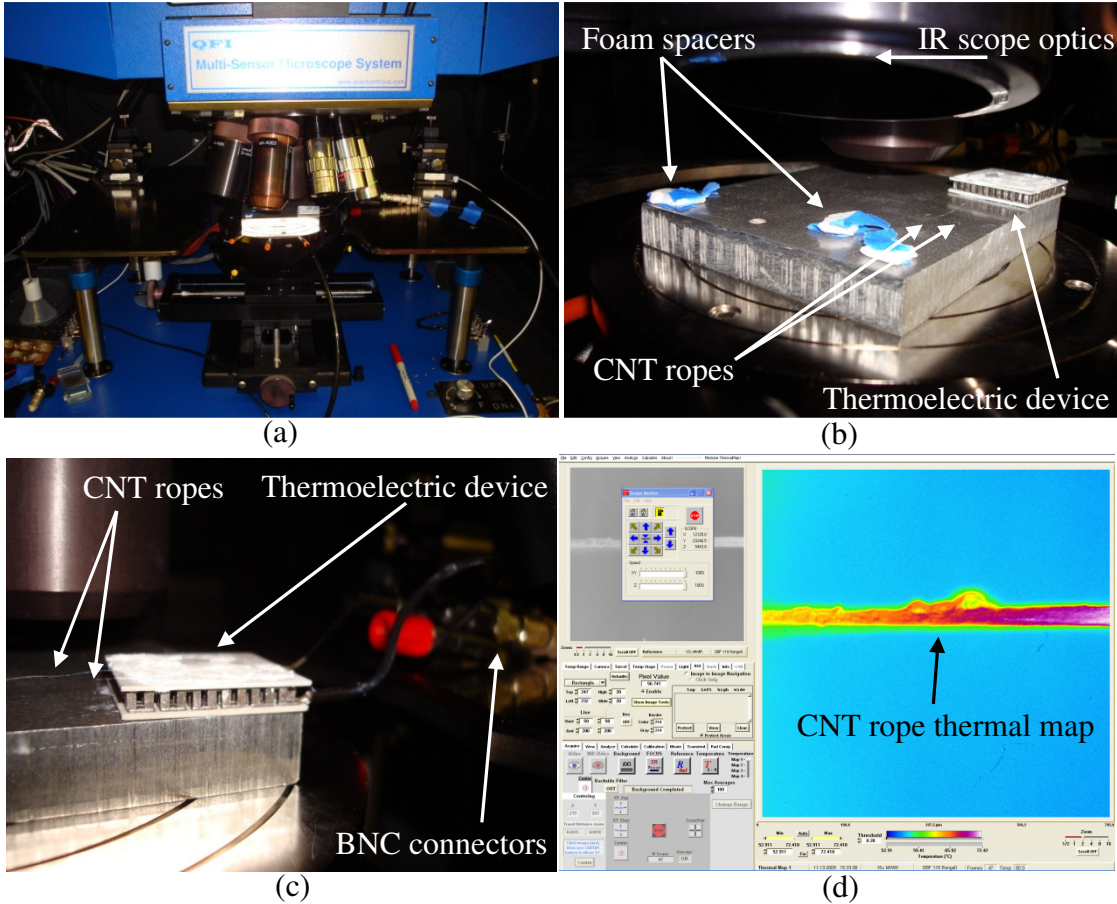


Figure 4.35: QFI thermal microscope system, CNT rope test setup: (a) test chamber, (b) close-up of test stage and unit under test, (c) thermoelectric device, and (d) operator view during data collection.

In Figure 4.35 (b), the test article is shown mounted atop an aluminum block on the QFI stage. In one corner of the block, a thermoelectric heater/cooler was mounted to the block with a thermal interface material conductive paste. In the other corners, Styrofoam spacers, 3 mm thick, were attached to the aluminum block using tape. These spacers are used to keep the test article level in the Z-axis, which facilitates more accurate focusing of the QFI imager. Also, they prevent direct contact conduction between the test article and the aluminum block. As shown in Figure 4.35 (c), the test articles are attached to the top of the thermoelectric device (TED) via thermal paste. The TED was used to provide

a consistent and repeatable heat or cooling source. With a stage temperature of 50 °C, the TED was capable of reaching a selected steady state temperature of between 14 °C and 145 °C within 45 seconds. Importantly, the selected temperature was repeatable to within 0.25 °C for a given input voltage. Due to the PVA beginning to decompose at temperatures above 180 °C, testing was not conducted at greater than 120 °C. This insured the PVA coating would not be degraded, which could skew test results. Figure 4.35 (c) shows two of the CNT ropes coming off the left side of the TED, suspended 3 mm above the aluminum block, running parallel about 3 mm apart from each other in the X-Y plane. This figure also shows the TED wiring going off the right hand side into a BNC connector, which is connected to a DC power supply.

For each of the three CNT rope samples, rope temperature verses distance away from the TED was measured. An example of this data collection is shown in Figure 4.35 (d). This data quantified how well each of the CNT braided rope samples could conduct heat along its length, and how quickly the heat would be “lost” to the surrounding air through convection and radiation.

4.3.4.2 Thermal imaging microscope temperature mapping test results

As detailed in Section 4.3.4.1, the test objective was to quantify how well each of the CNT braided rope samples could conduct heat along its length, and how quickly the heat would be “lost” to the surrounding air through convection and radiation. CNT rope temperature verses distance away from the TED was measured and mapped. Much of the data collection process was recorded on video/audio and is available upon request.

Figure 4.36 illustrates, from the thermal imaging microscope operator’s perspective, how the data collection took place. With the sample and background at a temperature of

50 °C, a reference sample is taken (Figure 4.36 (d)). Note the sample is slightly cooler

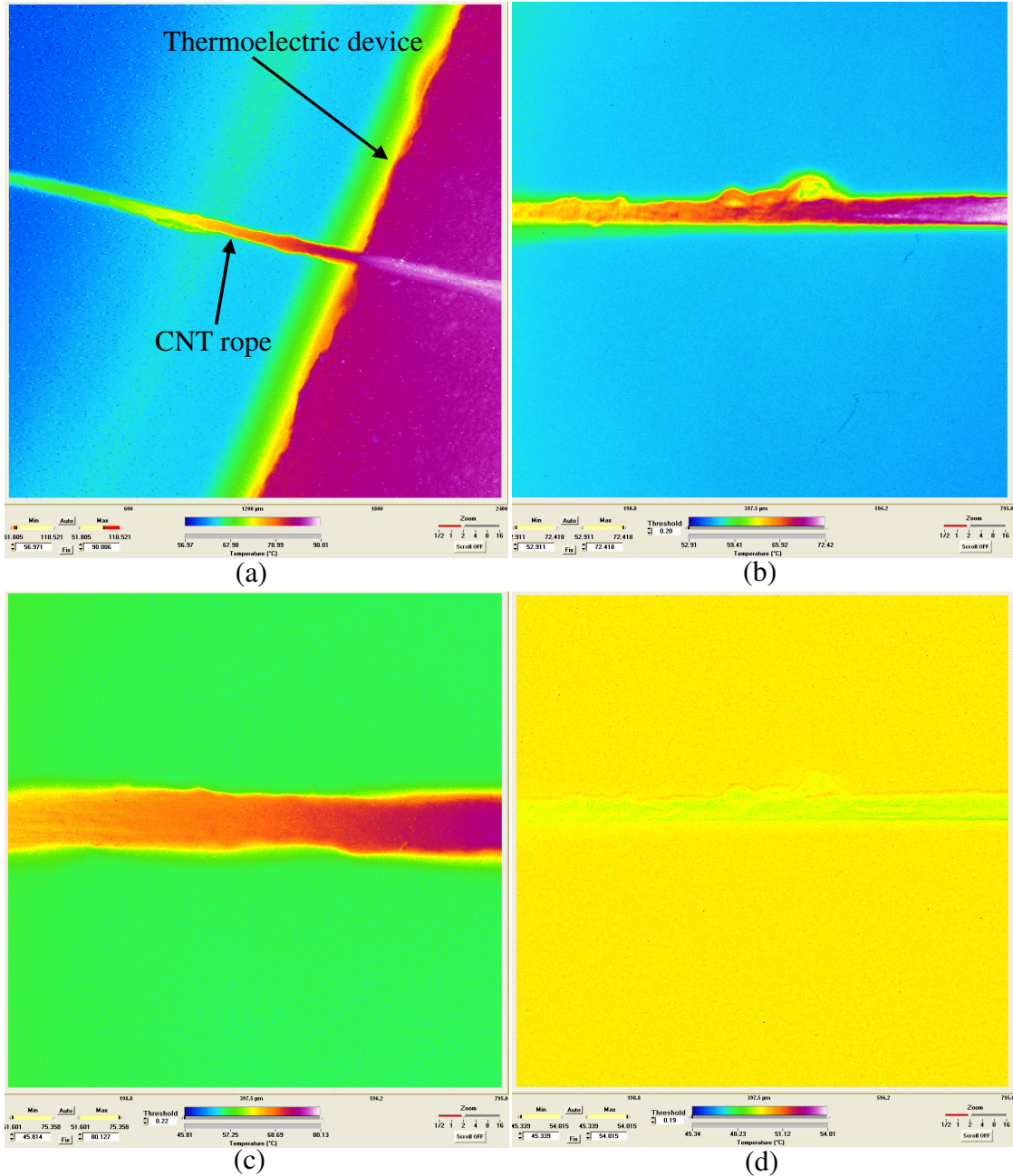


Figure 4.36: CNT rope thermal imaging data collection examples. In (a), a CNT rope sample is shown coming off of the thermoelectric device. In (b) and (c), examples of the operators view during data collection are shown. In (d), the CNT rope's thermal signature when the thermoelectric is unpowered is shown. Note that when unpowered the sample is slightly cooler than the background stage temperature.

(less than 1 °C cooler) than the background due to it being elevated 3 mm above the heated stage. Next, a DC potential was applied to the TED, causing it to rapidly heat up to ≈ 89 °C (Figure 4.36 (a)). Once the TED had reached its steady state temperature, 30 frames of temperature data were averaged (measured at 16 frames per second). The resulting image is as shown in Figure 4.36 (b) and (c). Using the thermal imaging system software, the averaged sample temperature versus distance from the TED was mapped, as listed in Table 4.7 and illustrated in Figure 4.37.

Table 4.7: CNT rope thermal imaging temperature mapping.

Distance from TED	Background Temperature (°C)	<u>1 Strand Uncoated Temperature (°C)</u>	<u>1 Strand PVA Coated Temperature (°C)</u>	<u>1X4 Strands PVA Coated Temperature (°C)</u>
At threshold	89	90	90	90
0.2 mm	72	85	89	88
0.4 mm	68	81	88	85
0.6 mm	65	77	87	84
0.8 mm	61	74	85	80
1.0 mm	59	71	84	78
1.2 mm	58	70	83	76
1.4 mm	57	67	78	74
1.6 mm	57	65	74	72
1.8 mm	56	65	71	71
2.0 mm	56	65	68	68
2.2 mm	56	64	66	67
2.4 mm	56	63	64	66
2.6 mm	56	62	63	66
2.8 mm	56	62	62	65
3.0 mm	56	60	60	64
3.2 mm	56	59	58	62
3.4 mm	55	58	57	61
3.6 mm	55	56	56	60
3.8 mm	55	54	55	58
scale jump	-	-	-	-
10 mm	53	51	52	53
15 mm	51	49	50	50
20 mm	50	48	49	49
30 mm	50	48	48	49
40 mm	50	48	48	49

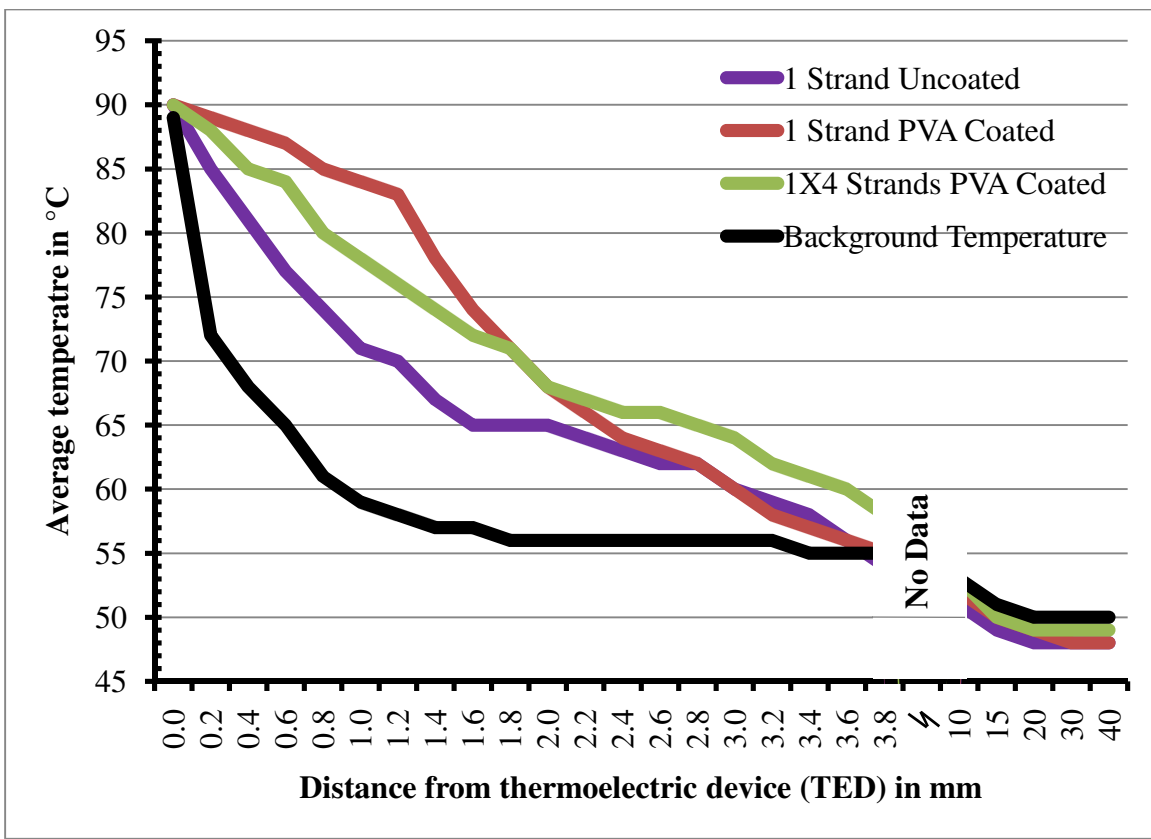


Figure 4.37: CNT rope average temperature verses distance from TED. Within 10 mm from the edge of the TED all three samples were at or below the background temperature. The uncoated CNT rope exhibited the lowest heat retention, approaching the background temperature more rapidly than the PVA coated samples.

As shown in Table 4.7 and Figure 4.37, the CNT rope samples dropped to approximately the background temperature within 4 mm of coming off the TED (dropped 35 °C in \approx 4 mm). This rapid loss of heat energy is likely due to the CNT ropes having very little mass and nearly no capacity to retain the heat applied by the TED. In fact, within 1 cm of coming off the TED, all three samples were at or below the stage temperature. Importantly, this test was conducted in a laboratory environment at 22 °C and approximately standard pressure, where these low mass and large surface area samples could rapidly lose heat through convection into the free air surrounding them. In

a low pressure environment such as spacecraft applications, these CNT ropes would likely have significant ballistic conduction along their length. However, in this standard pressure testing, the convective losses (radially) over the rope's large surface areas were the dominant heat transfer mechanism.

4.4 Summary

4.4.1 Thermal metamaterial device characterization summary

Each of the thermal metamaterial proof-of-concept devices was evaluated for its structural response, electrical conductivity/resistivity, and thermal heat transfer and management capabilities. This data quantified the extent to which actuation of the metamaterial structural elements could impact the system's overall heat transfer capabilities and electrical conductivity. The devices can be interfaced with such that they can provide a temperature dependent or user commanded σ and κ within a certain operational range.

4.4.2 CNT braided rope device characterization summary

The diameter, electrical resistivity and conductivity, and heat transfer characteristics of the three CNT braided rope prototypes was determined. These CNT ropes provide an uncommon combination of exceptional tensile strength, electrical conductivity that rivals a heavily doped semiconductor, and heat transfer capabilities. They provide these characteristics in a durable and very flexible form factor. These performance attributes should prove useful to a future thermal metamaterial design.

Conclusion and Recommendations

5.1 Conclusion

5.1.1 Thermal metamaterial design conclusion

Thermal metamaterials are an emerging technology, and are just now beginning to be acknowledged and developed by the microelectronics and material sciences community. This thesis effort analyzed the current state of thermal metamaterial research, examined the physics and theory of heat transfer and electrical conductivity in thin film microelectronic designs, and then developed, modeled, fabricated, and characterized a series of proof-of-concept thermal metamaterial devices. Modeling and testing of these prototypes showed that the σ and κ of the devices can be switched within a certain operational range, and that this switching is a function of actuation of the metamaterial's structural elements, not just its chemical composition.

5.1.2 CNT braided rope prototypes conclusion

In addition to the thermal metamaterial related accomplishments just discussed, this thesis presented the physics and fundamental principles of carbon nanotubes. This background work supported later detailed description of a series of prototype CNT braided ropes. The diameter, electrical resistivity and conductivity, and heat transfer characteristics of these CNT braided rope prototypes was determined. These unique prototypes exhibited performance attributes that should prove useful to future thermal metamaterial designs. This includes exceptional tensile strength for their weight and size, electrical conductivity that rivals a heavily doped semiconductor, and heat transfer capabilities. Furthermore, they provide these in a durable and very flexible form factor.

5.2 Recommendations

5.2.1 Thermal metamaterial recommendations

The ultimate goal of a thermal metamaterial design is to control and exploit the thermal properties of a thin film or material in a way that is not possible using existing materials and chemical compounds. It is executed on a scale that, until recently, would have precluded a mechanical structure solution.

While the ten proof-of-concept designs presented in this thesis were able to provide a switchable σ and κ over a certain range, they did not decouple these two material properties. A thermal metamaterial design that provided for an independently selectable σ and κ would represent a vast improvement in capability over the designs shown here.

A significant limitation of the designs presented is that the silicon nitride layer used to provide electrical isolation between the polysilicon structural elements and substrate was not thick enough to be an effective thermal insulator. This resulted in much of the total power input to the system to be conducted into the substrate through the nitride layer. If a modified version of these prototypes was to be designed, heat transfer performance in the X-Y plane could be significantly enhanced by depositing a thicker layer (3-4 μm or thicker) of a thermal insulator (such as SiN or SiO_2) down before processing the designs structural elements. This of course would preclude use of the PolyMUMPS fabrication process used here, but would yield better heat transfer capabilities.

An additional limitation of the thermal metamaterials designed in this effort was that there was no provisioning made for the devices to be hermetically sealed/packaged. This severely limited the serviceable lifespan of each device, because oxidation occurred due

to exposure to the environment. Just a very small amount of oxidation or contamination on the cantilever beam tips would significantly impact the σ and κ of the operating system. This would not have occurred in a properly sealed package. Any future updates to this design should provision up front for appropriate device packaging.

5.2.2 CNT braided rope prototype recommendations

The CNT braided ropes offer an attractive option for designs which are required to operate in extremely high shock, vibration, or humidity environments where more fragile silicon based structural elements would be vulnerable to breaking or oxidation damage. The most significant limiting factor in characterizing the CNT ropes was that a hermetically sealed test fixture was not developed to support the testing events performed here. Because the CNT ropes have very little mass and exceptionally low heat capacity, executing thermal mapping in a standard lab environment resulted in rapid heat loss due to thermal convection into the surrounding moving air. Had the ropes been hermetically packaged, an accurate determination of their κ could have been made. Any future testing of these unique ropes should provision for design and fabrication of a sealed test fixture.

5.3 Contributions and Applications

This thesis represents AFITs first attempt at defining, designing, producing, and characterizing a thermal metamaterial. Specific contributions made by this effort include:

- Established the first published definition of thermal metamaterials
- First published effort in which thermally-tuned metamaterials were designed, fabricated, and characterized

- Demonstrated that the σ and κ of the thermal metamaterials can be switched or tuned within a certain operational range
- Characterized the electrical conductivity and heat transfer performance of a series of CNT yarn prototypes

Potential applications of these ideas include use as a back-end processed “thin film” with tunable electrical conductivity. Currently employed thin films, such as a sputtered-on conductive metals or an insulative epilayer of silicon dioxide, could be augmented or potentially replaced in some situations by thin layers of thermal metamaterial MEMS structures. The advantage of the thermal metamaterial structure is that it possesses switchable or tunable properties, comparing favorably in some applications to the fixed properties of a standard thin film.

A second potential application is as part of a micro-satellites thermal management system. In this case, during times of extreme cold it is often beneficial to have reduced thermal conductivity in the cold plate near certain vehicle subsystems. This reduced conductivity could be provided by a switchable thermal metamaterial design. During periods of elevated temperature or increased heat generation by the subsystem under thermal management, the thermal metamaterial could switch to a high conductivity configuration. This would then allow for increased heat transfer from the space vehicles subsystem or component, into the cold plate, and finally conducted out into a radiative heat exchanger.

A final potential application is for use as part of a thermal obfuscation scheme. Some techniques for compromising cryptographic equipment’s traffic, algorithm, and keying material involve thermal mapping of the microelectronic circuit or device processing the

data. As seen in the thermal mapping results, the bimorph cantilever beam arrays possess a “thermal spoofing” characteristic against MWIR imaging under certain operational conditions. By properly employing arrays of these beams as a back-end process above certain parts of the cryptographic circuitry – the circuit’s temperature could appear skewed under infrared microscope inspection by an adversary.

Although not an AFIT design, the characterization efforts of the CNT braided rope prototypes could potentially be utilized by AFIT or another institution to develop a CNT rope based thermal metamaterial. This applied nanotechnology possesses several exceptional qualities - as was detailed in this thesis.

Appendix A. Prototype Devices Detailed Images

This appendix provides larger, more detailed pictures of the ten fabricated thermal metamaterial devices and the three CNT rope samples.

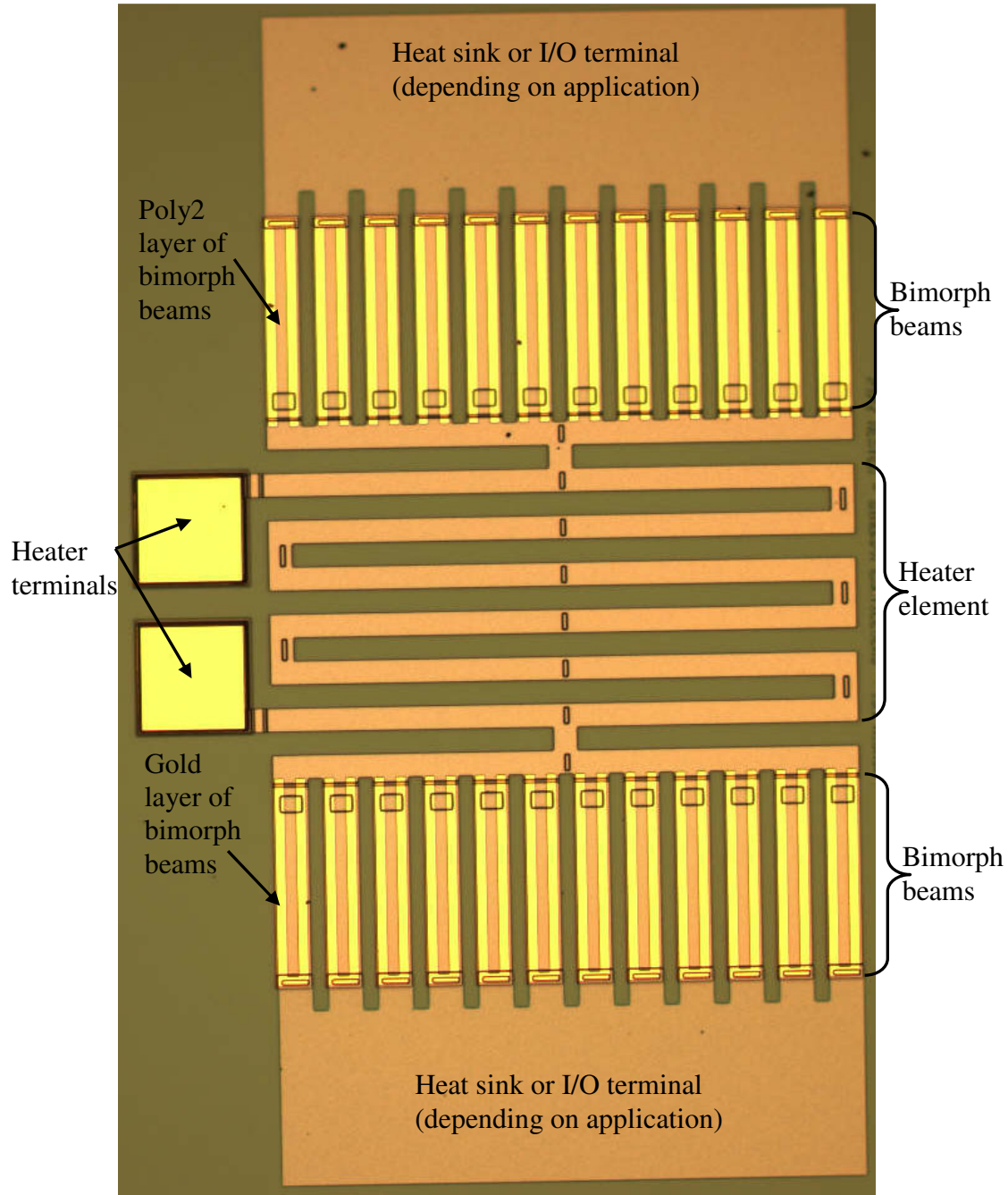


Figure A.1: 150 μm version of bimorph cantilever beam based thermal metamaterial prototype after release.

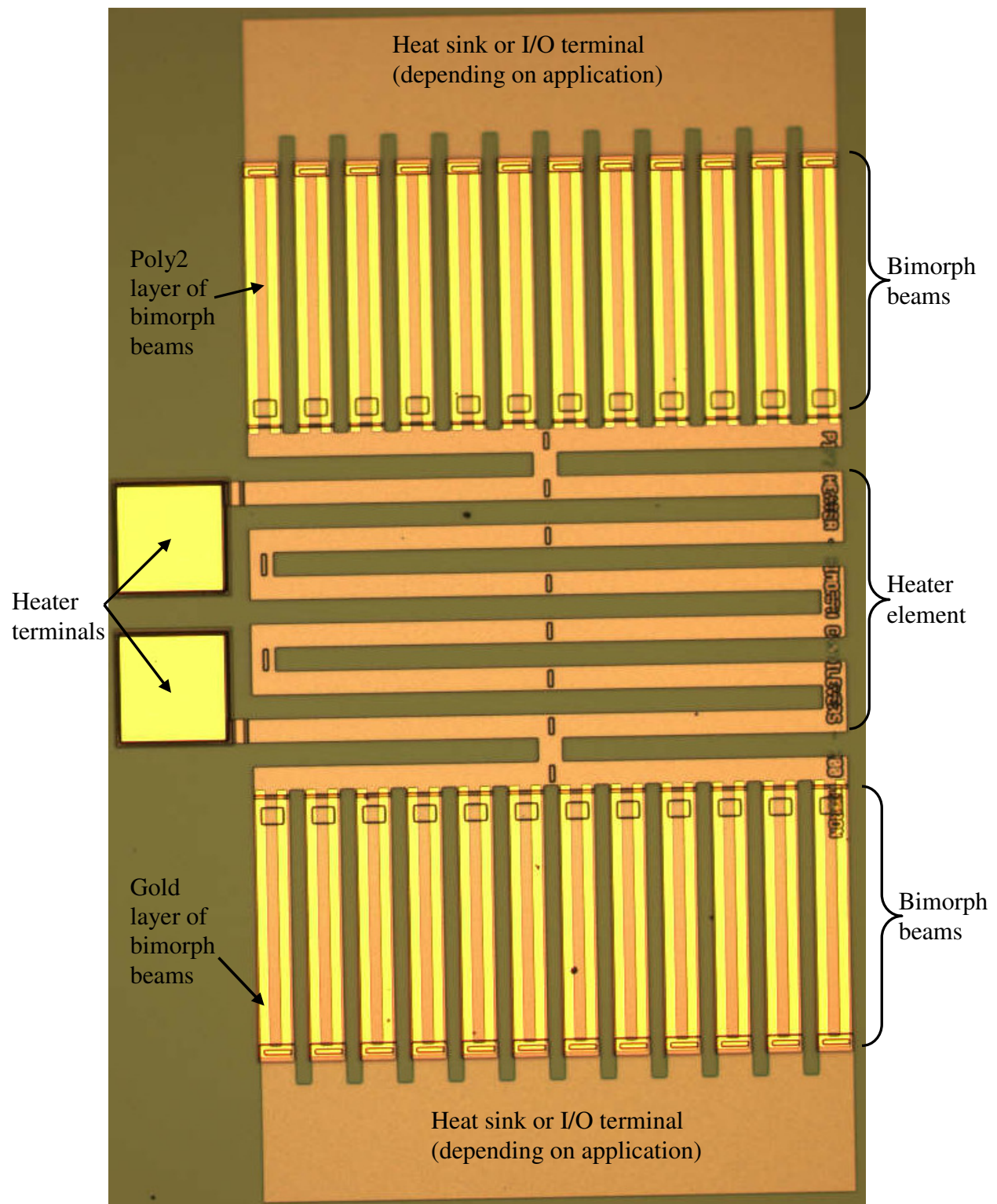


Figure A.2: 200 μm version of bimorph cantilever beam based thermal metamaterial prototype after release.

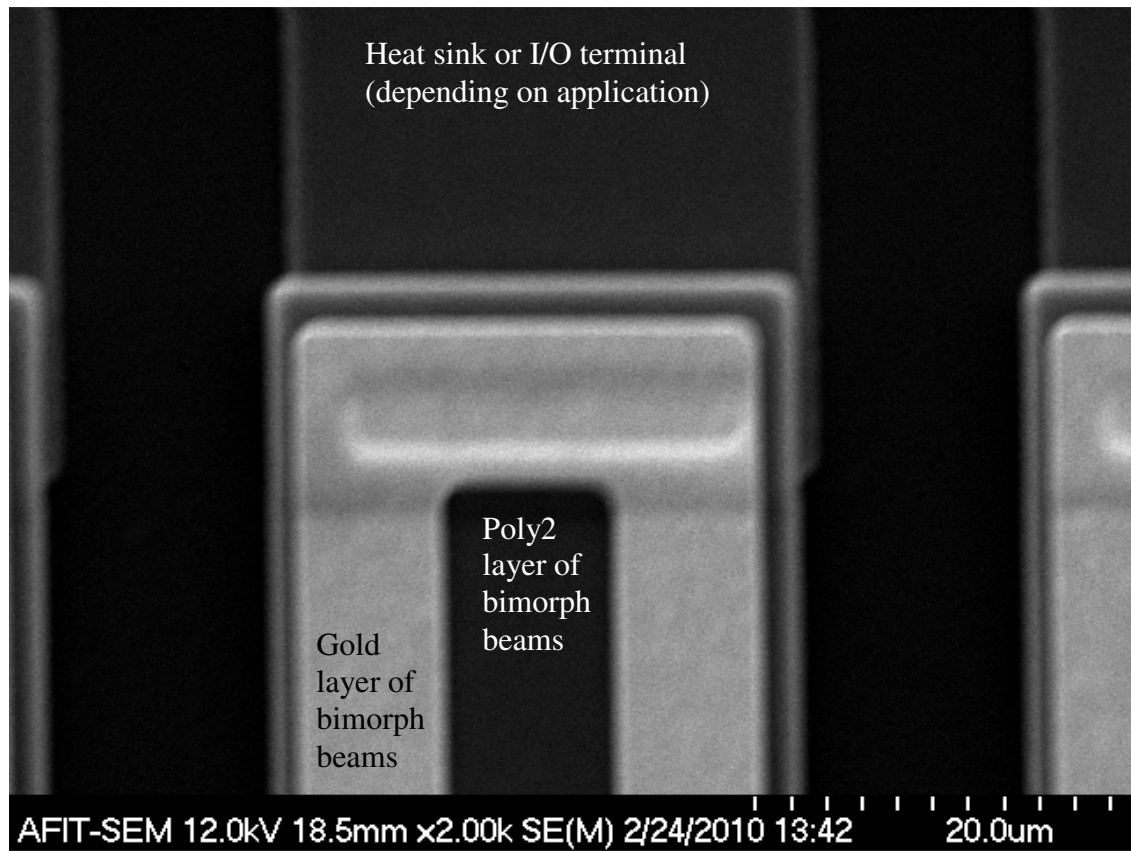


Figure A.3: SEM image of 200 μ m version of bimorph cantilever beam based thermal metamaterial prototype showing detail near the beam tip.

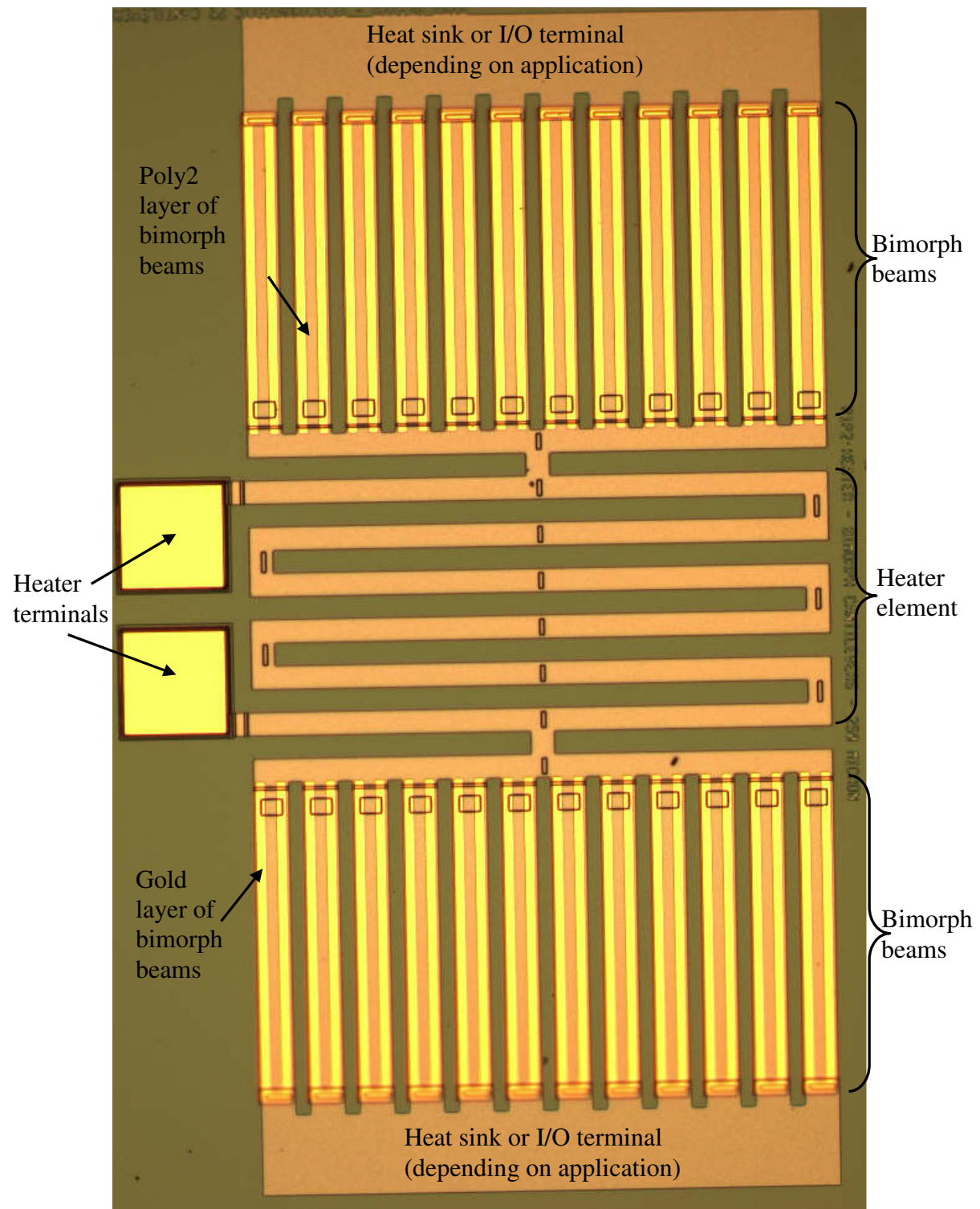


Figure A.4: $250 \mu\text{m}$ version of bimorph cantilever beam based thermal metamaterial prototype after release. Beam tips appear out of focus due to their significant upward curl at room temperature.

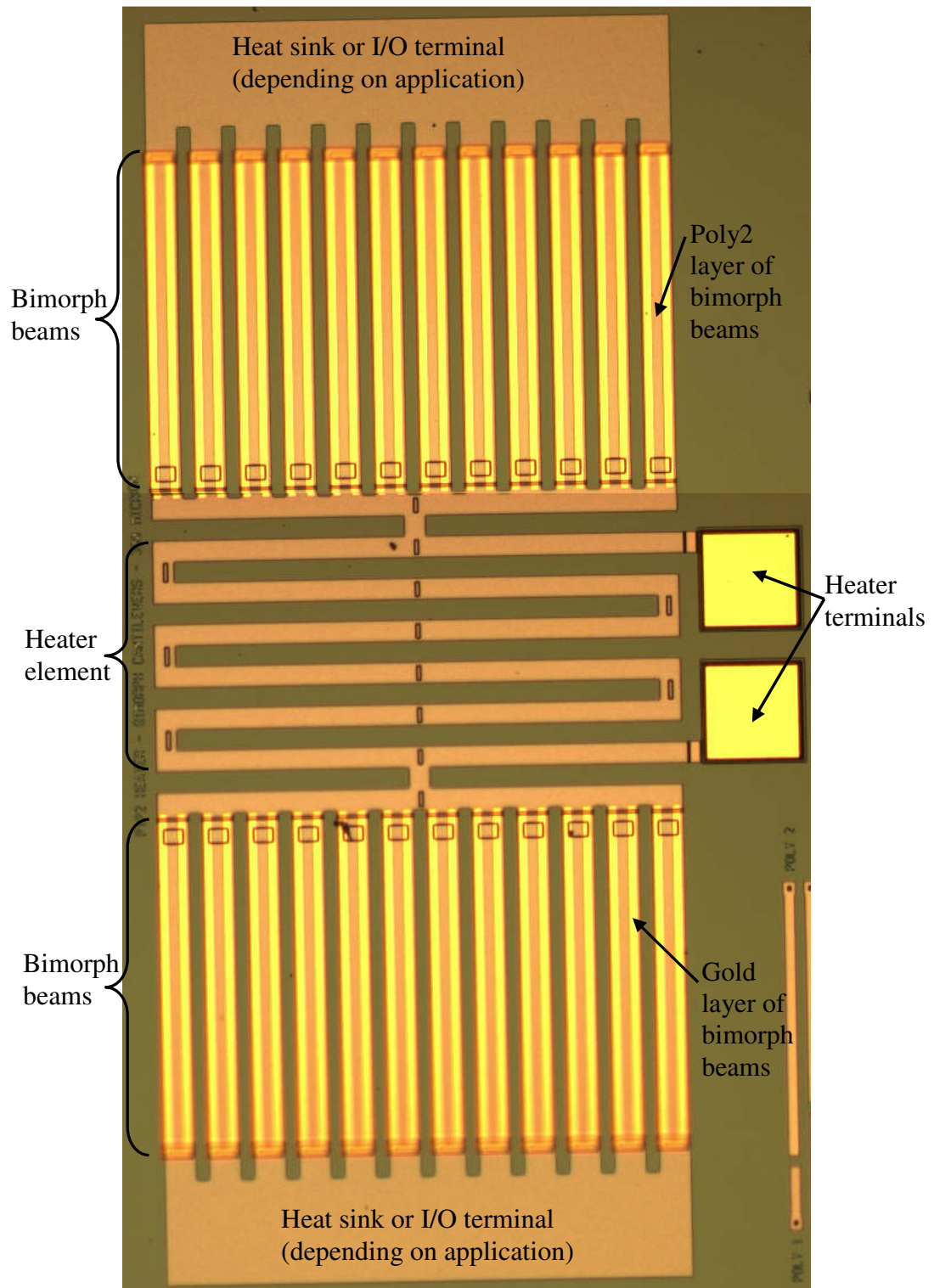


Figure A.5: 300 μm version of bimorph cantilever beam based thermal metamaterial prototype after release. Beam tips appear out of focus due to their significant upward curl at room temperature.

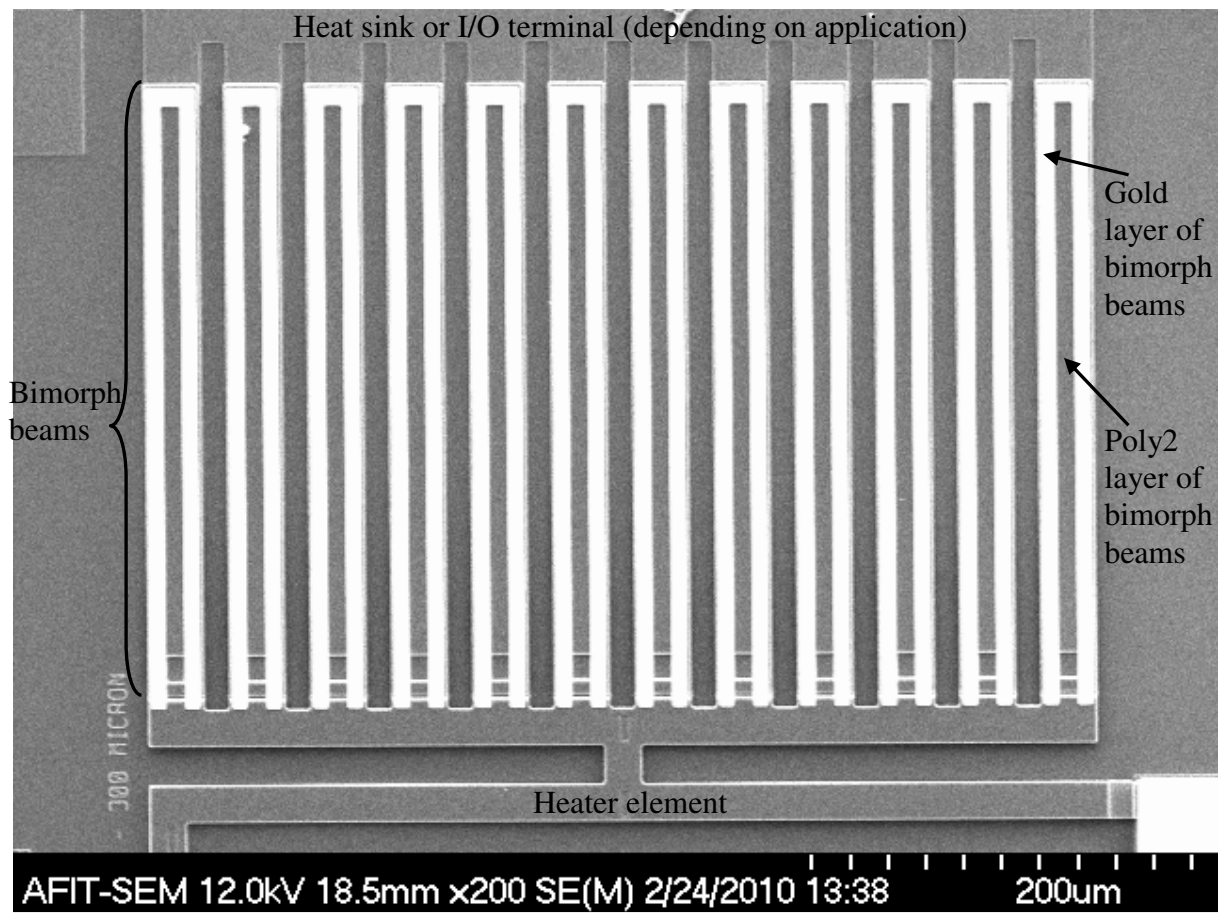


Figure A.6: SEM image of the 300 μ m version of bimorph cantilever beam based thermal metamaterial prototype after release.

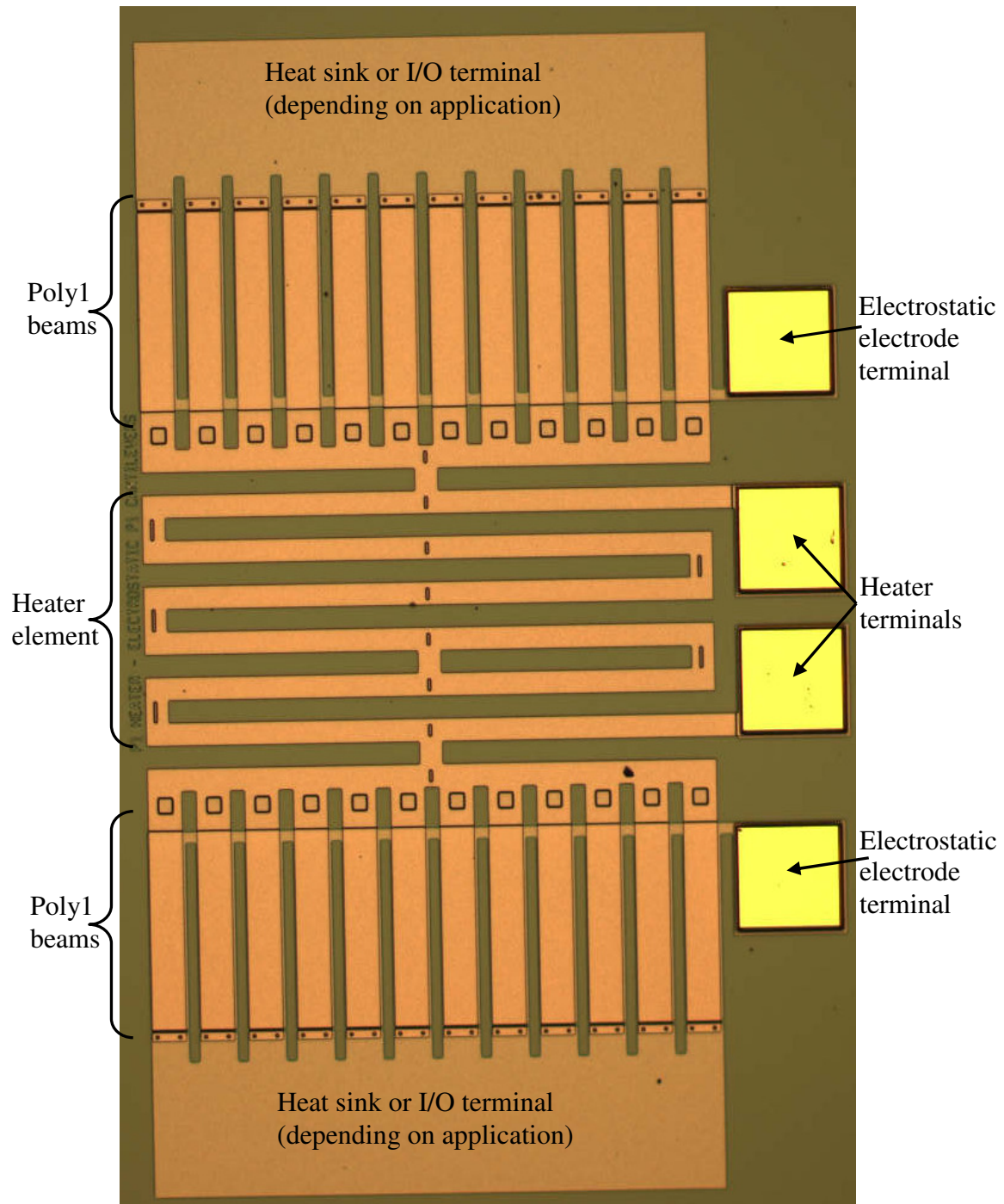


Figure A.7: Version 1 of the electrostatic actuated cantilever beam based thermal metamaterial prototypes after release. This version features Poly1 beams and a Poly1 heater grid.

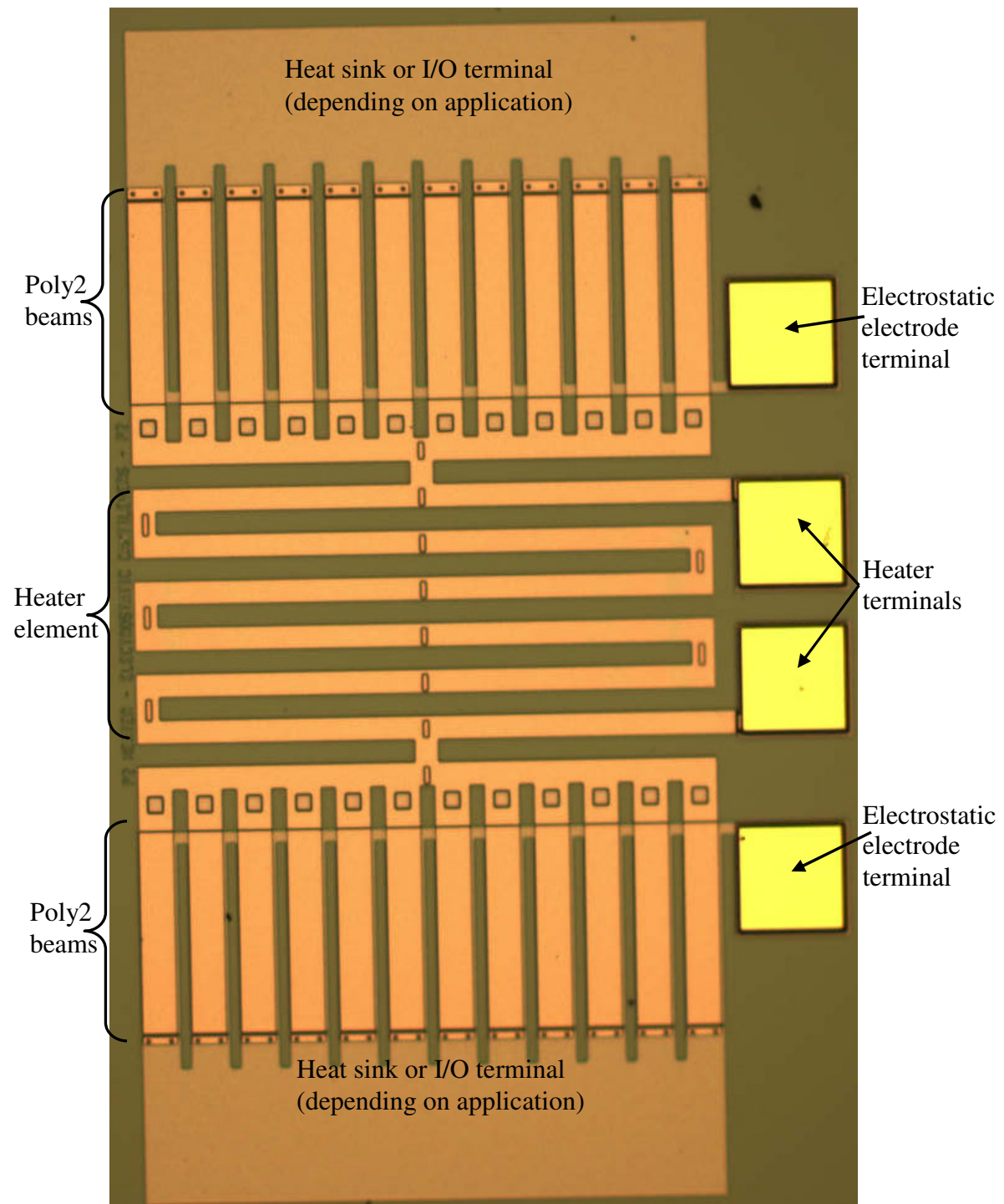


Figure A.8: Version 2 of the electrostatic actuated cantilever beam based thermal metamaterial prototypes after release. This version features Poly2 beams and a Poly2 heater grid.

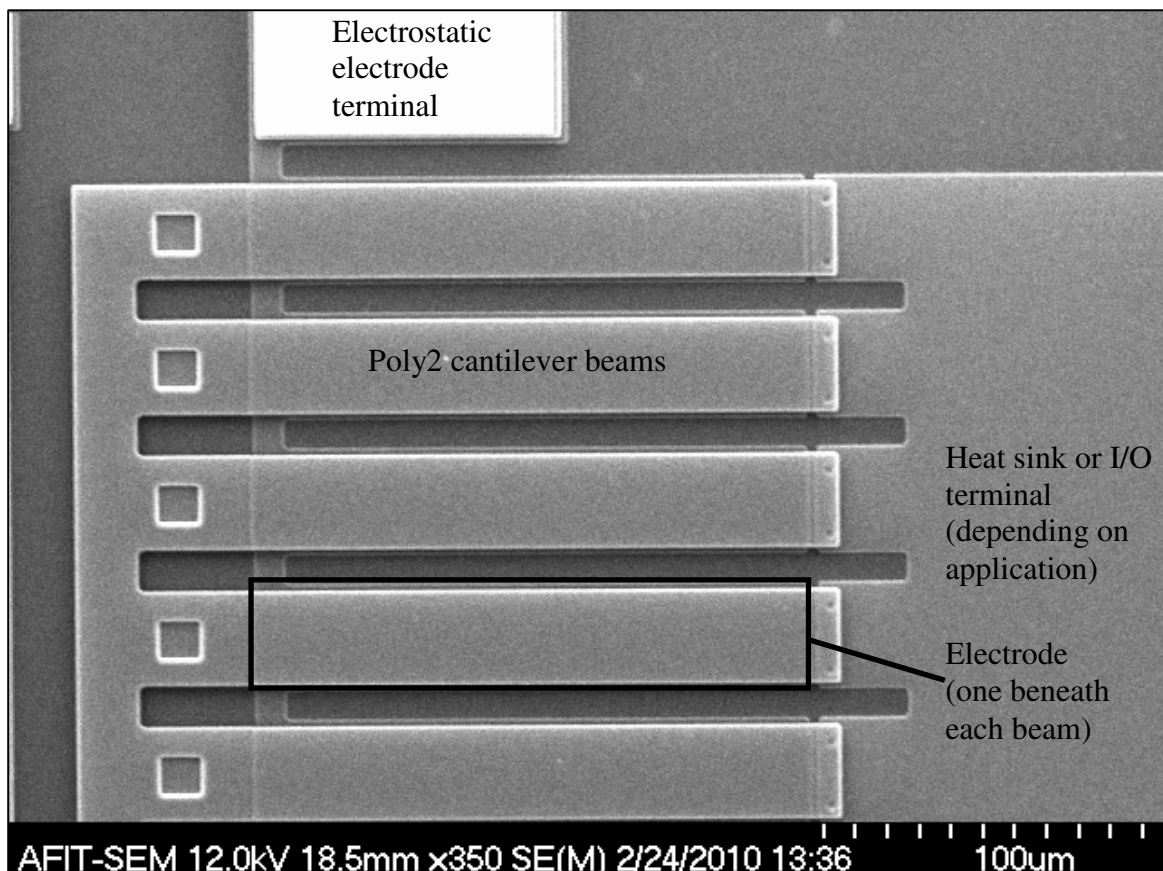


Figure A.9: SEM image of version 2 of the electrostatic actuated cantilever beam based thermal metamaterial prototypes showing detail of the cantilever beams and electrodes.

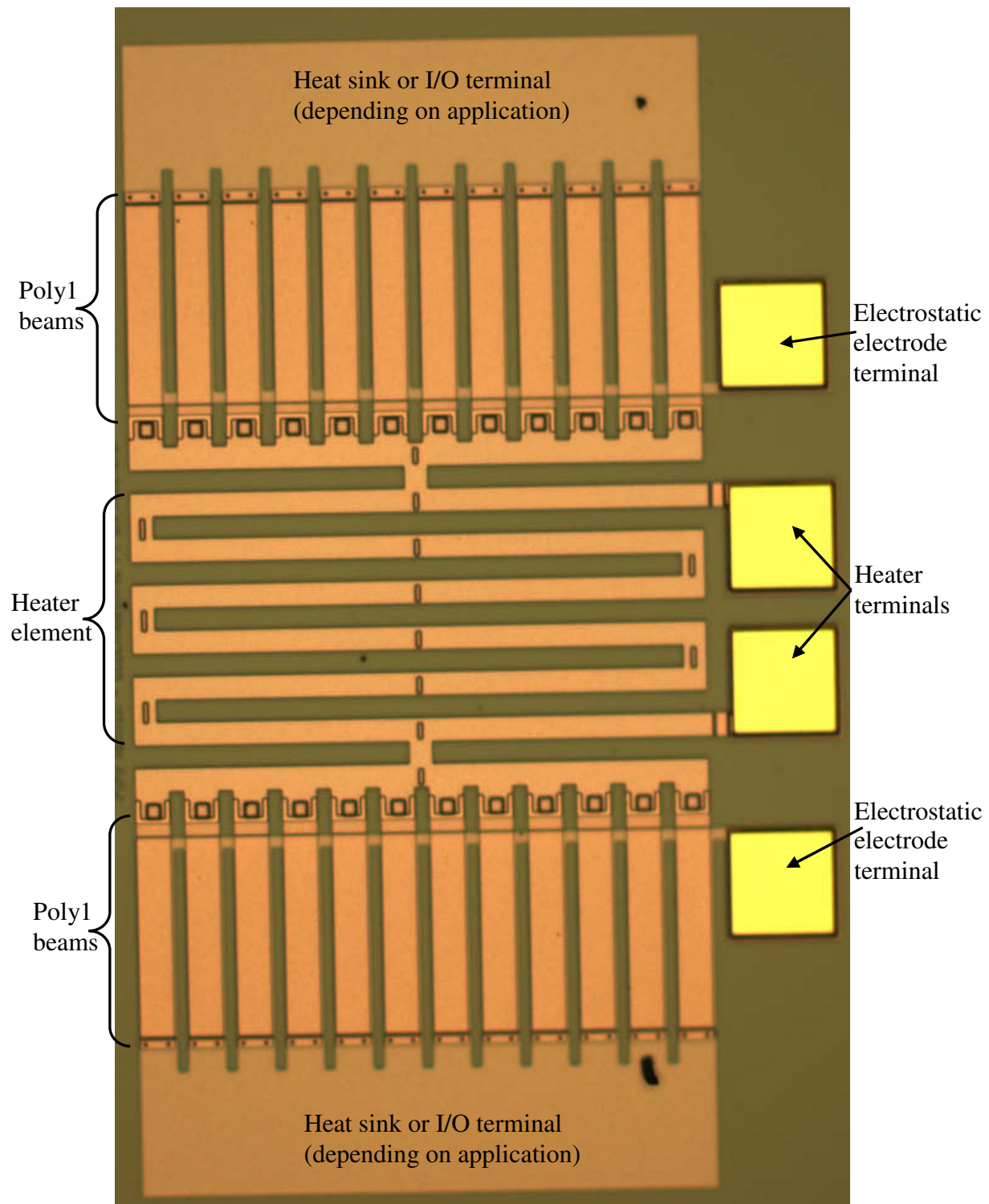


Figure A.10: Version 3 of the electrostatic actuated cantilever beam based thermal metamaterial prototypes after release. This version features Poly1 beams and a two-layer (Poly1/Poly2 stacked) heater.

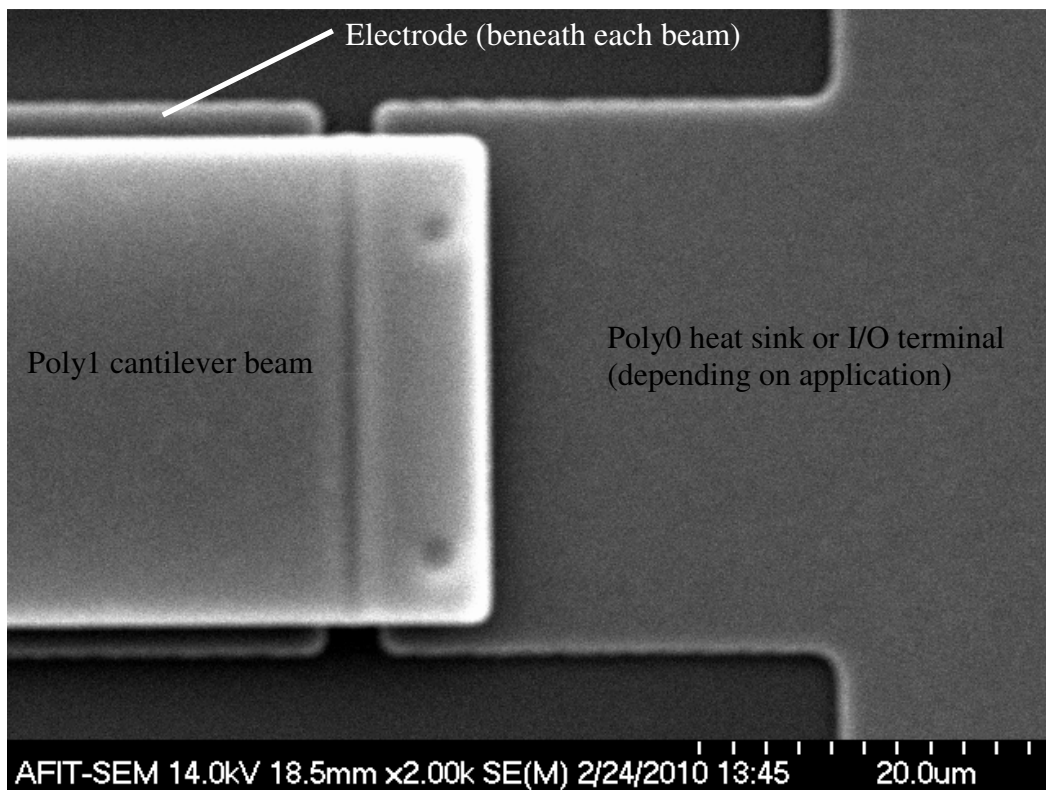


Figure A.11: SEM image of version 3 of the electrostatic actuated cantilever beam based thermal metamaterial prototypes showing detail of the cantilever beam tip.

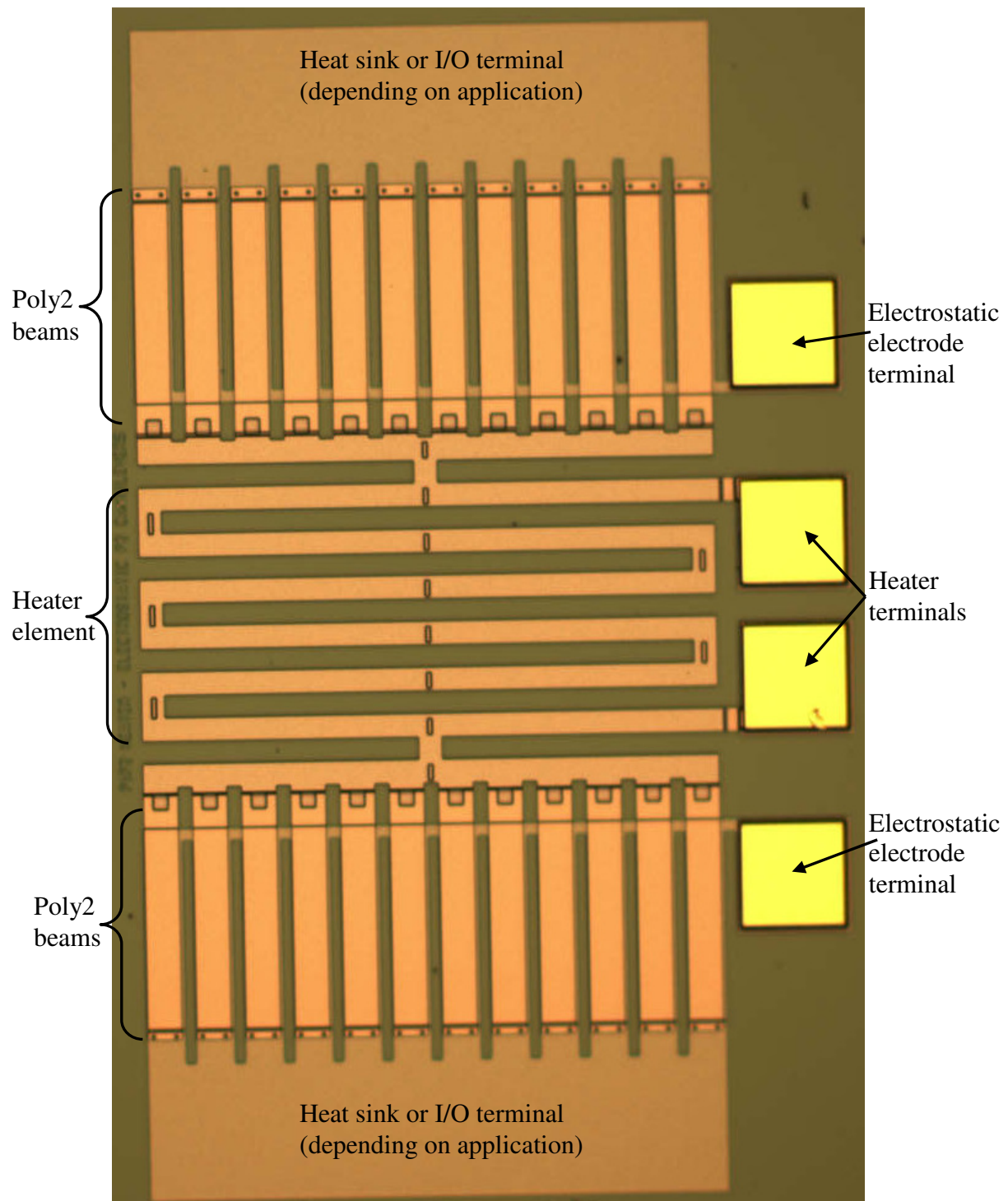


Figure A.12: Version 4 of the electrostatic actuated cantilever beam based thermal metamaterial prototypes after release. This version features Poly2 beams and a two-layer (Poly1/Poly2 stacked) heater.

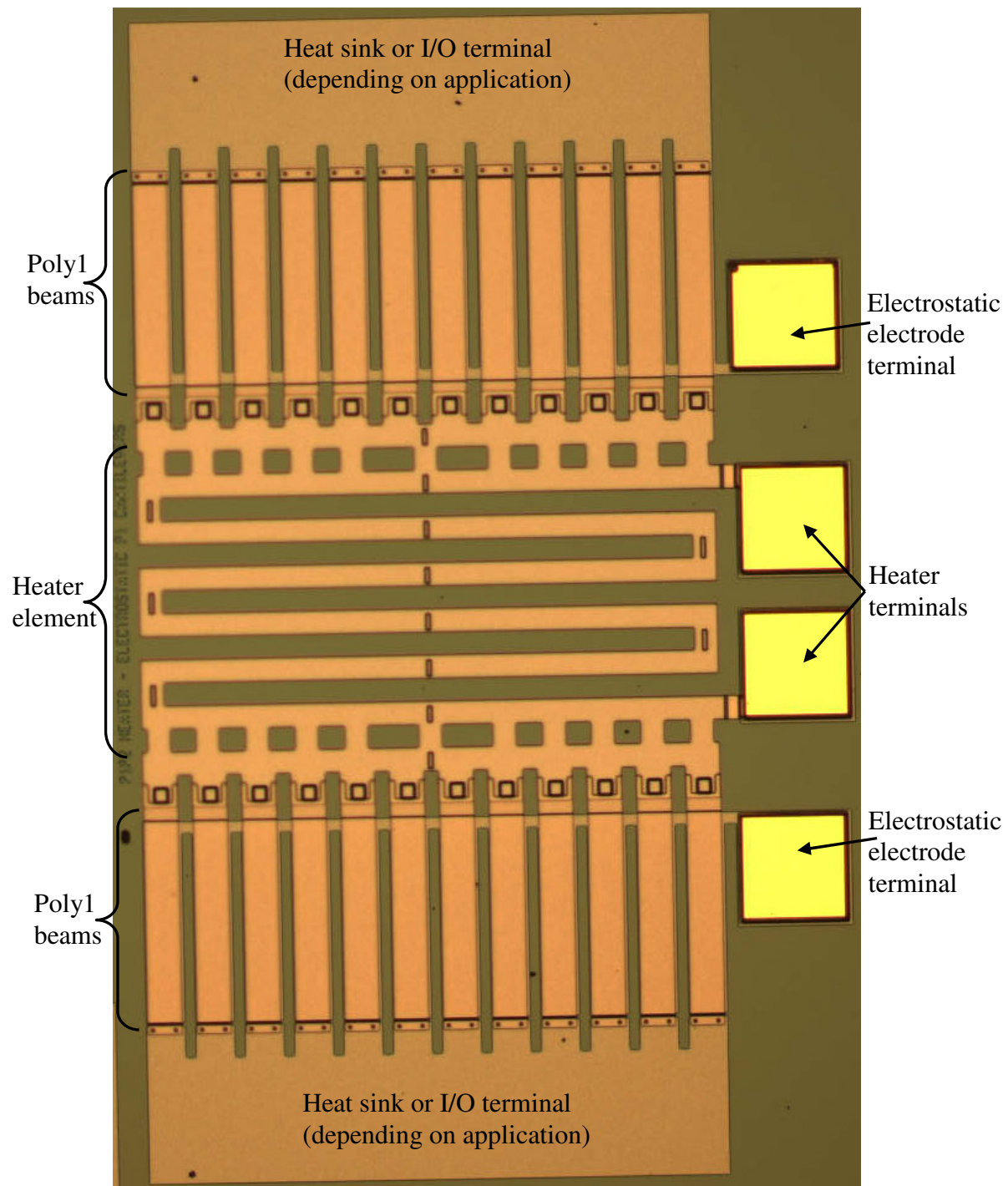


Figure A.13: Version 5 of the electrostatic actuated cantilever beam based thermal metamaterial prototypes after release. This version features Poly1 beams and a modified, two-layer heater grid (Poly1/Poly2 stacked).

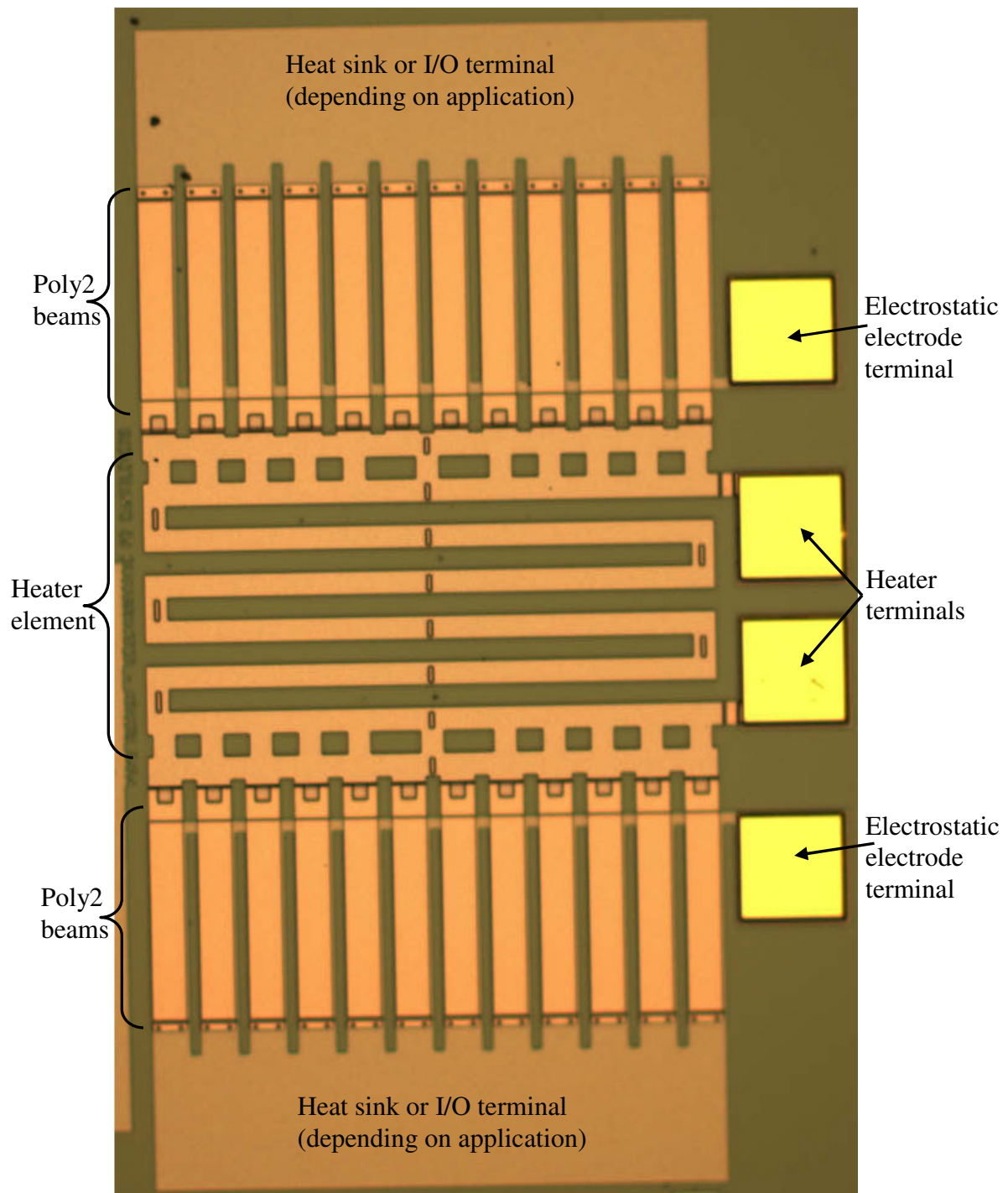


Figure A.14: Version 6 of the electrostatic actuated cantilever beam based thermal metamaterial prototypes after release. This version features Poly2 beams and a modified, two-layer heater grid (Poly1/Poly2 stacked).

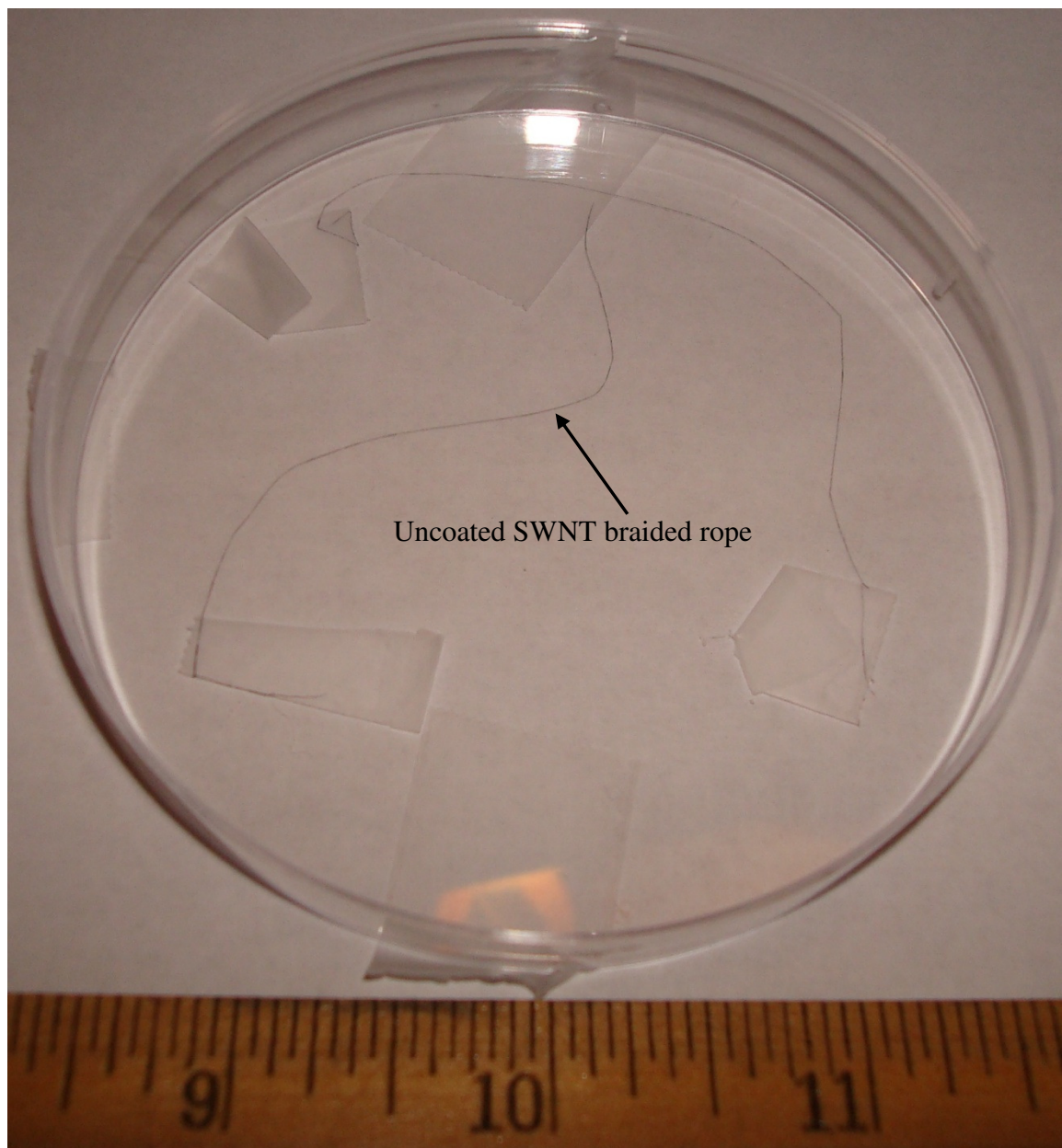


Figure A.15: Uncoated SWNT braided rope.

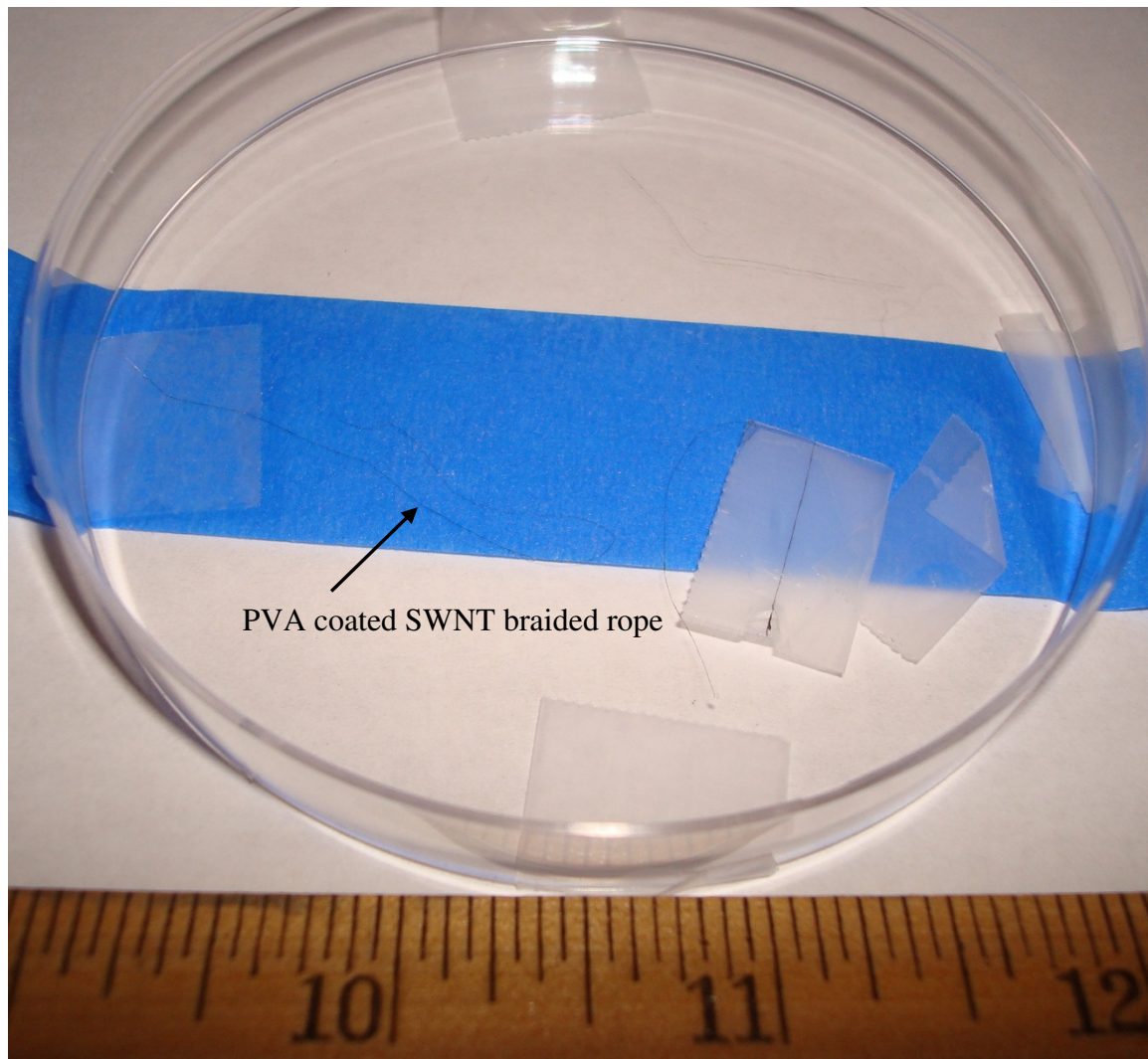


Figure A.16: PVA coated SWNT braided rope.

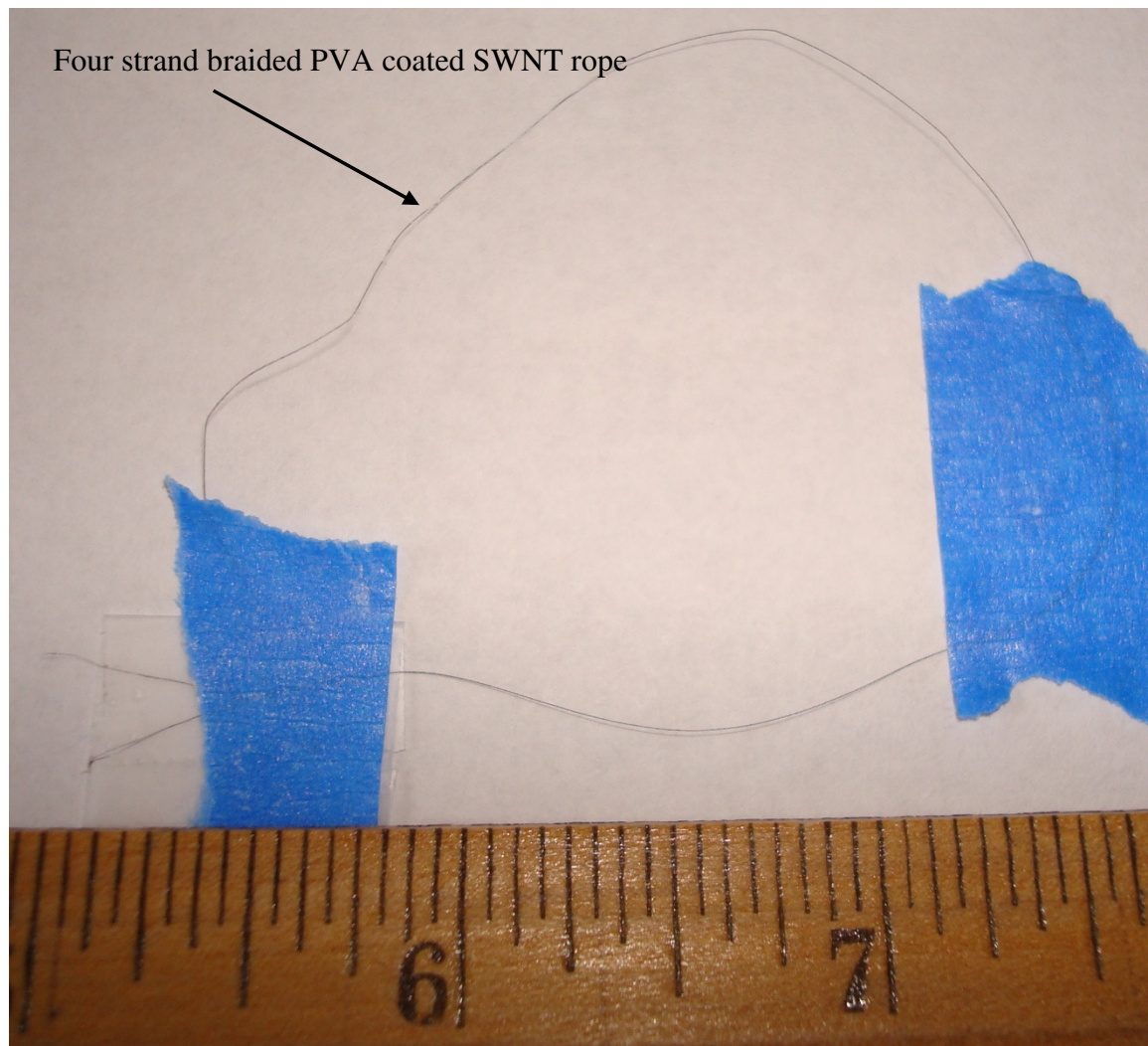


Figure A.17: Four braided (1X4) PVA coated SWNT ropes.

References

- [1] Engheta, N., Ziolkowski, R. "Metamaterials, Physics and Engineering Explorations." Wiley Interscience. 2006.
- [2] "Electromagnetic Metamaterials." Meta Group, Duke University. 2009. <http://people.ee.duke.edu/~drsmith/about_metamaterials.html>.
- [3] Dudis, D. "Metamaterials for Thermo-electrical Control in Laminated Architectures." Air Force Research Lab, Nonstructural Materials Branch presentation. Aug 2009.
- [4] Carter, J., Cowen, A, Busbee, H., *et al*, "PolyMUMPs™ Design Handbook," Revision 11.0. MEMSCAP Inc. 2005.
- [5] Nave, R. "Heat Transfer." Georgia State University Physics Department. 2005. <<http://hyperphysics.phy-astr.gsu.edu/hbase/thermo/heatra.html>>.
- [6] Dechev, N. "MECH 466 Microelectromechanical Systems Home Page." University of Victoria, Department of Mechanical Engineering. 2009. <<http://www.me.uvic.ca/~mech466/>>.
- [7] Bordia, R. "MSE 311 Class Slides, Laboratory 9, Thermal Conductivity Laboratory." University of Washington, Department of Materials Science and Engineering. 2004.
- [8] "PolyMUMPs material properties database." CoventorWare MEMS. 2009.
- [9] Wang, Z. "Thermal diffuse scattering in sub-angstrom quantitative electron microscopy – phenomenon, effects, and approaches." Micron, Volume 34, 141-155. 2003.
- [10] Lott, C. "Electrothermomechanical Modeling of a Surface Micromachined Linear Displacement Microactuator." Master's thesis, Brigham Young University, Aug 2001.
- [11] "PolyMUMPS FAQ Revision 2.0." MEMSCAP. 2004. <www.memscap.com/mumps/documents/PolyMUMPs.faq.v2.pdf>.
- [12] Stojanovic, N., Yun, J., Washington, E., Berg, J. "Thin-Film Thermal Conductivity Measurement Using Microelectrothermal Test Structures and Finite Element Model Based Data Analysis." Journal of MEMS Systems, Vol. 16, No. 5. Oct 2007.

- [13] "Air Properties: Temperature, density, specific heat, thermal conductivity, expansion coefficient, kinematic viscosity and Prandtl's number for temperatures ranging -150 - 400 °C." The Engineering Toolbox. 2005. <http://www.engineeringtoolbox.com/air-properties-d_156.html>.
- [14] Yovanovich, M., Culham, J., Teertstra, P. "Calculating interface resistance." Cooling Zone, Thermal Management of Electronics. 2005. <<http://www.coolingzone.com/library.php?read=369>>.
- [15] Bookrags Staff. "Thermal Radiation." 2005. <<http://www.bookrags.com/research/thermal-radiation-wop/>>.
- [16] Cengel, Y. "Heat Transfer: a Practical Approach, 2nd edition." McGraw-Hill. 2003.
- [17] "Electromagnetic Spectrum." Wikipedia Article. 2009. <http://en.wikipedia.org/wiki/Electromagnetic_spectrum>.
- [18] Kruschwitz, J. "High Reflectors, Thin Film Design & Applications." 2009. <<http://www.kruschwitz.com/HR's.htm>>.
- [19] Zou, J., Balberg, M., Byrne, C., Liu, C. "Optical Properties of Surface Micromachined Mirrors with Etch Holes." Journal of MEMS Systems, Vol. 8, No. 4. Dec 1999.
- [20] Xhang, X., Mehra, A., Ayon, A. "Development of Polysilicon Igniters and Temperature Sensors for a Micro Gas Turbine Engine." Massachusetts Institute of Technology, Department of Aeronautical Engineering. <web.mit.edu/aeroastro/.../publications/Mems02_paper2.pdf>.
- [21] Yovanovich, M., Culham, J., Teertstra, P. "How Thermal Conductivity Relates to Electrical Conductivity." Cooling Zone, Thermal Management of Electronics. Dec 2005. <<http://www.coolingzone.com/library.php?read=445>>.
- [22] Starman, L. "EENG 596 Class Slides, Chapter 1." Air Force Institute of Technology, Department of Electrical and Computer Engineering. 2008.
- [23] Lagouge, M. "Electrostatic actuators." MEMS World. 2006. <<http://matthieu.lagouge.free.fr/mems/electrostatic.html>>.
- [24] Ledet, M. "Utilizing Microelectromechanical Systems (MEMS) Micro-Shutter Designs for Adaptive Coded Aperture Imaging (ACAI) Technologies." Master's thesis, Air Force Institute of Technology. Mar 2009.

- [25] Seeger, J., Boser, B. "Dynamics and Control of Parallel Plate Actuators Beyond the Electrostatic Instability." *Transducers '99, 10th International Conference on Solid State Sensors and Actuators*, pp 474-477. Jun 1999.
- [26] Butler, J. "Development and Packaging of Microsystems Using Foundry Services." Dissertation, Air Force Institute of Technology. Aug 1998.
- [27] Zheng, L., O'Connell, M., Doorn, S. "Ultralong Single-Wall Carbon Nanotubes." *Nature.com*. Sep 2004. <<http://www.nature.com/nmat/journal/v3/n10/abs/nmat1216.html>>.
- [28] Ajayan, P., Zhou, O. "Applications of Carbon Nanotubes". *Applied Physics*. 2001, Vol. 80.
- [29] Monthioux, M. "Who should be given credit for the discovery of carbon nanotubes." *Science Direct*. Mar 2006. <http://www.sciencedirect.com/science?_ob=ArticleURL&_udi=B6TWD-4JWMT99-1&_user=10&_rdoc=1&_fmt=&_orig=search&_sort=d&_docanchor=&view=c&_acct=C000050221&_version=1&_urlVersion=0&_userid=10&md5=fb304cd36ec29449ec183cd4940710b>.
- [30] Martel, R. "Single and multi wall carbon nanotube field effect transistors." 2447-2449, *Applied Physics Letters*, 1998, Vol. 73.
- [31] NEC. "Tests verify carbon nanotube enable ultra high performance transistor." Sep 2003. <<http://www.nec.co.jp/press/en/0309/1901.html>>.
- [32] Kanellos, M. "Carbon nanotubes enter Tour de France." *Cnet News*. July 2006. <http://news.cnet.com/Carbon-nanotubes-enter-Tour-de-France/2100-11395_3-6091347.html?tag=fd_cars1>.
- [33] Holister, P., Harper, T. "Nanotubes." *CMP Cientifica*. Las Rozas, Spain. 2003.
- [34] New World Encyclopedia. "Carbon Nanotube". *New World Encyclopedia*. Mar 2009. <http://www.newworldencyclopedia.org/entry/Carbon_nanotube>.
- [35] Staii, C. "Carbon Nanotubes: a brief introduction." Jun 2005. <http://www.princeton.edu/~cstaii/CN/Carbon_nanotubes.html>.
- [36] Electro-optic systems laboratory, Georgia Tech Research Institute. "Information on carbon nanotubes." Electro-optic systems laboratory. Aug 2009. <<http://nano.gtri.gatech.edu/index.html>>.
- [37] Daenen, M. "Wonderous world of carbon nanotubes." Eindhoven University of Technology. Feb 2003. <<http://students.chem.tue.nl/ifp03/synthesis.html>>.

- [38] Wilson, M. "Nanotechnology: Basic Science and Emerging Technologies." Taylor & Francis, Inc. New York, NY. 2002.
- [39] Lee, Y. H. "Yarns from Carbon Nanotube Forest." Center for Nanotubes and Nanostructured Composites, Sungkyunkwan Advanced Institute of Nanotechnology, Sungkyunkwan University. 2009.
- [40] Wong, N. "Thermal Control of Micro/Nano Spacecraft Using MEMS Technology." University of California, San Diego, Department of Mechanical Engineering. Dec 2007. <<http://www.scribd.com/doc/19885449/Thermal-Control-of-Micro-Nano-Spacecraft-Using-MEMS-Technology>>.

Vita

Captain Calvin Roman is a graduate electrical engineering student at the Air Force Institute of Technology, Wright-Patterson Air Force Base (AFB). His degree focus is in microelectronics fabrication and MEMS. Calvin's previous assignments include two years as a spacecraft systems engineer, assigned to the Special Projects Directorate of the Cryptologic Systems Group, Lackland AFB. He spent 2.5 years working as a test engineer and later as a test manager at the 746th Test Squadron, 46th Test Group, Holloman AFB. While at the 746th Test Squadron, he worked on a variety of GPS and MEMS-based inertial navigation system (INS) test programs. In 2001, Calvin was selected for the Airman Education and Commissioning Program (AECP) to complete a bachelor's degree in electrical engineering. He attended the University of Florida (UF), and graduated Cum Laude in 2003. From 1994-2001, Calvin worked as an aircraft avionics systems technician, assigned to the 16th Special Operations Wing at Hurlburt Field. While at the 16th SOW, he deployed with Joint Special Operations Task Force Two for Operation Joint Guard as part of an AC-130U gunship maintenance team. In 1994, he completed Basic Training at Lackland AFB and technical training at Keesler AFB.

Calvin was born and raised in Niagara Falls, NY. He met his wife while they were attending classes at UF in 2002. They currently have no children and two cats. Calvin's personal interests and hobbies include shooting and collecting firearms, working on cars and computers, camping and hiking, and taking cruises. His professional interests include spacecraft radiation shielding design and analysis, spacecraft communication system design, GPS/INS aided munitions design, and cryptography design.

